BRNO UNIVERSITY OF TECHNOLOGY
VYSOKÉ UČENÍ TECHNICKÉ V BRNĚ

FACULTY OF MECHANICAL ENGINEERING
FAKULTA STROJNÍHO INŽENÝRSTVÍ

INSTITUTE OF PHYSICAL ENGINEERING
ÚSTAV FYZIKÁLNÍHO INŽENÝRSTVÍ

MULTIPHOTON AND NON-LINEAR RAMAN MICROSCOPY THROUGH A MULTIMODE FIBRE
VÍCEFOTONOVÁ A NELINEÁRNÍ RAMANOVSKÁ MIKROSKOPIE SKRZ MULTIMODOVÉ VLÁKNO

DOCTORAL THESIS
DIZERTAČNÍ PRÁCE

AUTHOR — **Ing. Tomáš Pikálek**
AUTOR PRÁCE

SUPERVISOR — **prof. Mgr. Tomáš Čižmár, Ph.D.**
ŠKOLITEL

BRNO 2023

Summary
Multimode fibres have recently shown promise as miniature endoscopic probes for imaging deep inside brain tissue of mouse animal models with minimal damage. By employing wavefront shaping, the speckle pattern associated with coherent light propagation through a multimode fibre can be transformed into a tightly focused point, essentially turning the fibre into a miniature point-scanning device. Many microscopic techniques have been successfully implemented through a multimode fibre, and even in-vivo imaging has been demonstrated. This work extends the capabilities to label-free non-linear microscopy with chemical contrast using coherent anti-Stokes Raman scattering (CARS), which can potentially extend the use of multimode fibre endoscopes to clinical applications for, for example, tumour diagnosis. The main focus is the optimisations of the endoscopic system and the fibre probe to allow efficient focusing of pulsed light through multimode fibres, including dispersion control and thus allowing implementation of non-linear imaging techniques. The optimised setup is then employed to demonstrate CARS imaging of biologically relevant tissue, such as myelinated axons in a mouse brain, and chemical selectivity is verified by imaging polymer beads. In addition, multimodal CARS and two-photon excitation fluorescence (TPEF) imaging of fixed mouse tissue is demonstrated.

Abstrakt
Multimodová vlákna je možné využít jako miniaturní endoskopy pro zobrazování hluboko uvnitř mozku myších zvířecích modelů s minimálním poškozením okolní tkáně. S využitím metod tvarování vlnoplochy je možné svazek vystupující z vlákna fokusovat do jediného bodu, a vytvořit tak miniaturní skenovací mikroskop. Různé mikroskopické zobrazovací metody již byly tímto způsobem implementovány, a to včetně několika in-vivo demonstrací. Tato práce se zabývá implementací zobrazování pomocí koherentního anti-Stokesova Ramanova rozptylu (CARS), nelineární metody umožňující zobrazování s chemickým kontrastem bez značení vzorku. Tato metoda má potenciální využití pro klinické aplikace například při diagnóze nádorů. Práce je zaměřena zejména na optimalizaci endoskopu a vláknových sond pro fokusaci světla z pulzních laserů včetně kontroly disperze s cílem umožnit nelineární zobrazování. Takto optimalizovaný systém je následně využit pro demonstraci zobrazování metodou CARS uvnitř tkáně (například lipidové dvojvrstvy buněčných membrán kolem axonů) a chemického kontrastu na polymerových kuličkách. Systém je též použit k demonstraci multimodálního zobrazování fixované myší tkáně kombinací CARS a dvoufotonové mikroskopie.

Keywords
multimode fibre imaging, endoscopy, non-linear microscopy, two-photon excitation fluorescence (TPEF), coherent anti-Stokes Raman spectroscopy (CARS)

Klíčová slova
zobrazování multimodovým vláknem, endoskopie, nelineární mikroskopie, dvoufotonová mikroskopie, koherentní anti-Stokesův Ramanův rozptyl

PIKÁLEK, Tomáš. *Multiphoton and non-linear Raman microscopy through a multimode fibre*. Brno, 2023. 163 pp. Doctoral thesis. Brno University of Technology. Faculty of Mechanical Engineering. Supervisor Tomáš ČIŽMÁR.

I hereby declare that I have written the Doctoral Thesis titled *Multiphoton and non-linear Raman microscopy through a multimode fibre* independently, under the guidance of my supervisor, prof. Mgr. Tomáš Čižmár, Ph.D., and using the sources listed in references.

Ing. Tomáš Pikálek

I want to express my most profound appreciation to Tomáš Čižmár and Johanna Trägårdh for their support and guidance throughout the project. Many thanks to other members of the Complex Photonics group at the Institute of Scientific Instruments of the Czech Academy of Sciences, namely Miroslav Stibůrek for the fibre splicing and preparation of the composite probes, Stephen Simpson for numerical simulations of light propagation through the composite fibre probe, Petr Jákl for the development of the camera toolbox, Martin Šiler for the development of the CUDA library for hologram generation, Petra Kolbábková for polishing some of the fibres, Petra Ondráčková and Tereza Tučková for harvesting the mice, Angel Cifuentes for using the system developed in this thesis for SHG imaging, Hana Uhlířová for help with the biology-related terminology in the tissue imaging section, Pavel Zemánek for valuable comments on this thesis and Hana Štolzová for long discussions on calculating the power ratio. Special thanks to Soňa Palečková for helping with all the paperwork associated with the Gate project. I would also like to recognise Rodrigo Amezcua-Correa and José Enrique Antonio-Lopez from The College of Optics and Photonics, University of Central Florida, for providing their custom-drawn graded-index fibres, and Tobias Meyer, Denis Akimov and Jürgen Popp from Leibniz Institute of Photonic Technology for giving us access to their laboratory and laser system. I would be remiss if I did not mention Zdeněk Buchta for supervising me during the beginning of my PhD studies and finding me a job in the Complex Photonics group.

The work was supported from European Regional Development Fund-Project *Holographic endoscopy for in vivo applications* (no. CZ.02.1.01/0.0/0.0/15_003/0000476).

Ing. Tomáš Pikálek

Contents

Introduction

Scattering effects make biological tissue mostly opaque to light, limiting the maximal depth for optical imaging. For state-of-the-art multiphoton imaging techniques and brain tissue, the penetration depth can exceed several hundred of micrometres (for two-photon excitation fluorescence) or even a millimetre (for three-photon excitation) [1–7].

While the development in focusing through complex media could overcome some of the scattering effects [8–10], the maximal imaging depth while maintaining subcellular resolution is still limited. Since other non-invasive imaging approaches, such as computed tomography or magnetic resonance imaging, do not allow for sufficient resolution, imaging deeper requires bringing the imaging instrument closer to the target area. Endoscopes are often used to reduce the damage to the surrounding tissue [11], typically based on fibre bundles [12–14] or graded-index (GRIN) lenses [15–25]. The diameter of such endoscopes starts at several hundreds of micrometres, making the impact on the tissue relatively large.

Advances in wavefront shaping have provided tools to transform a single multimode fibre into a miniature endoscope [26, 27]. The diameter of such fibre is typically in the range of 100 μm, and the numerical aperture of the fibre determines the spatial resolution of the endoscope [28, 29]. These properties make multimode fibres suitable for minimally invasive imaging deep inside sensitive tissue.

Practically, imaging through multimode fibres is not as straightforward as using a GRIN lens, for example, as images are not preserved when light is propagated through the fibre. Instead, when coherent light is coupled into one end of a multimode fibre, a seemingly random speckle pattern can be observed at the other end. To overcome this issue, the excitation beam coupled into the fibre is typically spatially modulated using a spatial light modulator [30, 31] to create a focus in the sample plane. Since a point can be generated at any position in the sample, it can also be raster-scanned, mimicking a point-scanning microscope. Creating the foci, however, requires the light propagation through the fibre to be characterised in advance. This calibration procedure can take several minutes, depending on the parameters of the fibre. It can be usable for several hours if the beam projected to the proximal end is stable [32], sufficiently long enough for many practical applications.

Due to their small diameter, multimode fibres are very flexible, making them good candidates for imaging in freely-moving animals. Unfortunately, the light propagation in the fibre depends on its shape, making the calibration very bent-sensitive [33–35]. Efforts have been seen to dynamically compensate for the effects using a coherent beacon source [36] or a partial reflector [37] at the distal end of the fibre. In addition, it has been shown that graded-index fibres are significantly less bent-sensitive than step-index fibres [38]. Nevertheless, the bend resilience demonstrated so far has not reached the level necessary for imaging using a long non-static fibres. Consequently, the fibres used for imaging are typically only a few centimetres long. Nevertheless, this is more than

sufficient for imaging, for example, throughout the whole depth of a head-fixed mouse brain.

Imaging techniques implemented to this date through a single multimode fibre include fluorescence imaging [39, 40], including in-vivo demonstrations [41–43], volumetric fluorescence imaging [44], wide-field [45], dark-field [46], far-field imaging [47], light-sheet [48], confocal imaging [49, 50], two-photon excitation fluorescence (TPEF) imaging [51–54], photoacoustic imaging [55], time-of-flight 3D imaging [56], compressive imaging [57–60] as well as label-free imaging methods such as linear Raman imaging [61, 62]. In addition, using point scanning at the end of a multimode fibre has been used for two-photon polymerisation [63] or micromanipulation [64, 65].

The goal of this thesis is the implementation of coherent anti-Stokes Raman scattering (CARS) imaging through multimode fibre. This technique allows label-free imaging with chemical contrast [66]. CARS and other non-linear techniques like TPEF and second-harmonic generation (SHG) are essential tools for performing optical biopsies for diagnosing tumours and other diseases [67]. Thus, implementing CARS through a multimode fibre would pave the way towards clinical applications of multimode fibre endoscopes.

The thesis is divided into five chapters. The first chapter in an introduction to imaging through a multimode fibre, and it describes the calibration procedure needed to turn the multimode fibre into, essentially, a laser scanning microscope that can be used to perform high-resolution imaging. In the second chapter, the endoscope is built and characterised, and its focusing performance is optimised. The other three chapters present the results of implementing non-linear imaging through a multimode fibre published in the following three papers [68–70]. In the third chapter, a wavelength-dependent characterisation of the multimode fibre endoscope is performed. The results are then used in the fourth chapter to demonstrate coherent anti-Stokes Raman scattering imaging through the multimode fibre endoscope using a picosecond laser system, and in the fifth chapter, to demonstrate multimodal two-photon excitation fluorescence and coherent anti-Stokes Raman scattering imaging through a multimode fibre using a femtosecond laser system.

1. Imaging through multimode fibres

When coherent light is coupled into a multimode fibre, a speckle pattern is created at the other end of the fibre due to the interference of different fibre modes. Therefore, in contrast to other imaging methods, an image of any object cannot be directly transported through the fibre. To use the multimode fibre as a miniature endoscopic probe for imaging, the light coupled into the fibre has to be shaped using a spatial light modulator in a way that creates a focused point at the other (distal) end of the fibre using methods known from the research on focusing through a complex media [71–74] and wavefront correction methods [75, 76]. This goal is achieved by characterising the light transport through the fibre before the imaging in a calibration procedure. A focused point can then be scanned across the imaging plane in front of the fibre, and the whole optical system can be used as a point-scanning microscope. The procedure for creating a scanning point behind a multimode fibre is discussed in this chapter.

1.1. Optical setup

A simplified drawing of the multimode fibre endoscope (here, used, for example, for fluorescence imaging) is in Figure 1.1. The beam from the laser is split into a signal beam and a reference beam. The signal beam is shaped using a spatial light modulator (SLM) which is used in off-axis configuration. In the following text, it is assumed that a phase-only liquid crystal SLM is used. The hologram displayed on the SLM is Fourier transformed using a lens. In the Fourier plane, an iris isolates the first diffraction order, which is then imaged onto the proximal facet of the fibre using a $4f$ system (a lens and an objective). The SLM is therefore placed in the far-field of the fibre facet.

It should be noted that another possible configuration of the optics focusing light into the multimode fibre can be chosen, with an even number (typically four) of lenses between the SLM and the fibre (used, for example, in [47, 77]). Thus, the SLM is imaged directly onto the input facet in this configuration. The blazed gratings on the SLM correspond to different plane waves coupled into the fibre instead of different points in the configuration used here. While for some experiments, only one of the configurations gains good results (for example, imaging in the far-field using a step-index fibre [47]), the conclusions of this thesis hold regardless of the configuration used.

If a digital micromirror device (DMD) [31, 78–80], a binary amplitude modulator, were used instead of the SLM, the procedures described in this chapter would still hold. The only difference would be that the calculated holograms would be binarised for the DMD by thresholding. Albeit DMDs are much faster than SLMs (for example, ViALUX V-7001 has a switching rate 22.7 kHz or even higher if only a part of the chip is used, compared to less than 200 Hz for Meadowlark HSP1920-1064-HSP8 liquid crystal SLM, used in this thesis), they are significantly less efficient. The lower efficiency is typically not an issue

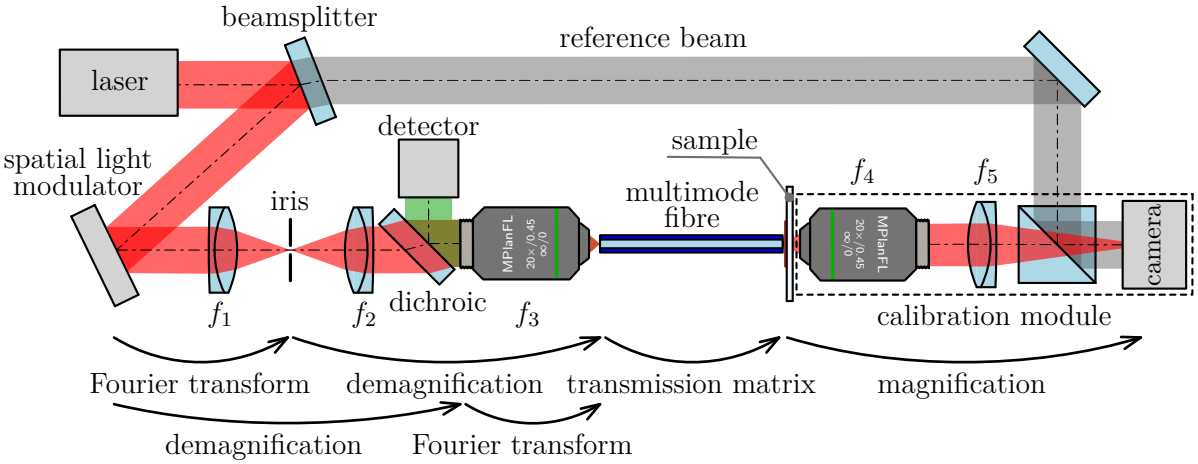

Figure 1.1: A simplified drawing of the multimode fibre endoscope.

for linear imaging, as the excitation power is typically orders of magnitude more than the output power of the laser. On the other hand, high excitation powers are often necessary for non-linear imaging techniques developed in this thesis. Hence, a liquid crystal SLM is used.

The light transport through the fibre has to be characterised in a calibration procedure to use the fibre as a point-scanning device (the calibration procedure is described in Section 1.4). This calibration requires access to the distal end of the fibre which is imaged onto a camera using another $4f$ system. The image of the distal end facet overlaps with the plane wave reference beam to measure amplitude and phase using phase-shifting interferometry. After the imaging system is calibrated, access to the distal end of the fibre is no longer needed, and the whole calibration module can be replaced with a sample. The fibre and the spatial light modulator perform as a point-scanning microscope. The signal (fluorescence, for example) is detected through the fibre on a detector placed on the proximal side.

1.2. Hologram generation

The hologram for the spatial light modulator (SLM) is generated using fast Fourier transform (FFT) [81]. Figure 1.2 shows the hologram generation procedure for a phase-only modulator placed in the far-field of the input facet of the fibre (a configuration shown in Figure 1.1. To make the individual pixels visible for the illustration, a spatial light modulator with a resolution of $64\,\mathrm{px} \times 64\,\mathrm{px}$ was assumed, about an order of magnitude lower than real spatial light modulators used in these applications. The hologram generation is demonstrated in a situation when three focused points with the same amplitude, but different phases are being generated at the input facet of the fibre.

In the first step of the hologram generation, a complex array with the exact resolution as the resolution of the SLM is allocated. The requested field is then inserted into the array. This array represents the plane at the input fibre facet. In this particular example, three elements of the array are set to non-zero values (Figure 1.2a) to create three points at the input facet of the fibre, each with a different phase. The quadrants of the array are then rearranged to prepare the array for the FFT algorithm (Figure 1.2b). The first

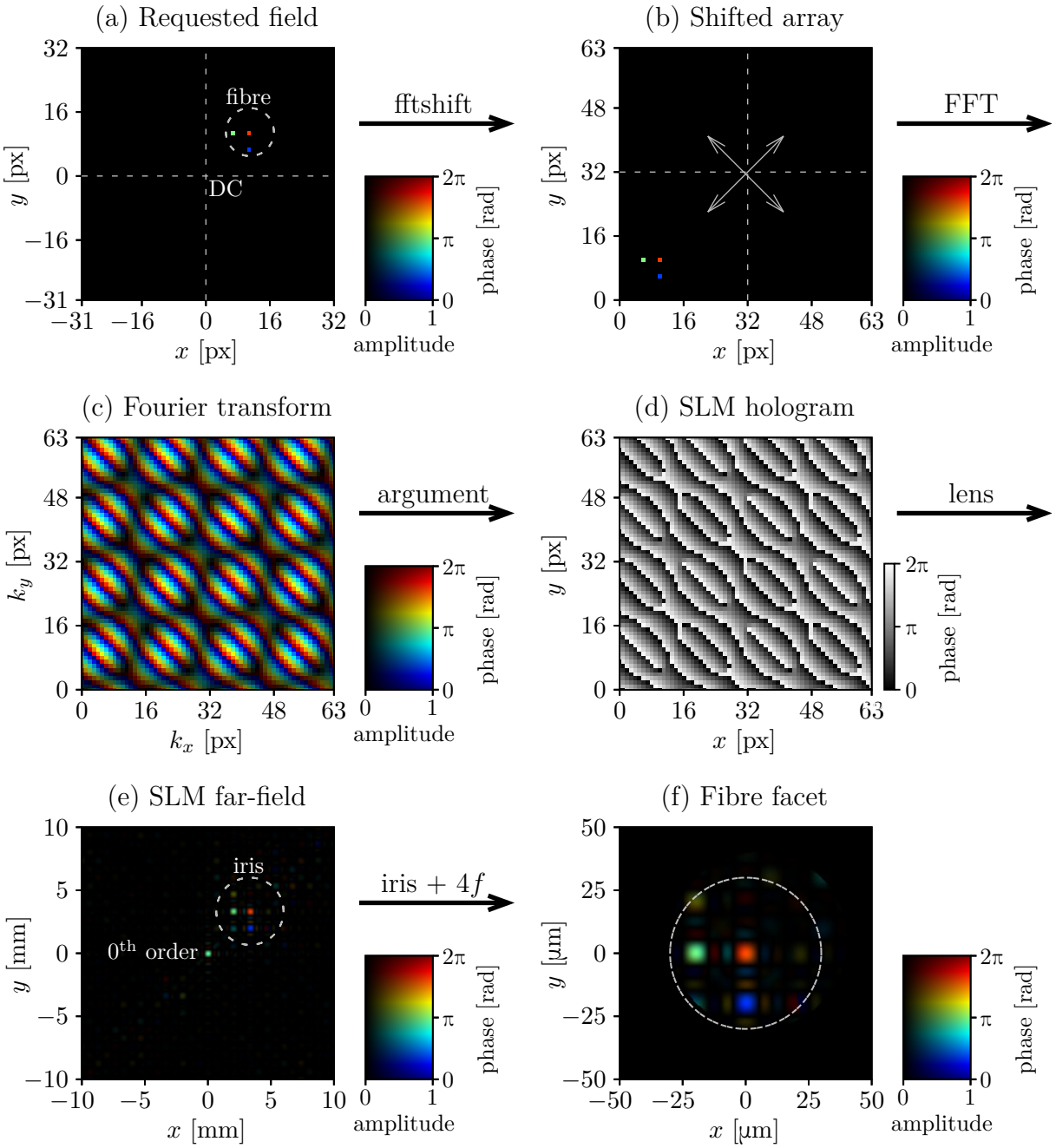

Figure 1.2: Hologram generation procedure for phase-only modulation. (a) An array (of complex numbers) with the same resolution as the resolution of the spatial light modulator (SLM) is allocated and filled with the required field at the input facet of the fibre. (b) The quadrants of the array are shifted in preparation for the fast Fourier transform. (c) A fast Fourier transform of the array is calculated. (d) Only the argument of the complex number in each pixel is used for the phase-only hologram. (e) The beam generated in the far-field of the SLM contains not only the 1$^{\text{st}}$ diffraction order, but also the 0$^{\text{th}}$ (reflection) and other diffraction orders. (f) The 1$^{\text{st}}$ diffraction order is separated using an iris and imaged onto the input facet of the fibre using a $4f$ system.

step of the procedure (Figure 1.2a) is often omitted to speed up the calculations, and the requested field is inserted in the array directly using the shifted coordinates.

Afterwards, a fast Fourier transform of the array is calculated (Figure 1.2c). The result of the Fourier transform is the field that needs to be generated in the SLM plane to obtain the requested field on the fibre facet. Since a phase-only modulator is used, only the phase of the field (i.e., the argument of each complex element of the array) is used (Figure 1.2d). That is, the amplitude of the field after the SLM is always near-uniform (determined by the profile of the laser beam). If a DMD, a binary amplitude modulator, were used instead, the calculated phase distribution would be binarised [82].

The beam diffracted off the SLM is Fourier transformed using a lens (Figure 1.2e). Due to a limited 1$^{\text{st}}$ order diffraction efficiency of the modulator, a 0$^{\text{th}}$ order beam (in essence, a reflection off the SLM) is being generated in addition to the requested field. Also, higher diffraction orders might be present. The 1$^{\text{st}}$ diffraction order is isolated using an iris and demagnified onto the input facet of the fibre using a pair of lenses forming a $4f$ system.

Figure 1.2f shows the resulting field on the input facet. The three points with the phases requested in the first step are projected. Due to the diffraction on the rectangular aperture of the SLM, the points are slightly rectangular and have side lobes, as expected from Fraunhofer diffraction on rectangular aperture. In addition to the three requested points, other points, also called ghost orders, are generated due to using a phase-only modulation. This imperfection could be avoided by using a complex modulation, essentially encoding both the amplitude and phase into the hologram [83–88]. Such modulation is, however, lossy and would decrease the total throughput of the fibre imaging system.

This method of hologram generation allows addressing a grid of points on the input facet of the fibre. For a SLM with resolution of $n_{\text{SLM}} \times n_{\text{SLM}}$ (pixels) and a pixel pitch of p_{SLM}, the grid of points created at wavelength λ in a focal plane of Fourier transform lens f_1 (the iris plane in Figure 1.1) has a pitch of

$$p_{\text{iris}} = f_1 \frac{\lambda}{n_{\text{SLM}} p_{\text{SLM}}} .$$

This grid is demagnified onto the input facet, creating a grid with a pitch of

$$p_{\text{in}} = \frac{f_1 f_3}{f_2} \frac{\lambda}{n_{\text{SLM}} p_{\text{SLM}}} .$$

The lenses f_1, f_2 and f_3 are optimally chosen when the far-field of the fibre (which creates a circle at the SLM plane) just fills the active area of the SLM, thus

$$2\,\text{NA} \frac{f_1 f_3}{f_2} = n_{\text{SLM}} p_{\text{SLM}} ,$$

where NA is the numerical aperture of the fibre. The pitch thus becomes

$$p_{\text{in}} = \frac{\lambda}{2\,\text{NA}} ,$$

independent of the resolution and dimensions of the SLM. The number of points that fit into the core of the fibre with a diameter of d is

$$N_{\text{in}} = \frac{\pi d^2}{4 p_{\text{in}}^2} = \frac{\pi d^2 \text{NA}^2}{\lambda^2} .$$

The number of modes supported by the fibre for a single polarisation state is

$$N_{\mathrm{SI}} = \frac{V^2}{4} = \frac{\pi^2 d^2\,\mathrm{NA}^2}{4\lambda^2}\,, \quad N_{\mathrm{GRIN}} = \frac{V^2}{8} = \frac{\pi^2 d^2\,\mathrm{NA}^2}{8\lambda^2}\,,$$

for a step-index (SI) and graded-index (GRIN) fibre, respectively, where V is the normalised frequency (V-number). The number of points corresponding to the core is thus higher by a factor of $4/\pi \doteq 1.3$ or $8/\pi \doteq 2.5$, for a step-index and graded-index fibre, respectively. Consequently, the grid of points created by this method should be sufficient to control the fibre modes fully. Decreasing the ratio $f_1 f_3 / f_2$ decreases the pitch on the input facet, unnecessarily increasing the number of input points that can be coupled into the fibre. Increasing the ratio leads to increasing the pitch, decreasing the number of points and undersampling the input of the fibre. In addition, the range of spatial frequencies coupled into the fibre gets limited, making the points at the distal end of the fibre larger.

1.3. Transmission matrix

Since the multimode fibre is a linear system, the light transport through the fibre can be described in terms of a transmission matrix TM [26, 89–93]. This matrix describes a linear transmission from the proximal (input) facet to the distal (output) facet (or any plane in front of the distal facet). Since the optical fields are complex (i.e., they have both amplitude and phase), the elements of the transmission matrix are complex numbers. If the transmission matrix is known, the optical field at the distal end of the fibre can be controlled by modulating the field at the proximal end of the fibre using the spatial light modulator (see Figure 1.3).

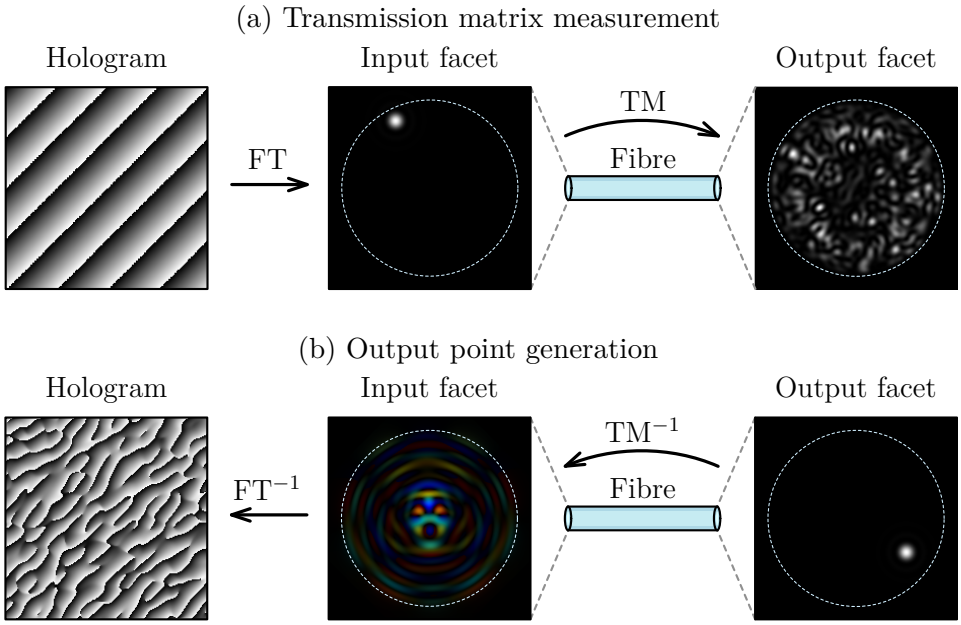

Figure 1.3: Measurement of the transmission matrix of the multimode fibre and output point generation.

Bases in both the input and output planes must be chosen to measure the transmission matrix. A convenient choice for a point-scanning device is a point-based basis. The spatial light modulator is placed in the far-field of the proximal facet of the fibre. Therefore, a single spatial frequency (a blazed grating) generates a diffraction-limited point on the proximal facet. In the following, these points are referred to as *input points*. The distal end of the fibre is projected onto a camera. Thus, points at the output plane correspond to individual pixels on the camera chip and are referred to as *output points*. In literature, these foci are often referred to as input and output modes [26].

1.4. Fibre calibration procedure

To create the foci on the output facet of the fibre, the light transport through the fibre has to be characterised by a calibration procedure, i.e., the transmission matrix of the fibre has to be measured. The procedure, in essence, finds the phase relationship between foci on the input facet (input points) needed to achieve a constructive interference in a point at the distal end of the fibre (output point).

The usable range of input points, that is, those that are focused on the core and therefore coupled into the fibre, is found by raster scanning a point across the input facet of the fibre by displaying consecutive gratings with different pitch on the SLM, and measuring the power transmitted by the fibre by integrating all the pixels corresponding to the fibre core on the camera (Figure 1.4). Only the points that give, e.g., at least 20 % light transmission (relative to the input points near the centre of the fibre) are selected.

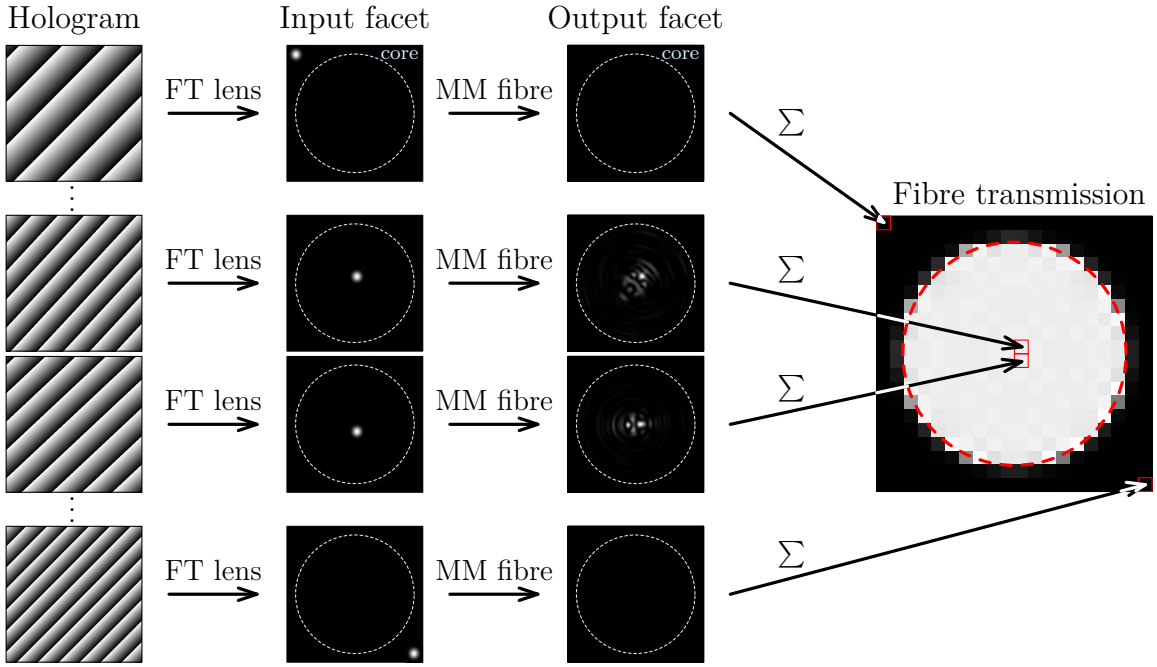

Figure 1.4: Input points selection. A point is raster-scanned across the input facet and the power transmission of the fibre are measured.

The selected input points are then displayed one by one. The speckle pattern for each input point in the sample plane is imaged onto the camera and overlapped with the plane reference wave. The reference wave might be generated externally or on the SLM as an additional grating. The phase and the amplitude of each output point for each input point are measured using phase-shifting interferometry (see Figure 1.5).

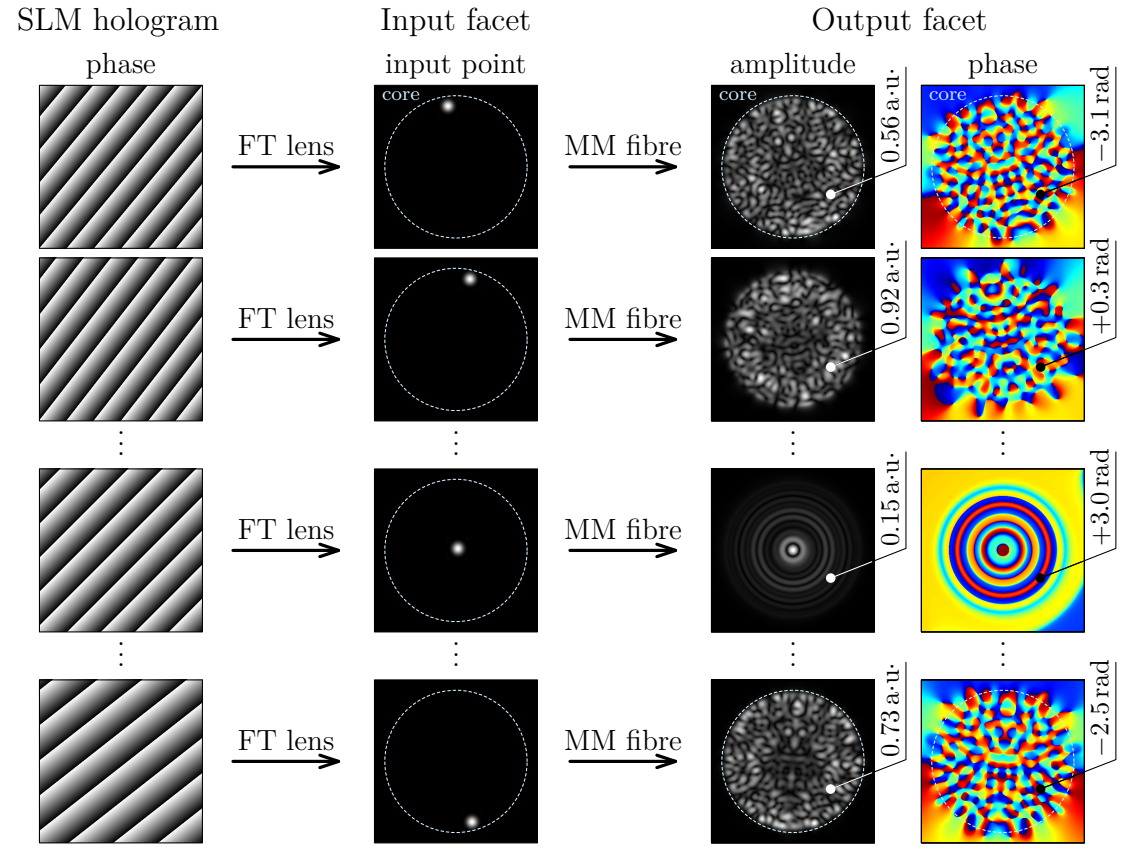

Figure 1.5: Transmission matrix measurement. Selected input points are scanned and the resulting optical field (amplitude and phase) is measured using phase-shifting interferometry.

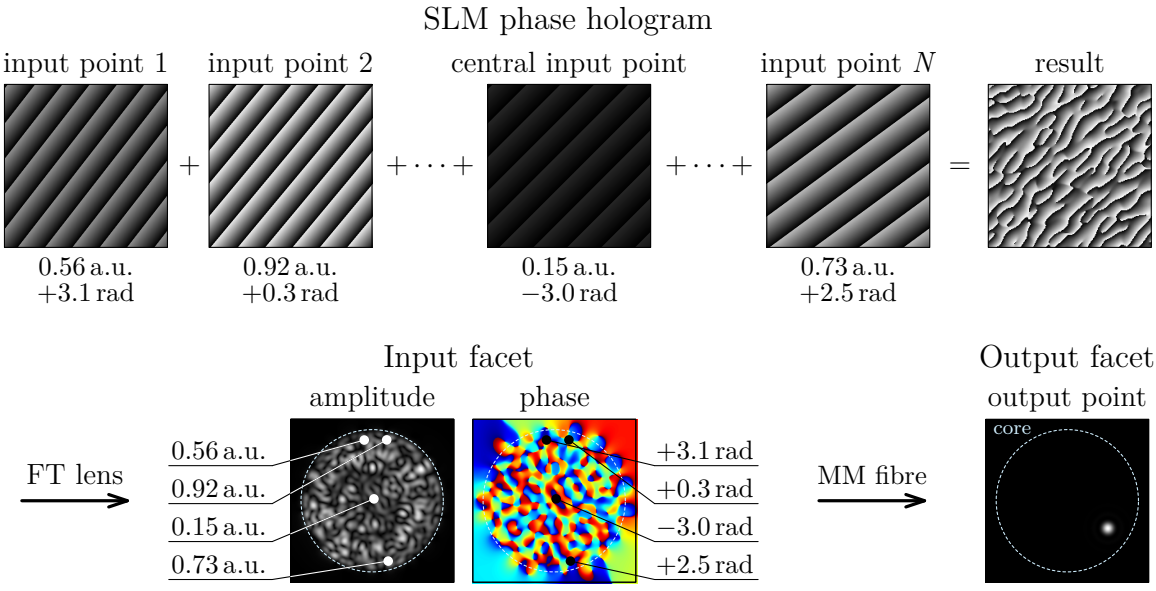

Figure 1.6: Output point generation. All the input points are displayed simultaneously with a phase set to the negated phase values and an amplitude set to the amplitude measured during the calibration (Figure 1.5). All the waves, therefore, constructively interfere in a single output point. The hologram generation is shown only schematically. In reality, the individual fields are summed, not the respective gratings.

A focused output point in the focal plane is then created by displaying all the phase gratings on the SLM corresponding to the input points simultaneously, with a phase set to the negated phase values and an amplitude set to the amplitude values measured in the desired output point as shown in Figure 1.6. Thus, constructive interference of all the waves corresponding to the input points is achieved in the output point in the focal plane. The amplitude information suppresses those input points that do not contribute to the interference in the selected output point and would, therefore, only increase the background.

An example of the focused point created at the distal end of the fibre is in Figure 1.7. The same point is shown in linear and logarithmic scales, revealing a speckled background around the point. The primary source of this background is the usage of the phase-only modulation. In essence, the wave coupled into the fibre is not being replicated accurately, which results in some of the power behind the fibre being randomly distributed across the field of view. Another source of the background in the simplified system discussed here is not controlling the polarisation of the light coupled into the fibre and thus not fully controlling all the fibre modes.

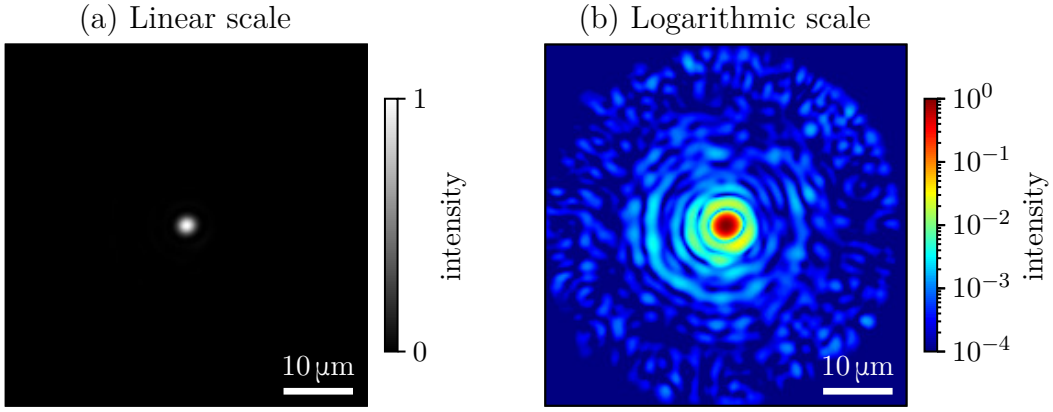

Figure 1.7: Output point example (the fibre was Thorlabs FG050LGA and the point was generated directly on the facet using a wavelength of 780 nm) in (a) linear scale and (b) logarithmic scale.

1.5. Other calibration and imaging approaches

The method for calibrating the multimode fibre is not the only possible approach to generate a scanning point at the distal end of a multimode fibre and use it for imaging. Many modifications or entirely different methods have been published.

One possible modification of the procedure is a different choice of the basis at the fibre input in which the transmission matrix is measured. This chapter used a plane-wave basis in the spatial light modulator plane. This choice implied that the hologram was generated using Fourier transform. Depending on the number of lenses between the modulator and the input fibre facet, these plane waves generate either points or plane waves at the input facet. Another possible basis is a so-called subdomain-based basis [26], where the spatial light modulator is divided into small rectangles (subdomains). During the calibration procedure, the phase of each subdomain is then optimised separately. The disadvantage of this approach is the very low intensity on the camera in the calibration module, as the very small subdomains must be calibrated one by one, sending most of the light into the

0^{th} diffraction order. Another possible basis is the Hadamard basis [94, 95]. Instead of modulating the light coupled into the fibre, the fibre itself can be mechanically deformed to, in essence, shape its transmission matrix so a point at the distal end is created [96].

Another approach to generating a point at the distal end uses digital phase conjugation [97]. For the calibration, a focused point from a laser is launched into the distal end of the fibre, and the field at the proximal end of the fibre is measured on a camera. The measured (phase-conjugated) field is replicated on a spatial light modulator to create the same point through the fibre. This method requires a precise alignment of the modulator and the camera. The point can also be generated iteratively [98] or employing other phase retrieval techniques [99, 100]. While this allows creating of a focused point without having to use a reference beam, the demonstrated intensity enhancements of the points were significantly lower than in most papers using holography.

The whole process of characterising the light propagation through the multimode fibre can be simplified by exploiting the memory effect of the fibre [101–104]. While using the memory effect could, in theory, reduce the calibration time, it requires a precise alignment of the laser beam and the fibre (in essence, the fibre could not be treated as a black box). So far, only very basic transmission imaging has been demonstrated in [103]. The calibration time could also be reduced by compressively sampling the transmission matrix [105].

Reconstruction of the transmission matrix of a multimode fibre without access to distal end has been demonstrated by detecting a back-reflection of a thin stack of structured metasurface reflectors deposited to the distal end [106].

The common denominator in all the papers mentioned above is the fibre system used as a point-scanning device. After characterising the light propagation through the fibre, the laser beam coupled to the fibre is modulated to create a single point at the distal end. A completely different approach is a digital reconstruction of the entire image transmitted through the fibre and scrambled into a speckle pattern [107], often in conjunction with deep learning [108, 109]. An optical-only approach to this reconstruction has been proposed in [110] but has only been demonstrated theoretically.

2. Characterisation of a multimode fibre endoscope

In this chapter, a multimode fibre endoscope is designed and characterised. The chapter includes a detailed description of the alignment process and a more in-depth explanation of the calibration procedure, briefly introduced in Section 1.4. In addition, methods for evaluating the quality of the foci are described in detail. The chapter thus serves mainly as an introduction to the terms and methods used in the following chapters.

2.1. Setup for fibre characterisation

A schematic drawing of the optical setup for multimode fibre characterisation is shown in Figure 2.1. The design of the system was changed multiple times throughout the experiments presented in this thesis due to different requirements for each experiment and availability of the components. The changes included, for example, using different light sources (continuous-wave laser, picosecond laser system, femtosecond laser system), detectors (photodiodes or photomultiplier tubes) or replacing the spatial light modulator. The configuration described in this section was used for the experiments presented in this chapter as well as for the wavelength-dependent characterisation in Chapter 3. The most important changes to the system for the experiments in other chapters are then described at the beginning of the respective chapter. Nevertheless, the differences in the timing of the data acquisition are, for better comparison, described in this section.

Two different lasers were coupled into the system. For most experiments presented in this chapter, a tunable narrowband continuous-wave (CW) titanium-sapphire (TiS) laser (M Squared SolsTiS SA PSX F, wavelength tuning range 725 nm–975 nm, maximal power of 1 W, pumped by Coherent Verdi G5, wavelength 532 nm, maximal power 5 W) was used. The beam power was controlled using a combination of an achromatic half-wave plate (HWP3; Thorlabs FBR-AQ2) and a polarising beamsplitter cube (PBS1; Thorlabs PBS052). Afterwards, the beam was coupled into a polarisation-maintaining single-mode optical fibre (PM SMF; Thorlabs P3-780PM-FC-2) using another achromatic half-wave plate (HWP5; Thorlabs FBR-AQ2) and an achromatic doublet lens (L1). Coupling the light into the single-mode fibre was necessary due to the low pointing stability of the laser after its wavelength was tuned. Without filtering the beam through the fibre, the beam position on the liquid crystal spatial light modulator (LC SLM) would change significantly with wavelength, affecting many measurements. With the fibre, the beam position on the SLM was stable at the cost of the coupling efficiency, and thus the power incident on the SLM was wavelength dependent. However, the power changes could be taken into account, and the data be corrected for this effect. The beam exiting the polarisation-maintaining single-mode fibre was collimated (L2; Thorlabs AC254-150-B-ML), and its polarisation

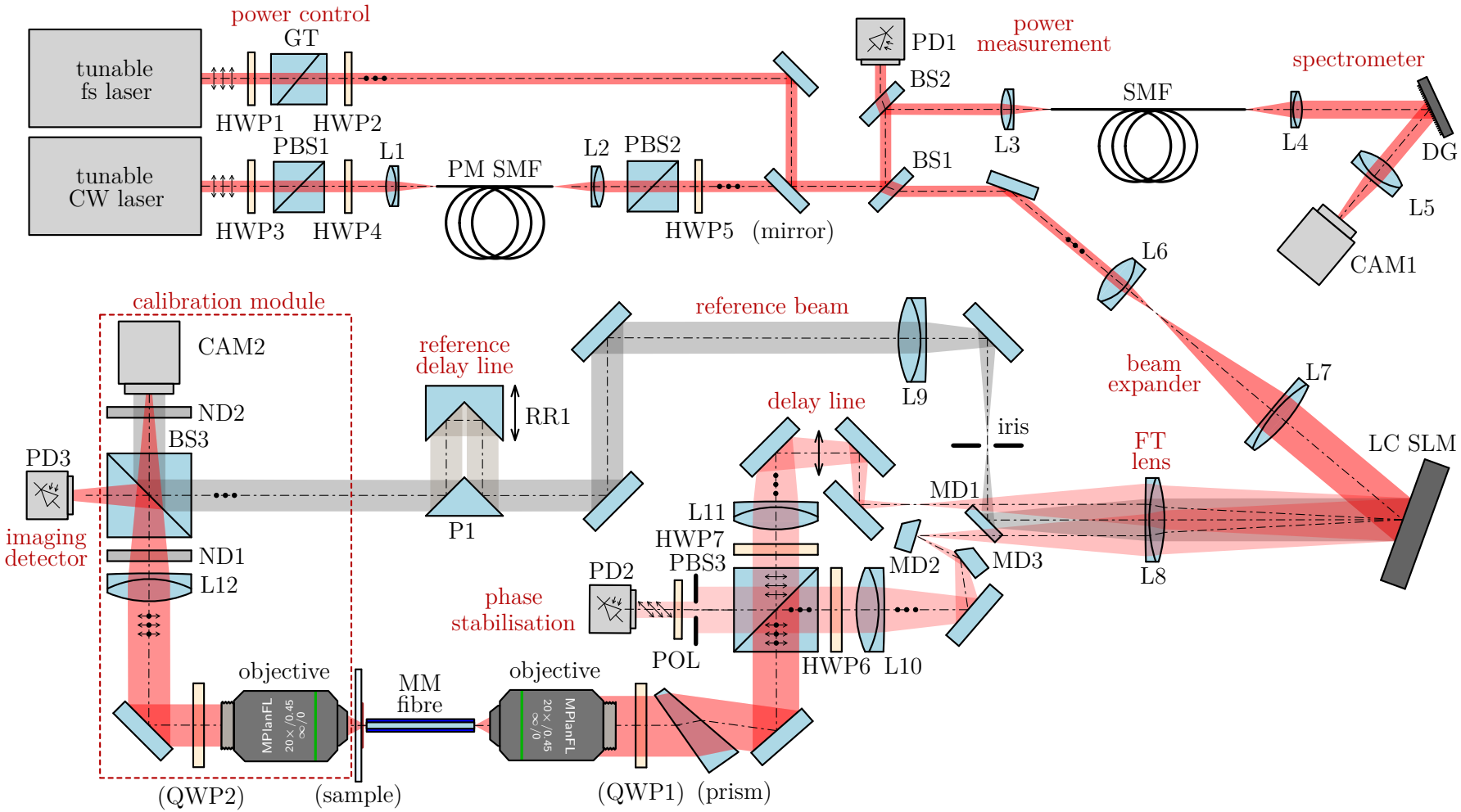

Figure 2.1: Schematic drawing of the setup for multimode fibre endoscope characterisation. BS – non-polarising beamsplitter, CAM – camera, GT – Glan-Taylor polariser, HWP – half-wave plate, LC SLM – liquid crystal spatial light modulator, L – lens, MD – D-shape mirror, MMF – multimode fibre, ND – natural density filter, PD – photodiode, P – knife-edge right-angle prism mirror, PM SMF – polarisation maintaining single mode fibre, PSB – polarising beamsplitter cube, QWP – quarter-wave plate, RR – hollow roof prism mirror, SMF – single mode fibre. The components in parentheses were present only in some experiments, as discussed in the text.

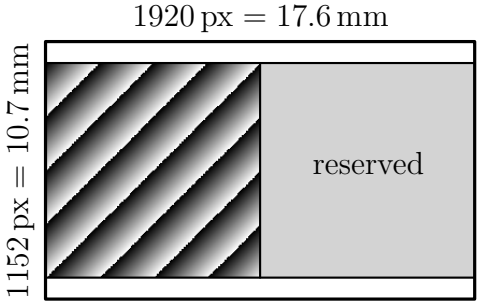

Figure 2.2: The spatial light modulator chip with a resolution of 1920 px × 1152 px was divided into four parts: two squares 960 px × 960 px (one was used for the experiments, and the other one was reserved for future use with multiple wavelengths) and two unused stripes 1920 px × 96 px (which were not used at all).

was filtered using a polarising beamsplitter cube (PBS2; Thorlabs CCM1-PBS252/M). The filtering ensured a stable polarisation of the beam entering the rest of the system. Using an achromatic half-wave plate (HWP5; Thorlabs AHWP05M-980), the polarisation of the beam was set to be vertical, which ensured the maximal efficiency of the SLM.

The second laser used in this chapter was a femtosecond laser (Coherent Chameleon Discovery). This laser produced two synchronised output pulse trains. One had a fixed wavelength of 1040 nm, power 4 W, pulse duration 140 fs and a repetition rate 80 MHz. This output was not used in this chapter. The second output was an optical parametric oscillator (OPO) with a tuning range of 660 nm–1320 nm, power up to 2 W (at 800 nm), pulse duration 100 fs, a repetition rate 80 MHz and a built-in pre-chirp pulse compressor. This output could be coupled into the setup using a mirror mounted on a flip mount. The power and polarisation of the beam were controlled using a pair of achromatic half-wave plates (HWP1, HWP2; Thorlabs AHWP05M-980) and a Glan-Taylor calcite polariser (GT; Thorlabs GT10-B).

A small portion of the beam was picked on a non-polarising beamsplitter (BS1; Thorlabs BSN11) to monitor the power and the wavelength of the laser. This beam was then split once more into two beams using another non-polarising beamsplitter (BS2; Thorlabs BSW11). One beam was used to monitor the power using a photodiode (PD1; Vishay Semiconductors BPW34, with a custom transimpedance amplifier). The second part was coupled into a single-mode fibre (SMF; Thorlabs P1-780A-FC-1) using a lens (L3, Thorlabs AC254-030-B-ML). The fibre was connected to a spectrometer consisting of a pair of lenses (L4, Thorlabs AC254-100-B-ML, and L5, Thorlabs AC254-125-B-ML), a grating (SG; Thorlabs GR25-1208) and a camera (CAM1; Basler ace acA1920-150um). The range of the spectrometer was (780 ± 19) nm for the measurements in this thesis, and it could be changed by rotating the grating. The spectrometer was necessary for measuring the wavelength of the tunable TiS laser during the wavelength-dependent characterisation of the endoscope since the laser did not provide sufficiently accurate information about its wavelength.

The beam was expanded using a pair of achromatic doublet lenses (L6 Thorlabs AC254-030-B-ML, and L7, Thorlabs AC254-250-B-ML) to significantly overfill the active area of a liquid crystal phase-only spatial light modulator (LC SLM; Meadowlark HSP1920-1064-HSP8) to provide near-uniform illumination of the chip. The resolution of the modulator was 1920 px × 1152 px. Only a square part of the modulator chip of 960 px × 960 px was used, as shown in Figure 2.2.

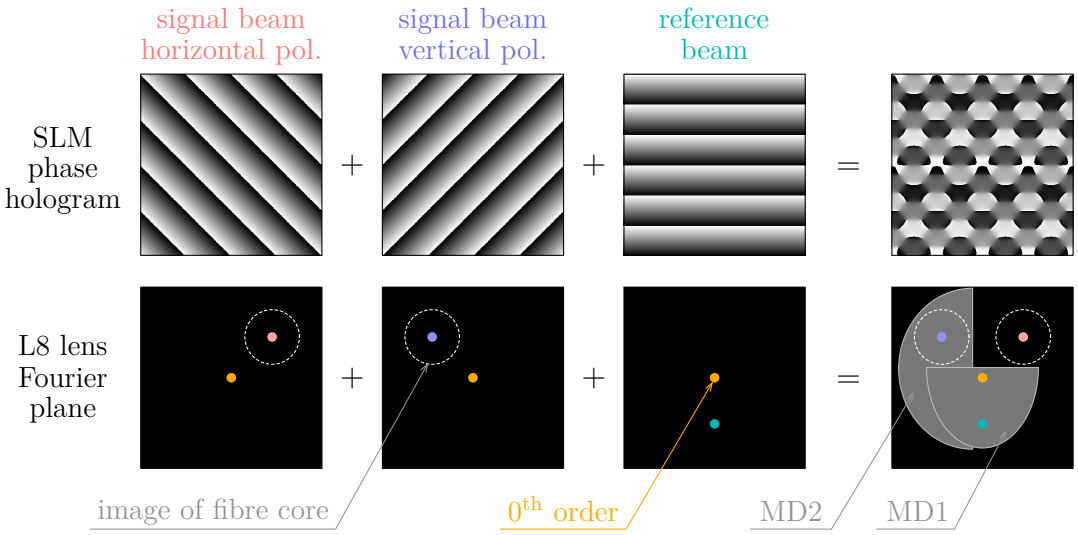

Figure 2.3: Phase holograms and corresponding intensity in Fourier plane.

After diffracting off the SLM, the beam was Fourier transformed using a lens (L8; Thorlabs AC254-250-B-ML), allowing separation of the diffraction orders. The SLM created four beams with different ranges of spatial frequencies (see Figure 2.3). The position of the regions in the Fourier space was chosen to minimise cross-talk, i.e., no diffraction order of any point in the region overlapped any other region.

The 0^{th} order (i.e., in essence, the direct reflection) was always present and was not used for the experiments. It was reflected off a D-shaped mirror (MD1; Thorlabs PFD10-03-P01) and blocked on an iris (Thorlabs SM1D12SS). When no hologram was displayed on the SLM, almost all the incident power ended up in the 0^{th} order. Thus, a stainless-steel iris was used because of its higher damage threshold.

Another two beams created by the SLM (one for each input polarisation) were coupled into the multimode fibre. These beams filled two circles in the Fourier plane, corresponding to the core of the multimode fibre. The beams were separated using another D-shaped mirror (MD2) and were both collimated (L10, L11; both Thorlabs AC254-200-B-ML). The polarisation of one of the beams was turned by 90° using an achromatic half-wave plate (HWP7; Thorlabs AHWP10M-980). The same type of half-wave plate was also placed in the other beam (HWP6) to minimise the differences between the two optical paths. Both beams were then overlapped using a polarising beamsplitter cube (PBS3; Thorlabs CCM1-PBS252/M). In essence, sending light in the path through L10 and HWP6 (i.e., in the top left quadrant of the Fourier plane in Figure 2.3) produced a vertically polarised pattern on the input facet of the fibre. Sending light in the path through L11 and HWP7 (i.e., in the top right quadrant of the Fourier plane) produced a horizontally polarised pattern on the input facet of the fibre. By setting the relative phase and amplitude of these two beams on the SLM, the polarisation state at the input of the fibre could be locally controlled. The input polarisation control was essential when graded-index fibres were used. These, unlike step-index fibre, do not maintain circular polarisation (this is described in Section 2.8 in detail). The polarisation basis could be changed from horizontal and vertical linear polarisation to a left-handed and right-handed circular polarisation by inserting two achromatic quarter-wave plates (QWP1, QWP2; both Thorlabs AQWP05M-980) into the system. Using two quarter-wave plates changed both the input and output polarisation basis.

The total number of reflections was even for one of the two beams and odd for the other. The difference was essential to use only a single prism for compensating the dispersion of the SLM (as discussed in Section 3.2). When a pulsed laser was used, keeping the optical path difference between the two beams below the pulse length was necessary. Two mirrors in one of the polarisation beams were placed on a motorised stage, forming a delay line. The optimal overlap was set by sending two plane waves into the polarisation control optics, one for each polarisation, and monitoring the interference contrast on photodiode PD2. The overlap had to be re-established after every re-alignment of the optics.

Since the focused points created at the sample plane at the distal end of the fibre resulted from the constructive interference of the two input polarisation beams, any phase drift between the two optical paths decreased the intensity of the point. For example, a phase drift of π resulted in destructive interference, dropping the excitation power near zero. Depending on the conditions (mainly temperature changes) during the imaging, this could happen in less time than it took to capture a single image. The phase difference between the two beams thus had to be stabilised to make the imaging possible. Since the system already had a phase modulator (the SLM), the relative phase difference could be kept constant (at a value corresponding to constructive interference at the sample plane) by changing the phase during the hologram generation. The relative phase had to, however, be measured. During the imaging, the distal end of the fibre could be potentially inserted inside tissue and thus be inaccessible. Consequently, the intensity of the excitation point could not be monitored on the camera in the calibration module. The measurement of the phase drift had to be implemented on the proximal side. The measurement was done by picking a small fraction of both beams on PBS3, and measuring the interference on a photodiode (PD2; Vishay Semiconductors BPW34). Since both beams had orthogonal polarisations, to achieve interference, a polariser (POL; Thorlabs LPVIS100-MP2) with its axis oriented at 45° was placed before the photodiode. The exact implementation of the measurement and phase correction is described in Section 2.5.

The input polarisation control is often implemented using one or two polarising beam displacers (see [43, 87, 90] for an example) instead of PBS3 and multiple mirrors around it in Figure 2.1. In such an approach, both beams are kept parallel, and thus both have a common path. However, the polarising beam displacers are unsuitable for focusing short pulses as there is no control over the optical path difference between the beams, and the displacement is wavelength-dependent. On the other hand, the approach with the beam displacers is preferable for narrowband light sources since it mitigates the drift between both beams.

The holograms displayed on the SLM had a form of a sum of blazed diffraction gratings, which caused the position of the beams in the Fourier plane to be wavelength-dependent. To correct for this effect, a wedge prism (Thorlabs PS812) could be placed in the beam. The position of the prism corresponded with the position of the image of the SLM created by lenses L8 and L10/L11. The details of the correction are described in Section 3.2.

The beam was afterwards focused onto the proximal end of the multimode fibre using a 20× objective (Olympus MPlanFL N 20×/0.45NA).

The fourth beam created by the SLM was the reference beam. It was reflected, together with the 0^{th} order off MD1. Afterwards, it was isolated using an iris and collimated (L6, Thorlabs AC254-150-B-ML). To measure the spectral phase (a phase as a function of the wavelength) of the output points in the fibre imaging plane, the optical path difference between the path through the fibre (the signal beam) and the reference beam path had to be as low as possible. Otherwise, the phase would change rapidly with the wavelength,

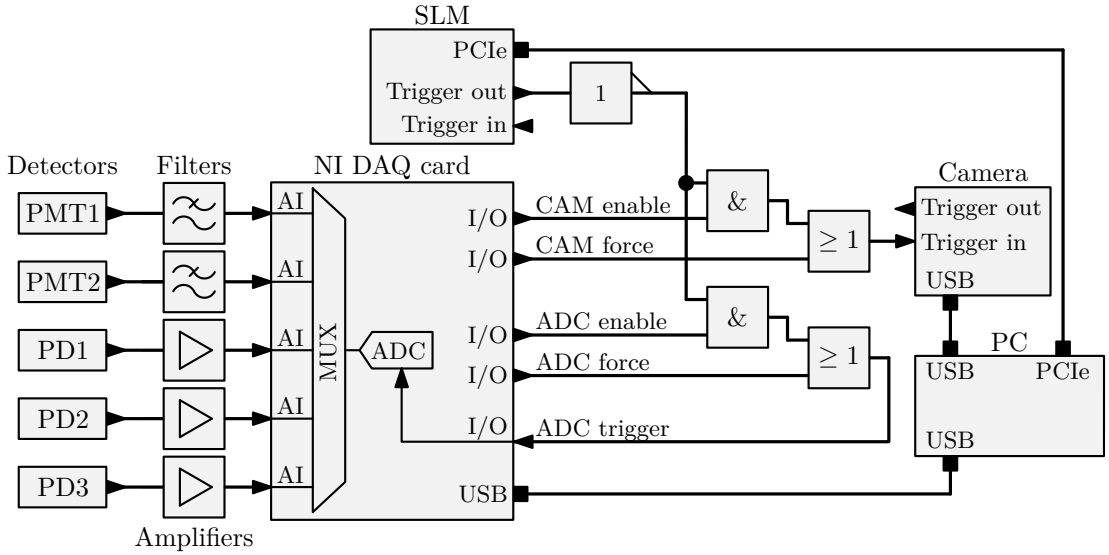

Figure 2.4: Schematics of the electronics. The detectors were connected to analogue inputs of a data acquisition (DAQ) card. The analogue to digital converter (ADC) in the card and the camera were triggered by the spatial light modulator (SLM). The trigger was additionally controlled by four digital outputs of the DAQ card. The photomultiplier tubes (PMTs) were used only for imaging in Chapters 4 and 5.

and measuring the spectral phase would not be possible (due to 2π jumps). Therefore, a delay line was placed in the reference beam, consisting of a knife-edge right-angle prism mirror (P1; Thorlabs MRAK25-P01) and a hollow-roof prism mirror (RR1; Thorlabs HRS1015-P01) placed on a motorised stage. The length of the delay line was set, so the interference pattern on the camera almost did not change while modulating the wavelength of the tunable CW laser by 100 GHz. The optical path difference for the laser wavelength was minimal at that position. Setting the optical path difference near zero was also crucial when using the femtosecond laser to achieve interference between the signal and the reference beam.

The reference beam could alternatively be picked on a beamsplitter before SLM. Generating the reference beam using a separate spatial frequency on the SLM allowed easier control over its intensity. It had, however, no effect on the results presented in this thesis.

The distal end of the multimode fibre was imaged onto a camera (CAM2; Basler ace acA1920-155um) using another 20× objective (Olympus MPlanFL N 20×/0.45NA) and an achromatic lens (L12; Thorlabs AC254-250-B-ML) to characterise the light propagation through the fibre and create a focused point at the distal end of the fibre. The image was then overlapped with the reference beam using a non-polarising beamsplitter cube (BS3; Thorlabs CCM1-BS014/M). A set of absorptive natural-density filters (ND1; Thorlabs NE30A-B, ND2; Thorlabs NE20A-B) was used to adjust the intensity on the camera.

For imaging in transmission, an amplified photodetector (PD3; Thorlabs PDA36A2) was placed in the beam reflected off the beamsplitter.

The electrical connection is outlined in Figure 2.4. The photodiodes, as well as photomultiplier tubes (PMTs, used in Chapters 4 and 5) were connected to a data acquisition card (DAQ; National Instruments USB-6343). In Chapter 5, the signals from the PMTs were additionally filtered using an active 10 kHz low-pass filter before being fed into the analogue inputs of the DAQ card.

The camera in the calibration module and the analogue to digital converter (ADC) in the data acquisition card were externally triggered by the SLM. The synchronisation was performed to make the calibration and imaging as fast as possible. Different timing schemes were tested and used for different experiments in this thesis. The optimal scheme (used for imaging in Chapter 5) is shown in Figure 2.5. With this timing, the system displayed about 170 holograms per second with an integration time of 2 ms or about 205 holograms per second if the integration time was 0.9 ms or lower.

Unlike many digital micromirror devices (DMD), the SLM used here did not have an internal memory for storing whole hologram sequences. Instead, each hologram had to be uploaded by the imaging software to the SLM separately before it was displayed. The upload took about 0.5 ms. Exactly 1.18 ms prior the SLM started displaying the new hologram, the SLM controller produced a negative pulse on its trigger output [111]. These 1.18 ms corresponded to the refresh frequency of the SLM, as the hologram was changed only in intervals corresponding to an integer multiply of this number. Consequently, a completely arbitrary frame rate was not possible. The pulse generated by the SLM controller was with a delay of 5 ms (after being inverted) used to hardware trigger the camera and the ADC. The delay was longer than 1.18 ms due to the slow response time of the liquid crystals. It took about 3.8 ms to achieve a sufficiently stable output. The next hologram was uploaded during the waiting period or the data acquisition. The delay before uploading the next hologram (measured since the pulse generated) was calculated so the hologram on the SLM was stable during the whole exposure or ADC integration time (the longer of the two). This delay was timed in the software. Ideally, during the imaging, the total per-pixel dwell time would consist only of the delay necessary to form the pattern on the SLM and the integration time. For a 2 ms integration time, the pixel dwell time was 5.9 ms. Since the dwell time was limited by the SLM to integer multiples of 1.18 ms, to decrease it, the integration time had to be reduced to 0.9 ms.

Depending on the current mode of operation, only the camera, the ADC or both were active. For example, only the camera was used during most of the calibration, and the ADC was not triggered. On the contrary, during imaging, only the ADC was used. The conditional activation of the trigger was controlled by two digital outputs of the DAQ card. In addition, two additional digital outputs were used to force-triggering the camera or the ADC converter without refreshing the hologram on the SLM. This logic was implemented using a series of 74HC00 NAND gates.

The acquisition card had only a single ADC. When multiple channels were to be measured, the input was multiplexed. Figure 2.5c shows the order of the channels in the multiplex. The ordering was changed in the experiments presented in this thesis. Thus, three different variants are shown. Three detectors were used for the experiments presented in this chapter: the power measurement detector, the phase stabilisation photodiode, and the transmission imaging detector. The three channels were interleaved. A similar scheme was used in Chapter 4. The scheme was changed in Chapter 5. Here, one sample was first measured for each photodiode for phase stabilisation. Afterwards, four samples were taken for each of the two PMTs. Eight samples were taken for the active channel when only one PMT was used. Increasing the number of samples for the imaging detectors leads to a reduction of the noise. Reducing the number of switches between the different inputs reduced the cross-talk between the channels. The frequency of the ADC was 500 kHz (maximal value supported by the DAQ card). The card was configured to capture as many samples for each channel as possible during the integration time. The samples for each channel were then averaged.

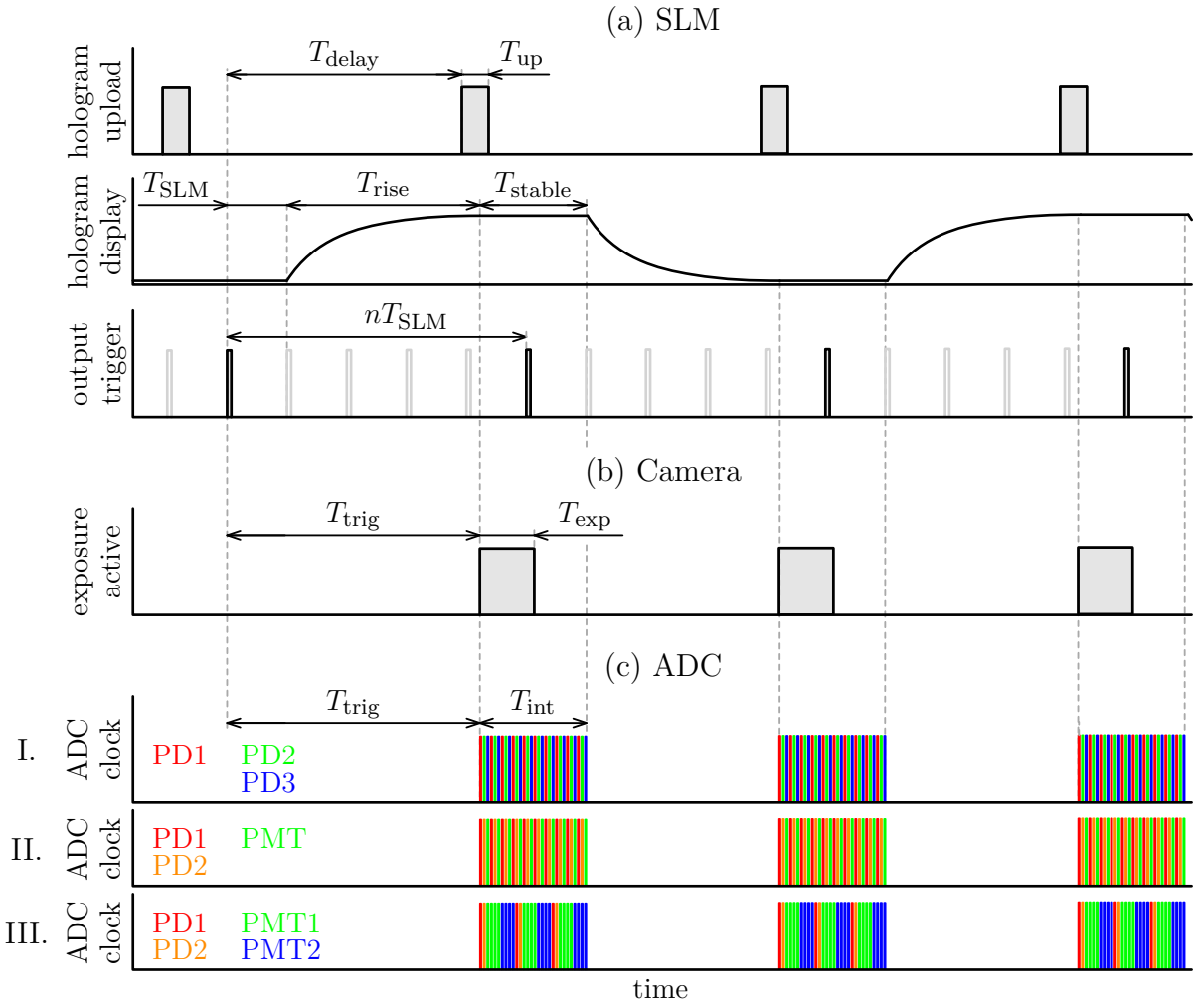

Figure 2.5: Timing diagram which shows the synchronisation of the camera and the analogue to digital converter (ADC) with the spatial light modulator (SLM). T_{delay} – delay between two consecutive hologram uploads (software controlled), $T_{\text{up}} \approx 0.5\,\text{ms}$ – time it took to upload a new hologram, $T_{\text{SLM}} = 1.18\,\text{ms}$ – refresh time of the SLM, $T_{\text{rise}} \approx 3.8\,\text{ms}$ – time to achieve a stable modulation, nT_{SLM} ($n \in \mathbb{N}^+$) – frame time (per-pixel dwell time), $T_{\text{trig}} = T_{\text{SLM}} + T_{\text{rise}} = 5\,\text{ms}$ – trigger delay, T_{exp} – camera exposure time (here, 1 ms), T_{int} – detector integration time (here, 2 ms). All the delays are to scale. The grey pulses in the SLM output trigger were not being generated and are shown only to emphasise the refresh frequency of the SLM. The diagram shows three variants for the ADC, which differed in the configuration of the channel multiplexing: I was used in this chapter, II in Chapter 4 and III in Chapter 5.

2.2. Multimode fibres

The list of all multimode fibres used in this thesis is in Table 2.1. The fibres were both commercial multimode fibres and custom-drawn fibres. Due to the limited availability of some types, not all fibres could be used for all experiments presented in this thesis.

Table 2.1: Specification of all multimode fibres used in this thesis.

Fibre	Type	Core	Cladding	NA
Thorlabs GIF50E	GRIN	50 µm	125 µm	0.20
Thorlabs GIF50C	GRIN	50 µm	125 µm	0.20
Thorlabs GIF625	GRIN	62.5 µm	125 µm	0.275
Prysmian DrakaElite	GRIN	50 µm	125 µm	0.29
IPHT GRIN 94f[a]	GRIN	78 µm	125 µm	0.30
CREOL F1[b]	GRIN	50 µm	125 µm	0.30
CREOL F3[b]	GRIN	62.5 µm	125 µm	0.30
CREOL F4[b]	GRIN	100 µm	200 µm	0.30
YOFC GI2017-C	GRIN	80 µm	125 µm	0.30
Thorlabs FG050LGA	SI	50 µm	125 µm	0.22
CeramOptec Optran Ultra WFGE	SI	100 µm	110 µm	0.37

[a]Custom fibre, drawn at Leibniz Institute of Photonic Technology
[b]Custom fibre, drawn at University of Central Florida College of Optics and Photonics

Preparing a probe for the imaging setup consisted of the following steps. The fibre was first stripped of the acrylate coating. Afterwards, the fibre was cleaved to a flat facet at both ends using a manual cleaver (Thorlabs XL411). The cleaved fibre was glued inside a ceramic ferrule (Thorlabs CF128 or Thorlabs CF230, depending on the outer diameter of the fibre), with the proximal end of the fibre being flush with the facet of the ferrule (see Figure 2.6a), using a UV curable glue (Norland Products NOA 65). This adhesive minimises the strain on the glued components. For better rigidity during imaging and easier replacement of the probes, two ferrules connected using a ceramic mating sleeve (Thorlabs ADAF1) were used (Figure 2.6b). The fibre was glued only to one of the two ferrules.

(a) Fibre in one ferrule

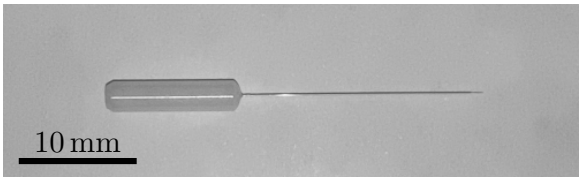

(b) Fibre in two ferrules

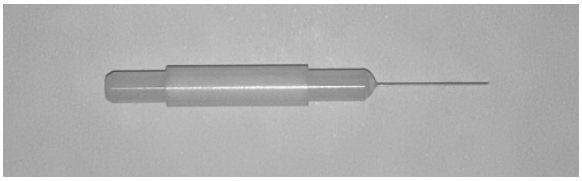

Figure 2.6: Multimode fibre glued inside (a) a ceramic ferrule, (b) two ferrules connected using a ceramic mating sleeve.

2.3. Spatial light modulator characterisation

The response (i.e., the relation between the voltage applied to the pixel and the actual phase stroke) of liquid crystal spatial light modulators (SLMs) is usually non-linear. The response had to be characterised to use it as an accurate phase modulator and maximise the diffraction efficiency. Two different methods for measuring the response were tested. The measured lookup table (LUT) was then applied to the holograms before uploading them to the SLM. Alternatively, the LUT could be uploaded to the SLM controller and applied directly in the hardware.

The first method (which is referred to as the diffractive LUT) was based on measuring the power in the 0^{th} diffraction order (see Figure 2.7a) while displaying binary phase gratings with different phase strokes (see Figure 2.7b). The manufacturer of the SLM recommends this method used here [112] and software for converting the measured response (Figure 2.7c) into the LUT (Figure 2.7d) was provided. In essence, if the grating amplitude was $0, 2\pi, 4\pi, \ldots$, the power in the 0^{th} diffraction order was maximal (as the SLM behaved essentially like a mirror). For $\pi, 3\pi, \ldots$, the power was minimal (as it was diffracted into other diffraction orders).

The second method (linear LUT) for calibrating the phase response of the spatial light modulator relied on the fact that the modulator phase range exceeded 2π, and a part of the response was linear (see Figure 2.7d). The goal was to find the start of the linear region (offset) and the length corresponding to 2π (amplitude). This was achieved by measuring the power in the 1^{st} diffraction order (Figure 2.8a) when displaying blazed diffraction gratings with different offsets and amplitudes (Figure 2.8b). The measured response (Figure 2.8c) then had a single maximum, which corresponded to a blazed grating with 2π steps (and thus an optimal blaze angle) consisting of linear ramps (having a triangular, sawtooth-shaped cross-section). Other positions corresponded to gratings with different steps (and thus less than optimal blaze angle) or using the non-linear part of the SLM response (and thus, the blazed grating ramps were not linear). The position of the maximum was then used to generate the linear LUT (Figure 2.8d).

Both methods described here achieved a similar 1^{st} order diffraction efficiency (ratio of the power in the 1^{st} diffraction order to the power incident on the SLM). There was, however, a significant difference in the speed of the SLM when using different lookup tables, as shown in Figure 2.9. The rise time was determined by measuring the power in the 1^{st} diffraction order on a photodiode (the same setup as in Figure 2.8a) connected to an oscilloscope, while an empty hologram (constant phase over the whole chip) and a blazed grating with an amplitude of 2π were alternated. In Figure 2.9a, the lower half of diffractive LUT was used (the whole LUT had a 4π range out of which a 2π long interval was used). The measured rise time was 1.9 ms, and the signal became stable at about 7 ms after the end of the hologram upload. This diffractive LUT was used in all experiments. When the upper half of the LUT was used (Figure 2.9b), the SLM was significantly slower with the rise time of 5.9 ms and the required delay for the signal becoming stable of more than 15 ms. The linear LUT (Figure 2.9c) resulted in a rise time of 4.3 ms and the signal being stable after more than about 12 ms. The rise time specified by the manufacturer was 3.3 ms. However, this value was specified at 1064 nm, while the measurements were done at 780 nm, i.e., a smaller part of the SLM voltage range was used to generate the 2π phase stroke (and thus the SLM was faster).

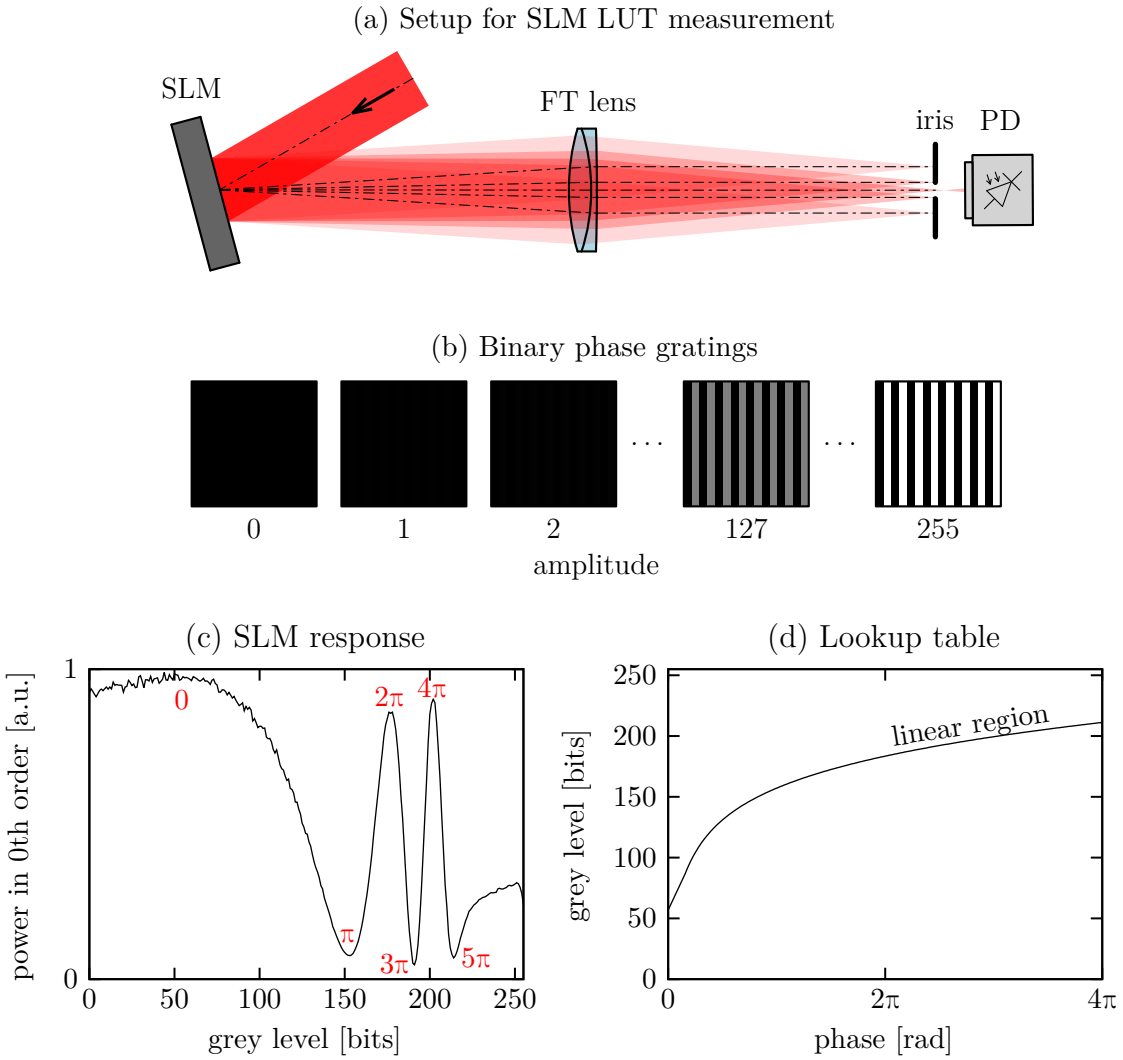

Figure 2.7: Diffractive method for SLM response calibration. (a) Setup for SLM lookup table (LUT) measurement. The SLM was illuminated with a collimated beam, the diffraction orders were separated using a lens and the power in the 0^{th} diffraction order was measured on a photodiode (PD). Since the grating had a 50 % duty cycle, there was no 2^{nd} diffraction order, so only 1^{st} and 3^{rd} are shown. (b) Sequence of binary holograms displayed on the SLM during the measurement. (c) Measured response of the SLM at 780 nm. The minima and maxima of the response correspond to integer multiples of π. (d) Lookup table calculated from the measured response using the software provided by the manufacturer of the SLM.

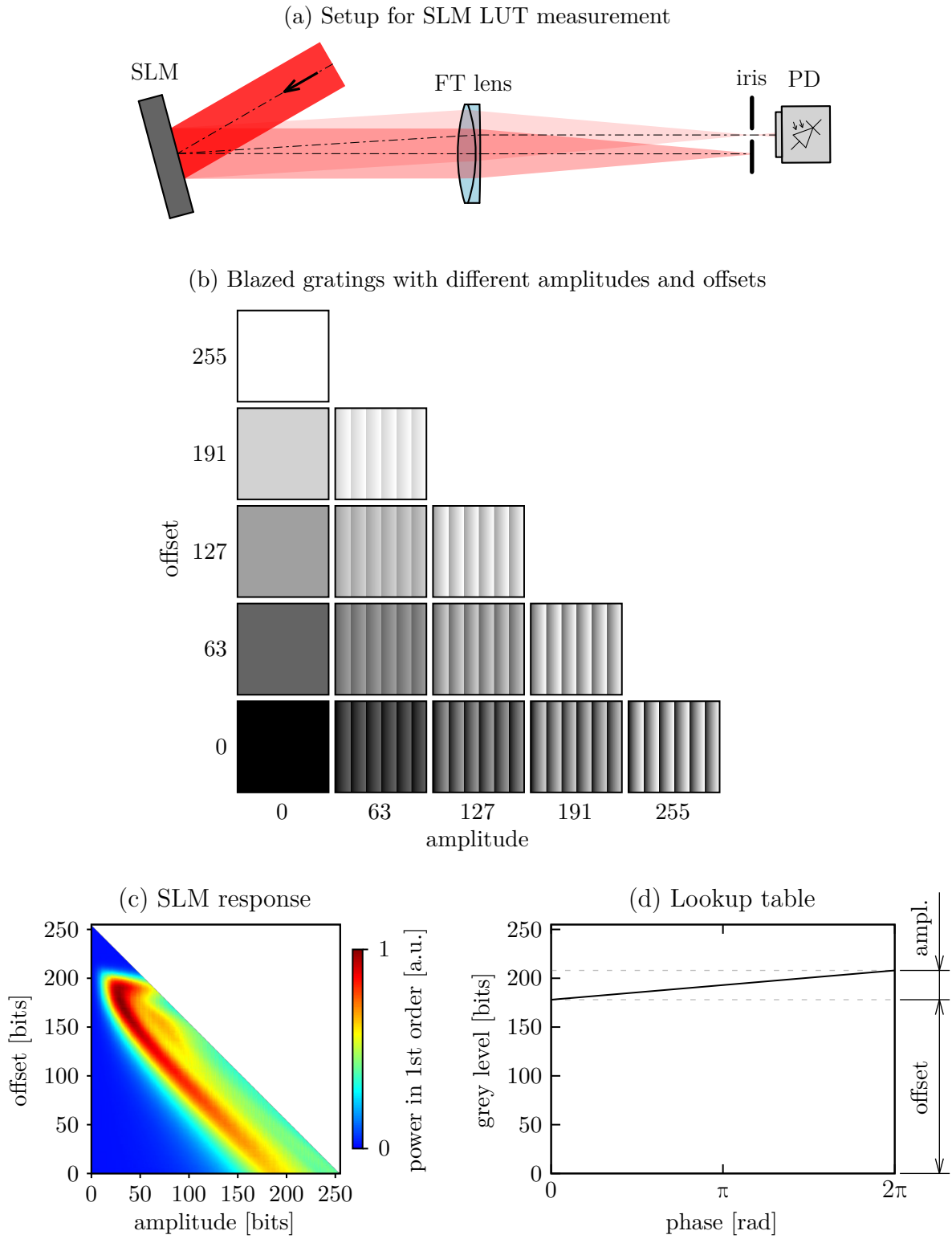

Figure 2.8: Linear lookup table (LUT) measurement. (a) Setup for SLM lookup table measurement. The SLM was illuminated with a collimated beam, the diffraction orders were separated using a lens and the power in the 1st diffraction order was measured on a photodiode (PD). (b) Sequence of blazed gratings displayed on the SLM during the measurement. (c) Measured response of the SLM at 780 nm. The position of the maxima was used to generate the LUT. (d) Lookup table calculated from the measured response.

(a) Diffractive LUT, 0–2π (b) Diffractive LUT, 2π–4π (c) Linear LUT

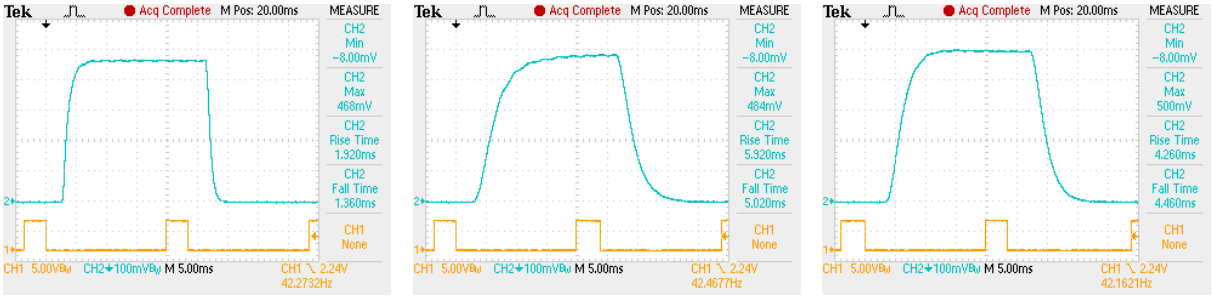

Figure 2.9: SLM time response measured at 780 nm using different lookup tables. Channel 1 (orange) was a TTL signal. The falling edge corresponds to the end of the new hologram upload to the modulator. Channel 2 (blue) was a power on the photodiode placed in the 1st diffraction order (Figure 2.8a). An empty hologram and a blazed grating with an amplitude of 2π were alternated on the SLM.

It should be noted that the rise or fall time measured on the oscilloscope was a standard 10 % to 90 % rise time. Due to the shape of the response, it took significantly longer to achieve a stable value. On the other hand, Figure 2.9 shows the most extreme situation, where two completely uncorrelated holograms were alternated. In the sequences of holograms displayed in the fibre setup, the two adjacent holograms were often partially correlated, making the response faster. For example, when a point was being raster scanned, the holograms for adjacent points on a line were correlated. Thus, the response of the SLM was faster. Holograms for a point at the end of one line and a point at the beginning of the following line were uncorrelated. The response of the SLM was thus slower. The optimal delay before the start of the data acquisition thus varied. The delay was set to the minimum acceptable value during imaging. Imaging with an integration time of 0.5 s was performed, and the delay was set to the minimal value, which did not cause additional noise or decrease the measured intensity. This delay was found to be 3.5 ms (measured from the trigger pulse generated by the SLM). That is 3.5 ms + 1.18 ms ≐ 4.8 ms after the falling edge of the TTL signal in Figure 2.9. While this value was optimal for most of the image pixels, the first column of each image was noticeably darker, suggesting that the delay was too short. This observation agrees with the response in Figure 2.9a, where it took about 7 ms to achieve a stable output. Instead of reconfiguring the acquisition hardware to change the delay for the first row of pixels, the hologram was sent to the SLM twice. Only the second measured value for this pixel was used to generate the image. Since only a small fraction of holograms needed to be repeated, the time penalty was minimal.

Figure 2.9 also shows that the power in the 1st diffraction order was very slightly oscillating. The oscillations were related to the refresh frequency of the SLM of about 850 Hz. In the fibre setup, this caused a flickering of the image on the camera in the calibration module. Also, the noise during the imaging was larger when short integration times were used. The experiments used integration times of 2 ms or longer to mitigate the effect of refresh frequency on the measurements. In addition, the data acquisition was triggered using the SLM, as discussed in Section 2.1. The triggering caused the flickering to be synchronised with the data acquisition, suppressing the noise induced by the flickering.

2.4. Fibre alignment

To properly align the multimode fibre in the system, both the position and the angle of the proximal facet had to be aligned with respect to the incident beam.

The position of the fibre had to be aligned, so one predetermined spatial frequency (referred to as the *central frequency*) on the SLM was focused to a point in the centre of the input facet. This alignment was performed by moving the fibre laterally and the focusing objective along its axis. Initially, the central frequency was displayed on the SLM. The power coupled into the fibre was maximised using a power meter placed at the distal end of the fibre. Maximising the coupling efficiency placed the fibre very close to the optimal position. Afterwards, the distal end of the fibre was imaged onto the camera in the calibration module (CAM2 in Figure 2.1) to perform a more precise alignment. By changing the spatial frequency of the grating displayed on the SLM (Figure 2.10a), a focused point was raster-scanned across the input of the fibre (this is referred to as the *grating scan*) around the central frequency. For each position, the power coupled into the fibre was measured by integrating the image on the camera. Only those points whose position corresponds to the fibre core produced a signal on the camera. Points focused on the cladding were initially coupled into the cladding. The refractive index of the glue (1.52) used to hold the fibre in the ferrule was higher than the refractive index of the cladding (about 1.45). This light coupled into the cladding was thus radiated out. Thus, these points produced only a little signal on the camera. The resulting image (Figure 2.10c) was, in essence, the image of the input facet of the fibre. Consequently, the grating scan indicated whether the input facet was clean or damaged. This procedure had to be performed each time the fibre probe was replaced, as the fibre mount was not precise enough to maintain the same position after fibre replacement. Only points on a cross-like pattern were initially scanned to speed up the process, measuring the vertical and the horizontal cross-sections of the grating scan (as shown in Figure 2.10c). Moreover, scanning the facet in full resolution was not necessary to perform the alignment. Scanning in reduced resolution further sped up the process.

The relative angle of the fibre and the beam had to be aligned, so the far-field of the fibre was centred on the SLM. The alignment was performed, for example, by laterally moving the objective that focused the light into the fibre. Of course, after each such change, the position of the fibre had to be re-adjusted using the grating scan. Thus, the alignment was an iterative process. This procedure was typically not needed after every probe replacement. A so-called *subdomain scan* was performed to verify the alignment. The grating for the central frequency was placed on a small area of the SLM, called a *subdomain*. Each subdomain corresponds to a different plane wave on the input facet. The subdomain was scanned across the SLM (Figure 2.10b), and the power coupled to the fibre was again measured using a camera. Only subdomains corresponding to plane waves with an angle lower than the fibre acceptance angle (determined by its numerical aperture) were coupled into the fibre. The resulting image (Figure 2.10d) was then, in essence, the image of the far-field of the fibre multiplied by the beam profile on the SLM. Thus, the subdomain scan could also verify the beam position on the SLM.

The setup presented in Figure 2.1 used two input polarisations. The fibre position and angle had to be appropriately aligned for both input beams. The system was initially aligned for one of the input polarisation beams. Afterwards, using the grating and subdomain scans, the beam for the other polarisation was centred in position and angle by aligning only the three mirrors placed in this beam.

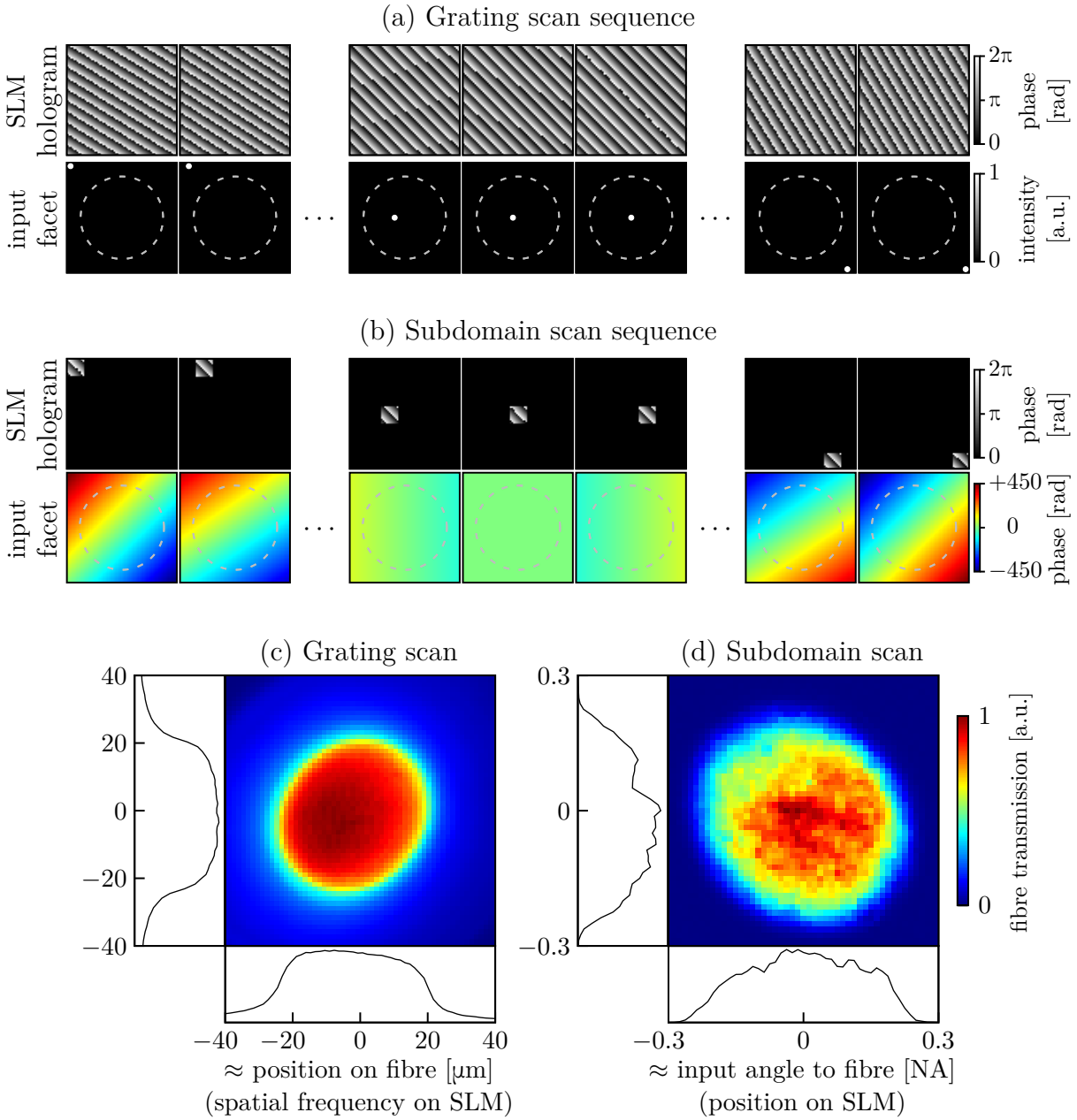

Figure 2.10: Grating scan and subdomain scan used for alignment of the fibre. (a) In the grating scan, different spatial frequencies were scanned on the SLM. Each corresponds to a point on the input facet. (b) In the subdomain scan, subdomains with the central frequency were scanned across the SLM. Each corresponds to a plane wave on the input facet. (c) An example of the gratings scan. The position in the grating scan corresponds to the position on the input facet. The bright area corresponds to the core of the fibre. The graphs show a cross-section through the centre of the measured scan. (d) An example of the subdomain scan. The position in the subdomain scan corresponds to the position on the SLM chip. The bright area corresponds to the numerical aperture of the fibre. The bright area is not sharp since a graded-index fibre was used. The exact intensity distribution depends on the beam profile on the SLM. The small ellipticity in both scans was caused by the prism placed in the beam path.

Instead of integrating the image on the camera, the photodiode PD3 in the setup presented in Figure 2.1 could be used to measure the power behind the fibre during both scans. However, such a photodiode is not often present in multimode fibre imaging setups (here, it was installed to allow imaging in transmission). On the other hand, the camera is, in any case, required to measure the transmission matrix of the fibre. Consequently, the camera was used for the alignment as well.

The output (distal end) was aligned after the fibre input was adequately aligned to the incident beam. The output facet was focused and centred onto the camera by moving the objective in the calibration module laterally and axially. Focusing the output facet onto the camera would measure the transmission matrix at the output facet. Thus, the focused points would be created on the output facet. Imaging directly on the facet was typically undesirable. A working distance (the distance between the output facet and the imaging plane) of a few tens of micrometres was often used. The transmission matrix could be later numerically propagated from the facet into the desired working distance. Moving the objective from the fibre by the working distance was a much easier option. Thus, a plane a working distance away from the fibre was imaged onto the camera during the calibration, and the points were created at the correct working distance.

When a pulsed laser was used as a light source, the length of the reference delay line had to be adjusted to obtain interference of the two signal beams (i.e., the two input polarisation beams propagating through the multimode fibre) and the reference beam. The reference delay adjustment was performed by sending the central frequency through the fibre (in either polarisation) and generating the reference beam. The delay line length was then adjusted to obtain the maximal amplitude of oscillations on the camera.

2.5. Fibre calibration and focus generation

The principles of the calibration were described in Section 1.4. There were, however, several technical details that were necessary for working and efficient implementation and were, for simplicity, omitted in Chapter 1. A more detailed explanation is thus provided here. The steps of the calibration procedure are outlined in Figures 2.11–2.17

As the first step of the calibration procedure, the intensity profile of the reference beam was measured. A hologram with the selected reference spatial frequency was displayed on the SLM (Figure 2.11a). The profile of the reference beam was then captured on the camera (CAM2 in Figure 2.1), as shown in Figure 2.11b. The amplitude of the reference beam was calculated as the square root of the measured intensity. It was used to correct the amplitudes of the signal beam measured during the calibration. This step was optional and unnecessary to perform the calibration and generate a scanning point (that is, the quality of the focused point would not have been affected by not taking the profile of the reference beam into account). However, it helped correct the averaged output amplitude discussed below and shown in Figure 2.16a. In addition, the profile of the reference beam had to be taken into account when numerical refocusing of the focused point was performed in Chapter 5.

As discussed in Section 2.8, two input polarisations were necessary when graded-index fibres were used. Parts of the calibration procedure thus had to be repeated for both input polarisations. These two consecutive runs differed only by the range of spatial frequencies generated by the SLM, as shown in Figure 2.3.

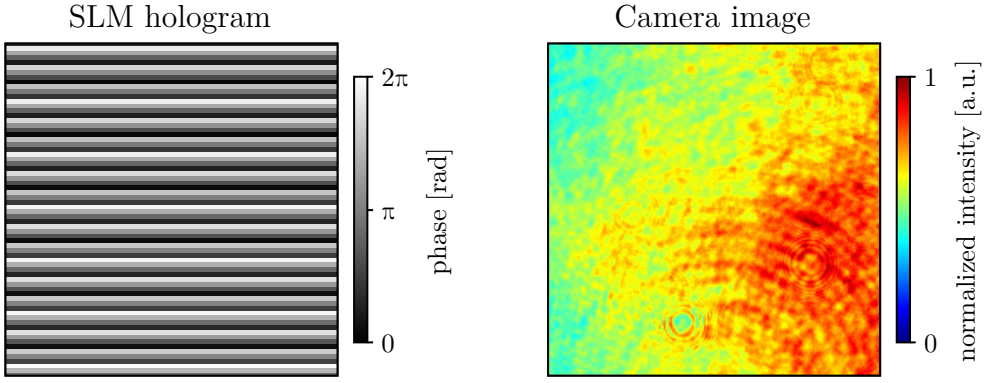

Figure 2.11: Measurement of the intensity profile of the reference beam. (a) Hologram displayed on the SLM with a single spatial frequency which produced only the reference beam (i.e., no light was coupled into the multimode fibre). Only a small area of the SLM is shown for clarity. (b) Intensity profile of the reference beam captured on the camera.

Similarly to the description in Section 1.4, the range of spatial frequencies coupled into the fibre was determined. A focused point was raster-scanned across the input facet of the fibre (Figure 2.12a) and the transmitted power was measured by summing the pixel values on the camera (grating scan), as described in Section 2.4. The grid of the scanned points was decimated by a factor of three to speed up the procedure. The decimation resulted in almost an order of magnitude faster measurement. The measured transmission (Figure 2.12b) was then upsampled to the original grid of points using bilinear interpolation and thresholded. Only points giving more than 20 % of the maximal transmission were selected to measure the transmission matrix. Setting the threshold even lower and thus allowing more input points to be coupled into the fibre had a minimal effect on the resulting point. However, setting the threshold significantly higher reduced the foci quality, as the transmission matrix was not fully measured.

The transmission matrix of the fibre was measured by overlapping the image of the output facet on the camera with a plane wave reference beam and employing phase-shifting interferometry. The measured phase was thus a phase difference between the signal and reference beams. Any phase drift (caused, e.g., by changes in the temperature or frequency of the laser) between the two optical paths during the transmission matrix measurement would thus skew the measured fields. The error in the measured phase would have decreased the power in the focused point, as the input beams would not interfere constructively. Consequently, this drift had to be measured and corrected. The correction was performed by periodically displaying the same pattern during the transmission matrix measurement and comparing the camera image with a lookup table of images with different phase drifts. This way, the phase drift was measured using a single camera image. A single point at the input of the fibre facet (typically close to the axis) and the reference beam were used to generate the lookup table. The phase of the point was shifted, and the resulting interference was recorded on the camera (Figure 2.13a). The signal measured in each pixel was a sinusoidal signal. Thus, three parameters could be obtained in each pixel: amplitude, phase and offset (Figure 2.13b,c). These parameters were then used to generate the lookup table for camera images with different phase shifts (Figure 2.13d).

Since the drift was caused mainly by changes in the ambient temperature, the drift significantly increased if the cover of the setup had been recently opened (to, for instance, change the fibre or insert a sample). The phase drift during the transmission matrix measurement can be eliminated by using internal references [26, 113–115], i.e., reference

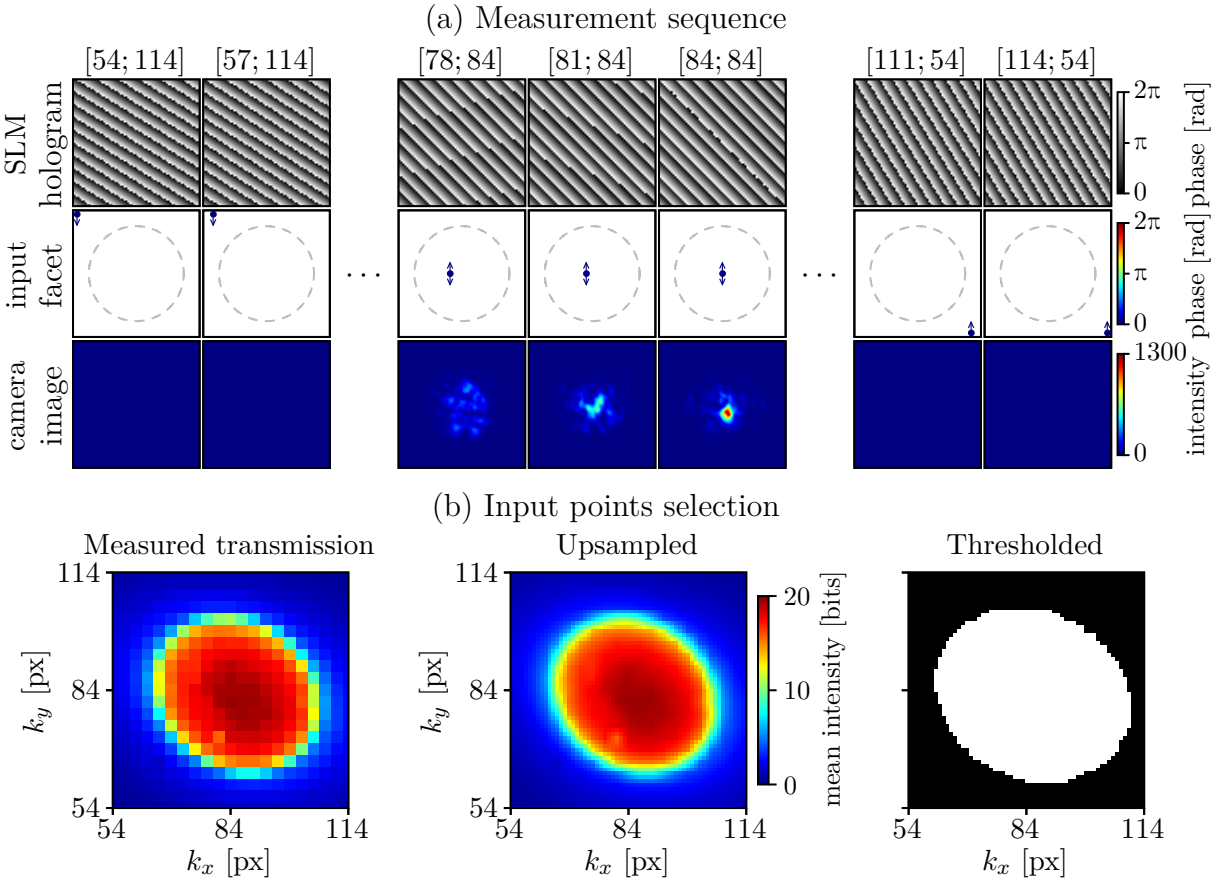

Figure 2.12: Selection of the input points for transmission matrix measurement. (a) The sequence of holograms applied on the SLM (grating scan), corresponding positions of the focused point on the input facet of the multimode fibre (the arrows show the polarisation direction) and images captured on the camera. (b) For each position of the focused point, the average intensity on the camera was measured. The result was upsampled to the grid of points used for the transmission matrix measurement. Only points giving more than 20 % of the maximal transmission were selected for the measurement.

beams that are sent through the multimode fibre itself. The reference and signal beams have the same path in such a case. Thus, the phase drift between them is minimal. However, due to the speckled nature of such references, the calibration must be performed multiple times with different carefully chosen reference beams to calibrate the entire field of view. The duration of the calibration is thus significantly increased.

The next step was to measure the transmission matrix. The reference beam was enabled, and the selected input points were scanned one by one, each with four phase steps (Figure 2.14). The four images captured on the camera were then processed to obtain the field (i.e., both the phase and amplitude), which was then corrected for the intensity profile of the reference beam, as discussed above. The selected central point was displayed periodically during the measurement, once every four input points. By comparing the camera image to all images in the lookup table (in Figure 2.13d), the phase drift was calculated (Figure 2.15). The value was then used to correct the phase for the following four input points. The field for each input point (after being corrected for the reference profile and the phase drift) was then saved to the hard drive.

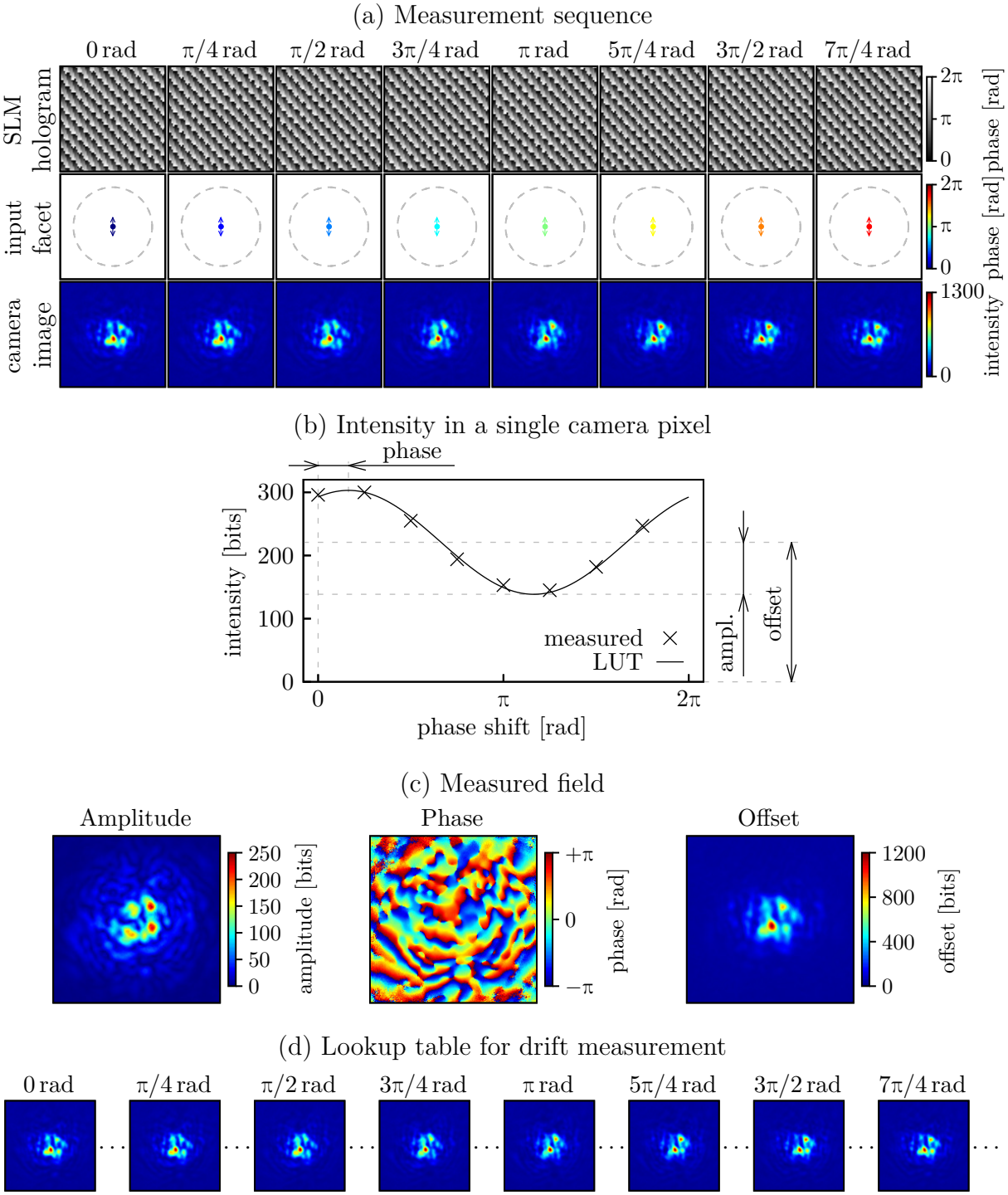

Figure 2.13: Measurement of the lookup table for correcting the phase drift during the transmission matrix measurement. (a) Sequence of holograms applied on the SLM (the reference beam as well as a single point at the input facet were generated), corresponding points (including the phase and polarisation) at the input facet and camera images. (b) Intensity measured in a single camera pixel and the result of phase-shifting. (c) Measured amplitude, phase, and offset of the signal across the field of view. (d) Lookup table of images with different phase drifts generated using the measured fields.

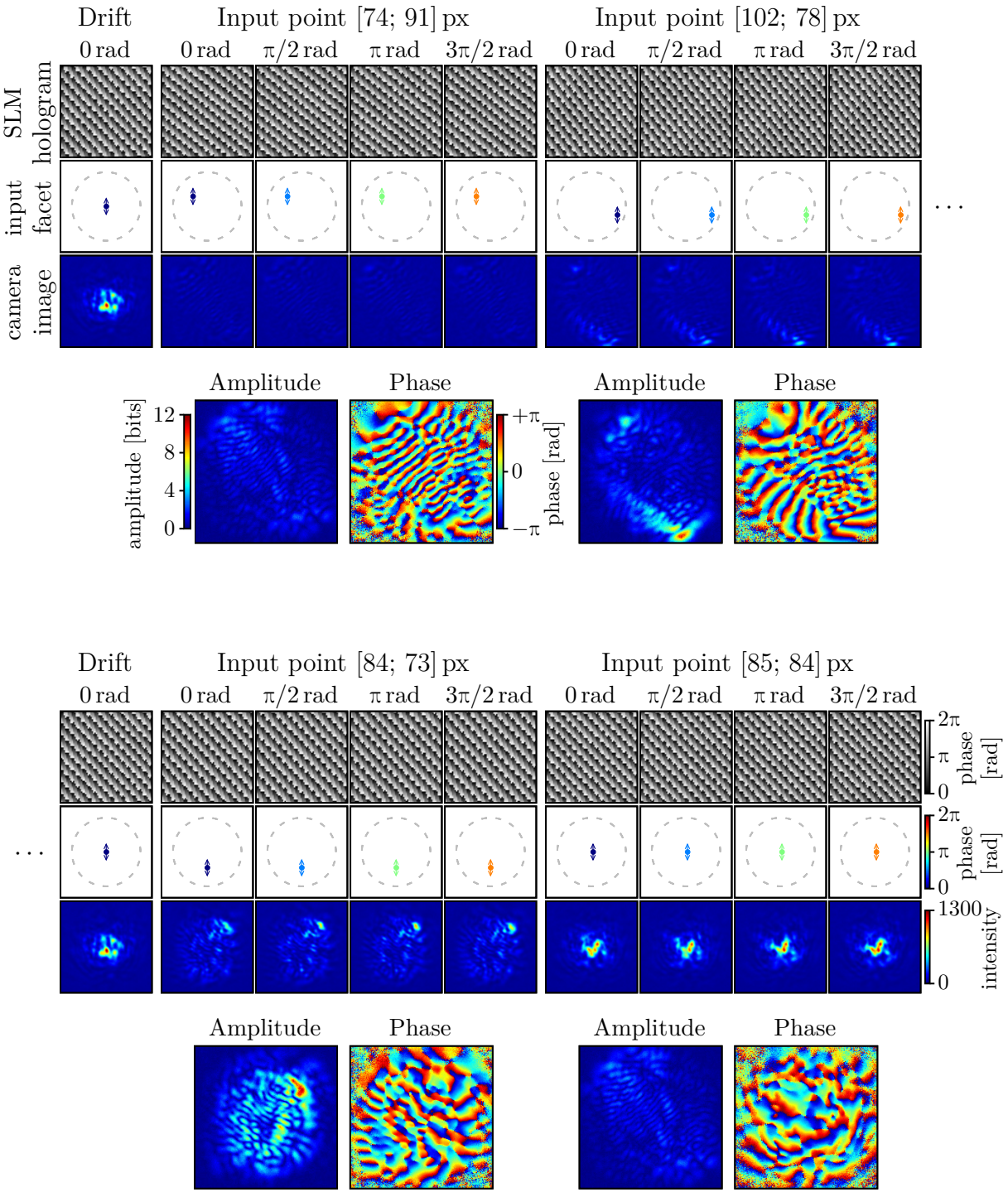

Figure 2.14: Measurement of the transmission matrix. Each input point selected in Figure 2.12b was scanned one by one. For each position, four images with different phase shifts were taken to calculate the amplitude and the phase of the field. During the measurement, the central point was displayed periodically to measure the drift by comparing the camera images to the lookup table generated in Figure 2.13d.

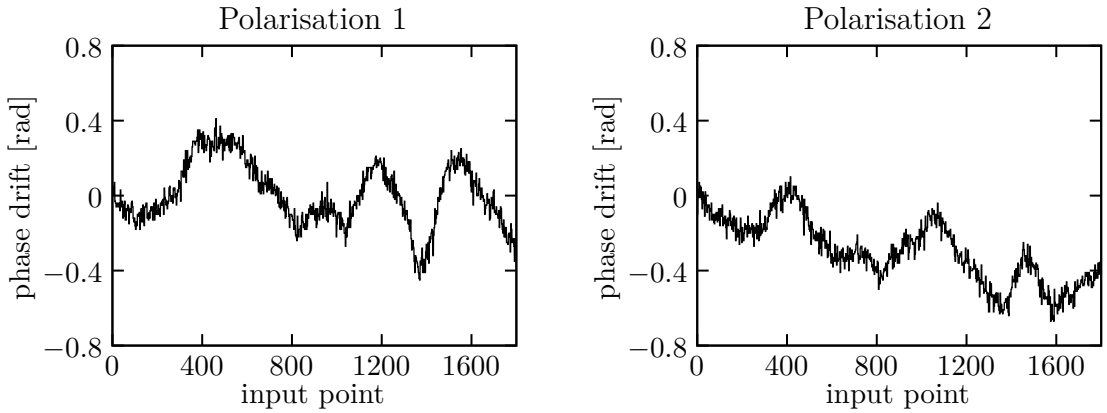

Figure 2.15: Phase drift between the signal and reference beam measured during the transmission matrix measurement. Since the drift was measured with respect to the phase at the beginning of the measurement for each polarisation, the values always started at zero.

During the measurement of the transmission matrix, the sum of the measured amplitude and the sum of the amplitude of the Fourier transform of the measured fields was calculated (Figure 2.16). The input points were scanned in random order to obtain indicative values shortly after the beginning of the transmission matrix measurement. The calculated averages were used to check the alignment of the calibration module. The measured averages in Figure 2.16a show that the amplitudes measured in both input polarisations were similar. The equal values were due to the polarisation not being maintained in the fibre. If the polarisation in the fibre was maintained, only one of the input polarisations would interfere with the reference beam. Thus, the amplitudes measured for the other input polarisation would be zero.

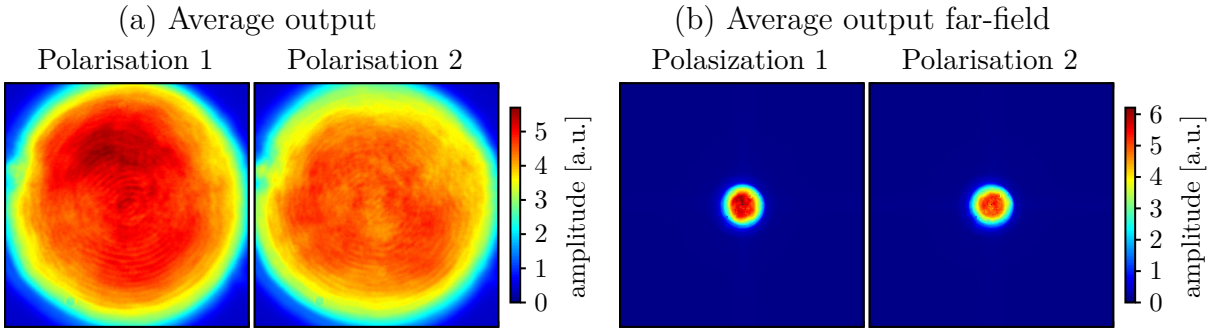

Figure 2.16: Averaged amplitude and averaged amplitude of the far-field at the output of the fibre calculated from the measured transmission matrix.

After the two transmission matrices (for the two input polarisations) were measured, each of them could be used to create a focused point in a single pixel of the camera (and thus at the distal end of the fibre or a working distance from the distal end) by displaying all the input points simultaneously, with their phases set to the negated phase values and amplitudes set to the amplitude values measured in that particular pixel. Due to the phase drift between the two input polarisation paths discussed above, the two points created by the two transmission matrices were not generally in phase. Thus, when created simultaneously, they did not interfere constructively. This is again in contrast with systems using polarising beam displacers, where the two points are always in phase

since there is no drift between the two input polarisation paths. Here, the optimal relative phase between the two input polarisation beams had to be found by shifting the phase of one of the two transmission matrices while monitoring the intensity of the focused point (Figure 2.17a,b). In this example, a point in the centre of the field of view was selected. However, since the phase difference between the transmission matrices was the same in all pixels, any output point could be chosen for this measurement. Thus, the phase shift that gave the maximal intensity for the central point resulted in optimal focus across the whole field of view.

As discussed in Section 2.1, the value of the relative phase shift was not stable over time due to phase drift between the two input polarisation optical paths. Since the calibration module and, thus, the camera was removed for imaging, the same method for finding the optimal phase difference could not be used to adjust the phase periodically. Instead, the relative phase difference was monitored on a photodiode (PD2 in Figure 2.1). A single plane wave was sent to each path to measure the relative phase between the two optical paths. The two plane waves interfered on the photodiode. The relative phase difference was then measured using phase-shifting, as shown in Figure 2.17c,d. The first measurement was performed as a part of the calibration procedure immediately after measuring the optimal relative phase on the camera. Afterwards, the measurement was periodically repeated during the imaging and the measured value was used to adjust the relative phase between the two transmission matrices. This stabilisation made the focused point stable over time despite the phase drift.

This procedure resulted in a stable focused point in the sample plane at the distal end of the fibre. The polarisation of the point on the camera was the same as the polarisation of the reference beam, thus, linear. Depending on the optics between the camera and the fibre (the quarter-wave plate), the polarisation of the point in the sample plane was either linear or circular. Output polarisation control would have to be implemented to obtain an arbitrary in-plane polarisation state, as discussed in Section 5.4.

When imaging at different distances from the facet was required, multiple calibrations could be performed. Performing calibrations at multiple distances would, however, be time-consuming. As an alternative, the transmission matrix could be propagated [116, 117] into an arbitrary plane. For the fibres and wavelengths used here, the propagation could be computed in about 10 to 20 seconds per plane (depending on the fibre used), which allowed fast refocusing during imaging. Since multiple transmission matrices could fit into the memory, the propagation of the transmission matrix was done only once and could be used repeatedly. The refocusing is demonstrated in Figures 5.20 and 5.35.

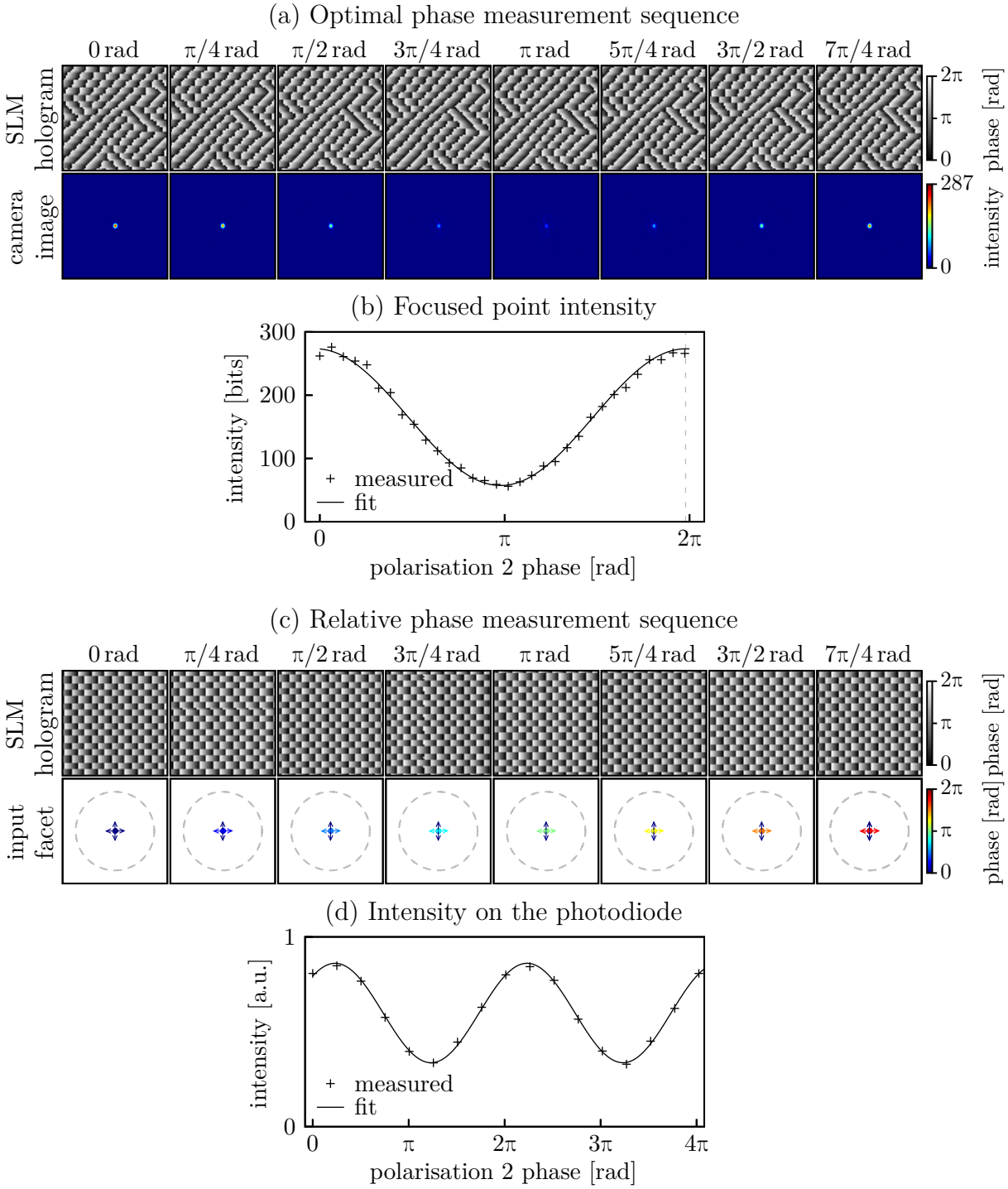

Figure 2.17: Measurement of the optimal relative phase between the two input polarisations. (a), (b) The relative phase of the two input polarisation beams was changed, and the intensity of the focused point on the camera was monitored to find the optimal value of the relative phase, resulting in constructive interference of the two input beams at that particular output point. (c), (d) A single plane wave was sent to each polarisation beam. The relative phase between the two beams was changed, and the resulting interference was monitored in a photodiode. This relative phase measurement allowed stabilisation of the relative phase during imaging, without access to the distal end of the fibre.

2.6. Focused point characterisation

To assess and optimise the performance of the fibre imaging system under different conditions, the quality of the focused points (which directly affected the imaging performance) had to be evaluated. The evaluation was done by analysing the image of the lateral point spread function (Figure 2.20a). For some experiments, a three-dimensional point spread function (see Figure 2.18) was measured by capturing images with the objective in the calibration module being focused on different planes.

Despite using a 12-bit camera, the dynamic range of the images was not sufficient to capture both the focused point and the speckled background simultaneously, as the background intensity was often more than three orders of magnitude lower than the peak intensity. Therefore, images with different exposure times were captured and used to generate a single high dynamic range (HDR) image (Figure 2.19). In the first step, overexposed and underexposed values from all images were removed (based on a threshold), except for underexposed values in the image with the longest exposure time and overexposed values in the image with the shortest exposure time (these should, however, not be present in the data, since it indicates that the shortest exposure time was still too long). The remaining (correctly exposed) values were divided by the corresponding exposure times. Assuming ideal camera linearity, the values obtained after these steps should be equal for all exposure times. Therefore, all the properly exposed values were averaged to minimise the noise.

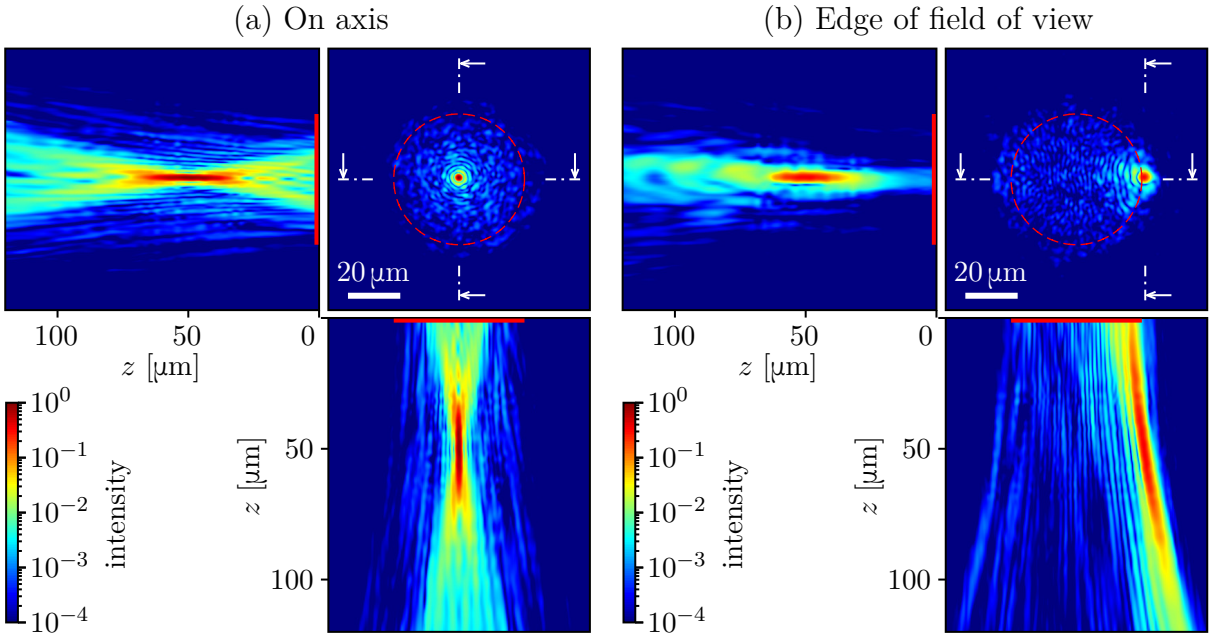

Figure 2.18: Three-dimensional point spread functions for two different positions of the focused point.

A typical lateral point spread function is shown in Figure 2.20a. Unlike point spread functions measured in a regular laser scanning microscope (which would ideally look close to Figure 2.20b), the point spread functions measured here contained a significant speckle background (a very rough estimate of the background is in Figure 2.20c). Not insignificant part of the power in the sample plane was randomly spread across the whole field of view. The fraction of the power contained in the focused point is called the *power*

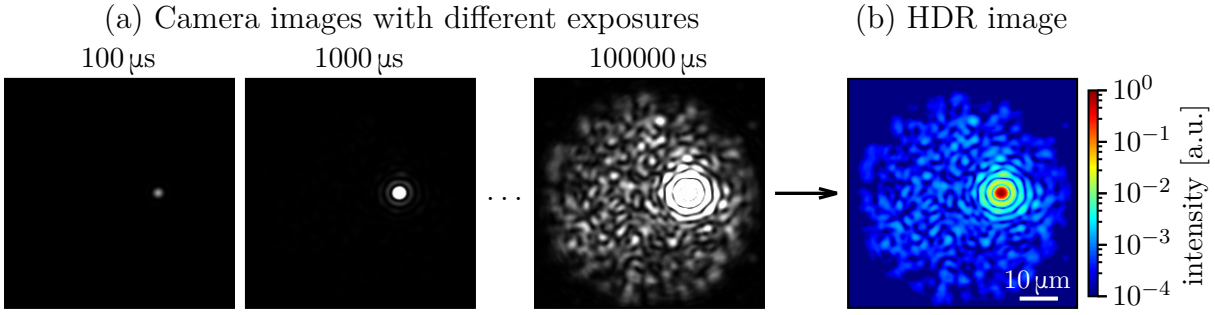

Figure 2.19: HDR image generation. (a) A 12-bit camera images taken using d1ifferent exposure times. (b) Calculated HDR image. The image is normalised to its maximal value and shown in logarithmic scale.

ratio. For demonstration, Figure 2.21 shows two points with significantly different power ratios. The primary cause of the power ratio not being equal to unity was the usage of phase-only modulation. Due to the missing amplitude modulation, the modulator did not precisely replicate the wavefront necessary to create a perfect focus at the distal end of the fibre. While there is no fundamental limit for the power ratio when a phase-only modulation is used for focusing through multimode fibres, the power ratio was typically below 80 %. Of course, achieving significantly higher power ratios is possible by employing complex modulation (i.e., modulating both the phase and amplitude) [118], by encoding the amplitude information into the phase-only hologram using, for example, a Gerchberg–Saxton algorithm [85]. However, such modulation is lossy and thus potentially unsuitable for non-linear imaging techniques requiring high excitation powers.

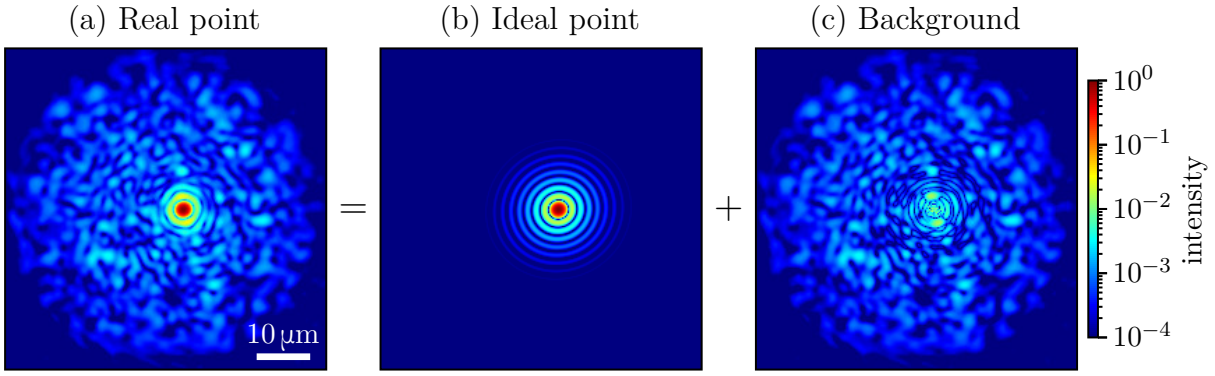

Figure 2.20: Real point created at the distal end of the fibre could be imagined as a superposition of an ideal point (here, an Airy disk, fitted to the measured point) and a speckled background (here, roughly estimated as an absolute value of the difference between the real point and the fit. This point spread function was measured at 780 nm, using a 5 cm long Prysmian fibre, 50 µm from the fibre facet.

Achieving high power ratios is particularly important for linear imaging, such as linear fluorescence (which was not used in this thesis) or transmission imaging (see Figures 2.28c and 3.5 for demonstration) since the random speckle background contributes to the image, decreasing the contrast. Methods for reconstructing the images based on measuring the exact distribution of the speckles around the focused point have been shown [119]. However, it has only been demonstrated for planar samples (1951 USAF resolution test chart and fluorescent beads on a glass slide), not in all three dimensions. By contrast, during non-linear imaging, the signal is excited practically only on the focused point and not in

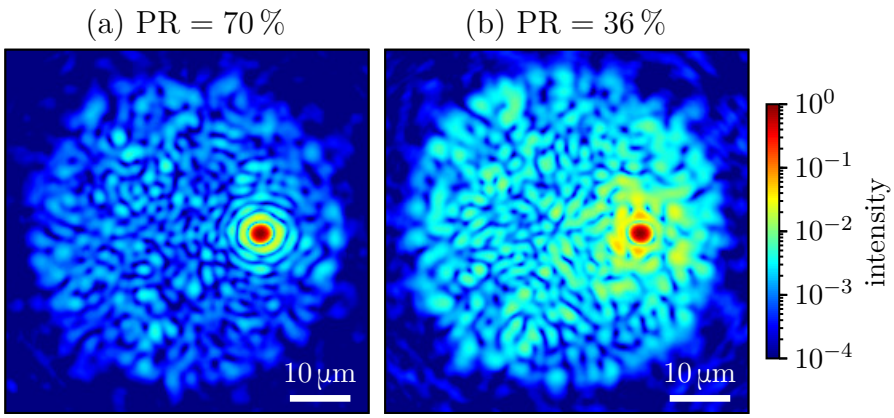

Figure 2.21: Typical point with (a) high and (b) low power ratio (Thorlabs GIF50E, 50 µm from facet, 780 nm). The difference of the power ratio was caused by disabling one of the two input polarisations (as described in Section 2.8).

the speckled background. For CARS, this is demonstrated in Figure 3.19. Nevertheless, achieving high power ratios was still essential, as it directly affected the efficiency of the imaging system and potentially the damage threshold of the sample.

The power in the focused point had to be estimated to calculate the power ratio from the HDR image. Thus, a model function was fitted to the data. The choice of the model function, which affected the accuracy of the calculated power ratio, was problematic in general. The point spread in a standard laser scanning microscope function is typically an Airy disc due to the circular aperture. While a point created on the axis at the distal of a step-index fibre may resemble an Airy disc, it is not generally a valid model, especially for graded-index fibres, points off the axis and far from the facet. In Figure 2.22, some examples of different point spread functions are selected from datasets presented in this thesis. The points were often elliptical, which had to be considered when designing the model. Not all points showed the concentric rings associated with an Airy disc. Thus, neither the Airy disc nor a Gaussian function could accurately model all the point spread functions measured in this thesis. An attempt was made to fit the data with a convolution of both functions. Such a model, however, had too many parameters to fit reliably. Thus, this thesis uses the Airy disc as the model function. Due to the ambiguity in calculating the power ratio, the uncertainty of the value can be very high, and caution must be taken when comparing the values for different fibres or configurations of the setup. Nevertheless, it was a significant quantity when, for example, calculating the excitation powers used during imaging.

The fit of the lateral point spread function was also used to determine the *spot size*. The full width at half maximum (FWHM) spot size was calculated directly from the parameters of the Airy disk. Since the model allowed the point to be elliptical, two dimensions were always calculated – the major and minor. If only one value is for simplicity presented in the graphs in this thesis, it is the major one, i.e., the larger of the two values. The theoretical limit for the lateral FWHM size of the point spread function is

$$\Delta\rho_{\mathrm{FWHM}} = \frac{0.51\lambda}{\mathrm{NA}},$$

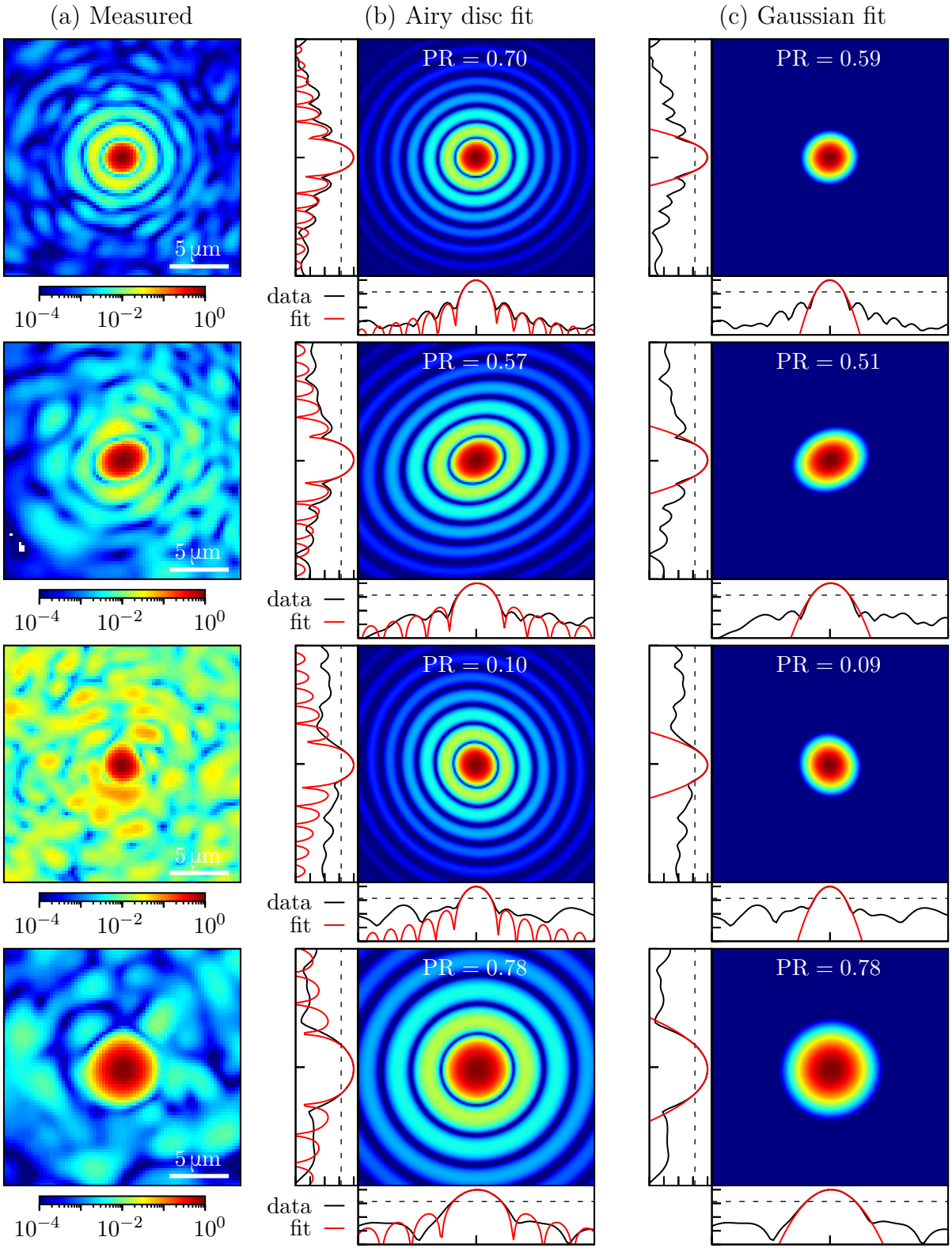

Figure 2.22: Examples of measured point spread functions and two different functions being fitted to them. PR is the power ratio. The dashed lines in the cross-sections are at $1/e^2$ of the maximal value.

where λ is the wavelength and NA the numerical aperture [120]. For the axial FWHM size of the point spread function, the theoretical value is

$$\Delta z_{\mathrm{FWHM}} = \frac{0.9\lambda}{n - \sqrt{n^2 - \mathrm{NA}^2}} \approx \frac{1.8n\lambda}{\mathrm{NA}^2},$$

where n is the refractive index of the medium, and the approximation is valid for small numerical apertures.

The third quantity used to describe the quality of the focused point is the *enhancement*. There are multiple different definitions of this quantity in the literature. The enhancement is often defined as the ratio between the optimised intensity and the intensity before optimising in papers dedicated to focusing through random media [72, 95, 98]. Another option is to define enhancement as the ratio between the peak intensity and the mean intensity of the background [40, 41, 62]. In this thesis, the following definition is used: The enhancement is the ratio of the average intensity in the focused point (defined as the area with intensity higher than $1/\mathrm{e}^2$ of the maximal value) and the average intensity in the field of view. This definition is similar to the definition in [36]. The enhancement essentially considers both the power ratio and the spot size. The drop in the power ratio and an increase in the spot size both decrease the enhancement. Consequently, it was used when a single quantity was needed to assess the performance of the fibre (for example, in Section 3.2 to measure the bandwidth). The enhancement can also be used to calculate the power ratio if the number of modes is known, as shown in [41, 118]. However, the necessary assumptions about the density of the modes are generally not met when graded-index fibres are being used, and the point is created at some distance from the facet. Consequently, this method was not used here.

2.7. Foci quality across the field of view

The power ratio and the spot size typically changed across the field of view, making the field of view inhomogeneous. The exact values were affected by many factors, including the type of the fibre (step-index or graded-index), its numerical aperture, the working distance (the distance between the focus and the facet) or the beam profile on the spatial light modulator. When a pulsed laser was used, the bandwidth of the fibre played a role as well.

An example of the properties of the focused points across the field of view for a step-index fibre and two working distances is in Figure 2.23. Since the beam exiting the fibre was divergent, the field of view size increased with increasing working distance. The size of the points, however, changed as well. While points created on the facet were almost perfectly circular, points at the edge of the field of view for 50 µm working distance were elliptical. The ellipticity was caused by a decrease in the effective numerical aperture at these positions. When used for fluorescence imaging with epi-detection, the collection efficiency for these points decreases as well, as shown in [39].

Graded-index fibres, on the other hand, behaved slightly differently. Even when focusing directly on the facet, off-axis points were elliptical due to the effective numerical aperture being lower in one direction. Therefore, the field of view was not homogeneous even when imaging directly on the facet or in its proximity. Figure 2.24 shows the properties of the foci across the field of view for different working distances. The power ratio was almost independent of the working distance, similar to the step-index fibre. The spot

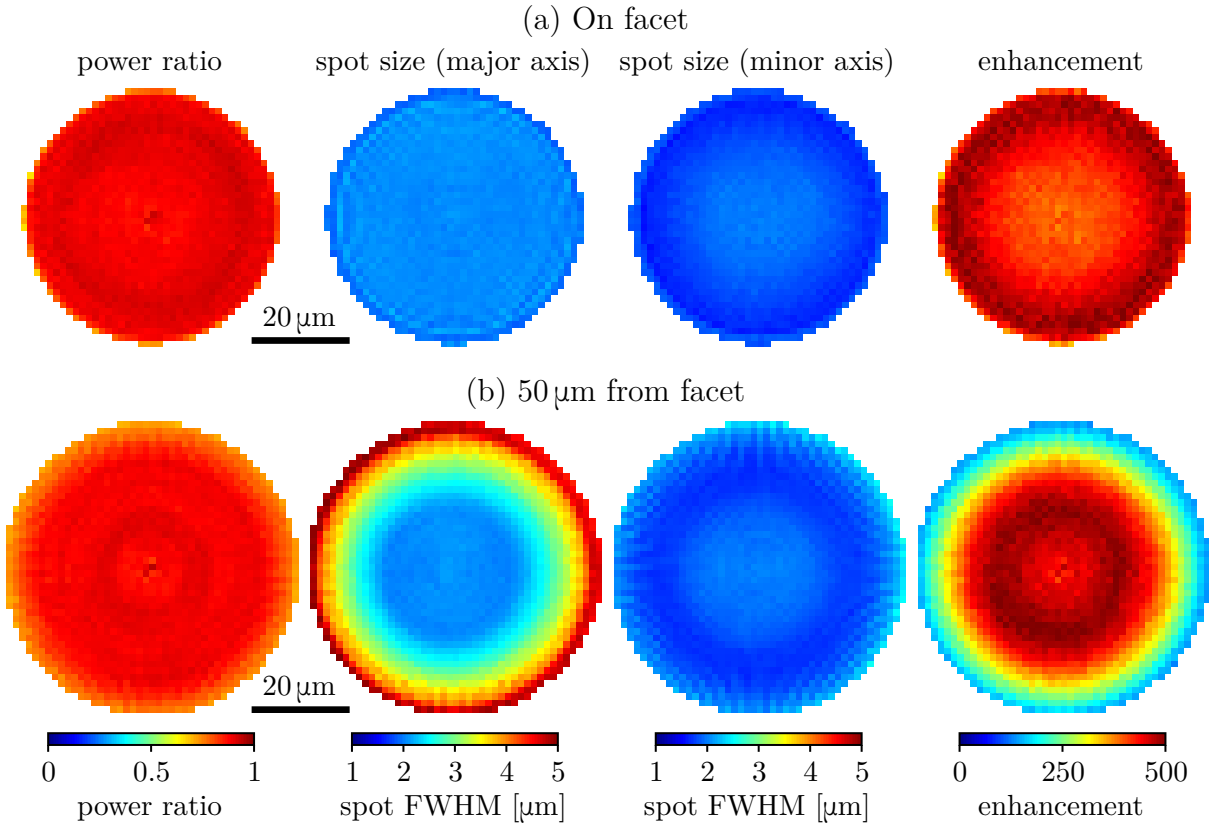

Figure 2.23: Evaluation of the properties of the focused points across the field of view for two different working distances for a step-index fibre (Thorlabs FG050LGA), measured at 780 nm.

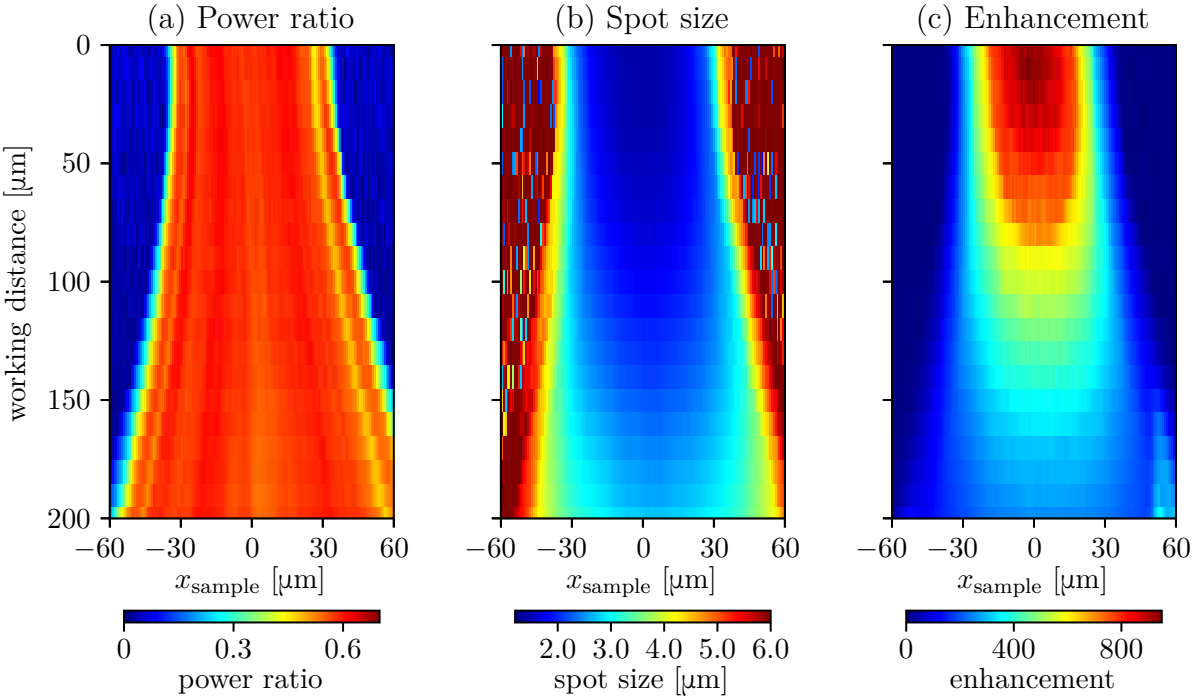

Figure 2.24: Focused point quality as a function of the working distance for a graded-index fibre (CREOL F3), measured at 780 nm. The slight tilt of the data was caused by the axis of the fibre and the axis of the objective not being perfectly parallel.

size increased (and thus the enhancement decreased) with increasing working distance both for points on and off-axis. While for step-index fibres, the diameter of the field of view increased linearly with the working distance, for graded-index fibres, the size of the field of view was almost constant up to some working distance (here, to about 50 µm) and started to increase only afterwards.

Due to the cylindrical symmetry of the fibres, the profiles in Figure 2.23 have a cylindrical symmetry as well. Consequently, to evaluate the performance, only a cross-section of the profiles (i.e. only points on a line across the field of view) was measured when a cylindrical symmetry was assumed. Under some circumstances, however, this symmetry was broken. A significant misalignment of the system was one of the possible causes (in that case, the alignment had to be examined as described in Section 2.4). For fibres with a low cladding-to-core diameter ratio (that is, with a thin cladding), artefacts caused by the cleaving procedure could also cause slight asymmetry. The asymmetry of the probe itself could also be caused by imperfect polishing or splicing (used in Chapter 5).

2.8. Polarisation in graded-index fibres

It has been previously shown that short straight low-NA step-index fibres maintain circular polarisation [90]. Therefore, if using a basis of circularly polarised input points, only one input polarisation (e.g. left-handed) is sufficient to create an output point with the same polarisation state with a high power ratio. If the imaging technique does not require the polarisation of the focused points to be controlled, this significantly simplifies the setup since the input polarisation control can be completely omitted like in many publications including [41, 54, 77, 121].

On the other hand, graded-index fibres do not have this useful property. The difference between step-index and graded-index fibres is demonstrated in Figure 2.25. Here, the enhancement for points on a line across the field of view was measured for one step-index and two graded-index fibres. The measurements were performed with (blue line) and without polarisation control (red and green lines), with the circular and linear polarisation basis. With the polarisation control, the choice of the basis had a negligible effect. Two orthogonal linear polarisations were used for all other experiments in this thesis.

For the Thorlabs step-index fibre, it was sufficient to use only a single circular polarisation (and thus omit the polarisation control in the setup) to create a circularly polarised point in the sample plane. This was due to the fibre maintaining circular polarisation during light propagation. Adding the second input polarisation had a negligible effect on the measured enhancement. On the other hand, when a linear polarisation basis was used, the quality of off-axis points dropped when only a single input polarisation was used. A polarisation control was required to obtain a linearly polarised point in the sample plane with maximal enhancement. Hence, the linear polarisation was not perfectly maintained in this fibre.

The graded-index fibres tested here maintain neither the circular nor the linear polarisation. The enhancement achieved without the polarisation control was, in general, about half of the values achieved with the polarisation control (an example of the point spread functions is in Figure 2.21). Moreover, with some fibres (Thorlabs GIF50E, for example), the enhancement significantly changed across the facet when only a single input polarisation was used. Consequently, when graded-index fibres were used, employing the input polarisation control was necessary to achieve the optimal performance of these fibres.

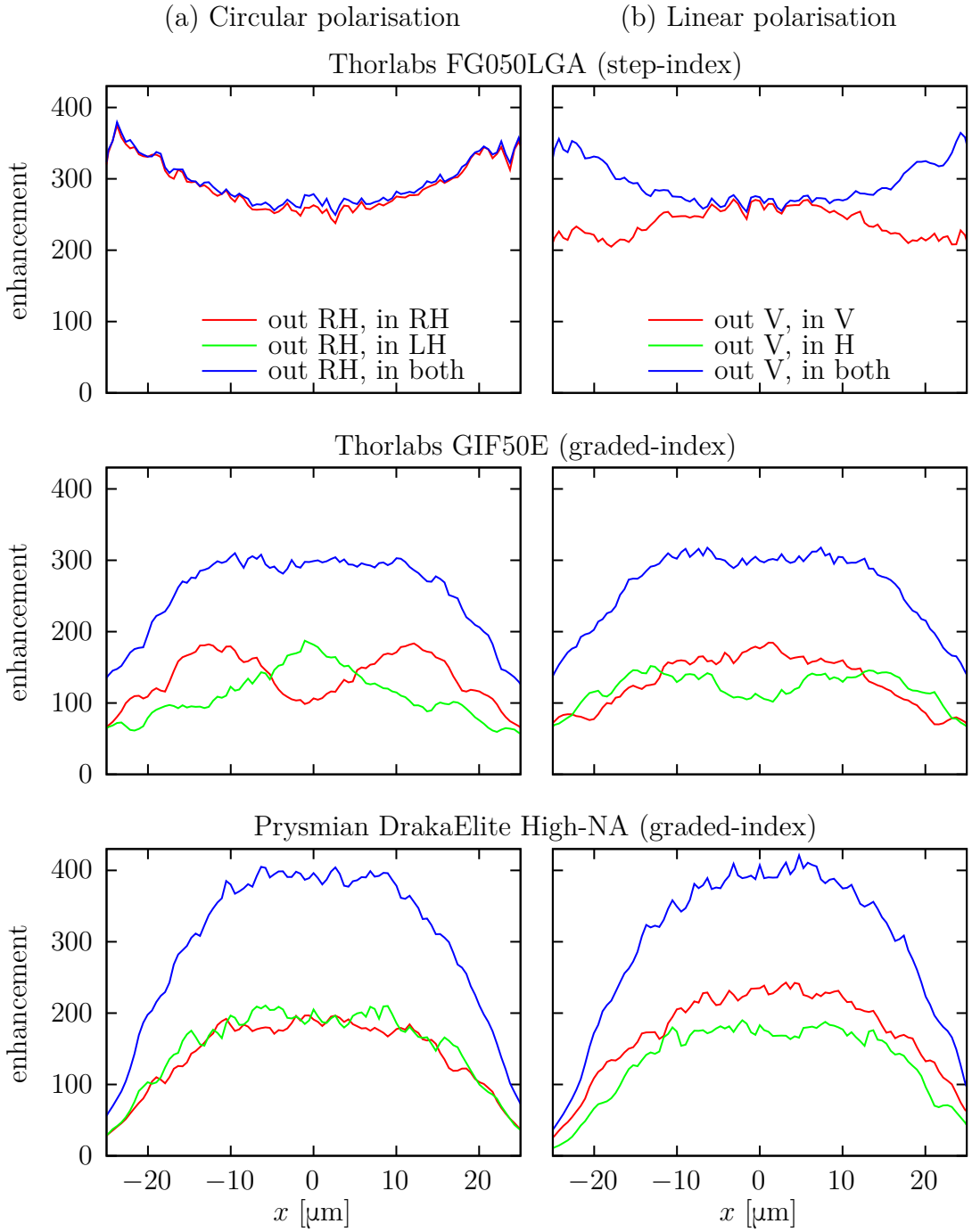

Figure 2.25: Polarisation maintaining in different multimode fibres. The images show enhancement for focused points on a line across the field of view for different polarisation basis. (a) Circular polarisation (RH – right-handed and LH – left-handed) was used both at the input and output. Since the step-index fibre maintained circular polarisation, generating the opposite polarisation at the output was impossible. (b) Linear polarisation (V – vertical and H – horizontal) was used.

The simplified explanation of the drop in the enhancement is the following: Consider that light with vertical linear polarisation was coupled into the fibre during calibration. After propagating through the fibre, the beam would have vertical and horizontal polarisation components. Only the vertical component would interfere with the vertically polarised reference beam. Thus only the vertical component would be considered when measuring the transmission matrix. When creating a focused point, the vertically polarised output component would constructively interfere in the desired output point. The uncontrolled horizontal component would create a random speckle background. Adding the second input polarisation would control a larger fraction of the fibre modes. Having better control over the fibre modes decreased the amount of uncontrolled light, decreasing the background and increasing the intensity of the focused point (and thus the enhancement).

Implementing the input polarisation control was also essential when the output polarisation control (i.e., generating an arbitrary in-plane polarisation state of the focused point) was desired. The output polarisation control is discussed in Section 5.4.

2.9. Reducing the number of input points

Although liquid crystal spatial modulators are much more efficient than digital micromirror devices, they are also noticeably slower. For some types, the rise time is in the order of tens of milliseconds. The delays then significantly increase the time required to calibrate the multimode fibre fully. With the SLM used here (Meadowlark HSP1920-1064-HSP8), the optimised timing (Figure 2.5) and a heavily parallelised software, the calibration of the Prysmian fibre at 800 nm could be performed in about one minute per input polarisation. However, some initial experiments were performed using a significantly slower Meadowlark HSP512-1064 spatial light modulator and unoptimised software. In this configuration, the calibration for the Prysmian fibre took up to half an hour. The slower SLM (however, with a more optimised software) was also used for some CARS images in Chapter 4. Consequently, the possibility of reducing the number of input points and thus the time required to perform the calibration was investigated.

The holograms for the SLM were generated using a discrete Fourier transform, as shown in Section 1.2. The range and the number of possible spatial frequencies (and thus the number and range of the possible locations of the point in the far-field of the SLM, that is, on the proximal facet of the fibre) were therefore determined by the dimensions and resolution of the SLM chip. Due to the properties of the discrete Fourier transform, increasing the resolution of the SLM increased the range of the spatial frequencies and increasing the size of the SLM increased the resolution in the far-field. The size of the SLM was typically fixed, so the numerical aperture of the fibre back-propagated to the SLM (where it formed a circle) exactly filled the active area. Therefore, for a given fibre, the number of input points was fixed and independent of the resolution of the SLM. To generate a different number of input points, the Fourier transform was oversampled (Figure 2.26), and the resulting holograms were subsequently cropped to the resolution of the active area on the SLM.

Figure 2.27 shows the power ratio and the enhancement for five points across the field of view for a different number of input points used during the calibration. Increasing the number of input points (and thus oversampling) had no measurable effect. Decreasing the number of points by about one-third had only a minor impact on the properties of the focused points. Any further reduction, however, resulted in a reduced power ratio

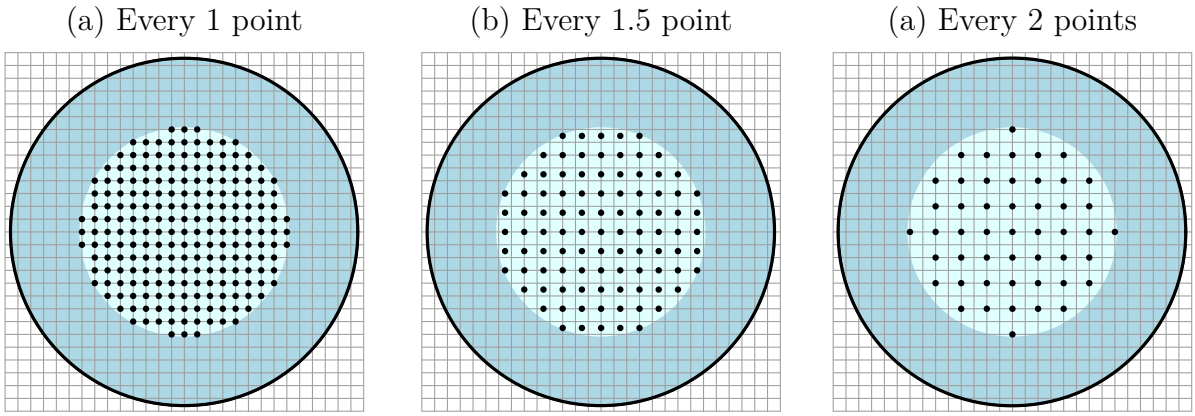

Figure 2.26: Illustration of the input facet of the fibre with different grids of input points. The mesh shows a grid of points that can be accessed directly using discrete Fourier transform without oversampling.

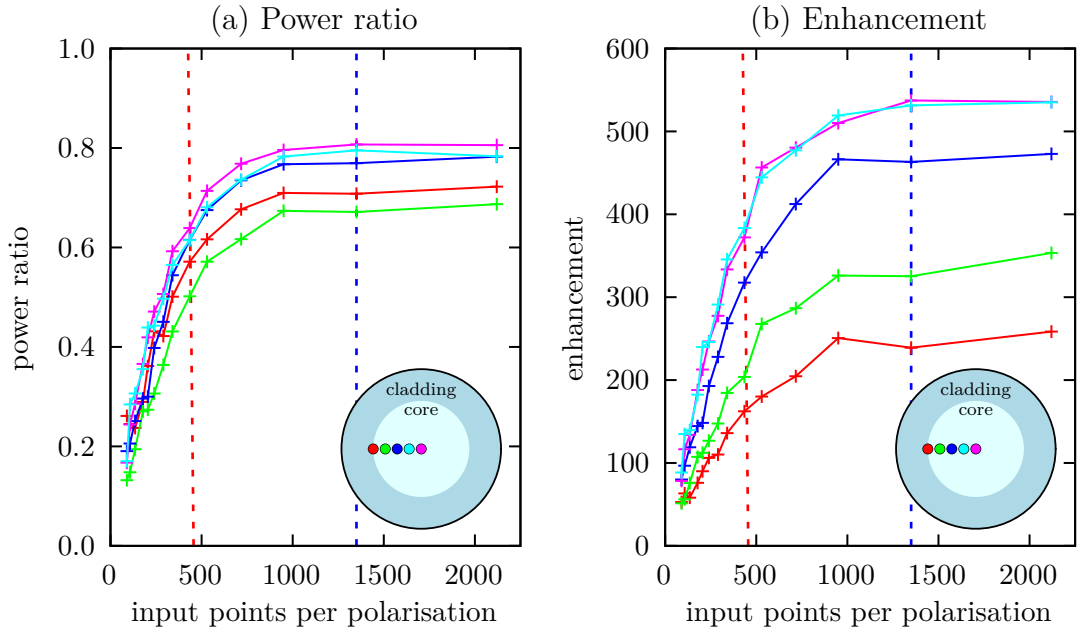

Figure 2.27: Quality of foci for a different number of input points. The solid lines are a guide to the eye. The red dashed line shows the actual number of guided modes per polarisation supported by the fibre. The blue dashed line shows the number of points achieved without oversampling. A graded-index fibre (Prysmian DrakaElite) was used. The measurement was performed at 780 nm.

and enhancement. Thus, only an unsubstantial decrease in the time required for the calibration would be possible at the cost of a more complicated hologram generation. Since replacing the SLM with a faster type and optimising the timing reduced the time required to finish the calibration by order of magnitude, this option was not used during any experiments.

2.10. Effect of the beam diameter

One of the variables while building a fibre imaging setup was the beam diameter on the SLM. When a phase-only modulation was used, the amplitude of the field on the SLM (and accordingly, in the configuration used here, the amplitude in the far-field of the fibre) was not controlled in any way. The beam profile thus determined it. As discussed in Section 2.6, using phase-only modulation generated a speckled background around the focused point, i.e., the power ratio was below unity. It could be assumed that different beam diameters (for practical reasons, only a Gaussian beam profile centred in the centre of the SLM was considered) have an impact on the achievable power ratio and spot size. The effect of the beam diameter on the performance of the endoscope was therefore experimentally investigated.

For the experiment, the actual beam diameter on the SLM was chosen to overfill the active area massively. Applying a mask on the SLM could reduce the diameter to the desired value. In essence, all holograms (during the calibration, testing the quality of the point and imaging) were multiplied by a Gaussian envelope, locally decreasing the 1st order diffraction efficiency (see Figure 2.28a). While this method was very inefficient, it allowed changing the effective diameter of the beam without changing any elements in the system, which was beneficial for testing. The optimal beam diameter would be achieved using a beam expander for practical use.

To measure the effective beam diameter (Figure 2.28b), a subdomain scan (described in Section 2.4) was performed, while the same mask was applied to the holograms. Instead of measuring the power coupled in the fibre (like in Section 2.4), the power in the 1st diffraction order was measured. For ease of understanding, the position on the SLM was converted to the units of numerical aperture. The $1/e^2$ radius of the beam was determined by fitting a Gaussian function to the measured profile.

Figure 2.28c shows the point spread functions and images of the 1951 USAF resolution test chart (imaged in transmission). The point spread functions show that the intensity of the speckled background increased (and thus the power ratio decreased) with increasing beam diameter and the spot size decreased.

For a graded-index fibre (Prysmian DrakaElite), a complete characterisation of the points for different beam diameters was performed. Figure 2.29a–d shows the spot size, enhancement and power ratio for points on a line across the field of view (50 µm from the facet) for different beam diameters. Figure 2.29 is a comparison for an on-axis point, showing the trade-off between the power ratio and spot size.

In this experiment, the power efficiency of the setup was estimated as well (Figure 2.29f). The SLM effectively changed the laser beam diameter by locally decreasing the diffraction efficiency. Since this resulted in a loss of power, the power being coupled into fibre for a given beam diameter was significantly lower than if the beam was magnified to this diameter using a beam expander. Accordingly, the efficiency could not be estimated by measuring the input laser power and the power in the focused point. Instead, three factors affecting efficiency were considered. The first was that if the beam exceeded the

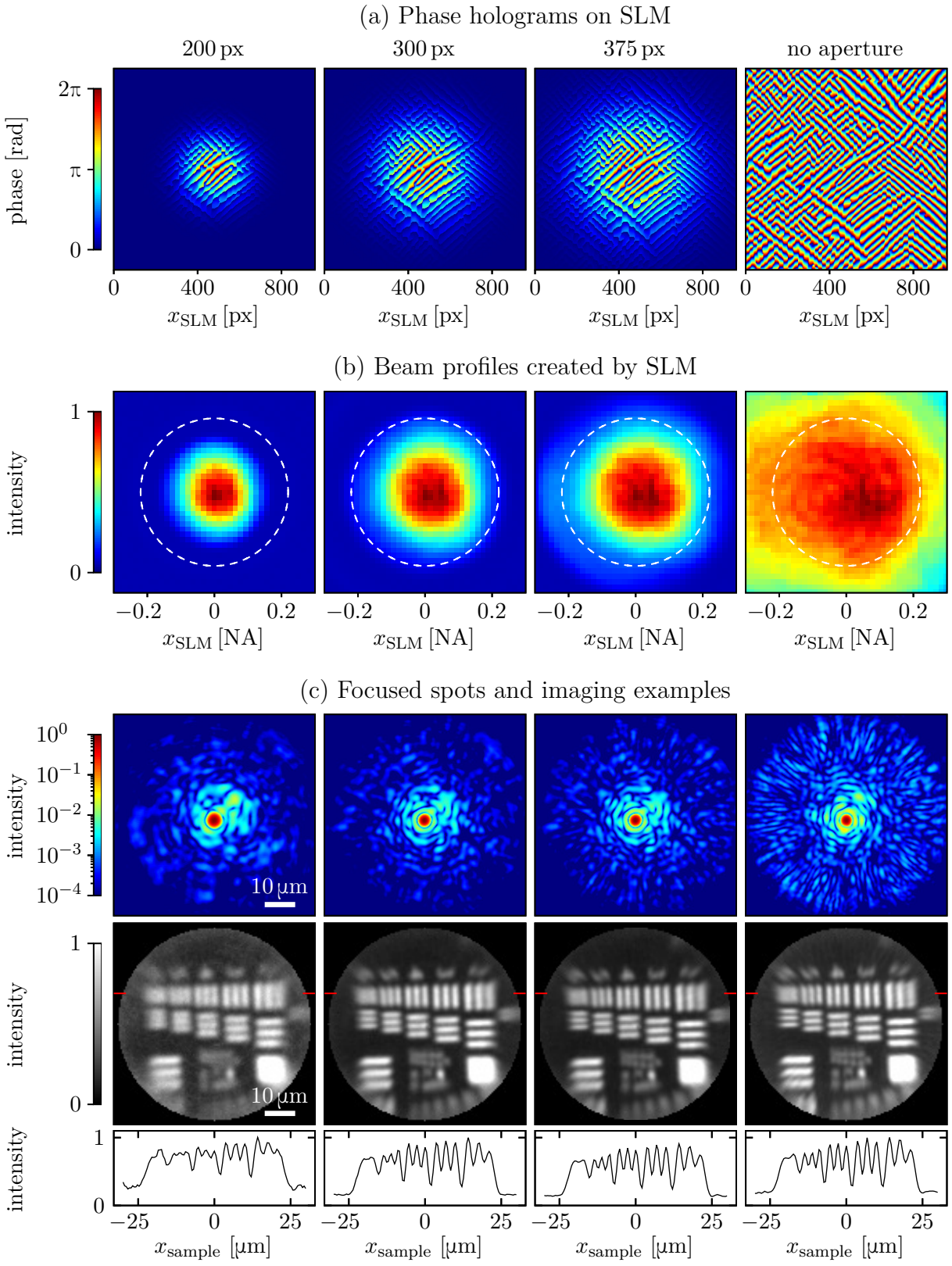

Figure 2.28: The effect of the beam diameter on the SLM on the size and power ratio of the focused points and the imaging. (a) Holograms on the SLM after applying a Gaussian envelope to effectively reduce the beam diameter. (b) Measured profiles of the beam. The dashed line corresponds to the acceptance angle of the fibre given by its numerical aperture. (c) Focused points created 50 µm in front of a facet of a Thorlabs FG050LGA step-index fibre and corresponding images of the USAF target (imaged in transmission).

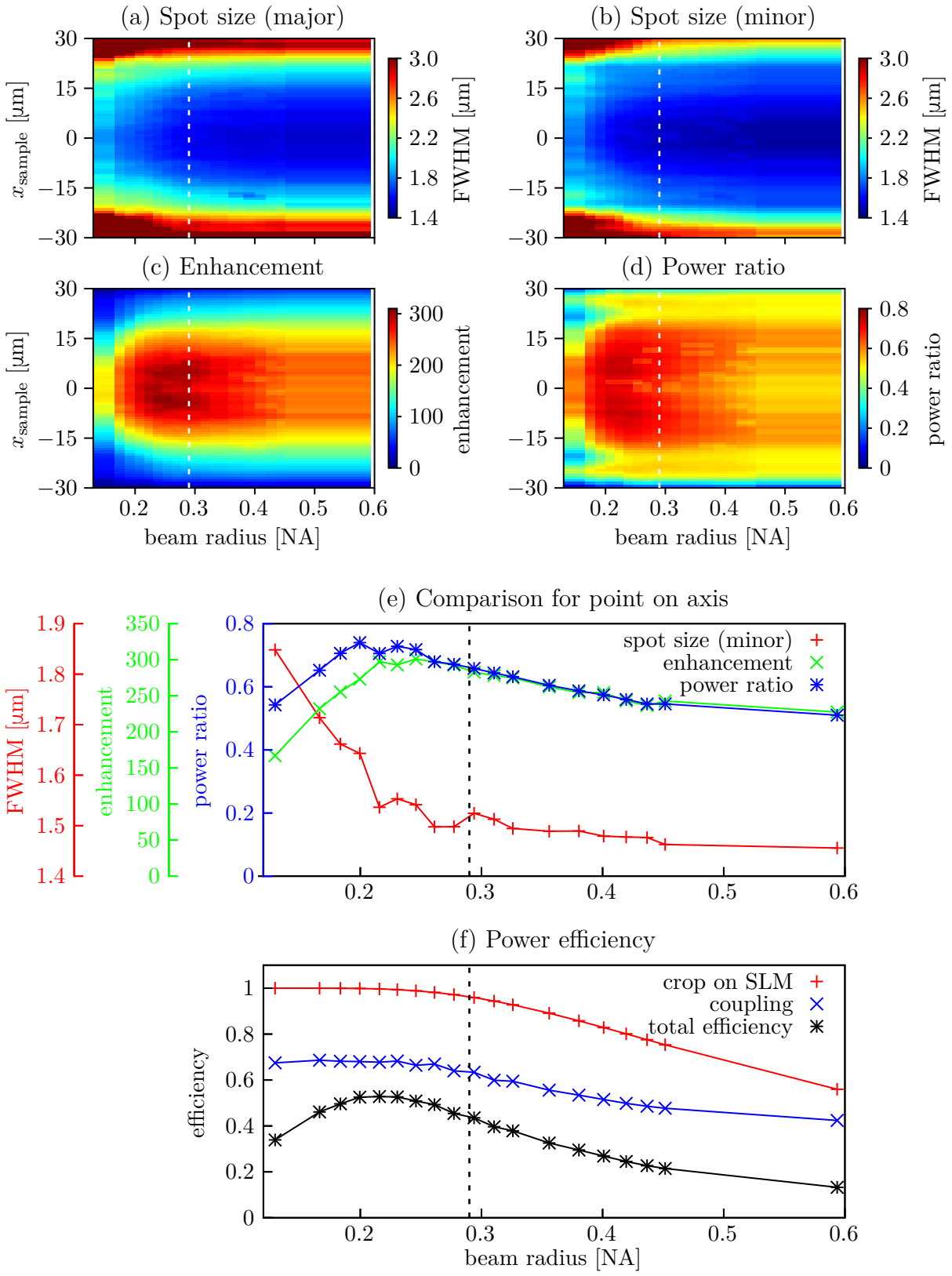

Figure 2.29: The effect of the beam diameter on the SLM on a graded-index fibre (Prysmian DrakaElite). (a)–(d) Properties of focused points created at different positions 50 µm from the facet for different beam diameters. The dashed lines represent the numerical aperture of the fibre. (e) Values for an on-axis point. The lines are a guide to the eye. (f) Relative power efficiency of the system. The efficiency decreased due to the beam being cropped on the SLM, losses when coupling the light into the fibre and the power ratio.

size of the SLM active area, the beam was cropped. This effect could be easily modelled, assuming a Gaussian beam profile. The second factor arose from the limited acceptance angle of the fibre, given by its numerical aperture. Thus, only a fraction of the power was coupled into the fibre. The coupling efficiency was measured by creating a point in the sample plane and measuring the power just before the first objective (it was not physically possible to insert the power meter between the fibre and the objective) and just after the second objective. The coupling efficiency could be calculated, taking the transmission of the objectives (79 % at 780 nm) into account. If the SLM chip were larger, the losses associated with cropping the beam would be lower. The losses when coupling the light into the fibre would, on the other hand, increase. The product of both should be similar. The third factor was the power ratio of the focused point, which further reduced the efficiency. By multiplying all three factors, the total relative efficiency was determined. This quantity was essential for non-linear imaging, where the power ratio was less critical than during linear imaging. Note that the measurement presented here was relative, i.e., it does not show the actual total efficiency of the system, which was noticeably lower, as the 1st diffraction efficiency of the SLM and the transmission of the optics were not taken into account. Nevertheless, these factors were almost independent of the beam diameter on the SLM, not changing the calculated optimal beam radius.

The data in Figure 2.29 show that the optimal beam radius for this graded-index fibre was close to the numerical aperture of the fibre. A smaller beam led to an increase in the spot size. When the beam radius was lower than the numerical aperture of the fibre, the size of the field of view decreased. The power ratio also dropped for beams with a radius below 0.2 NA. Significantly overfilling the numerical aperture led to a decrease in the power ratio and the transmission efficiency of the setup. The decrease in spot size was insignificant. For a beam diameter approaching the numerical aperture, the power ratio and transmission efficiency were slightly below the maximal values, the spot size was slightly above the minimum, and the field of view size was unaffected.

2.11. Summary

In this chapter, a multimode fibre endoscope was built, which used a combination of a tunable continuous-wave laser and a tunable femtosecond laser as a light source. The system included polarisation control of the beam coupled into the fibre, which was crucial for achieving high focus quality using graded-index fibres, which (unlike step-index fibres) do not maintain circular polarisation. Introducing the polarisation control for pulsed lasers necessitated implementing phase drift correction during the imaging (without access to the distal end of the fibre), which is typically not needed in multimode fibre endoscopic systems built for continuous-wave lasers. The drift correction made the focused point stable over long periods, which was an essential step for imaging.

The alignment and calibration procedure of the system was described in detail Furthermore, the foci generated at the distal end of the fibre were characterised. The speed and power efficiency of the system was maximised by optimising the triggering of the data acquisition and calibrating the response of the spatial light modulator. In addition, the effect of the beam diameter on the spatial light modulator was studied, which showed the trade-off between the spot size and the power ratio achievable with phase-only modulation, as well as the impact on the total transmission efficiency of the system.

3. Wavelength-dependent behaviour of a fibre endoscope

Implementing non-linear imaging, such as two-photon excitation fluorescence (TPEF), coherent anti-Stokes Raman scattering (CARS) or second-harmonic generation (SHG) imaging, through a multimode fibre puts several requirements on the endoscopic imaging system. In particular, it is necessary to focus light from pulsed lasers. Since the propagation of light through multimode fibres is wavelength-dependent, the bandwidth of such fibres is limited, potentially limiting the ability to focus short pulses. In addition, the pulse length should be kept short and equal across the field of view, which might require employing dispersion compensation techniques. CARS imaging through a multimode fibre then puts additional demands on the endoscope. To implement CARS, two wavelengths separated by around $3000\,\mathrm{cm}^{-1}$ must be focused simultaneously, ensuring a spatial and temporal overlap of both beams in the sample plane. It is also beneficial to be able to tune one (or both) of the two wavelengths in a small range (ideally about $250\,\mathrm{cm}^{-1}$, i.e., $\approx 15\,\mathrm{nm}$) to target different molecules (lipids, proteins and DNA, for example) without the necessity of repeating the calibration.

In previous research on non-linear imaging through a multimode fibre, out of the three mentioned methods, only TPEF imaging has been implemented [51–54]. Focusing of pulsed lasers through multimode fibres has thus been demonstrated [122–124]. Nevertheless, the quality of the foci demonstrated typically did not match the one achievable with continuous-wave (CW) lasers during linear imaging using similar fibres, and no in-depth investigation of the differences between different fibres has been conducted. Thus, it is unclear how to choose a fibre for the endoscope and what modifications are required compared to a system used for linear imaging.

In this chapter, the multimode fibre endoscope built in Chapter 2 is used to characterise the modifications necessary to fulfil the above-discussed requirements and allow efficient implementation of TPEF, CARS and SHG. The bandwidth of the system is discussed, and methods for correcting the dispersion of the spatial light modulator are presented. The dispersion-corrected system is then used to measure the bandwidth of different multimode fibres, including a demonstration of the effect of the bandwidth on focusing light from a femtosecond laser. The dispersion of the fibre used as an endoscope is measured as well. Lastly, a method for simultaneously focusing two wavelengths using a single spatial light modulator is evaluated.

3.1. Spatial light modulator dispersion compensation

The ability to tune the excitation wavelength after calibration is a valuable property for CARS imaging as it allows exciting different Raman shifts without the necessity to perform multiple calibrations. The fibre imaging system contained two elements that significantly changed the behaviour with wavelength. One of the elements was the SLM used in an off-axis configuration. The holograms displayed on the SLM had a form of sums of blazed diffraction gratings. Therefore, the diffraction angle changed when the wavelength changed, which changed the pattern projected to the proximal end of the multimode fibre. This effect and methods for correcting the dispersion of the SLM is studied in this section. The second highly wavelength-dependent element was the multimode fibre itself, which is studied in Section 3.2.

The effect of the SLM dispersion is outlined in Figure 3.1a. When broadband light was diffracted on a blazed grating on the SLM, different wavelengths were diffracted under different angles. The input facet of the fibre was placed in the far-field of the modulator. Thus, different wavelengths focused on different positions on the proximal facet of the fibre. Consequently, when the wavelength of the laser was tuned after the calibration, the pattern projected to the proximal end to create a point at the distal end changed (it both shifted and scaled, as shown in Figure 3.2), causing a degradation of the focused point. When such a system was used for imaging, the image contrast decreased as the wavelength was tuned (see Figure 3.5a).

The hologram displayed on the SLM for the central frequency was a blazed grating. The diffraction angle, θ, thus varied with wavelength, λ, according to

$$\theta \approx \frac{\lambda}{d}, \tag{3.1}$$

where d is the pitch of the grating. The pitch of the grating could be changed according to this equation to keep the diffraction angle (and, therefore, the position on the input facet of the fibre) constant after tuning the wavelength. This method is referred to as the *SLM-based correction* (Figure 3.1b). This correction was applicable only for one wavelength at a time; it could not be used to correct the dispersion for a broadband light. The SLM-based correction required the hologram to be recalculated after each wavelength change. Due to the limited spatial resolution of the method for hologram generation (discussed in Section 1.2), the Fourier transform of the hologram had to be upsampled to achieve a sufficient resolution of the correction. If a single polarisation was used, a phase ramp could be added to the hologram to steer the beam finely. When two polarisations were used, each required a different ramp, making this method inapplicable in this simple form. Consequently, the shift was applied before the Fourier transform.

Another option for dispersion compensation involved placing another dispersive element in the beam path, like a grating [125, 126] or a prism [127]. Another blazed grating with the same pitch would have the same but opposite effect (if correctly oriented) as the grating displayed on the SLM. Alternatively, the SLM could be used as another diffraction grating if the beam was redirected back onto it, similarly to [128]. Gratings are, however, inefficient, which would further lower the transmission efficiency of the system. On the other hand, a prism can have a high transmission and high enough dispersion to compensate for the dispersion of the hologram on the SLM. A wedge prism was placed in a conjugate plane to the plane of the SLM (i.e., the SLM was imaged into the prism)

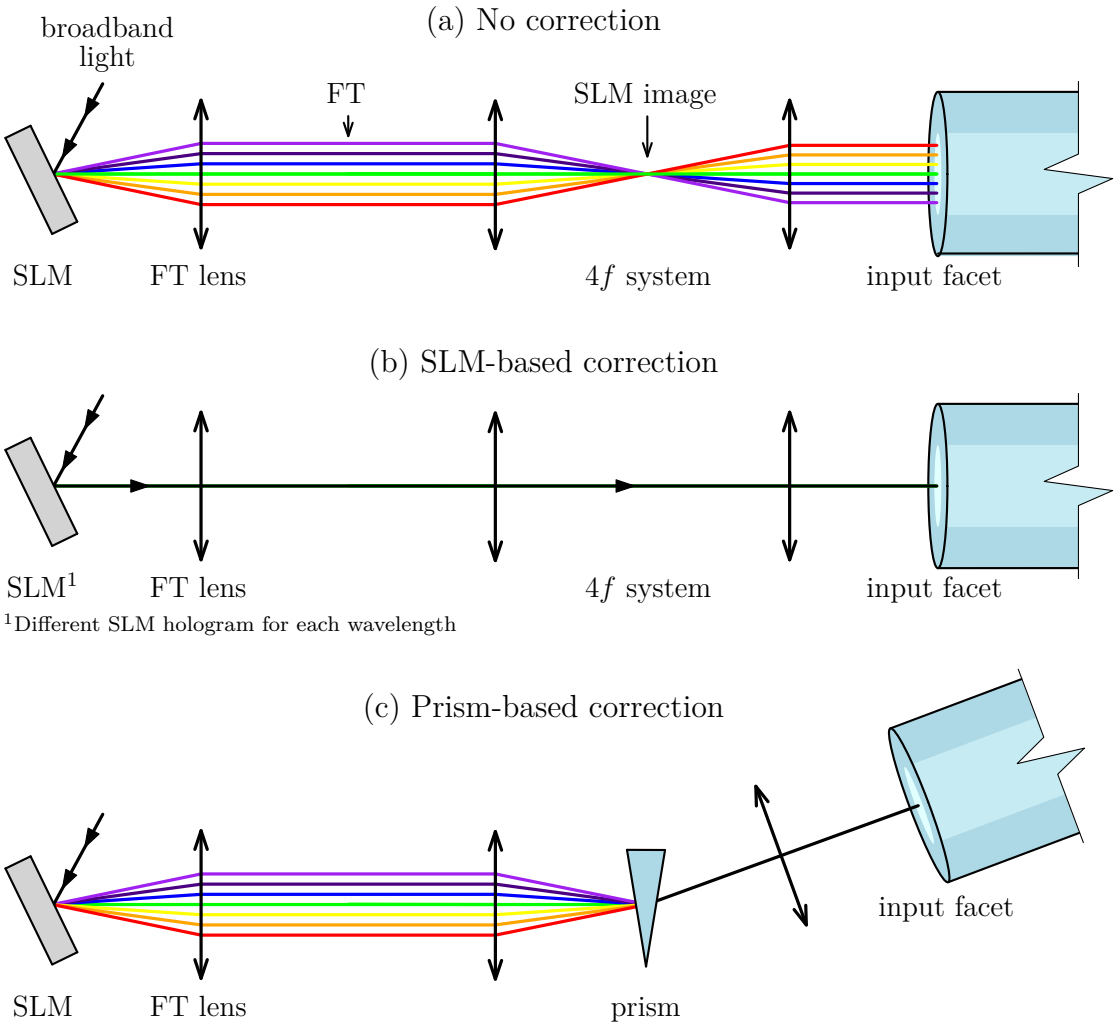

Figure 3.1: Dispersion of the hologram (blazed diffraction grating) displayed on the SLM. (a) The SLM diffracted different wavelengths in different directions. The pattern projected to the proximal end of the fibre thus shifted with the wavelength. (b) By changing the hologram on the SLM, the shift could be corrected. However, the correction worked only for one wavelength at a time (i.e., different holograms were needed for each wavelength). (c) Another dispersive optical element (here, a prism) placed into the image of the SLM could compensate for the shift. The prism-based correction also worked for broadband light.

to implement this correction in the endoscope, as shown in Figure 3.1c. This method is referred to as the *prism-based correction*.

In Figure 3.1, the dispersion and the compensation methods were described for a single spatial frequency on the SLM. In the imaging system, a range of spatial frequencies was used to fill the entire core of the fibre at its proximal end and to create a focused point at the distal end of the fibre. Since the fibre was circular, the spatial frequencies filled a circle in the Fourier transform of the hologram (Figure 3.2a). The position of the centre corresponded to the central frequency. When the wavelength was tuned, the central point shifted, as described above. The circle, however, moved with the central frequency and scaled with wavelength (Figure 3.2b). The prism-based correction and the implementation of the SLM-based correction used here corrected only for the shift, not the scaling (Figure 3.2c).

According to (3.1), the diffraction angle changes faster with wavelength for a smaller grating pitch (higher spatial frequency). Therefore, the pattern shift in the Fourier plane was higher for higher central frequency, as shown in Figure 3.2b. The wavelength tuning range thus depended on the choice of the central frequency when no dispersion correction was used. In such cases, choosing as low a central frequency as possible without coupling the higher diffraction orders into the fibre was beneficial. The prism type and the angle of incidence for the prism-based correction also had to be chosen according to the central frequency.

Both dispersion compensation methods could be implemented when two input polarisations were used. The SLM-based correction required no modification as it did not depend on any optical element. For the prism-based correction, two different approaches were possible. In the first approach, two prisms would be used, one in each input polarisation beam. The orientation of each prism would then be matched to the direction of the dispersion. For the setup in Figure 2.1, this would mean increasing the distance between PBS3 and the half-wave plates (HWP6 and HWP7) and placing the prisms there.

The second approach would use only a single prism and is outlined in Figure 3.3. The polarisation control used two different central frequencies (they only differed in the horizontal direction of the wave vector), as shown in Figure 3.3a,b. The two points created by them in the Fourier plane moved with wavelength along a line going through the 0^{th} diffraction order (Figure 3.3c). The polarisation direction of one of the beams was rotated by 90° using a half-wave plate, while the polarisation of the other beam was kept the same (Figure 3.3d). The change in the polarisation did not affect the dispersion. Afterwards, both beams were spatially overlapped. If the number of reflections was odd in both beams or even in both beams, the overlap would look like in Figure 3.3e, i.e., the direction of the dispersion would be different in both beams. Placing a prism in such a beam would compensate for the dispersion only for one of the two polarisations. If the number of reflections was odd in one beam and even in the other beam (as is in Figure 2.1), the direction would be mirrored in one of the beams, and the directions would become the same (Figure 3.3f). A single prism would thus be sufficient to compensate for the dispersion in both beams simultaneously. This approach was preferred due to the easier alignment of the input polarisation control optics. However, it only worked if the central frequencies for the two polarisations were on a diagonal. Figure 3.3g–i shows the input facet without and with the dispersion correction.

The performance of both methods for dispersion compensation is evaluated in Figure 3.4. The fibre imaging system with a 50 mm long Prysmian DrakaElite fibre was calibrated at 780 nm. Afterwards, the wavelength of the laser was tuned. The quality of

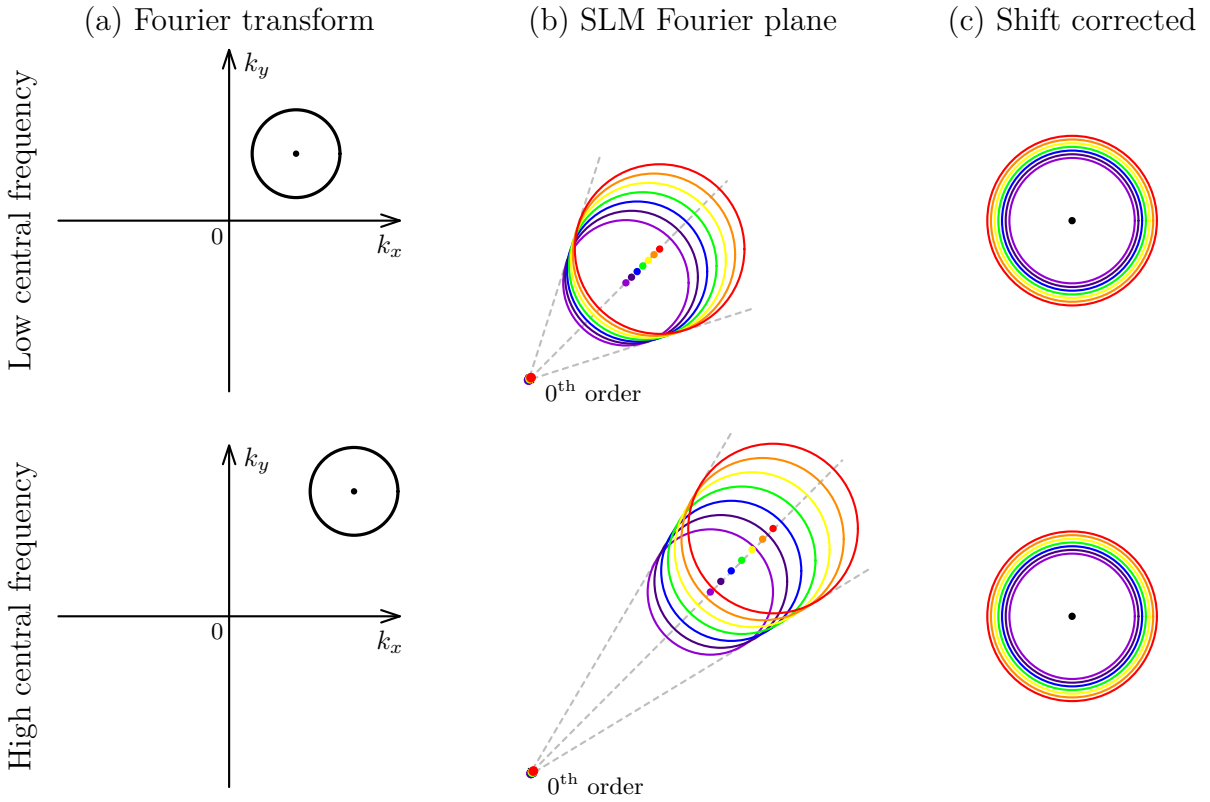

Figure 3.2: Dispersion compensation for more than one spatial frequency on the SLM. (a) Fourier transform of a hologram that (for one wavelength) creates a point (corresponding to the central frequency) and a circle (corresponding to the radius of the core) in the Fourier plane of the SLM. (b) Due to the dispersion, the circle in the Fourier plane both shifts and scales with the wavelength. The different colours (purple to red) represent different wavelengths (850, 900, 950, 1000, 1050, 1100 and 1150 nm, or different wavelengths with the same ratios between them). (c) The SLM-based correction compensates for the shift but not the scaling. The figure shows the situation for two different central frequencies.

the focused points across the field of view was evaluated for a range of wavelengths. The experiment was performed for three configurations: with no correction (i.e., the prism was not installed in the setup, and all points were generated using the identical hologram for all wavelengths), with prism-based correction (i.e., the prism was installed in the setup and all points were generated using the identical hologram for all wavelength) and with SLM-based correction (i.e., the prism was not installed, and the set of holograms was different for each wavelength). When no correction was used, the wavelength tuning range was the lowest (± 7 nm from the calibration wavelength). However, the exact width of the tuning range depended on the central frequency, as discussed above. The prism-based correction increased the wavelength tuning range by a factor of about 2. The resulting tuning range of ± 17 nm from the calibration wavelength would be sufficient for CARS imaging of lipids and proteins. The SLM-based correction increased the tuning range by a factor of 3 to about ± 24 nm. However, as discussed in Section 3.2, the tuning range was, in this case, likely limited not by the SLM, but rather by the bandwidth of the multimode fibre.

The effect of the SLM dispersion compensation was further demonstrated by imaging a 1951 USAF resolution test chart in Figure 3.5. The figure shows point spread functions

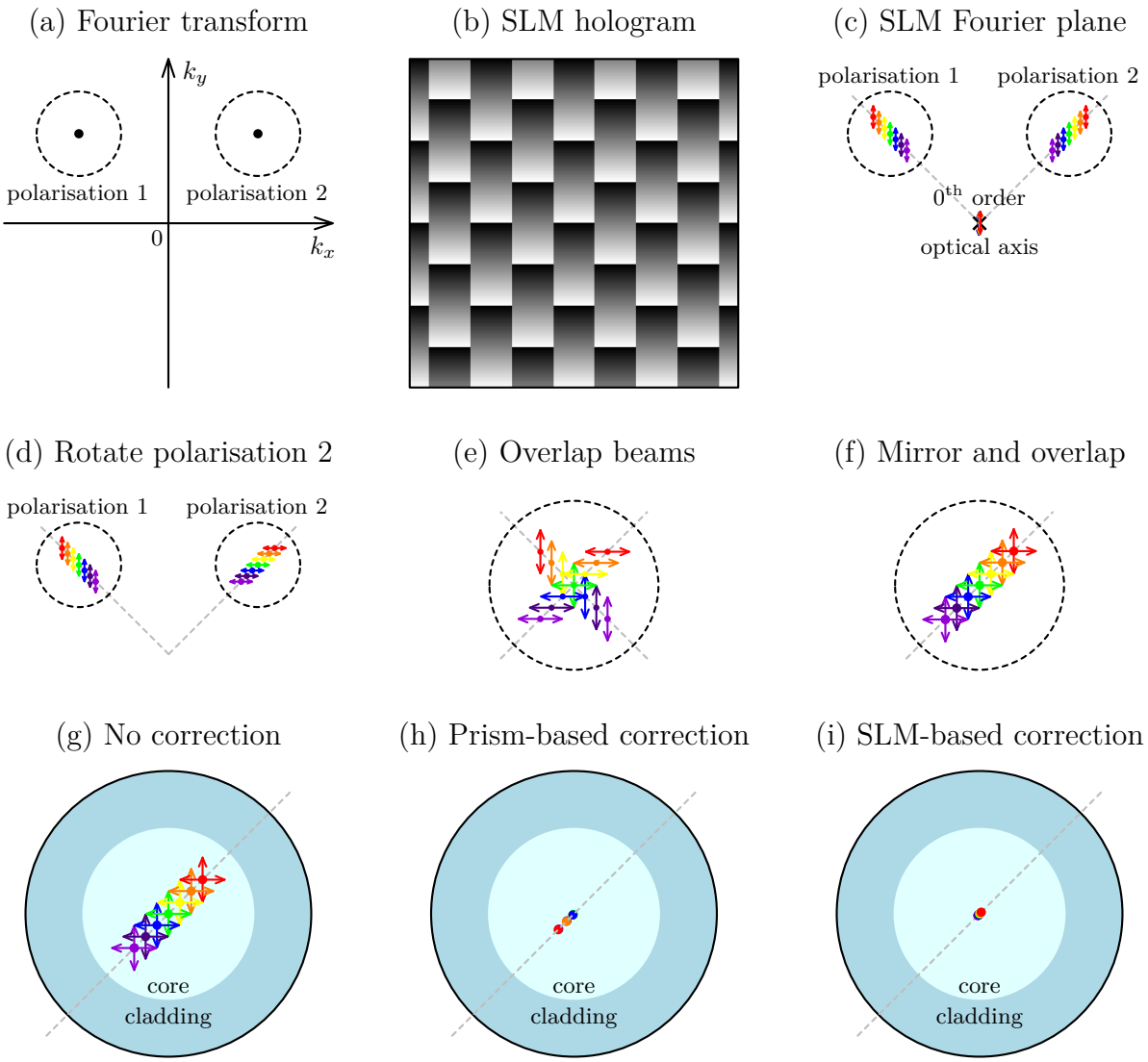

Figure 3.3: Spatial light modulator grating dispersion compensation for two input polarisations. (a) Fourier transform of a hologram that for a certain wavelength generated two points at the centre of the fibre facet, one for each polarisation. The dashed line shows the range of spatial frequencies that could be coupled into the fibre (they corresponded to the core of the fibre). (b) Hologram calculated by inverse Fourier transform of (a). (c) Intensity in the far-field of the spatial light modulator (focal plane of L8 lens in Figure 2.1) at different wavelengths (represented by different colours). The arrows show the polarisation of the beam. (d) The polarisation of one of the beams was rotated by 90° using a half-wave plate. (e) Both beams overlapped in space. Here, the number of reflections in each beam were the same. (f) By placing a mirror in one of the beams before overlapping them, the direction of the dispersion was mirrored. (g) Intensity at the input fibre facet for different wavelengths with no dispersion correction. (h) Intensity at the input fibre facet when using a prism for dispersion compensation (with the identical hologram for all wavelengths). (i) Intensity at the input fibre facet when the hologram was corrected for the wavelength change, i.e. each point was created using a different hologram.

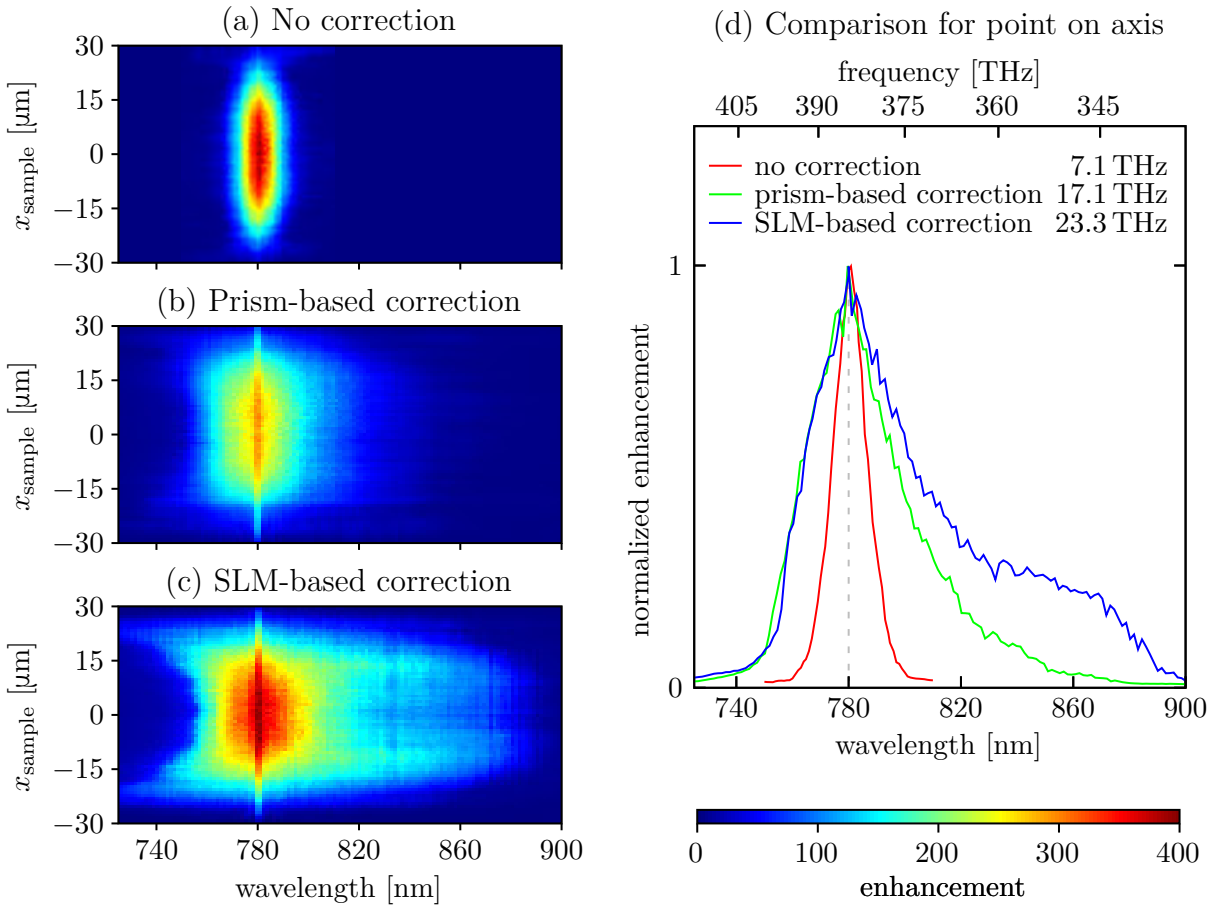

Figure 3.4: Comparison of the methods for SLM dispersion compensation. The figure shows the enhancement of points along a line over the field of view after the wavelength of the laser was tuned from the calibration wavelength of 780 nm (a) when no correction was used, (b) when the prism-based correction was used (using a single prism), (c) when the SLM-based correction was used. (d) shows a comparison for an on-axis point. The numbers in the legend show the bandwidth, calculated as the FWHM of the measured curve. A 50 mm long Prysmian DrakaElite fibre was used.

after the wavelength was tuned from the calibration wavelength of 780 nm. These points were used for imaging the resolution test chart in transmission. With no correction, the contrast in the images dropped to near zero after a 15 nm wavelength change, as the power ratio of the point dropped significantly. When the SLM-based correction was used, the drop in the power ratio was slower, allowing imaging over a broader range of wavelengths without recalibrating the endoscope. These results demonstrate the necessity for correcting the SLM dispersion for applications where wavelength tuning is required.

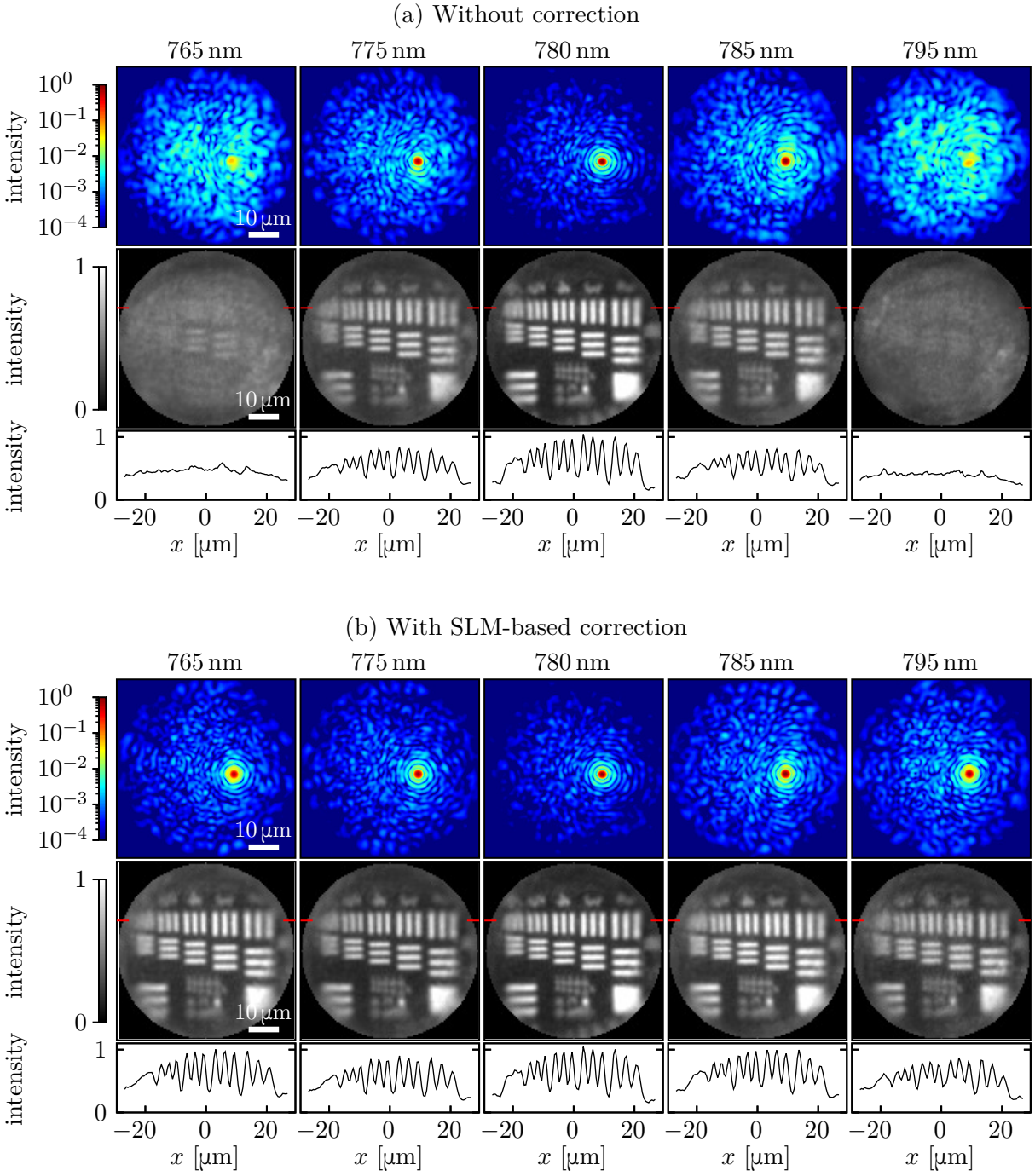

Figure 3.5: Imaging at different wavelengths using the same fibre calibrated at 780 nm without and with SLM dispersion correction. The top figures show an example of the focused point in the logarithmic scale (normalised to the maximal intensity at the calibration wavelength). The middle figures are images of group 8 of a 1951 USAF resolution test chart imaged in transmission. The bottom figures are cross-sections of the images. The fibre was a 50 mm long graded-index Prysmian DrakaElite.

3.2. Bandwidth of multimode fibres

The impact of the spatial light modulator on the wavelength tuning range (referred to as the *bandwidth*) was discussed in Section 3.1. Another wavelength-dependent element in the setup which limited the wavelength tuning range was the multimode fibre. The bandwidth of the commercial fibres is typically specified at 850 nm or 1300 nm, wavelengths typically used for telecommunication applications, and specified in the units of MHz·km^{-1}. The specified values of the bandwidth for the commercial fibres are in Table 3.1. However, it is not immediately apparent how this specified value corresponded to the wavelength tuning range when the multimode fibre was used as an endoscope. In addition, the bandwidth of the fibres would typically be optimised for the telecommunication wavelengths and could be significantly different for wavelengths used for imaging [129]. Consequently, the bandwidth of different multimode fibres was measured using the fibre imaging system.

The effect of the SLM dispersion had to be eliminated to study the impact of the multimode fibre on the wavelength tuning range. Consequently, the SLM-based correction of the SLM dispersion was used, which performed better than the prism-based one (Figure 3.4).

The bandwidth of the step-index fibres was distinctively lower than any of the graded-index fibres. The impact on the wavelength tuning range is demonstrated in Figure 3.6. The endoscope was calibrated at 780 nm for both fibre types. Afterwards, the wavelength of the laser was tuned away from this value while still monitoring the focused point on the camera in the calibration module. While for the graded-index fibre, the focused points persisted over tens of nanometres, for the step-index fibre, it completely vanished within less than one nanometre.

The focused point for the step-index fibre did not disappear completely for small wavelength changes, as might seem from Figure 3.6 (which was measured in a single plane). Instead, due to the chromato-axial memory effect in step-index multimode fibres described in [130], it shifted along the axis of the fibre (Figure 3.7). In [130], the authors characterised this effect by calculating the correlation of the speckle patterns measured at different distances from the facet for different wavelengths. Here, instead of creating a speckle pattern, the beam coupled into the fibre (Thorlabs FG050LGA, (31 ± 1) mm long) was spatially modulated to create a focused point at the distal end. After tuning the wavelength, the three-dimensional point spread function was measured (Figure 3.7a). The axial shifts were obtained for three different focused points across the field of view by finding the plane with maximal intensity for each wavelength. This shift would correspond to a defocus during imaging (Figure 3.7b). The shift was measured to be $\mathrm{d}z/\mathrm{d}\lambda = = -24\,\mu\mathrm{m}\cdot\mathrm{nm}^{-1}$ (the negative sign symbolises that the point moved towards the facet for longer wavelengths) at 800 nm, identical for all three measured focal points. The shift was proportional to the length of the fibre. Thus, the normalised shift (per millimetre of the fibre) for this fibre was $-0.77\,\mu\mathrm{m}\cdot\mathrm{nm}^{-1}\cdot\mathrm{mm}^{-1}$, a value comparable to values reported in [130]. Figure 3.7 shows that the power ratio of the three focused points (measured in the plane with maximal intensity) quickly dropped as the wavelength was tuned. This drop implies that the chromato-axial memory effect was limited to a few nanometres. In contrast to step-index fibres, the shift for graded-index fibres was typically about two orders of magnitude lower (see Figure 5.22), thus negligible. Although the wavelength-dependent position of the focus could be useful for fast refocusing, it makes the step-index fibres unsuitable for non-linear imaging due to the inability to focus light from pulsed laser sources, as discussed in Section 3.3. In addition, when used for CARS, it would not allow

Table 3.1: Specified and measured bandwidths of the fibres used in the experiment. The parameters of the fibres are in table 2.1.

Fibre	Bandwidth [MHz·km]	
	specified[a]	measured[b]
Thorlabs GIF50E	3500	860
Thorlabs GIF50C	700	520
Thorlabs GIF625	≥ 200	190
Prysmian DrakaElite	≥ 500	1106
IPHT GRIN 94f		116
CREOL F1		194
CREOL F3		668
CREOL F4		257
Thorlabs FG050LGA	15	17

[a]Overfilled modal bandwidth at 850 nm (820 nm for Thorlabs FG050LGA)
[b]For fibre imaging; measured using enhancement at 780 nm

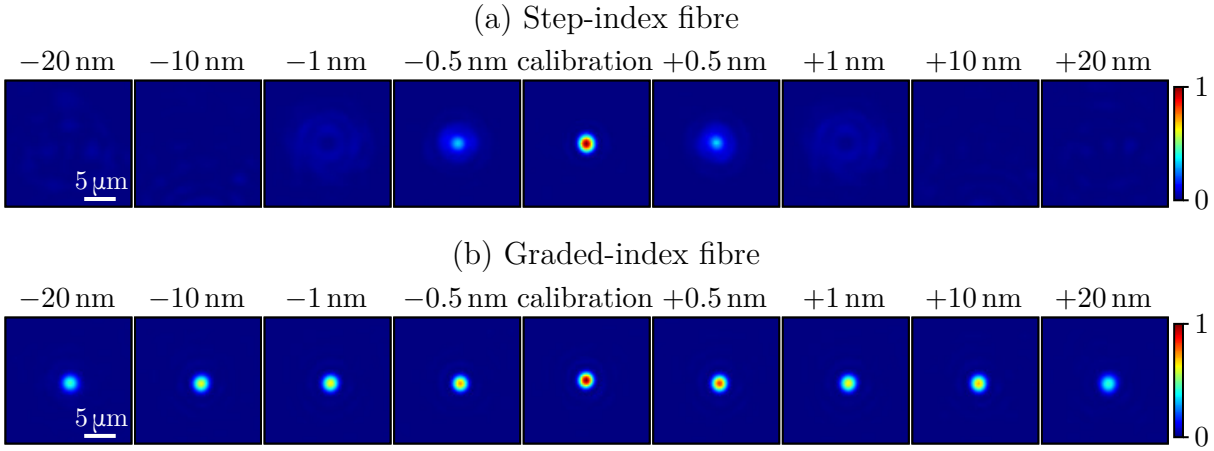

Figure 3.6: Focused points at the imaging plane for different wavelengths (relative to the calibration wavelength of 780 nm) for a step-index fibre (Thorlabs FG050LGA) and a graded-index fibre (Thorlabs GIF50E) with SLM dispersion correction applied. Both fibre types have 50 µm core diameter and similar numerical aperture (0.22 for step-index and 0.20 for graded-index). Both fibres were 50 mm long.

imaging for multiple Raman shifts using a single calibration, as the spatial overlap of the pump and Stokes beams would vanish after the wavelength of one of the two beams was tuned. For these reasons, in this thesis, higher emphasis was put on characterising graded-index fibres than step-index fibres.

The bandwidth measurement for the graded-index fibre was performed for three different lengths of the fibre to verify that the bandwidth was inversely proportional to the length of the fibre (Figure 3.8e) [131]. This measurement shows that even a low-bandwidth fibre could have sufficient bandwidth for an application if only a short piece of fibre is used.

The graphs in Figure 3.8a–c show that the measured data has side-lobes (local maximums for other than the calibration wavelength). The side-lobe is also visible in the cross-section in Figure 3.8d as a local maximum at about 745 nm for the 150 mm long fibre. Since the measurement was performed at a single plane (at a fixed distance from the fibre), the second maximum of the axial point spread function became in focus for some wavelengths due to the chromato-axial memory effect.

Calculating the spot size and power ratio involved fitting a model function to the measured HDR image of the points spread function, as described in Section 2.6. Only a speckle pattern remained in the image when the wavelength was tuned far from the calibration wavelength. The algorithm still performed the fit for a speckle with the highest intensity in the image. The result did not indicate an actual focused point being generated. These artefacts are visible in the spot size and the power ratio in Figure 3.8c. These graphs include areas with a small spot size and a meagre power ratio and areas with a low power ratio but large spot size. These points should not be plotted since they do not represent actual foci useful for imaging. They were, however, left in the graphs to demonstrate another issue in calculating the power ratio. On the other hand, the enhancement does not suffer from this artefact.

The bandwidth measurement was performed for all fibres that were available for the measurement to select fibres suitable for non-linear imaging. The data from the measurement is shown in Figure 3.9a. The bandwidth of each fibre was calculated as a FWHM of the enhancement averaged across the field of view (Figure 3.9b). The measured and specified bandwidths are in Table 3.1. The results show a significant difference between the graded-index fibres. The highest bandwidth was measured for the Prysmian fibre, making it optimal for non-linear imaging. Another suitable fibre was the custom-drawn CREOL F3 fibre. Thorlabs GIF50E and Thorlabs GIF50C fibres, despite their relatively high bandwidth, were unsuitable for non-linear imaging due to the low numerical aperture.

Another method for measuring bandwidth was tested. Instead of creating a focused point at the distal end and monitoring its quality after the wavelength tuning (Figure 3.10a), a single point was created at the proximal end of the fibre, and the speckle pattern at the distal end was measured on the camera in the calibration module (Figure 3.10b). Afterwards, the correlation coefficient of the speckle patterns before and after wavelength tuning was calculated. The second method did not involve creating a focused point at the distal end. Thus, it eliminated the issues with evaluating the quality of the focused point (Section 2.6). Figure 3.11 shows that both methods produced similar results both for step-index and graded-index fibres.

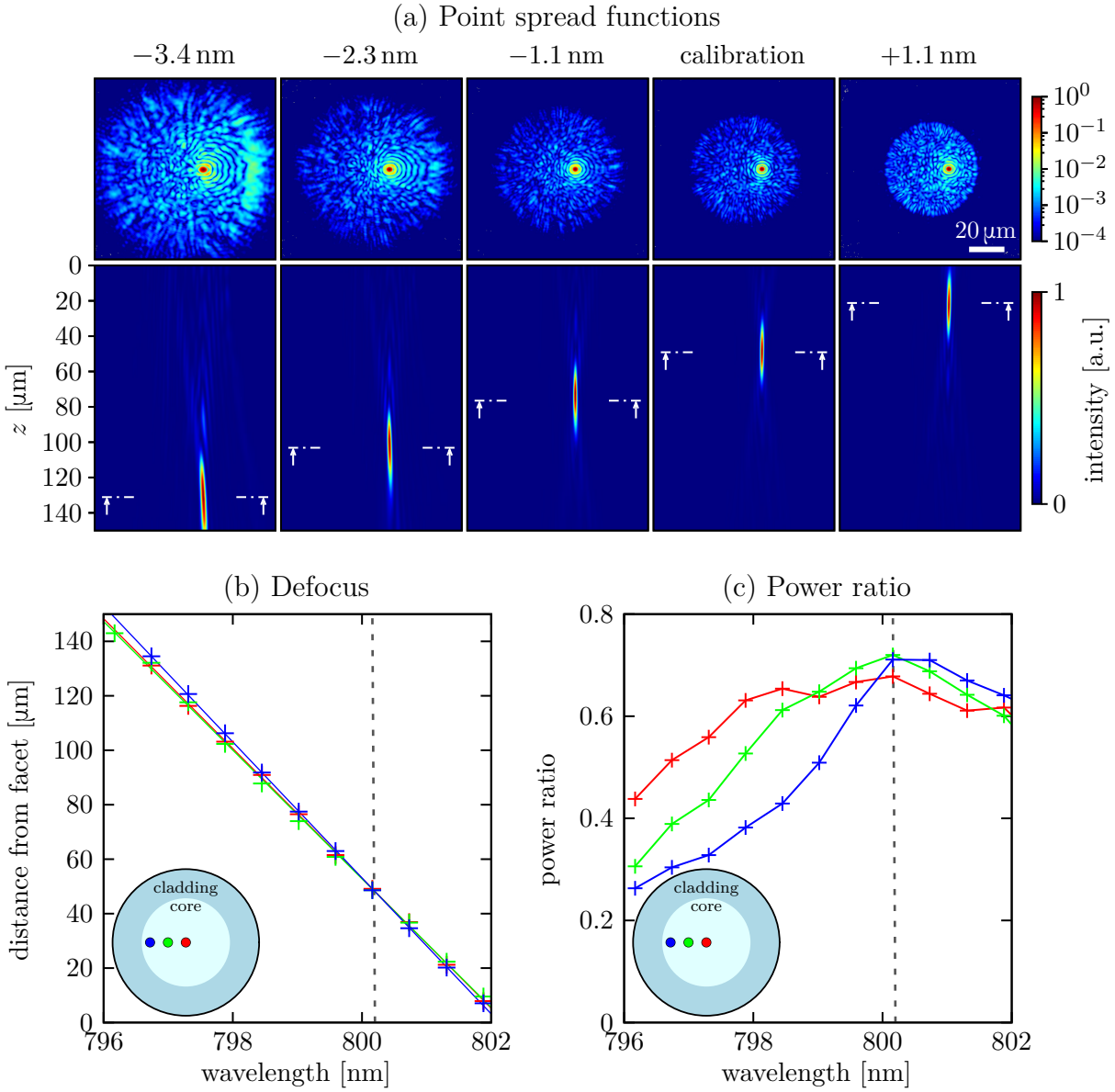

Figure 3.7: Wavelength-dependent focus of a step-index fibre (Thorlabs FG050LGA, (31± ± 1) mm long). (a) Point spread functions (lateral in logarithmic scale and axial in linear scale) measured at the calibration wavelength and after the wavelength was tuned from the calibration wavelength. (b) Axial position of the point after the wavelength was tuned for three different positions of the point in the field of view. The system was calibrated at 800.2 nm, 50 µm from the facet. The dashed line denotes the calibration wavelength. The lines are linear fits. (c) Power ratio after wavelength tuning. The lines are a guide to the eye.

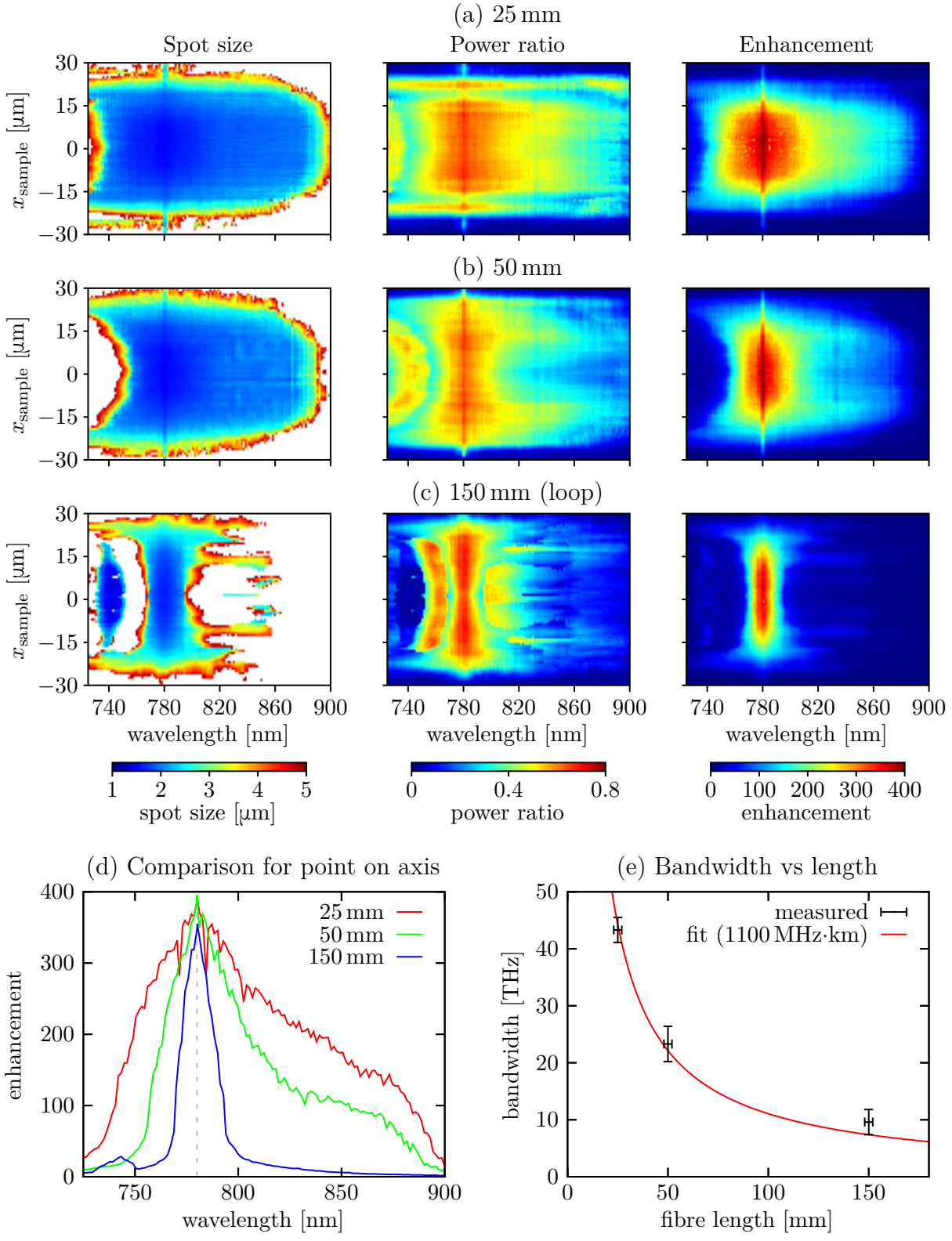

Figure 3.8: Fibre bandwidth for different fibre lengths. The Prysmian fibre was used. (a)–(c) Spot size, power ratio and enhancement across the field of view after the wavelength was tuned from the calibration wavelength of 780 nm. (d) Comparison of the enhancement measured for a point of axis for the three fibres. (e) Bandwidth dependence on the length of the fibre. The red line is a reciprocal fit.

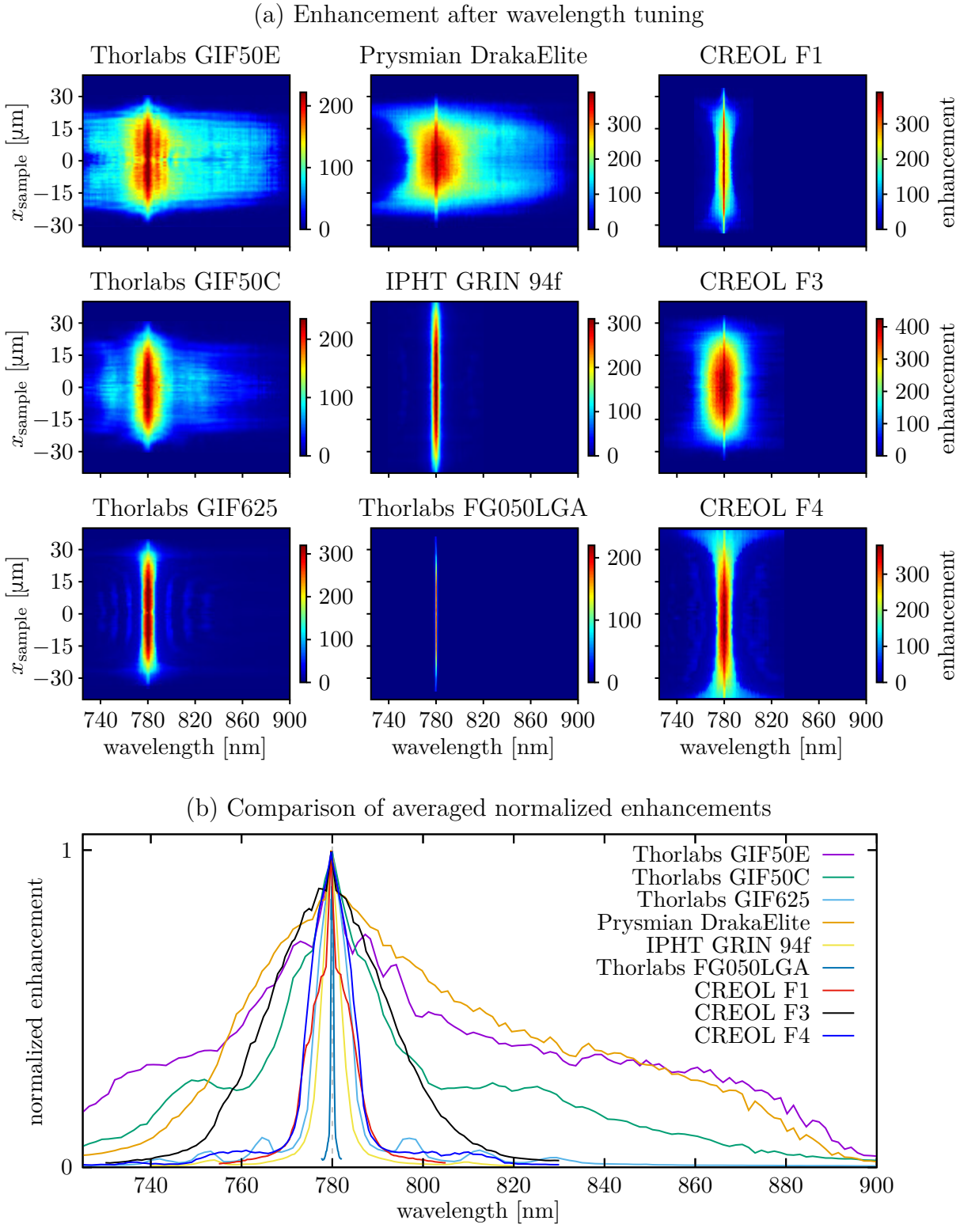

Figure 3.9: Fibre bandwidth for different fibre types. (a) Enhancement along a line across the field of view after the wavelength was tuned from the calibration wavelength of 780 nm. (b) Comparison of the bandwidth of different fibres. Since the maximal enhancement was different for different fibre types (due to different numerical apertures), it was normalised for better comparison. The measured bandwidths are in Table 3.1.

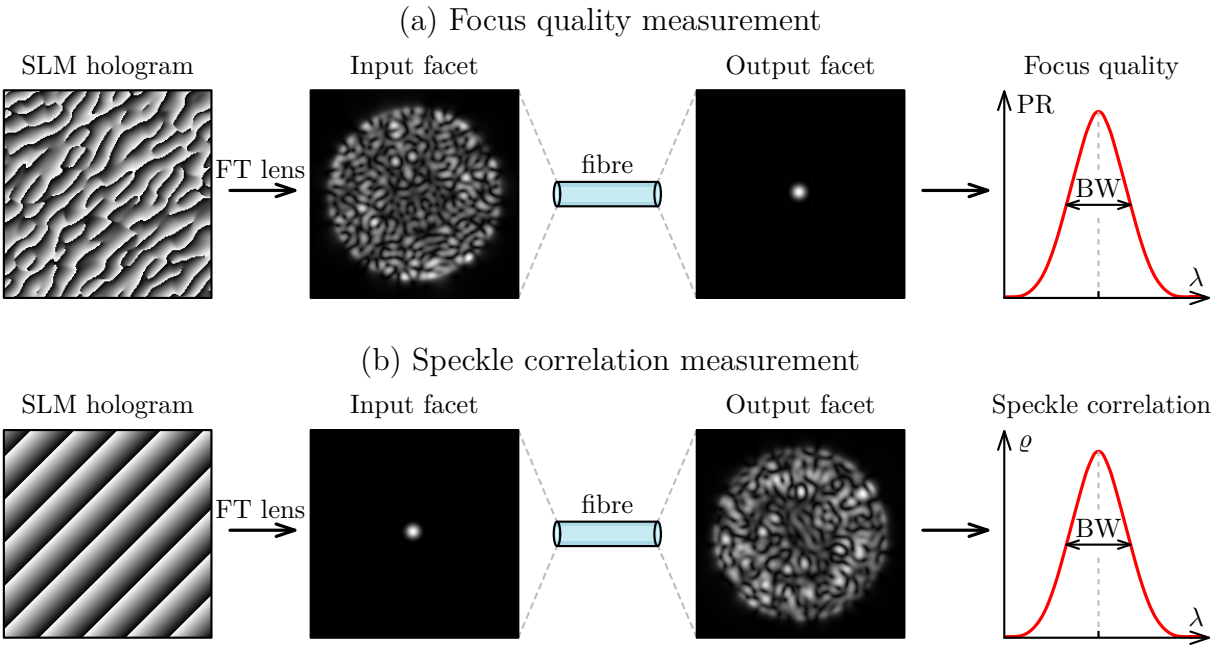

Figure 3.10: Two methods used for fibre bandwidth measurement. (a) A focused point was created at the output fibre facet using the transmission matrix. The quality of the point was measured while changing the wavelength. (b) A focused point was created at the input fibre facet. The correlation coefficient of the speckle pattern on the output facet measured each wavelength and the speckle pattern measured at the calibration wavelength was calculated.

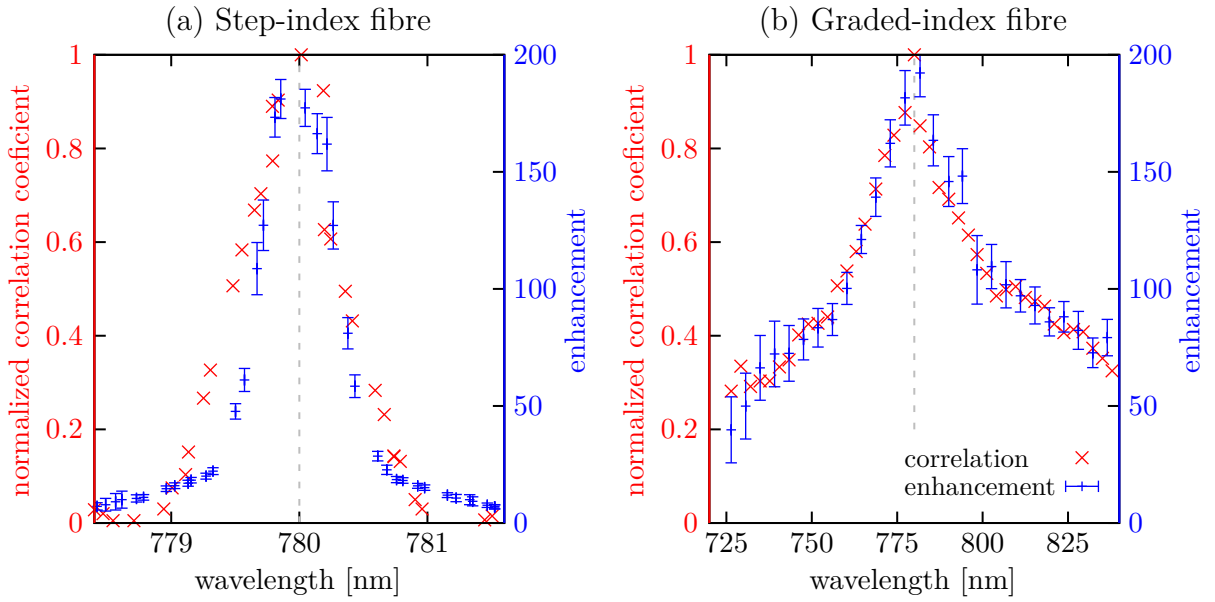

Figure 3.11: Comparison of two methods for bandwidth measurement (shown in Figure 3.10) for two different fibres. The error bars for the enhancement show a standard deviation across a 30 μm long line across the field of view centred at the fibre axis. The dashed line shows the calibration wavelength for the enhancement measurement. The step-index fibre was a 50 mm long Thorlabs FG050LGA, the graded-index fibre was a 50 mm long Thorlabs GIF50E.

3.3. Femtosecond laser focusing

The bandwidth of multimode fibres affects their ability to focus broadband light, such as light from pulsed lasers. The effect is demonstrated in Figure 3.12, where three different fibres were used to focus light from the femtosecond laser. The Prysmian DrakaElite fibre had a larger bandwidth than the spectral width of the laser and produced a point with a power ratio (and size) comparable to the values achieved with a CW laser. The bandwidth of Thorlabs GIF625 fibre was lower than the spectral width of the laser, which caused a lower power ratio. As discussed in Section 3.2, bandwidth of step-index fibres (here, Thorlabs FG050LGA) was much lower than graded-index fibre. The focused point thus had a meagre power ratio. This shows the importance of choosing a high-bandwidth fibre when using a pulsed source.

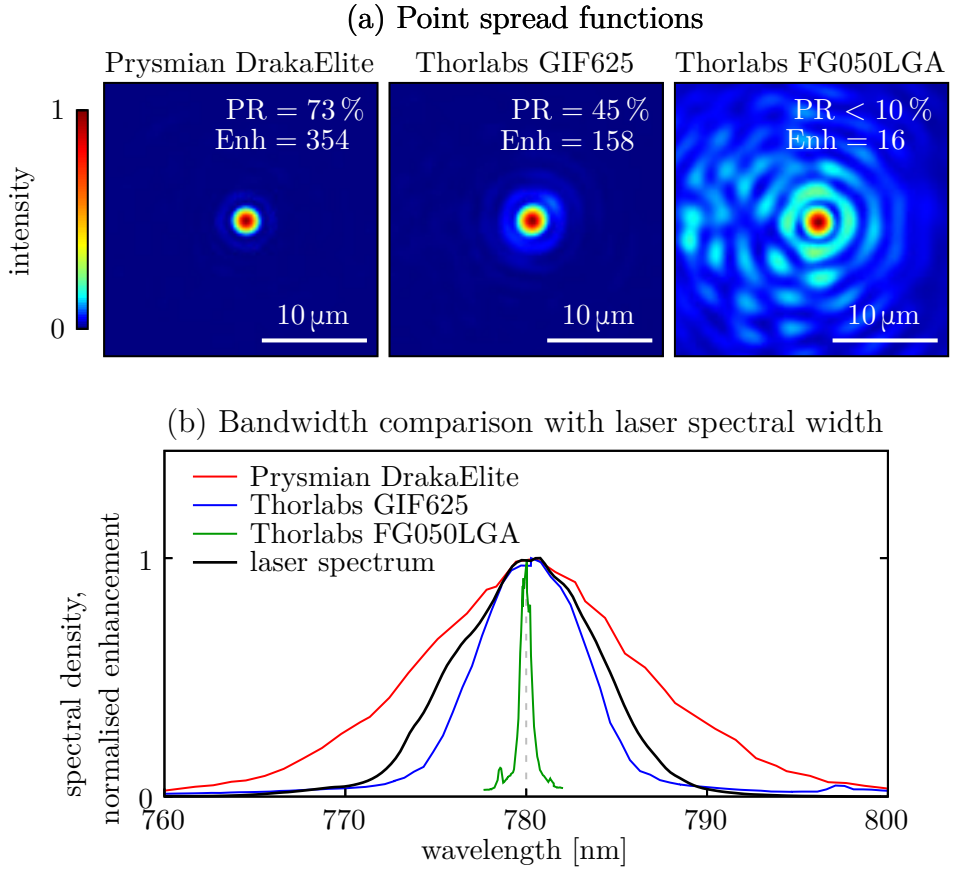

Figure 3.12: Femtosecond laser focusing through a multimode fibre. (a) Point spread functions for a high-bandwidth (higher than the spectral width of the laser) graded-index fibre, low-bandwidth (lower than the spectral width of the laser) graded-index fibre and a step-index fibre. The images also show the power ratio and enhancement. All fibres were 50 mm long. (b) Comparison of the bandwidth of the three fibres with the spectral width of the laser. Since the dispersion of the SLM was not corrected, the bandwidth was limited not only by the fibre itself but (in the case of the Prysmian fibre) by the SLM dispersion.

In Figure 3.8, it was shown that the bandwidth of the fibre was inversely proportional to its length. Consequently, the bandwidth of the Prysmian DrahaElite fibre might not be sufficient to focus the light from the femtosecond laser if a much longer piece of fibre was used. On the other hand, the bandwidth of the step-index fibre was so low that it

could not properly focus the pulses for any practically usable length of the endoscopic probe.

No method for compensating the SLM dispersion was used in this demonstration, as the bandwidth of the system (not accounting for the fibre) was larger than the spectral width of the laser. For a more broadband source, however, using the prism-based correction would be necessary (as discussed in Section 3.1, the SLM-based correction was not suitable for broadband light).

As shown in Figure 3.7, step-index fibres have a significant axial chromatic aberration due to the chromato-axial memory, i.e., they focus different wavelengths into different planes. The broad range of wavelengths in the femtosecond pulse thus caused the point spread function to be elongated significantly beyond the diffraction limit (this is demonstrated in Figure 5.17d). While such foci were used to demonstrate volumetric two-photon fluorescence imaging of live neurons using a multimode optical fibre [54], step-index fibres are currently unsuitable for non-linear imaging in general. The reason is twofold. The very low achievable power ratios make the system very inefficient. More importantly, the elongated point spread function appreciably limits the sectioning capability of the endoscope. For CARS imaging, the chromatic aberration could also be detrimental to chemical contrast, as different Raman shifts could be excited in different planes within the length of the point spread function. No method for correcting these effects has been demonstrated so far. Consequently, for most experiments in this thesis, graded-index fibres were used.

3.4. Spectral phase of the focused point

Controlling the pulse length in the imaging plane is essential for non-linear imaging. When the laser pulse propagates through the multimode fibre, it broadens due to dispersion. Thus, the dispersion must be compensated to obtain a transform-limited pulse in the sample plane.

Different methods for characterising the pulse from a multimode fibre exist [132, 133]. The technique used here was based on measuring the spectral phase of a focused point created using the calibration procedure described in Section 2.5. That is, the measurement was performed with a configuration as close as possible to the intended application of the fibre. Moreover, the measurement technique did not require any modifications to the setup.

A laser pulse in time-domain (Figure 3.13a) can be described in terms of the time-dependent electric field given by

$$E(t) \propto \sqrt{I(t)} \exp\left[\mathrm{i}\left(\omega_0 t - \Phi(t)\right)\right],$$

where $I(t)$ is the (time-dependent) intensity, ω_0 is the carrier frequency and $\Phi(t)$ is the (time dependent) phase. Employing the Fourier transform and centring the pulse around the carrier frequency, the electric field can be rewritten in the frequency domain (Figure 3.13b)

$$\tilde{E}(\omega) \propto \sqrt{S(\omega)} \exp\left[-\mathrm{i}\varphi(\omega)\right],$$

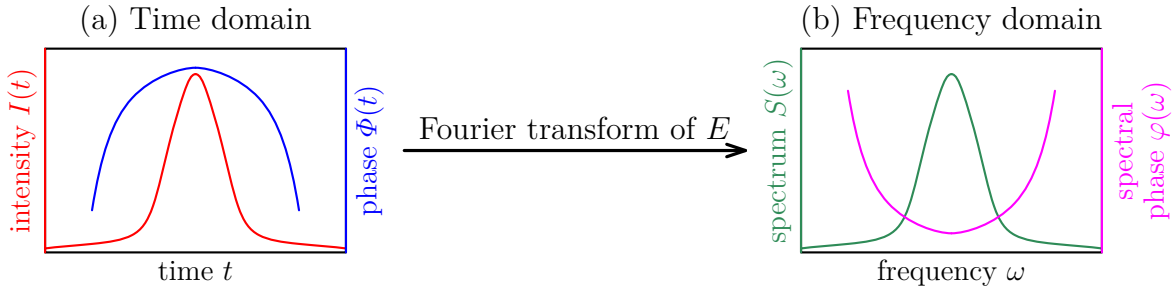

Figure 3.13: Describing the laser pulse in (a) time domain using the intensity $I(t)$ and phase $\Phi(t)$ and in (b) frequency domain using the spectrum $S(\omega)$ and spectral phase $\varphi(\omega)$.

where $S(\omega)$ is the spectrum (the intensity of each frequency in the pulse) and $\varphi(\omega)$ is the spectral phase (the phase of each frequency in the pulse). Expanding the spectral phase into a Taylor series yields

$$\varphi(\omega) = \varphi(\omega_0) + \underbrace{\left.\frac{\partial\varphi}{\partial\omega}\right|_{\omega=\omega_0}}_{\substack{\text{group}\\\text{delay}}} (\omega-\omega_0) + \underbrace{\left.\frac{\partial^2\varphi}{\partial\omega^2}\right|_{\omega=\omega_0}}_{\substack{\text{group}\\\text{delay}\\\text{dispersion}}} \frac{(\omega-\omega_0)^2}{2!} + \underbrace{\left.\frac{\partial^3\varphi}{\partial\omega^3}\right|_{\omega=\omega_0}}_{\substack{\text{third}\\\text{order}\\\text{dispersion}}} \frac{(\omega-\omega_0)^3}{3!} + \dots$$

The 0^{th} order term is irrelevant unless the pulse is only a few cycles long. The 1^{st} order only delays the pulse in time; thus, it is also irrelevant to this analysis. The 2^{nd} order term (group delay dispersion, GDD) causes the pulse frequency to change linearly in time. Such a pulse is called a linearly chirped pulse. The third-order dispersion (TOD) and possibly the higher-order terms also change the shape of the pulse. Disregarding the higher-order dispersion terms, the group delay dispersion and the third order dispersion are thus the values essential for describing the behaviour of a pulse. Both values can be calculated from the measured spectral phase.

To describe the pulse behaviour after being propagated through the fibre, the spectral phase was measured twice: with the fibre and without the fibre. The difference was the spectral phase change introduced by the fibre. The group delay dispersion introduced by the fibre was calculated using a polynomial fit. This value was then used to calculate the group velocity dispersion (GVD), i.e., the group delay dispersion per unit length of the fibre.

The spectral phase measurement was performed using the tunable CW laser and is demonstrated in Figure 3.14. The spectral phase of the focused point at each wavelength was measured by overlapping the focused point on the camera with the reference beam. Eight images with different phase shifts were captured (Figure 3.14) and used to calculate the phase and amplitude distribution in the image (Figure 3.14). The phase of the focused point was then the phase in the pixel with maximal amplitude at the calibration wavelength.

For this measurement, the optical path difference between the signal (i.e., through the multimode fibre) and reference paths was set to near zero to minimise the linear term (group delay) in the measured spectral phase to allow phase unwrapping. The position of the reference delay line stage had to be moved by 6.4 mm for the 25 mm fibre and by 12.8 mm for the 50 mm fibre compared to the position without the fibre to obtain a zero optical path difference between the signal and reference paths at 780 nm. That means the

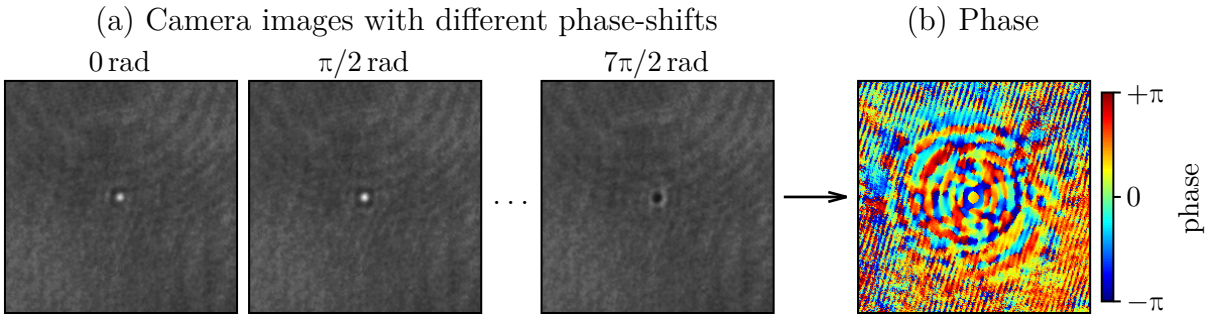

Figure 3.14: Spectral phase measurement of a focused point. The focused point was overlapped with a plane wave reference beam. (a) Images with different phase shifts of the reference beam. (b) Calculated spatial distribution of the phase. The noisy values at the edges are a result of very low amplitude.

delay line length had to be increased by 0.512 mm per millimetre of the fibre. This value corresponds to an effective group refractive index of the fibre of 1.51.

The spectrometer range was (780 ± 17) nm. Outside this range, only the wavelength reported by the laser was available, which was not accurate. Consequently, the measured phase dependence would be inaccurate, and thus the measurements were limited to the usable range of the spectrometer.

Since measuring all wavelengths and point positions took about an hour, the phase drift between the two optical paths had to be compensated. Therefore, the laser was periodically tuned back to the same wavelength, and phase-shifting was performed for one of the positions of the focused point. If there were no drift, the measured phase for this point at the calibration wavelength would be constant during the whole measurement. Any measured difference was thus due to the phase drift.

The measured spectral phase for two lengths of the Prysmian fibre, as well as the spectral phase measured with no fibre in the setup, are in Figure 3.15a. The phases were unwrapped, and the constant and linear terms (corresponding to the optical path difference between the signal and the reference beams) were subtracted. After subtracting the spectral phase measured without the fibre, the spectral phase introduced by the fibre (i.e., the dispersion of the fibre) was calculated. Figure 3.15b shows the difference for two fibre lengths and five positions of the focused point across the field of view.

Performing a polynomial fit of the measured spectral phase yielded the group velocity dispersion value of $50\,\mathrm{fs}^2{\cdot}\mathrm{mm}^{-1}$. The measured value was higher than the value for fused silica ($38\,\mathrm{fs}^2{\cdot}\mathrm{mm}^{-1}$ [134]), which was likely caused by the doping of the fibre core. Nevertheless, this value was independent of the position of the output point. The fact that the value was constant for a given length of the fibre implies that a standard pulse compressor, such as a prism compressor, can compensate for the dispersion introduced by the fibre. In addition, it was found that the spectral phase was purely parabolic, i.e., the fibre introduced no third-order dispersion.

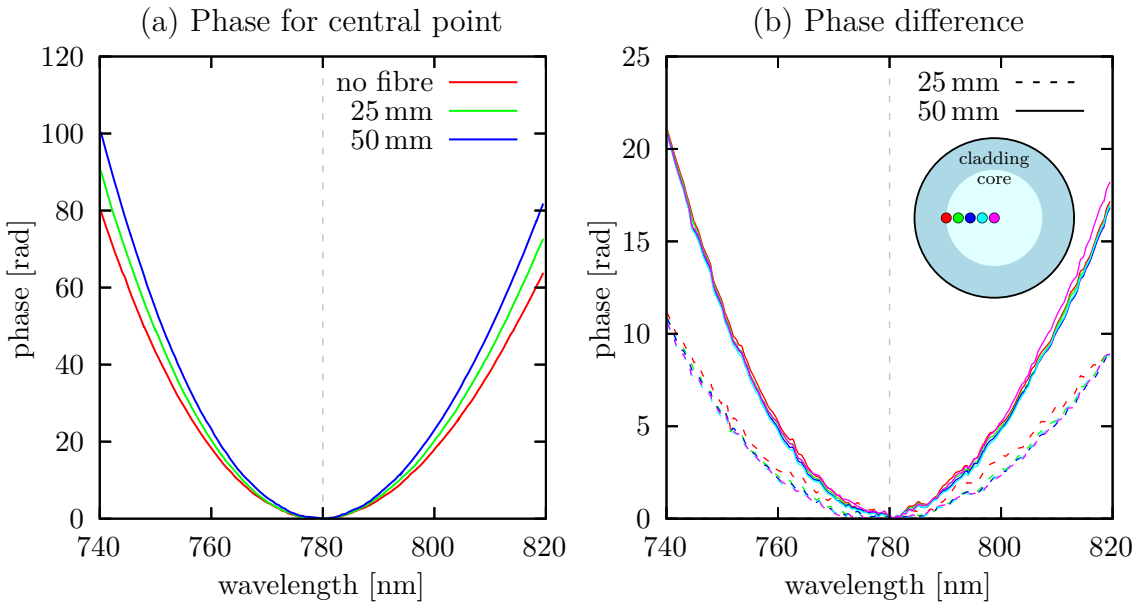

Figure 3.15: Spectral phase measurements results. (a) Spectral phase of the focused point measured with no fibre and two different lengths of the Prysmian fibre for a point in the centre of the field of view. (b) Spectral phase difference for two different fibre lengths and five different positions of the focused point in the field of view.

3.5. Simultaneous focusing of two wavelengths

Focusing the pump and Stokes beams to the same point through a multimode fibre endoscope is essential for implementing coherent anti-Stokes Raman scattering (CARS) imaging. The wavelength difference between these two beams is given by the Raman shift being excited. Typically, the range used for bio-imaging is around $3000\,\mathrm{cm}^{-1}$, corresponding to a wavelength difference in the order of hundreds of nanometres. As shown in Section 3.2, the bandwidth of the multimode fibres was not sufficient to cover such a broad wavelength range using a reasonably long fibre (30 mm or more). Therefore, two independent calibrations had to be performed, one for each wavelength. An optimal solution for modulating two discrete wavelengths would be to use two spatial light modulators or split the modulator into two halves, one for each beam. While such configuration was planned for future versions of the setup, it would make the setup and the software noticeably more complicated. Hence, both beams were spatially overlapped and focused simultaneously using a single hologram.

Methods for combining holograms for multiple wavelengths exist for spatial modulators with a phase range extending over several multiples of 2π [135]. While the modulator used here had a 5π range at the wavelength of 780 nm (which was used as the CARS pump beam in Chapter 5), as shown in Figure 2.7, at 1040 nm (CARS Stokes in Chapter 5), the range was only 3π. Consequently, a different approach had to be employed.

The transmission matrices for the two wavelengths were added before generating the hologram to create a joint hologram for both wavelengths. Such a hologram created a focused point at any of the two wavelengths. The cost for the simplicity was the increased speckled background. In essence, transmission matrix TM_1 measured at wavelength λ_1 produced a focused point at the distal end at λ_1. At wavelength $\lambda_2 \neq \lambda_1$, only a random speckle pattern was produced. Analogously, transmission matrix TM_2 measured at wave-

length λ_2 produced a focused point at the distal end at λ_2 and a speckle pattern at λ_1. Transmission matrix $TM_1 + TM_2$ produced both the points and the background at both wavelengths λ_1 and λ_2. Thus, simultaneous focusing of two wavelengths was achieved at the cost of increased background.

Figure 3.16 schematically shows this approach. In Figure 3.16a, the regions in the Fourier transform of the hologram for the two wavelengths and the two input polarisations are shown. Only the regions for the respective wavelength were enabled when focusing light at a single wavelength. Simultaneously focusing both wavelengths required enabling all regions. Figure 3.16b–e schematically shows the light distribution on the input facet of the fibre at both wavelengths. At both wavelengths, the input facet contained light that created a focused point at the distal end and unwanted light from the transmission matrix for the other wavelength. A fraction of the unwanted light was coupled into the core, increasing the background at the distal end. The rest was not coupled in (more precisely, it was coupled into the cladding and later radiated out due to the glue, as discussed in Section 2.4) and thus did not contribute to the signal measured at the distal end. The exact orientation of the unwanted light on the input facet depended on the number of reflections the two input polarisation beams undertake before being overlapped (Figure 3.16b,c or Figure 3.16d,e).

The transmission matrices for the two wavelengths had to be normalised when implementing this method in the software. The normalisation was necessary because the amplitudes measured during the calibration depended on the laser power, the transmission efficiency of the system, and the camera sensitivity. All three factors were wavelength dependent. If not normalised, the efficiency of the resulting hologram at the two wavelengths would thus depend on the exact conditions during the calibration.

Here, it was assumed that the prism-based dispersion compensation was not used. In that case, the ratio of the central frequencies for the two wavelengths was equal to the ratio of the two wavelengths. Thus, the higher the ratio of the two wavelengths, the lower the overlap and the higher the achievable power ratios. When the prism-based compensation was installed, the dispersion was partially compensated, and the overlap of the patterns for the two wavelengths was larger. The larger overlap caused an additional decrease in the power ratios at both wavelengths since more unwanted light was coupled into the fibre. It was, however, only the background that was affected. The power in both the focused points did not change. Thus, the effect on non-linear imaging was minimal. Suppose the wavelength tuning range was not an issue. In that case, the orientation of the prism could be reversed to create the opposite behaviour, i.e., to separate the patterns for the two wavelengths even more. The increased separation would increase the power ratios at both wavelengths compared to the situation without the prism. Depending on the ratio of the two wavelengths, the overlap of the spatial frequencies could then be zero. In such case, the joint hologram would create points with maximal achievable power ratio at both wavelengths. However, the total transmission efficiency for each wavelength would still be halved compared to when two spatial light modulators were used.

Simultaneous focusing of two wavelengths is experimentally demonstrated in Figure 3.17. The system was calibrated using the tunable CW laser at two different wavelengths (730 nm and 860 nm). When only the transmission matrix for the current wavelength of the laser was used, the power ratios were high. Using the transmission matrix for the incorrect wavelength produced only a random speckle pattern. A focused point was produced for both wavelengths when the composite hologram was used. However, the background intensity increased, and the intensity of the focused points decreased. The

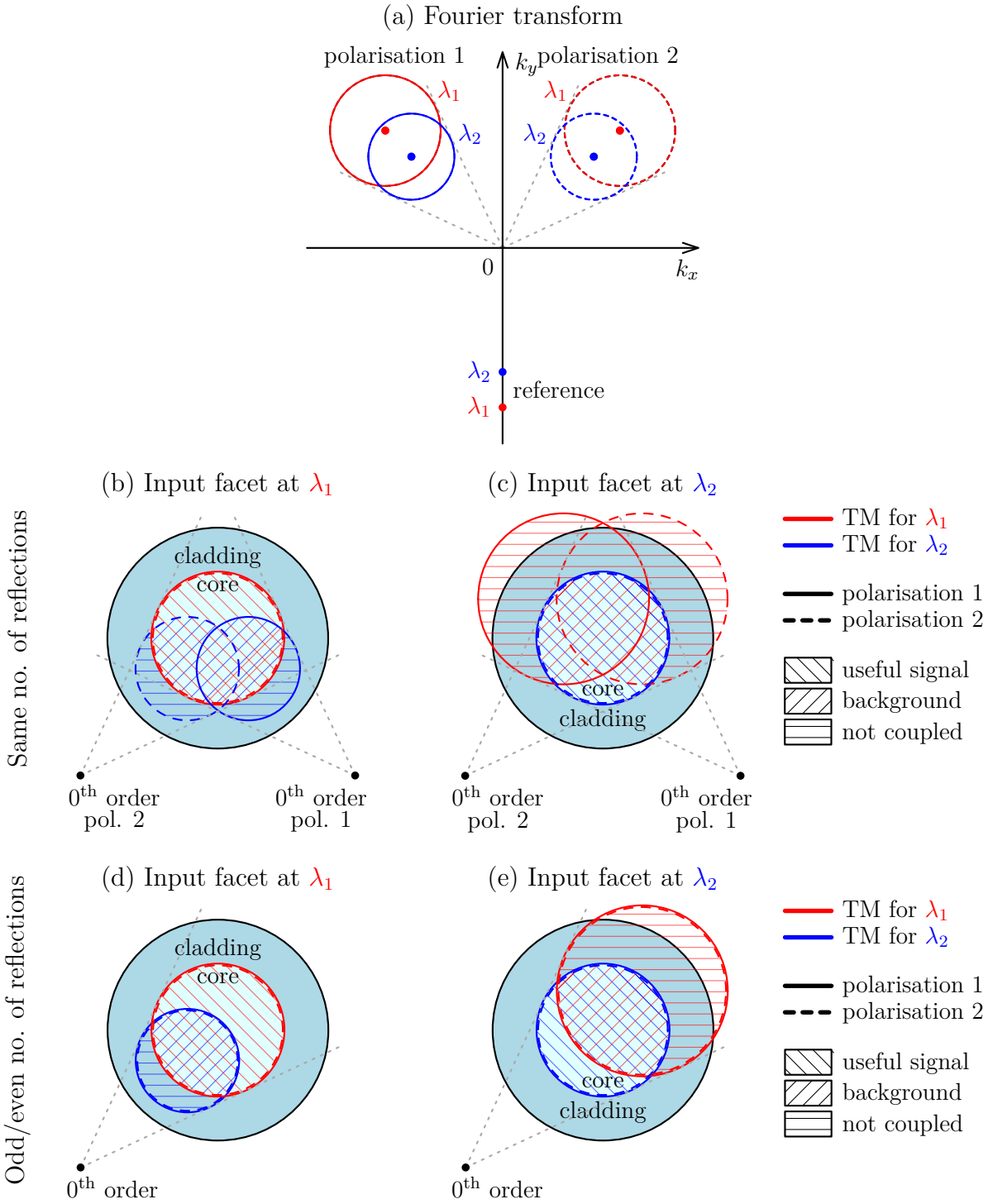

Figure 3.16: Simultaneous focusing of two wavelengths using a single SLM. (a) Schematics of the Fourier transform of the hologram, showing the regions used for the two wavelengths ($\lambda_1 < \lambda_2$) and two input polarisations. The circles correspond to the core of the fibre, their centres are the central frequencies. For each wavelength, a different spatial frequency was used to generate the reference beam. (b)–(e) Input facet of the fibre at the two wavelengths. The spatial frequencies in the hologram for the correct wavelength were coupled into the core and generated the focused point at the distal end of the fibre. The spatial frequencies for the incorrect wavelength were coupled into the fibre only partially and increased the background of the focused point. The drawing shows two situations: (b), (c) when the number of reflections was the same for both polarisations beams and (d), (e) when an extra mirror was placed into one of the beams (here, to polarisation 1).

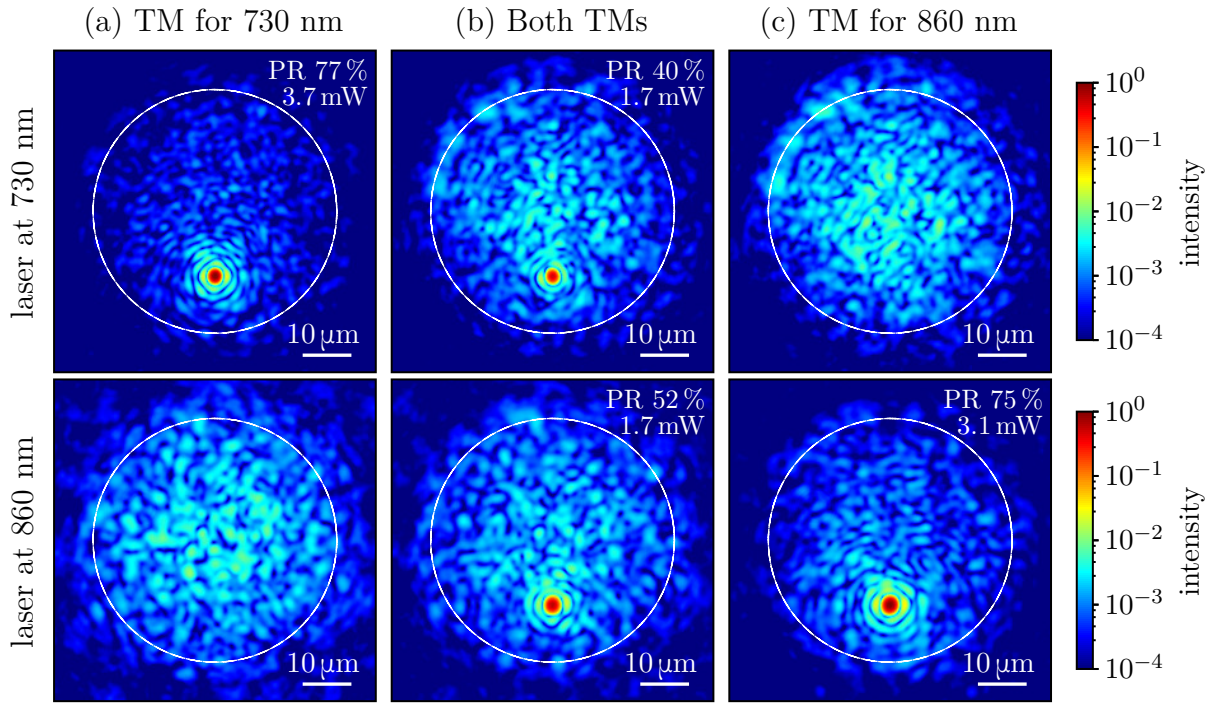

Figure 3.17: Results of simultaneous focusing at two wavelengths using a single spatial light modulator. The image shows point spread functions (in the logarithmic scale) measured at two wavelengths with three different holograms displayed on the spatial light modulator. The power ratios (PR) as well as the power in the focused points are shown.

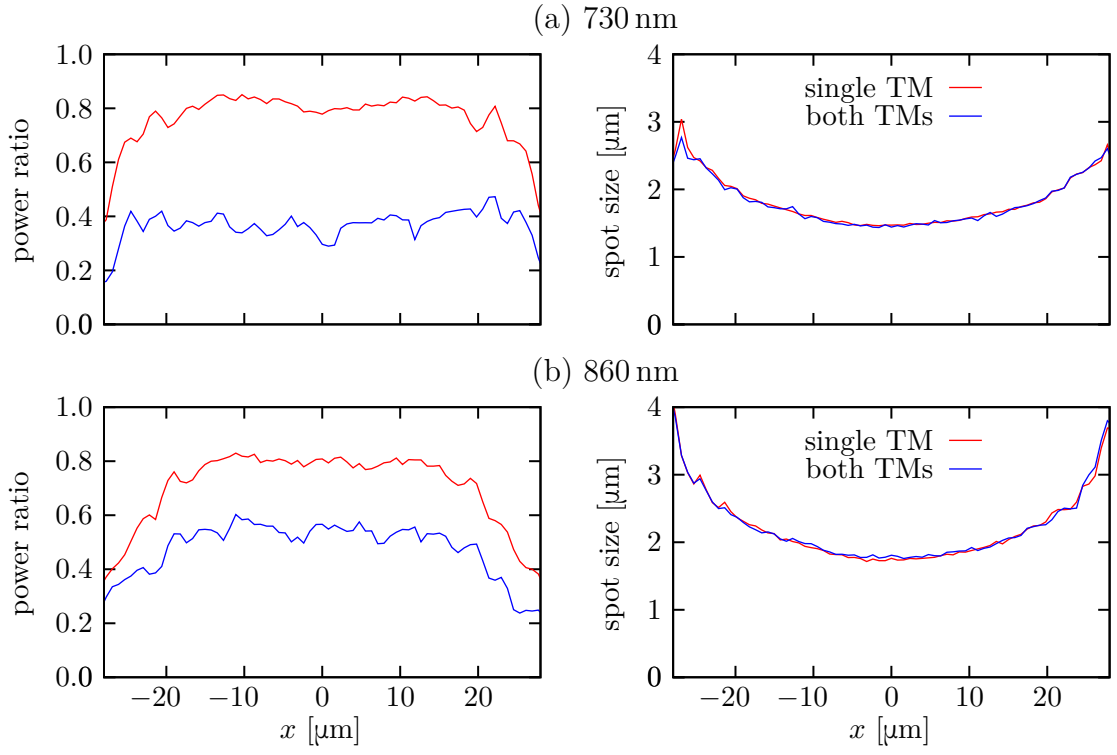

Figure 3.18: Evaluation of the power ratio and spot size for points on a line across the field of view for a situation when the points were created only using the respective holograms and when a joint hologram for both wavelengths was used.

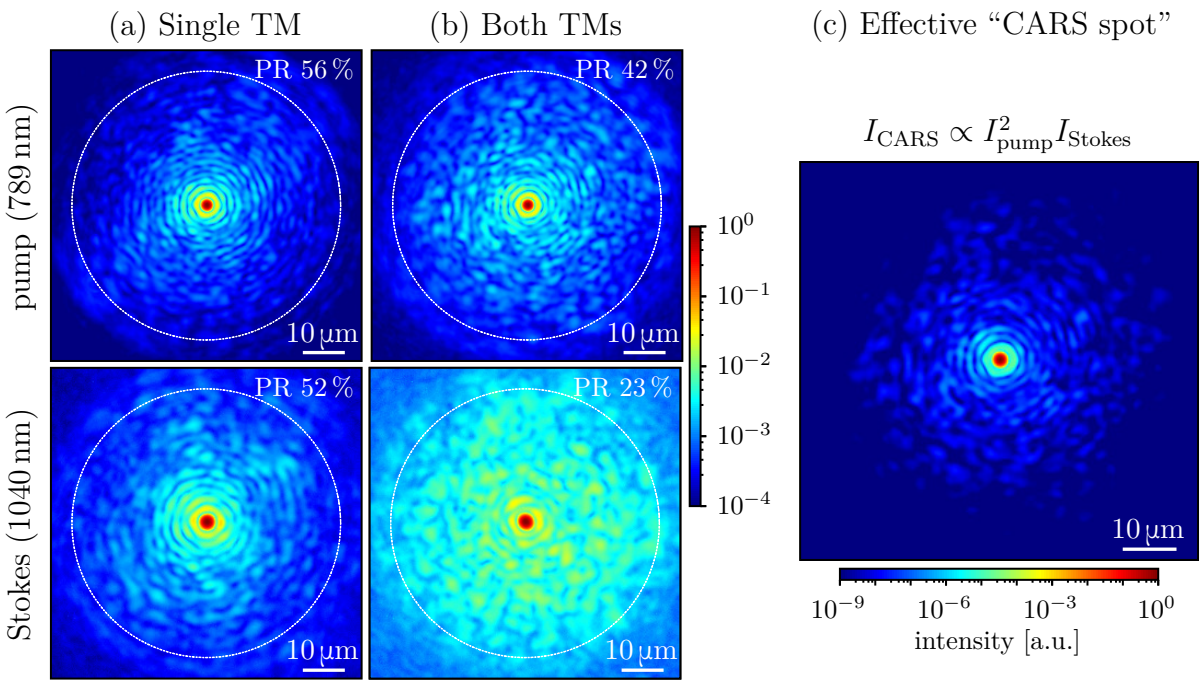

Figure 3.19: Simultaneous focusing of two wavelengths from the femtosecond laser for CARS. (a) Point spread functions (in the logarithmic scale) measured at two wavelengths (the frequency difference between them was optimal for exciting polystyrene) when the spatial light modulator displayed two different holograms, one for each wavelength. (b) Point spread functions measured when the SLM displayed a single hologram, resulting in a combined focus for both wavelengths. The two transmission matrices for the two wavelengths were added with a 2 : 1 (pump : Stokes) ratio to increase the CARS signal. (c) An estimate of the effective CARS point spread function, calculated from point spread functions in (b), assuming quadratic dependence on the pump and linear dependence on the Stokes intensity. Note that the colour scale differs from (a) and (b).

power ratio and the power in the focused point were thus always lower when using the composite hologram.

Figure 3.18 shows that while the power ratio dropped when both wavelengths were focused simultaneously, the spot size was not affected by summing the transmission matrices. The drop in the power ratio was higher for the shorter wavelength. This effect can be, in a simplified way, explained in Figure 3.16d,e, assuming that the power distribution was near uniform in all the circular regions (which would be the case for a step-index fibre, but it is not a correct assumption for graded-index fibres). The unwanted signal (blue in Figure 3.18d, red in 3.18e) was always only partially coupled into the core. Due to the scaling caused by the dispersion, a larger fraction of this unwanted signal was coupled into the core at the shorter wavelength compared to the longer wavelength. Thus, the intensity of the unwanted background was higher at the shorter wavelength, and the power ratio was lower.

The described method had the same outcome when the femtosecond laser was used. In Figure 3.19, two wavelengths separated by $3059\,\mathrm{cm}^{-1}$ (optimal for CARS imaging of polystyrene) were focused simultaneously through a graded-index fibre. In contrast to Figure 3.17, the ratio of the two transmission matrices was set to 2 : 1 (pump : Stokes). The higher weight of the pump beam caused a lower drop in the intensity of the pump beam when combining both transmission matrices. On the other hand, the intensity of

the Stokes beam got lower than in the case of the 1 : 1 ratio. The 2 : 1 ratio increased the intensity of the CARS signal generated in the sample due to the CARS intensity being quadratic in the pump and linear in the Stokes intensity. The measured point spread functions were used to estimate the effective CARS point spread function (Figure 3.19). The point had a minimal level of background as a result of the non-linearity of the process and the speckled backgrounds for the two wavelengths being uncorrelated. Thus, the CARS signal would be generated only in the focused point.

3.6. Summary

In this chapter, the multimode fibre endoscope built in Chapter 2 was used to characterise the wavelength-dependent behaviour of different multimode fibres with the goal to efficiently focus light from a pulsed laser source and allow non-linear imaging through a single multimode fibre.

When tuning the wavelength after the calibration of the fibre, the quality of the focus drops. The degradation was caused by two factors: the wavelength dependence of the optics projecting the pattern on the proximal end of the fibre and on the fibre itself. The most wavelength-dependent component in the system was the spatial light modulator, used in off-axis configuration. The holograms displayed on the SLM have a form of a sum of diffraction gratings. This grating-like behaviour causes the pattern projected on the proximal end to shift with wavelength. Two methods for correcting the wavelength dependence were tested. Since the dispersion of the hologram is known, it can be recalculated for another wavelength (SLM-based correction). Another option is using another wavelength-dependent optical element, such as a prism, to compensate for the dispersion of the SLM (prism-based correction). The SLM-based correction provided a wider wavelength tuning range. Consequently, it was used to measure the bandwidth of different fibres, where the wavelength had to be tuned over a range of many tens of nanometres. On the other hand, the prism-based correction does not require recalculating the holograms while still providing a sufficient level of compensation for many applications, such as targeting different Raman shifts during CARS imaging.

After the dispersion of the SLM was compensated for, the bandwidth of different fibres was measured. Different types of fibres were calibrated using a tunable continuous-wave laser, and the quality of the focus was observed after the wavelength of the laser was tuned from the wavelength used for the calibration. It was observed that the focused point shifts axially with wavelength for step-index fibres due to the chromato-axial effect. While this property could be, in principle, applicable for fast refocusing by small tuning of the excitation wavelength, it makes the step-index fibres unsuitable for focusing light from broadband sources. Graded-index fibres, on the other hand, do not have this property and were able to maintain the focus over a few tens of nanometres (for a 5 cm long piece of fibre). The difference in the bandwidth of different graded-index fibres was almost an order of magnitude, demonstrating that choosing the suitable fibre is crucial for non-linear imaging. The highest bandwidth was measured for the Prysmian DrakaElite fibre, followed by Thorlabs GIF50E. The Thorlabs fibre, however, has a lower numerical aperture, thus, is not suitable for non-linear imaging. The custom-drawn CREOL F3 fibre also had a bandwidth sufficient for focusing light from a femtosecond laser while having a larger core diameter (and thus a larger field of view) than the Prysmian fibre.

The bandwidth directly affects the ability of the fibre to focus light from pulsed light sources and, thus, its suitability for non-linear imaging. The suitability for non-linear imaging was demonstrated by calibrating the fibres with a femtosecond laser. With a graded-index fibre with a bandwidth higher than the spectral width of the laser, the power ratio of the focused point was similar to one achieved with a narrow-band continuous-wave laser. Due to using a high-bandwidth fibre and controlling the input polarisation, the achiever power ratios were significantly higher than in previous demonstrations of focusing femtosecond pulses through multimode fibres [53]. Conversely, the low bandwidth of step-index fibres renders them unsuitable for pulsed lasers, as the achievable power ratios are very low, and the resulting point spread functions are much longer than expected from the numerical aperture. The shape of the point spread function would make multiphoton excitation very inefficient and drastically limit the sectioning capabilities (as previously shown in [54]). Consequently, graded-index fibres are preferable for non-linear imaging.

The spectral phase of the focused point was measured to characterise the dispersion of the fibres and examine the options for its compensation. For the Prysmian DrakaElite fibre, the group velocity dispersion was measured to be $50\,\mathrm{fs}^2{\cdot}\mathrm{mm}^{-1}$ at 780 nm, with almost no third order dispersion. This value was independent of the position of the focused point. Thus, a standard pulse compressor, such as a prism pulse compressor, is sufficient to compensate for the group velocity dispersion in the multimode fibre when used for non-linear imaging.

Simultaneous focusing of two wavelengths through a multimode fibre using a single spatial light modulator was presented. Adding the respective transmission matrices created a joint focus at both wavelengths. This method allowed multiple wavelengths to be focused without using multiple modulators and possibly complicated modifications to the system, which might make the optics significantly harder to align. Although the increased speckled background around the point decreased the efficiency, it did not impose an issue for non-linear imaging, as the background did not generate any measurable signal.

Results presented in this chapter, mainly the simultaneous focus for two wavelengths from a pulsed laser source through the multimode fibre with the ability to tune the wavelength after the calibration constitute a substantial step towards implementing coherent anti-Stokes scattering imaging and possibly other non-linear imaging techniques through a multimode fibre endoscope.

Some results presented in this chapter (including the SLM dispersion compensation, bandwidth measurements, dispersion measurement and demonstration of focusing of femtosecond pulses) were published in [68].

4. Coherent anti-Stokes Raman scattering through fibre

Confocal and multi-photon fluorescence microscopy has become state-of-the-art imaging techniques for imaging living organisms. For many applications, however, labelling the sample is not an option and other imaging techniques with molecular specificity are needed. One such technique is confocal Raman microscopy [136], which allows three-dimensional label-free imaging. Spontaneous Raman imaging, however, requires high excitation powers and very long integration times, mostly incompatible with in-vivo imaging. These shortcomings can be overcome by the use of coherent Raman scattering (CRS) techniques, such as stimulated Raman scattering (SRS) or coherent anti-Stokes Raman scattering (CARS) [66, 137–142] Compared to spontaneous Raman microscopy, CARS microscopy offers not only orders of magnitude shorter per-pixel integration times [143–145], but also has higher biochemical specificity [138, 146]. Typical applications of CARS imaging include optical biopsies for diagnosing tumours and other diseases [67, 147–151], label-free imaging of lipid-rich tissue structures such as myelinated axons [152–154] or lipid droplets [155].

In CARS, the oscillations of the molecules are driven by the difference frequency $\omega_{\text{pump}} - \omega_{\text{Stokes}}$ between the pump and Stokes beam. When this frequency difference approaches a transition of the dielectric medium, the oscillations are driven very efficiently and can be probed by the probe beam at ω_{probe}, generating anti-Stokes emission at $\omega_{\text{CARS}} = \omega_{\text{pump}} - \omega_{\text{Stokes}} + \omega_{\text{probe}}$ (the energy diagrams are in Figure 4.1). Typically, the pump beam is used as the probe beam. Thus, $\omega_{\text{CARS}} = 2\omega_{\text{pump}} - \omega_{\text{Stokes}}$. Since CARS is a coherent process, not only the energy (Figure 4.1c) but also the momentum is preserved. Due to the phase-matching condition (Figure 4.1d), the CARS signal is generated predominantly in the forward direction, making epi-detection reliant on scattering [156].

Both linear and non-linear Raman imaging is also used in endoscopy, including biomedical applications [145, 157]. The endoscopes are, however, typically bulky with an outer diameter of a few millimetres. While this might be acceptable for many applications, many others could benefit from the significantly smaller dimensions of multimode fibre endoscopes. In Chapter 3, it was demonstrated that focusing light from pulsed laser sources through a multimode fibre endoscope is possible. These results open up possibilities for implementing non-linear imaging techniques through multimode fibres. This chapter presents the first implementation of coherent anti-Stokes Raman scattering imaging through a single multimode fibre.

A laser system generating two synchronised pulse trains at two wavelengths separated by about $3000\,\text{cm}^{-1}$ (which is the typical range used for bio-imaging) is necessary for CARS imaging. As a suitable laser system was not available in the Complex Photonics laboratory of the Institute of Scientific Instruments of the CAS in Brno at the time, the

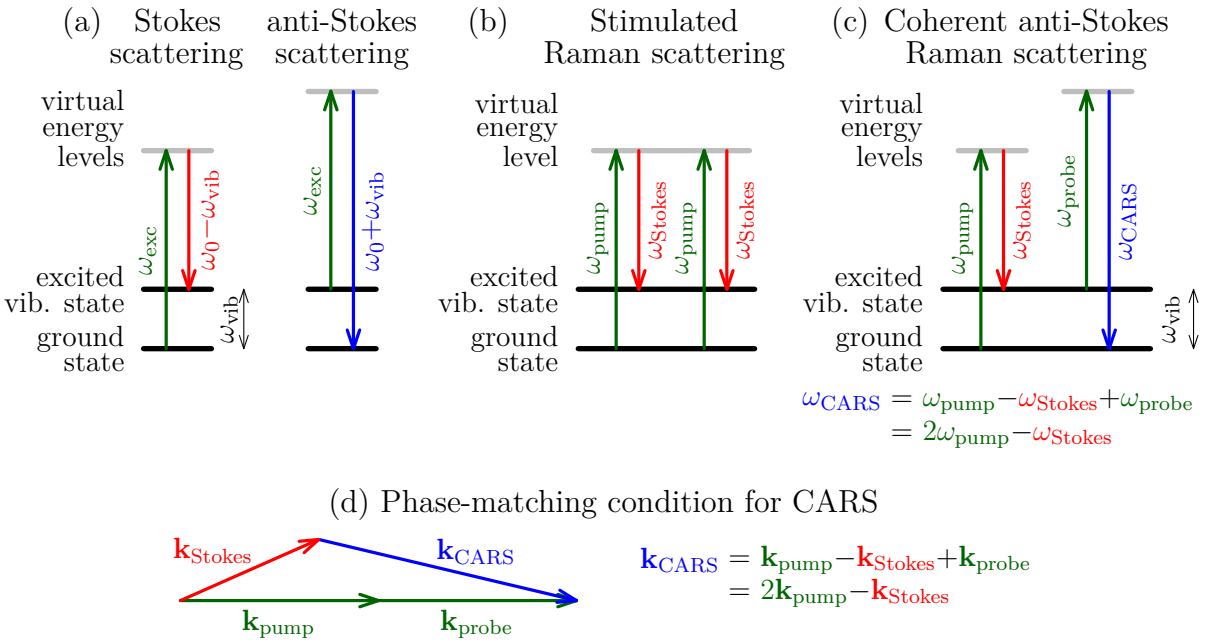

Figure 4.1: Energy diagrams for (a) linear Raman scattering, (b) stimulated Raman scattering (SRS) and (c) coherent anti-Stokes Raman scattering (CARS). (d) Phase-matching condition for CARS.

experiments presented in this chapter were performed at the Department of Spectroscopy and Imaging at Leibniz Institute of Photonic Technology (IPHT), Jena, Germany. The fibre imaging system was built in Brno on a portable breadboard and transported to IPHT, where a suitable picosecond laser system was kindly provided to conduct the experiments. In total, two two-week-long visits were carried out. The first visit aimed to verify that focusing a picosecond laser through graded-index fibres is possible and to test the first CARS imaging through a single multimode fibre with the signal collected in transmission, including testing a chemical contrast. In between the two visits, the optical system was modified. The spatial light modulator was replaced with a faster type. The system was optimised and, more importantly, modified to allow epi-detection, i.e., collecting the light through the fibre. The goal of the second visit was thus to show that epi-detection is possible so that the imaging system can work as an endoscope. The data in this chapter is labelled as *dataset 1* and *dataset 2* to distinguish the two configurations of the system.

4.1. Optical setup

The setup for CARS imaging (Figure 4.2) was based on the setup used for fibre characterisation described in Chapter 3. Consequently, only the differences are described here. The setup (excluding the light source) was built on an optical breadboard (120 cm × 60 cm, Thorlabs PBH51507) to make the system portable, which made it possible to move the system to the laboratory at IPHT, Jena to use a suitable laser system available there.

The light source consisted of a 832 nm picosecond laser (Coherent Mira HP-P), pumped using a 532 nm CW laser (Coherent Verdi V18), and an optical parametric oscillator (OPO; APE OPO). The laser pulse durations were 1 ps to 2 ps, the bandwidth of the pump beam was 13 cm^{-1} to 22 cm^{-1} (depending on the wavelength and the pumping condition

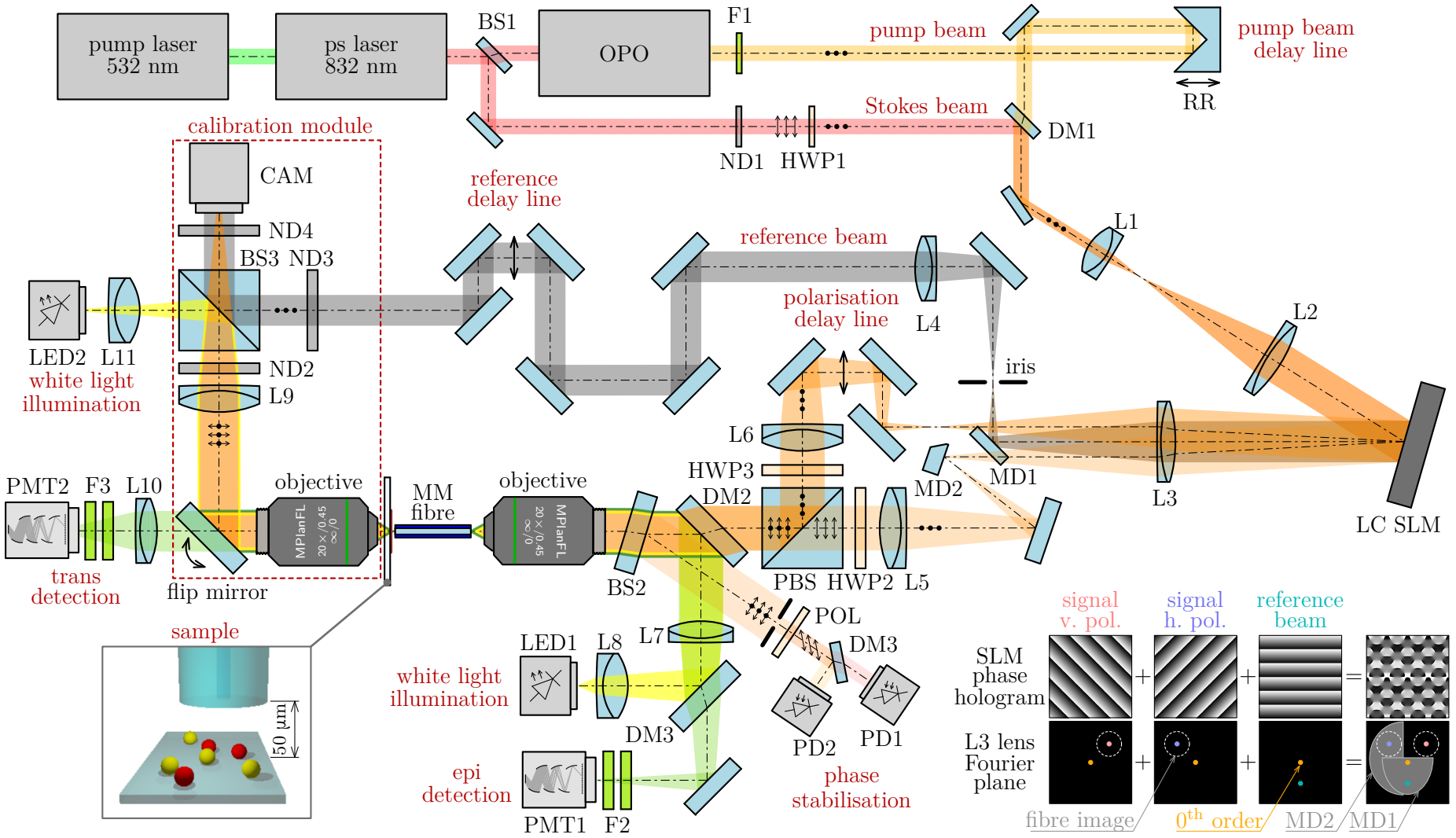

Figure 4.2: Schematics of the setup for CARS imaging through a multimode fibre using a picosecond laser system. BS – non-polarising beamsplitter, CAM – camera, DM – dichroic mirror, F – filter, HWP – half-wave plate, LC SLM – liquid crystal spatial light modulator, L – lens, MD – D-shape mirror, MM fibre – multimode fibre, ND – natural density filter, PD – photodiode, PMT – photomultiplier tube, PSB – polarising beamsplitter cube, RR – retro-reflector. The inset shows the position of the beams in the focal plane of lens L3 and the respective holograms on the SLM.

of the OPO) and the bandwidth of the Stokes beam was approximately $10\,\mathrm{cm}^{-1}$. The wavelengths of both beams were monitored on a spectrometer.

Both beams were combined on a dichroic mirror with an adjustable time delay of the pump beam. The combined beam was expanded to fill the active area of the liquid crystal spatial light modulator. For the two datasets, two different SLMs were used. For dataset 1, Meadowlark HSP512-1064 was used and was calibrated using the linear lookup table measurement (Figure 2.8). For dataset 2, Meadowlark HSP1920-1064-HSP8 was used instead, and its response was calibrated using the diffractive method (Figure 2.7). In both cases, the timing of the SLM, camera and DAQ card were controlled in software, i.e., the timing described in Figure 2.5 was not used. Consequently, both the calibration and the imaging were significantly slower (by a factor of about 3 for the Meadowlark HSP1920-1064-HSP8 and 2 ms integration time) than would be possible with the SLM that was used. Also, not triggering the detector using the SLM (and thus not synchronising it with the refresh frequency of the SLM) increased noise for short integration times due to the flickering.

Similarly to the setup in Section 2.1, the SLM created three beams that were separated using a lens and multiple mirrors. The reference beam was filtered using an iris and collimated. Both input polarisation beams were collimated, the polarisation of one was rotated by 90°, and both beams were overlapped, with an adjustable delay, on a polarising beamsplitter cube. A small portion of the beam was picked on an uncoated glass window (BS2, Thorlabs WG41050) to stabilise the phase difference between the two input polarisation paths. Unlike in the setup in Section 2.1, the pump and Stokes beams were split on a dichroic mirror (DM3; Thorlabs DMLP805T), and two photodiodes were used to stabilise the relative phase difference. Using two photodiodes was necessary to stabilise the relative phase for the two beams (wavelengths) simultaneously, without blanking one of the beams at a time. The stabilisation of the relative phase was performed at the beginning of every 2 lines of the image for dataset 1 and every 10 lines for dataset 2. Unlike in the setup in Section 2.1, both input polarisation beams undertook an even number of reflections. This change was possible since the prism-based correction of the SLM dispersion was not used here. The change made the system less sensitive to the alignment of the laser beams, as a small change in the angle of the beam did not result in a drop of interference contrast on the two photodiodes.

The beam was focused on the proximal end of the fibre. The distal end was then imaged onto a camera and overlapped with a reference beam, identically to Section 2.1.

Prysmian DarkaElite was used for the experiments in this chapter. The probe length was 30 mm to 35 mm. The fibre was stripped of the coating and cleaved using a manual cleaver (Thorlabs XL411). The fibre was glued in a single ceramic ferrule (Thorlabs CF128) using Norland Products NOA1375 adhesive. The adhesive had a lower refractive index (1.375) than the refractive index of the fibre cladding. Using a low-refractive-index adhesive reduced the losses of light guided in the cladding and, potentially, increased the collection efficiency since the light was collected not only by the core but also by the cladding.

The sample (beads on a glass slide) was mounted on a three-axis stage built of Thorlabs LNR25D/M stages, allowing both the focus and lateral movement of the sample. The focusing was performed using Thorlabs Z825B motorised actuator mounted in one of the stages. The lateral movement of the sample was manual only.

For imaging in transmission, the signal was collected through the objective in the calibration module, filtered using a short-pass filter (Semrock Brightline SP650) and a band-

(a) Image from Logitech webcam (b) Image from Basler camera

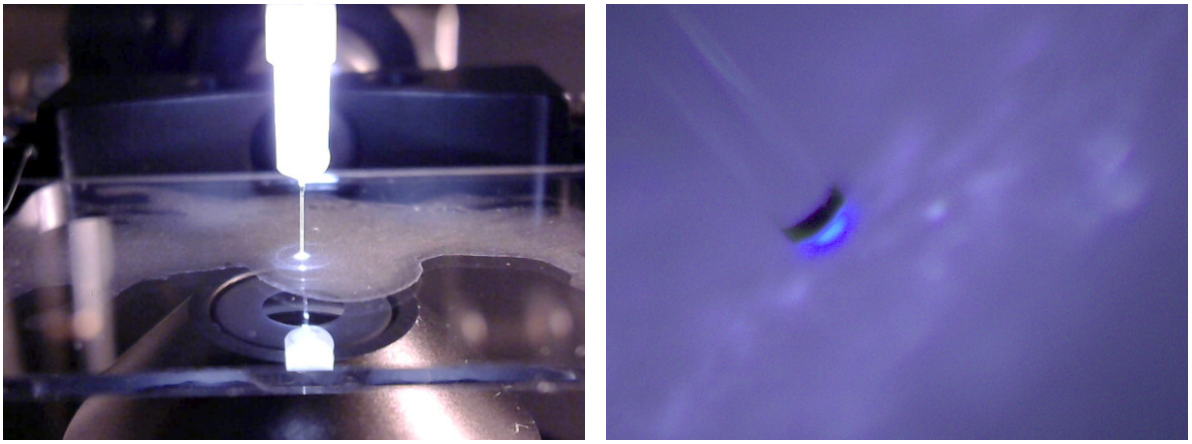

Figure 4.3: A layer of beads on a glass slide viewed from two cameras mounted in the setup. Both cameras were focused on the distal end of the fibre. (a) Image from a Logitech webcam, used for navigation over the sample. (b) Image from a Basler camera with custom optics. Due to the high magnification, this camera was used to estimate the distance between the sample.

pass filter (Semrock Brightline 550/88) and focused onto a multialkali PMT (for dataset 1; Hamamatsu H10723) or a GaAsP PMT (for dataset 2; Thorlabs PMT2101/M). For dataset 2, epi-detection was implemented. The signal collected through the fibre was reflected off a long-pass dichroic mirror (Thorlabs DMLP605), filtered using a short-pass filter (Thorlabs FESH0600) and a band-pass filter (Brightline 550/88) and focused onto a GaAsP PMT (Thorlabs PMT2101/M). The signal from the PMT was collected on a DAQ card at 165 kHz and was averaged during the entire integration time (typically 2 ms).

The setup was equipped with two extra cameras to allow navigation over the sample and estimation of the distance between the fibre and the sample. For navigation, Logitech C270 webcam focused on the distal end of the fibre was used since it offered a large field of view (Figure 4.3a). Basler ace acA640-750uc was used to find the correct sample distance from the fibre before the imaging. The distal end of the camera was magnified onto the camera using two lenses with sufficient magnification to estimate the gap between the fibre and the sample when white light from LED1 was coupled into the fibre (Figure 4.3b). For the samples with a thin layer of beads, a wide-field image could be performed on the camera in the calibration module (Figure 4.8a), using LED1 or LED2 for illumination.

The pump and Stokes pulses had to overlap in the imaging plane in space and in time to generate the CARS signal. While the calibration procedure established the spatial overlap of the focused points (which could be adjusted in the software if needed), the temporal overlap had to be set externally by a delay line placed in the pump beam. As an indicator of the time overlap, sum-frequency generation in a non-linear crystal (BBO, β-barium borate) was used, see Figure 4.4. Three new wavelengths were generated if both spatially overlapped beams were focused on the crystal at a suitable angle. Two of them corresponded to the second-harmonic generation of the two beams and were always present. Therefore, they could be used to align the crystal. The third wavelength generated by sum-frequency generation was only present when the pulses overlapped in time. The time overlap was first established before the SLM, where both beams had

high power and thus generated a visible signal in the crystal. Afterwards, the crystal was moved in place of the multimode fibre, a 1″ non-polarising beamsplitter cube was placed before the SLM to simulate the fibre dispersion, and the time overlap was adjusted accordingly. The final adjustment of the time overlap was made during the imaging by maximising the detected CARS signal.

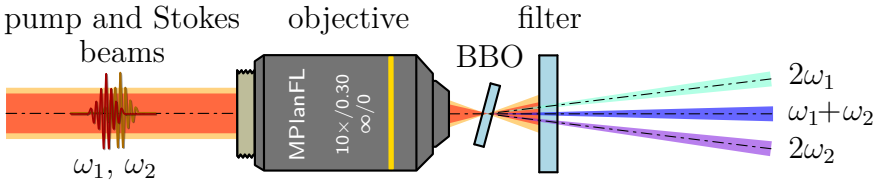

Figure 4.4: Setting a time overlap of two beams using sum-frequency generation in a BBO crystal. When both beams were focused on the crystal, the second-harmonic of both frequencies ω_1, ω_2 was generated. If the pulses overlapped in time, the sum frequency was generated as well.

4.2. Fibre calibration and focus generation

The calibration procedure necessary to create a scanning focus in the sample plane was identical to Section 2.5. The working distance (i.e., the distance of the focus from the facet) was chosen to be 50 µm. For CARS, two spatially overlapping foci with two wavelengths were required. Each wavelength was calibrated separately (by physically blocking the other beam). The OPO was tuned to 667.7 nm, corresponding to Raman shift of 2958 cm^{-1}. Before the calibration for each wavelength, the length of the delay line in the reference beam was adjusted to achieve interference of the signal and reference beam. For the Meadowlark HSP1920-1064-HSP8 SLM, the complete calibration took approximately 15 minutes and was useable for a few hours of imaging.

To create a joint focus at both wavelengths, the two transmission matrices measured were added (as described in Section 3.5) with 2 : 1 (pump : Stokes) ratio. This ratio increased the intensity of the generated CARS signal, since the CARS signal depends quadratically on the pump intensity and linearly on the Stokes intensity.

The spatial overlap of the points for both wavelengths could be controlled in software by adjusting the offset between the transmission matrices if needed. The focused point could be created at positions corresponding to a camera pixel. Here, the pixel spacing in the sample plane (determined by the camera pixel size and the objective and lens imaging the sample plane onto the camera) was 0.26 µm. Since the diffraction-limited FWHM size of the focused points was 1.4 µm for the pump and 1.7 µm for the Stokes beam, the pixel spacing was sufficient to set the lateral spatial overlap of the two beams in the sample plane. As for the axial spatial overlap, it was assumed that the axial chromatic aberration of the optics imaging the sample plane onto the camera was significantly lower than the size of the axial point spread function. Thus, laterally overlapping beams on the camera resulted in laterally overlapping beams in the sample plane.

4.3. Endoscope characterisation

After calibrating the endoscope at both excitation wavelengths, the quality of the focused points across the field of view was evaluated (as described in Section 2.6), see Figure 4.5. For the pump beam, the power ratio and spot size were symmetrical about the axis of the fibre. However, the power ratio did not have this symmetry for the Stokes beam. Typically, such behaviour was caused by a misalignment of the beam on the spatial light modulator. In this case, it was caused by a non-symmetrical profile of the Stokes beam. Nevertheless, the spot size at both wavelengths approached the diffraction-limited values given by the numerical aperture, and the achieved power ratios were sufficient for imaging.

The transmission of the setup (ratio of the power in the focused point and the power at the input of the setup) was 7.5 % for the pump beam and 2.5 % for the Stokes beam.

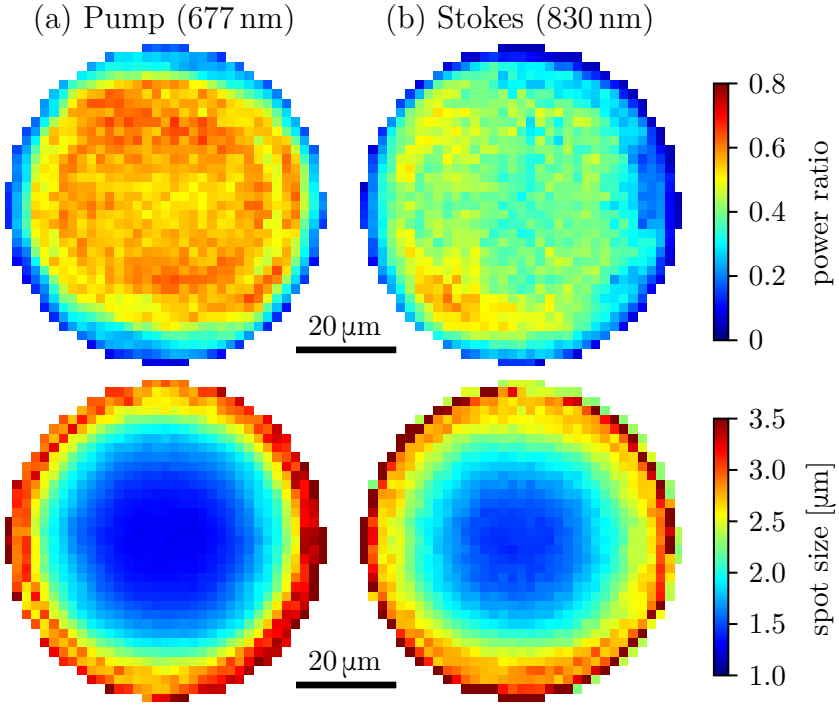

Figure 4.5: Power ratio and spot size across the field of view for both excitation beams (dataset 2). The spatial light modulator was displaying a combined hologram for both wavelengths as described in Section 3.5 with 2 : 1 (pump : Stokes) ratio.

The imaging system allowed tuning the OPO wavelength (used as the pump beam for CARS imaging) after calibration. As described in Section 3.2, the power ratio of the focused point dropped and its size increased as the OPO was tuned from the calibration wavelength. As a result, the intensity of the generated CARS signal dropped. This change had to be taken into account when performing wavelength sweeps. Consequently, the bandwidth of the system was measured in the same manner as described in Sections 3.1 and 3.2. Figure 4.6 shows the power ratio and spot size after wavelength tuning for dataset 2. This data was used to correct the wavelength-dependence of the intensity of CARS signal during wavelength sweeps (Figure 4.11). The small wavelength tuning range of approximately ±4 nm around the calibration wavelength was caused by not using any method for SLM dispersion compensation. The data cannot be directly compared to the data in Figure 3.4, as a different wavelength and central spatial frequency of the holograms were used, affecting the wavelength tuning range when no compensation method was used.

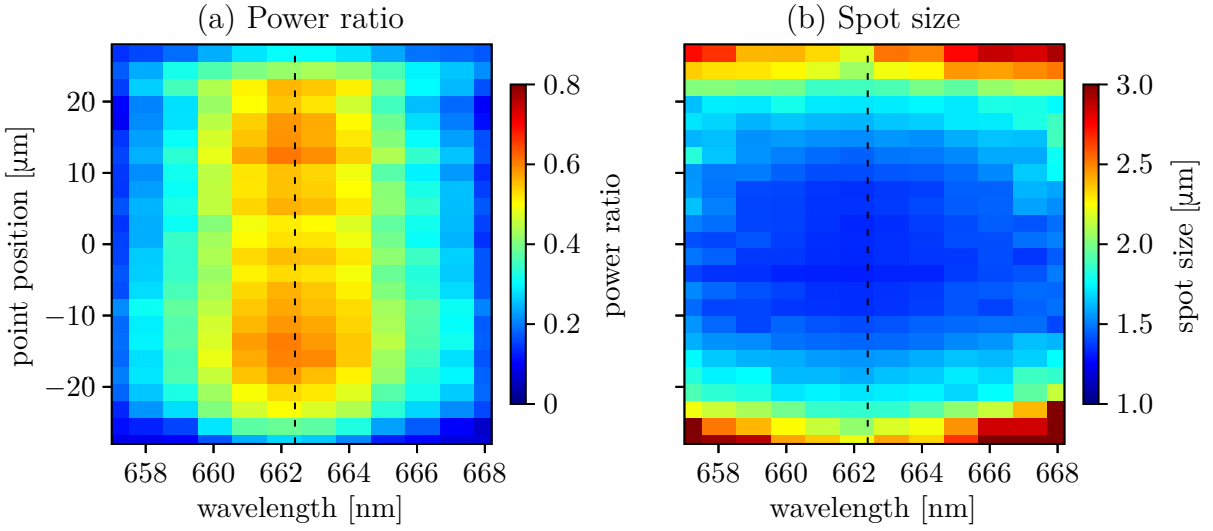

Figure 4.6: Power ratio and spot size on a line across the field of view after the OPO wavelength was tuned from the calibration wavelength of 662.4 nm, indicated by the dashed line (dataset 2).

4.4. Imaging of polymer beads

CARS imaging through multimode fibre was tested on 2 µm (Sigma Aldrich 78452-5ml-F) and 7 µm (Sigma Aldrich 78462-5ml-F) polystyrene (PS) and 2.5 µm polymethyl methacrylate (PMMA; Bang laboratories PP05N) beads on a cover glass. For some samples, a scattering layer consisting of 3 % intralipid solution (Sigma Aldrich I141-100ML) in epoxy was deposited on the reverse side of the coverslip to increase scattering and, thus, the intensity of the epi-detected signal. The intralipid concentration was chosen to have a similar scattering coefficient to brain tissue [158]. Nevertheless, since the layer was deposited on the reverse side of the cover glass (and thus 170 µm from the beads being imaged), the increase of the back-scattered signal coupled into the multimode fibre was likely small.

The power in the focused point during the imaging was about 7 mW (dataset 1) or 8.5 mW (dataset 2) for the pump beam and about 6 mW (dataset 1) or 3 mW (dataset 2) for the Stokes beam. These values were lower than typical for standard CARS microscopy, where the excitation powers of tens of milliwatts are typically used. While the transmission of the system would allow higher laser powers, the maximal power was limited by the sample damage due to the long per-pixel dwell time. As discussed in Section 2.1 the per-pixel dwell time consisted of the integration time and the delay necessary to update the hologram on the SLM. For dataset 1, the wait time was 25 ms. For dataset 2, the wait time was set to 15 ms for short integration times up to 2 ms. The wait time for longer integration times was reduced to 10 ms. During most of the wait time, the sample was still exposed to the excitation beams, creating foci on the sample, while no signal was collected. The damage threshold could be thus lowered by optimising the timing of the SLM hologram upload and data acquisition (as discussed in Section 2.1) and beam blanking during the wait time.

For dataset 1, the signal was collected in transmission. For dataset 2, the signal could be detected both in transmission and in epi, i.e., by collecting the signal through the same multimode fibre used to deliver the excitation beams. Since the software for these

experiments supported only a single detector for imaging, trans and epi-detection images could not be obtained during a single scan. Instead, two scans were performed when comparing trans and epi, and the detector was switched between them.

Figure 4.7 shows a z-stack of PS beads on a glass slide captured by physically moving the sample. The figure shows the intensity in the area corresponding to the beads and around them (i.e., generated in the glass). When the sample was too far away from the facet (the position in Figure 4.7 is negative), almost no signal was generated, similar to when the sample was removed from the system. By bringing the sample closer to the fibre, the beads became focused. Apart from the resonant CARS signal from the beads, a non-resonant signal inside the glass was generated. When the sample was closer than the working distance, the intensity of the beads decreased (they became out of focus). In contrast, the intensity of the signal generated in the glass increased as a larger fraction of the point spread function was inside the glass slide. Figure 4.7 demonstrates that exciting CARS in structures as small as 2 µm through a multimode fibre is possible, despite the low numerical aperture of the fibre and the low laser power used for excitation.

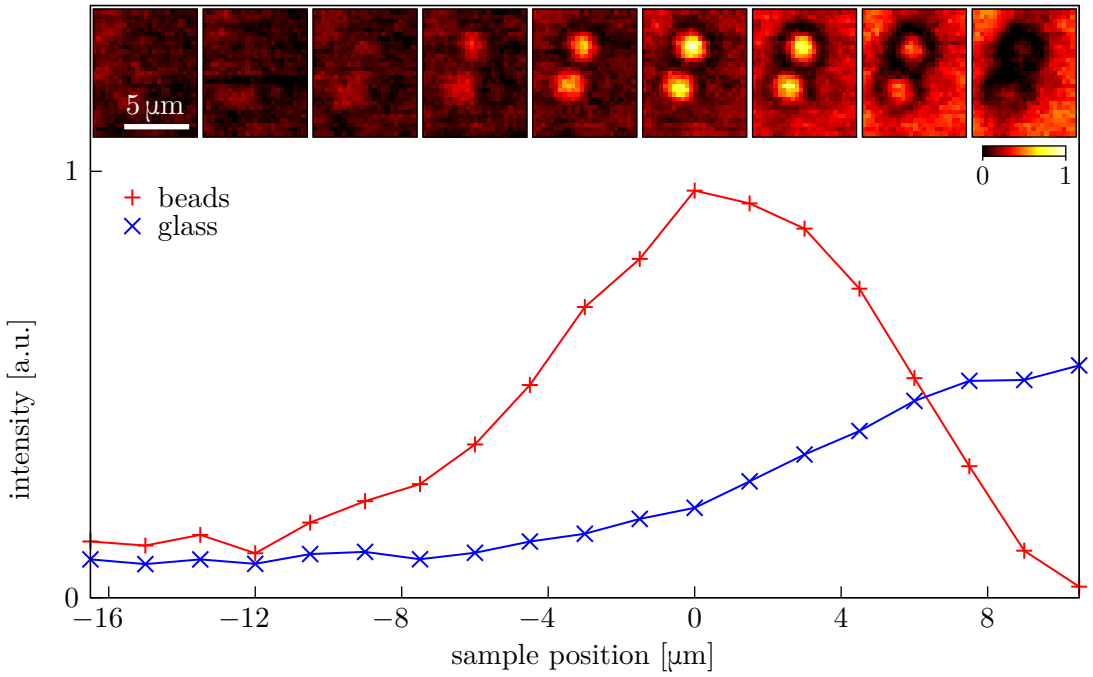

Figure 4.7: CARS z-stack of PS beads (dataset 1) with the signal collected in transmission. A positive sample position means that the sample was closer to the fibre than the working distance of 50 µm. The figure shows a subset of images taken with different positions of the sample. The intensity of the beads and the area without the beads (thus corresponding to the signal generated in the glass) was evaluated. The lines are a guide to the eye.

The diffraction-limited axial length (FWHM) of the points spread function was 14 µm at the pump wavelength and 17 µm at the Stokes wavelength [120]. The measured depth of focus for the beads was about 12 µm, i.e., comparable to the expected length of the point spread function (the depth of focus was lower due to CARS being a non-linear process). This value verified that the length of the point spread function was not noticeably affected by using a pulsed laser source (when a high-bandwidth graded-index fibre was used).

In Figure 4.7, the CARS signal generated in the sample (the beads and the cover glass) was collected in transmission. However, this configuration would not be possible if

the fibre was used as an endoscope inside a tissue. In this situation, the generated signal must be collected using the same multimode fibre to deliver the excitation beams. CARS signal is generated predominantly in transmission due to the phase-matching condition. Epi detection in tissue thus relies on back-scattering. The sample in this experiment consisted of a single layer of beads on a cover glass. Therefore, there was no scattering layer below the beads. Epi detection was still possible due to the weak reflections on the cover glass. The imaging with epi detection is demonstrated in Figure 4.8. A single layer of PS beads on a cover glass was imaged in transmission and with epi-detection. As expected, the signal in epi was significantly weaker, and the image was thus noisy. Nevertheless, the beads were visible. Despite low collection efficiency, this experiment demonstrated that epi detection through the multimode fibre was possible. An example of a significantly more scattering sample is in Figure 4.9. A thicker layer of 7 μm PS beads on a cover glass was imaged here. The larger beads generated a stronger signal (due to their size being more comparable to the length of the point spread function), and the lower layers of beads acted as a scattering media, significantly increasing the intensity of the signal on the epi detector. Such scattering samples better mimicked imaging inside a tissue.

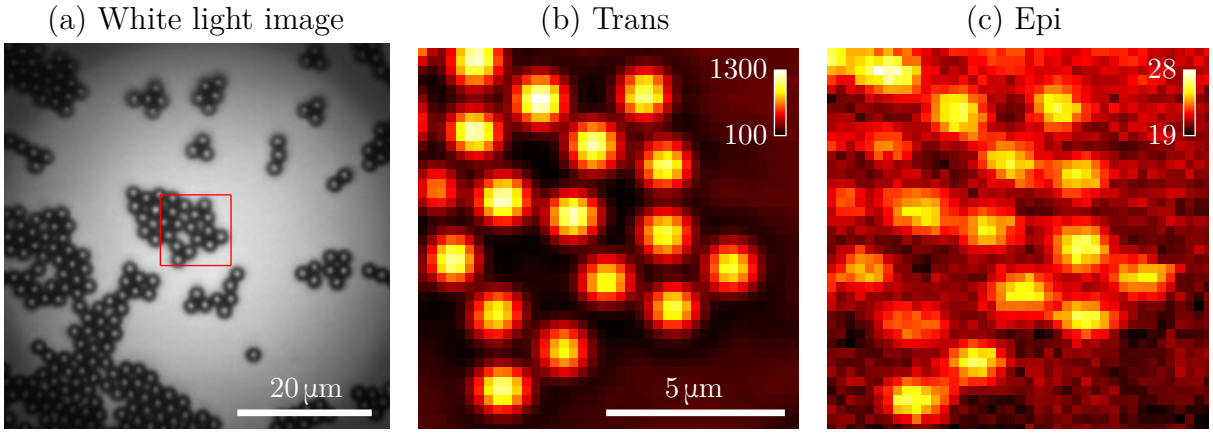

Figure 4.8: CARS imaging of 2 μm polystyrene on a cover glass. (a) White light image of the sample taken in transmission. The sample was illuminated through the multimode fibre using a white LED. The image was captured on the camera in the calibration module. (b) CARS image with the signal collected in transmission. (c) The same image with epi-detection (the signal collected through the multimode fibre).

Figure 4.10 shows a comparison of two epi-CARS images of a single layer of 2 μm and 7 μm polystyrene beads on a cover glass with different integration times of 2 ms and 1 ms. Reducing the integration time increased the noise in the images. The prevailing reason for the drop in signal-to-noise ratio was the flickering of the SLM, resulting in periodic changes in the excitation intensity, which was not in sync with the integration time. Nevertheless, at 1 ms integration time, the 2 μm beads were still visible with a sufficient signal-to-noise ratio.

The chemical sensitivity of CARS is demonstrated in Figure 4.11. Two samples (2.5 μm PMMA and 2 μm PS beads on a cover glass) were imaged with the signal being detected in transmission. The wavelength of the OPO was tuned, which resulted in different Raman shifts being excited. Figure 4.11c shows the measured spectra of PMMA and PS, corrected for the limited wavelength tuning range of the system (as discussed in Section 4.3) and

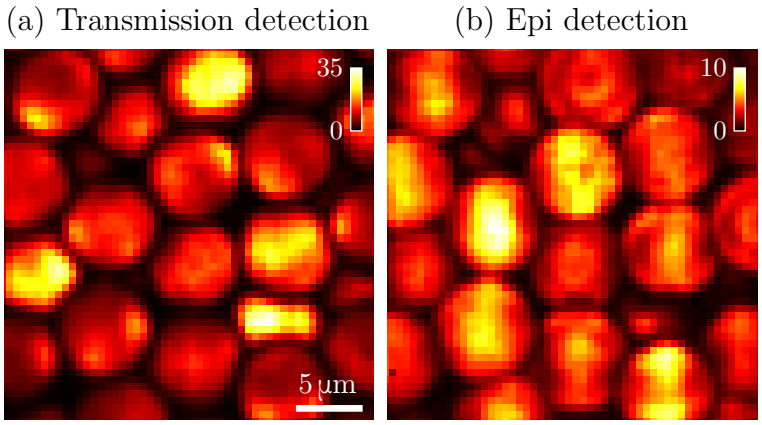

Figure 4.9: Images of the same area of the sample of a thick layer of 7 µm polystyrene beads on a cover glass with the signal collected (a) in transmission and (b) with epi-detection. Due to the strong scattering in the thick layer of beads, both images have a similar intensity.

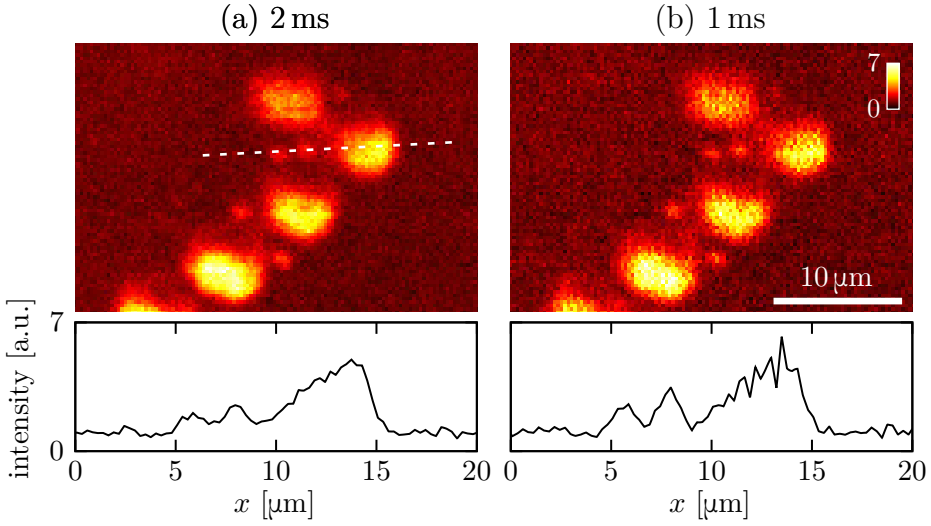

Figure 4.10: The effect of the integration time on CARS imaging a mix of 2 µm and 7 µm polystyrene beads on a cover glass with epi-detection. The graphs show a cross-section of the images along the dashed line.

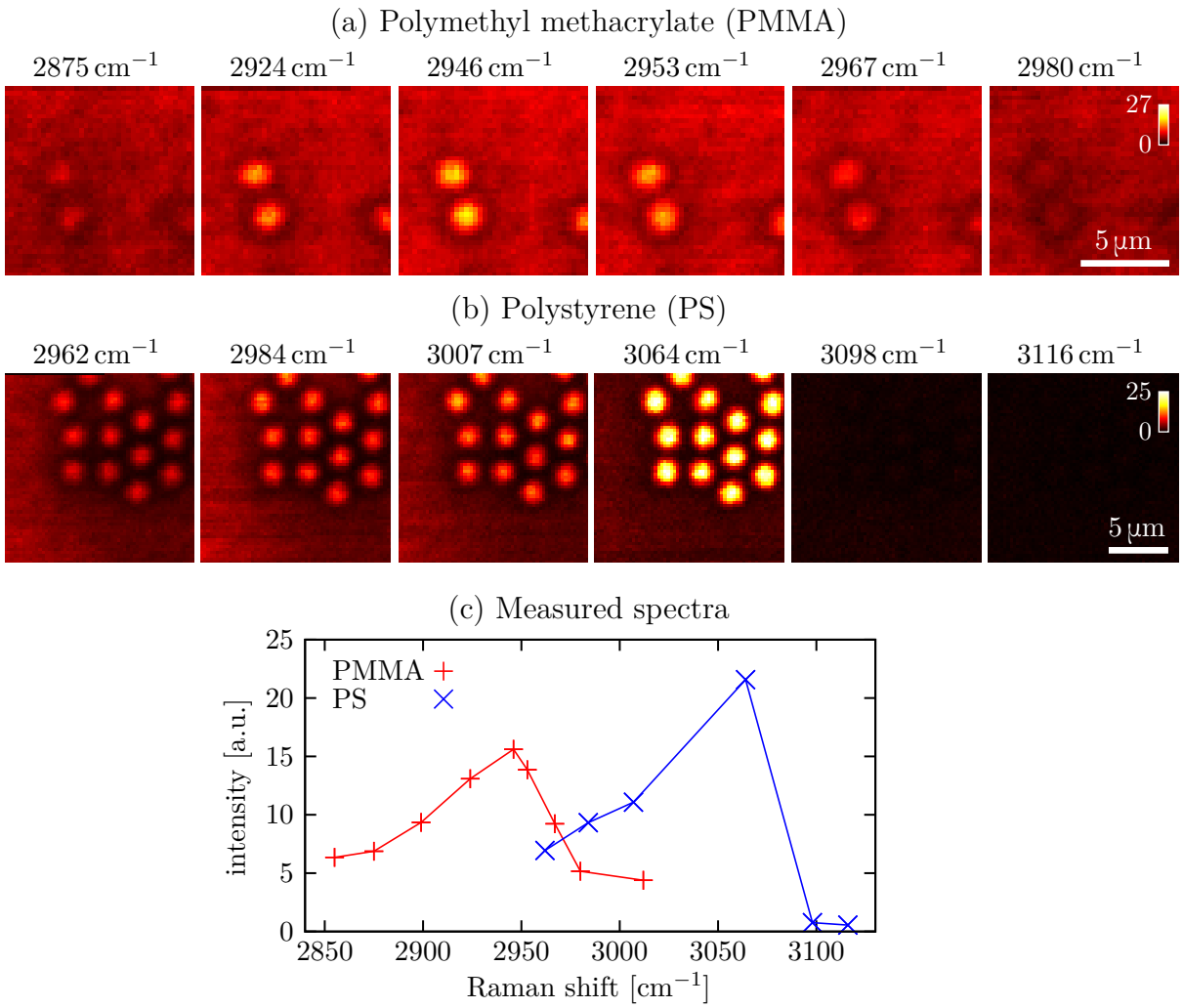

Figure 4.11: Wavelength sweep of 2 µm PS and 2.5 µm PMMA beads on a cover glass. (a), (b) CARS images of beads taken at different Raman shifts. The images were corrected for the limited bandwidth of the system (Figure 4.6) and variations of OPO power. (c) Intensity of the beads as a function of the Raman shift. The lines are a guide to the eye.

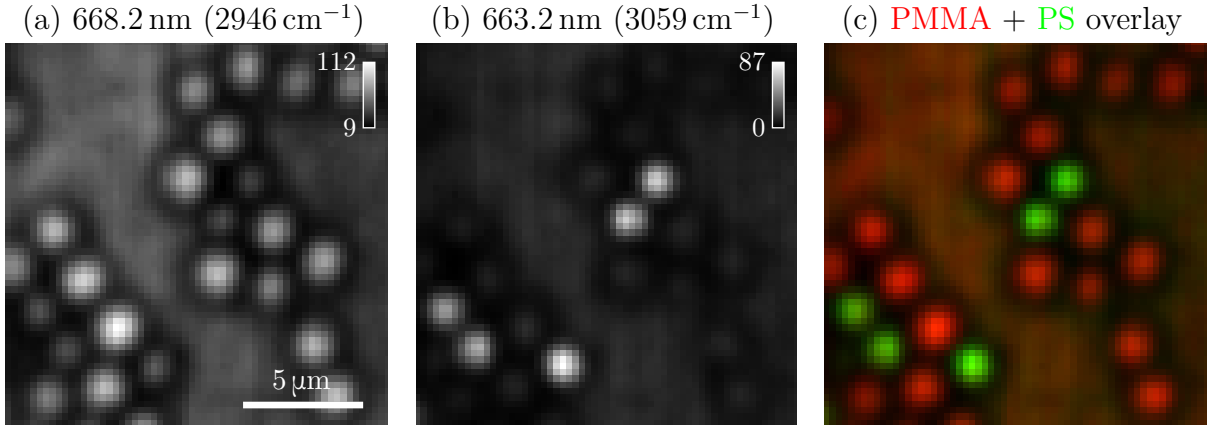

Figure 4.12: Demonstration of chemical contrast on CARS imaging a mix of 2 µm PS and 2.5 µm PMMA beads on a cover glass. The signal was collected in transmission. (a), (b) Two images recorded at two different OPO wavelengths (corresponding to two different Raman shifts). (c) Overlay of the two images showing the chemical contrast.

the variations of the OPO power, assuming quadratic dependence of the generated signal on the pump intensity and linear dependence on the Stokes intensity. The bandwidth of the system was sufficient to cover both the PS and PMMA resonances using a single calibration at 2958 cm^{-1}.

Figure 4.12a,b shows a CARS image of a mixed sample of PS and PMMA beads on cover glass, captured at two different Raman shifts (corresponding to the peaks in Figure 4.11c). Figure 4.12c shows an overlay of both images, demonstrating the chemical contrast allowing the differentiation between PS and PMMA. The signal was collected in transmission. The same effect was demonstrated using epi-detection in Figure 4.13. Here, a thicker layer of beads was used to increase scattering in the sample and, thus, the intensity of the epi-collected signal. The results clearly illustrate that CARS imaging with a chemical contrast through a multimode fibre endoscope is possible.

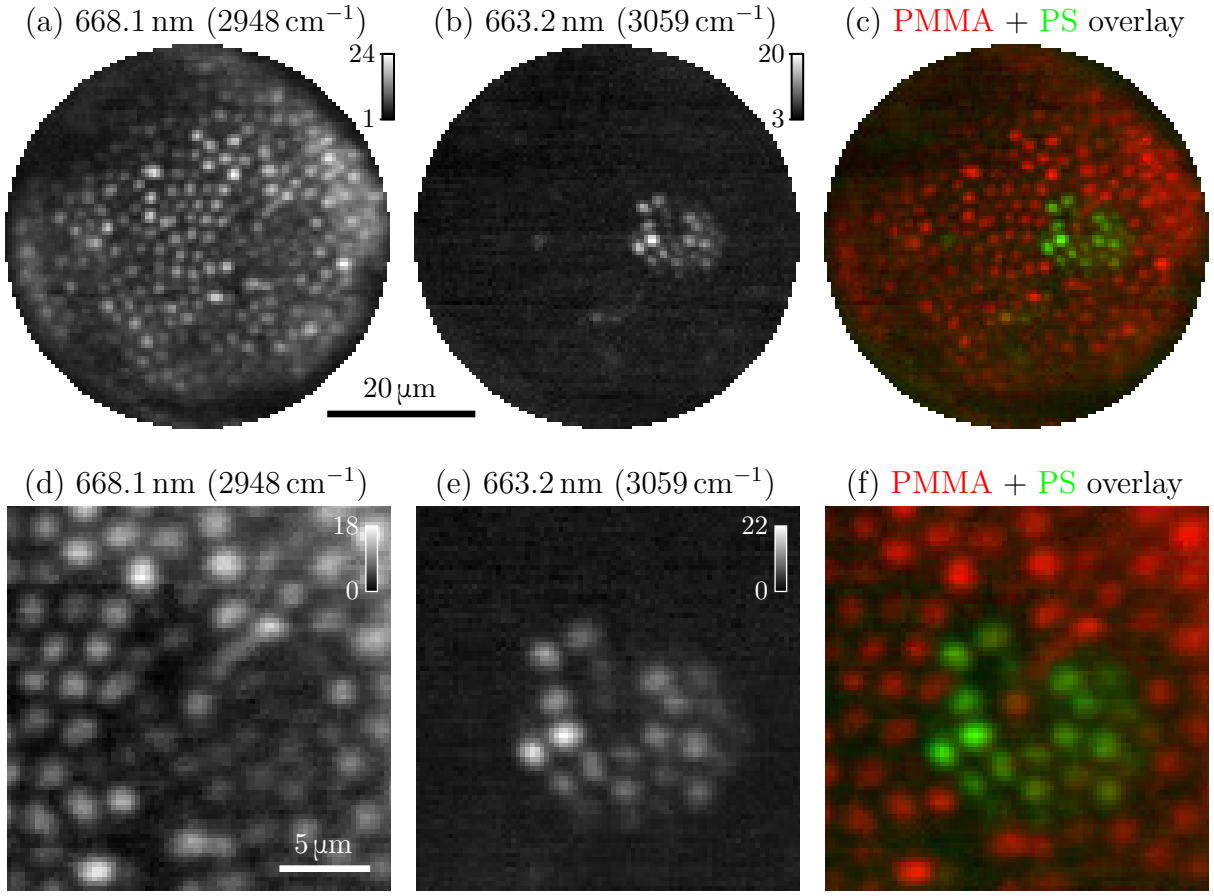

Figure 4.13: Demonstration of chemical contrast on CARS imaging a thick layer (to increase scattering) of a mix of 2 µm PS and 2.5 µm PMMA beads on a cover glass. The signal was collected using epi detection (i.e., through the fibre). (a), (b) Two images recorded at two different OPO wavelengths (corresponding to two different Raman shifts). (c) Overlay of the two images showing the chemical contrast. (d)–(f) Detailed images scanned with higher resolution.

4.5. Summary

In this chapter, the first implementation of coherent anti-Stokes Raman scattering (CARS) imaging through a multimode fibre was presented.

An endoscopic system developed and characterised in Chapter 3 was used with a picosecond laser system consisting of a picosecond laser (Stokes beam) and an optical parametric oscillator (pump beam). Both spatially overlapping beams were focused through a multimode into the same point, allowing the generation of the CARS signal in the sample. The fibre imaging system was still under development during the experiments presented in this chapter. Many optimised features introduced in Chapter 3 had not been implemented yet. The most significant was not using the optimised timing and triggering of the data acquisition, which resulted in significantly longer per-pixel dwell times and increased image noise due to SLM flickering. Due to sample damage, the longer dwell times also limited the maximal excitation laser powers. In addition, not using any SLM dispersion correction decreased the wavelength tuning range, reducing the power ratio of the focused points during the demonstration of the chemical contrast, further reducing the intensity of the detected CARS signal. Nevertheless, despite the potentially suboptimal performance of the fibre imaging system during the experiments, the results presented in this chapter were conclusive.

CARS imaging of 2 µm and 7 µm polystytene (PS) and 2.5 µm polymethyl methacrylate (PMMA) beads on a glass slide was demonstrated. The signal generated in the sample was collected in transmission as well as through the same fibre used for the delivery of the excitation beam, i.e., epi-detection. The epi-detection was possible despite the CARS signal being generated predominantly in the forward direction and thus relying on scattering (for thick layers of beads) or the reflection on the air to glass interface (for a single layer of beads). These results show that the fibre endoscope could be used for endoscopic applications inside the tissue. This potentially paves the way for the implementation of other imaging techniques with similar emission patterns like stimulated Raman spectroscopy (SRS) or third-harmonic generation (THG), where epi-detection is also reliant on back-scattering from the tissue [159].

Imaging with chemical contrast was demonstrated on a mix of PS and PMMA beads. Changing the wavelength of the pump beam allowed different Raman shifts to be targeted. Combining the two images could determine the composition of the mixed sample.

Imaging of 2 µm PS beads was possible using a 1 ms integration time while still having a good signal-to-noise ratio. As expected for CARS [143–145], the integration time was significantly shorter compared to linear Raman imaging, which was implemented through multimode fibres in [61, 62]. The difference in integration time for the implementations through a multimode fibre is three orders of magnitude while still having specificity to distinguish cell components, which makes CARS mode suitable for clinical applications. The integration time was limited by the flickering of the SLM and by the excitation power being limited by sample damage due to the long per-pixel dwell times. The effect of the SLM flickering could be minimised by synchronising the acquisition with the SLM, which would also allow shorter per-pixel dwell times (as discussed in Chapter 3), limiting the exposure of the sample. Moreover, the sample damage could be limited by beam-blanking during the hologram formation.

Nevertheless, the demonstrated CARS implementation was still slow compared to other endoscopic CARS implementations, where a single image typically takes a few seconds at maximum [160, 161], compared to several minutes (depending on the size

of the field of view and resolution) demonstrated here. The limiting factor in speed was the refresh frequency of the liquid crystal spatial light modulator, set to about 55 Hz (pixels per second). A more efficient implementation of the timing, already discussed in Chapter 3, could increase the speed to 170 Hz for the same integration time. Additional improvement could be gained by overdriving the SLM [162]. Nonetheless, a liquid crystal SLM would still be slower compared to digital micromirror devices (DMDs) used for linear imaging through multimode fibres, typically operating at a refresh frequency of about 23 kHz [41]. Currently available DMDs are binary amplitude modulators, thus inherently inefficient. Additionally, they suffer from significantly higher dispersion than SLMs, due to using tilted micromirrors, which would have to be compensated for [128]. These attributes make them hard to use for non-linear imaging, where high excitation powers and pulsed laser sources are required. In future, however, phase-modulating micromirror devices (PLMs) [163–167] could provide efficiency approaching one of the liquid-crystal SLMs, while maintaining fast refresh rates.

The diameter of the fibre probe (Prysmian DrakaElite, about 30 mm long) was 125 µm with a 50 µm diameter field of view (FoV) and numerical aperture of 0.3. The dimensions of the probes were thus significantly smaller compared to other endoscopic CARS approaches, where the probes typically have a diameter of a few millimetres. For instance, in [160], the diameter of the probe was 2.2 mm (with a 230 µm field of view), in [161] it was 2.4 mm (180 µm FoV), and in [168] 8 mm (about 500 µm FoV). The small dimensions make the multimode fibre probes significantly less invasive than any other CARS endoscope reported.

The endoscope presented here, however, did not have a similar spatial resolution to the other discussed endoscopes due to the relatively low numerical aperture of the fibre used. Nevertheless, the numerical aperture is not unreasonably small, as shown in [169]. The resolution of a multimode fibre endoscope depends only on the numerical aperture of the fibre and is thus independent of the fibre diameter. Consequently, if higher numerical aperture graded-index fibres become available in the future (providing that such fibres have sufficient bandwidth), the resolution could be increased without increasing the endoscope size. Thus the amount of damage this endoscope would have for imaging inside the tissue. A thinner cladding fibre could also increase the field of view size to probe diameter ratio. The cladding of a multimode fibre can be very thin. Consequently, unlike the other endoscopic probes discussed above, the field of view size of a multimode fibre (when imaging close to the output facet) could be the same as its diameter. Alternatively, since commercially available fibres typically have a much thicker cladding, the distal end of the fibre could be polished into a cone-like shape as shown in [41, 65] and in Chapter 5 to minimise the impact on the tissue.

The speckled background around the focused points, typical for focusing light through a multimode fibre, did not affect the images due to the non-linearity of the process and the fact that the speckle patterns for the pump and Stokes beams were uncorrelated. These factors caused the amount of signal generated anywhere else but the focused point to be undetectable. This is in contrast to linear imaging (e.g., one-photon fluorescence or linear Raman imaging), where the speckled background decreases the contrast in the images (in the case of one-photon fluorescence imaging) or could cause the measured spectra to be smeared across the field of view (in the case of linear Raman imaging). Another source for reducing the contrast could be any signal generated in the fibre. Due to the self-imaging property of graded-index fibres, the focus created at the distal end of the fibre is being re-imaged multiple times inside the fibre, potentially exciting four-wave mixing

in the glass fibre. Nevertheless, during the experiments, the intensity measured with no sample in the system (or a sample far from the imaging plane) was more than an order of magnitude lower than the signal generated in the sample. No detrimental level of the unwanted background was thus observed.

To conclude, this study demonstrates that it is feasible to perform label-free CARS imaging with chemical contrast through a single multimode fibre of structures as small as 2 µm, with epi-detection and integration times of 1 ms.

The results presented in this chapter were published in [69], which is the first demonstration of label-free non-linear imaging with chemical contrast through a multimode fibre endoscope.

5. Non-linear imaging using a femtosecond laser

In Chapter 4, coherent anti-Stokes Raman scattering (CARS) imaging through a single multimode fibre with a chemical contrast was demonstrated. The chemical contrast was achieved by using a narrowband picosecond laser system and tuning the wavelength of one of the two excitation beams, which resulted in different molecules being excited. CARS imaging can also be performed using femtosecond lasers, which are more commonly available in bio-imaging labs and more suitable for other imaging modalities like two-photon excitation fluorescence (TPEF) or second-harmonic generation (SHG) imaging.

When such a broadband laser source is used, the spectral resolution is reduced due to the large instantaneous bandwidth of the source. Assuming both the Stokes and pump pulses are near transform-limited in the sample plane (which would be optimal for, for example, TPEF or SHG), many different Raman shifts get excited during the duration of the pulse, as shown in Figure 5.1. To get a sufficient spectral resolution with a broadband laser source, spectral focusing is commonly implemented [170–177]. In essence, both the pump and the Stokes beams are stretched to decrease the instantaneous bandwidth of the source. The spectral resolution of CARS microscopy (in terms of wavenumbers $\tilde{\nu}$) is given by

$$\Delta\tilde{\nu} = \frac{2\ln 2}{\pi c}\sqrt{2\left(\tau_{\mathrm{p}}^{-2} + \tau_{\mathrm{S}}^{-2}\right)} \doteq 20.8\,\mathrm{ps{\cdot}cm^{-1}}\sqrt{\tau_{\mathrm{p}}^{-2} + \tau_{\mathrm{S}}^{-2}}\,, \tag{5.1}$$

where c is the speed of light and τ_{p} and τ_{S} are the pulse widths for the pump and Stokes beams, respectively [177]. This equation is valid either for transform-limited or equally chirped pulses (that is, the same amount of group delay dispersion is applied to both the pump and Stokes pulse). Increasing the pulse lengths thus decreases $\Delta\tilde{\nu}$, increasing the spectral resolution. The increase of the pulse length is done by applying group delay dispersion (GDD), typically using glass blocks. The GDD stretches the pulse width τ_0 of the transform-limited pulse to

$$\tau = \tau_0\sqrt{1 + \left(\frac{4\ln 2 \cdot \mathrm{GDD}}{\tau_0^2}\right)^2}\,. \tag{5.2}$$

Applying different amounts of GDD to both beams or applying third order dispersion results in a decrease in the spectral resolution. When the spectral focusing is implemented, different Raman shifts (within the spectral width of the pulses) then can be targetted by changing the relative time delay of the pump and Stokes pulses (as shown in Figure 5.1). The time delay change $\mathrm{d}t$ can be converted into wavenumber change $\mathrm{d}\tilde{\nu}$ using

$$\mathrm{d}\tilde{\nu} = \frac{\mathrm{d}t}{2\pi c \cdot \mathrm{GDD}} \doteq 5.3\,\mathrm{ps{\cdot}cm^{-1}}\frac{\mathrm{d}t}{\mathrm{GDD}}\,. \tag{5.3}$$

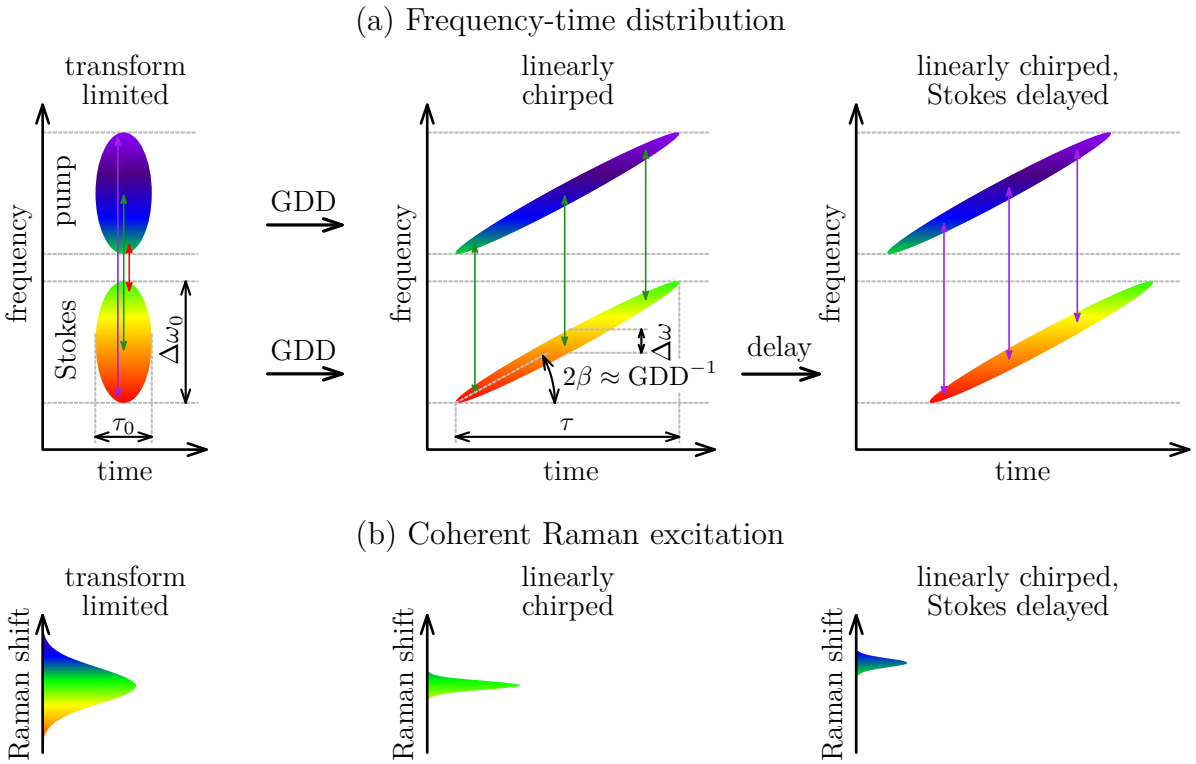

Figure 5.1: Explanation of spectral focusing for coherent anti-Stokes Raman scattering imaging. (a) Frequency-time distribution of the pump and Stokes pulses for a transform-limited pulse and a linearly chirped pulse (spectral focusing). Applying the group delay dispersion (GDD) to the transform-limited pulse increases the pulse length τ and decreases the instantaneous bandwidth $\Delta\omega$. The chirp parameter β describes the linear slope of the frequency-time distribution for the chirped pulse. (b) Illustration of the Raman shifts being excited during the whole duration of the pulse. Chirping the pulse decreases the spectral width, increasing spectral resolution. Adjusting the time overlap then allows targeting different Raman shifts.

The use of pulsed sources allows the implementation of other non-linear imaging techniques such as TPEF [178] or SHG [179] (Figure 5.2). In essence, the implementation of CARS imaging through the multimode fibre automatically allows for imaging using these two techniques by just changing the filter on the detector.

Compared to linear fluorescence imaging, TPEF offers inherent sectioning resulting from the non-linearity of the process. This effect is used in laser scanning microscopes to suppress out-of-focus fluorescence. In a multimode fibre endoscope, the non-linearity also suppresses signal generation in the speckled background around the focused point. In essence, achieving a high power ratio of the focused point at the distal end of the fibre is thus not nearly as critical as for linear imaging. Another key advantage over linear imaging is the increased penetration depth due to lower scattering at infrared wavelengths. This property is, however, perhaps not as important when imaging through a multimode fibre endoscope, as the imaging is typically performed close to the facet. In addition, the photobleaching is lower [180].

TPEF imaging through a multimode fibre has been demonstrated in [53]. A femtosecond laser and a graded-index fibre were used. However, the achieved power ratio was only 28 % due to using a long fibre and not controlling the input polarisation, similarly do a demonstration in [52]. Two-photon imaging in shown [181] used a combination

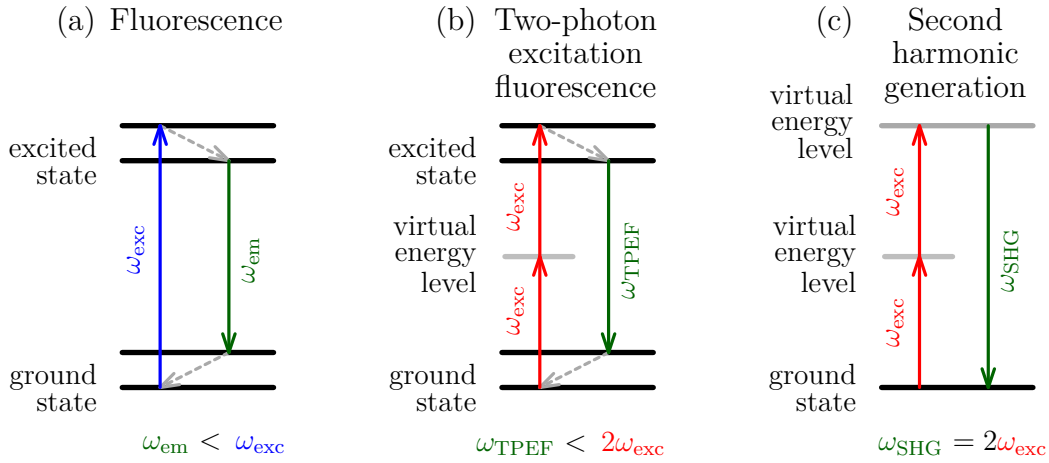

Figure 5.2: Energy diagrams for (a) fluorescence, (b) two-photon excitation fluorescence (TPEF) and (c) second-harmonic generation (SHG)

of a step-index fibre and a femtosecond laser, resulting in a much longer focus than would be expected for the numerical aperture and, thus, significantly limited sectioning. Consequently, employing the results presented in Chapter 3, a more optimal endoscopic system should be possible.

In this chapter, an implementation of coherent anti-Stokes Raman scattering (CARS) and two-photon excitation fluorescence (TPEF) through a single multimode fibre and using a femtosecond laser as the excitation source is presented. In addition, the endoscopic system shown here can perform polarisation-resolved second-harmonic generation (SHG) imaging. The main focus of this chapter is the suppression of a strong background signal during CARS imaging, which is generated in the fibre probe due to the self-imaging property of graded-index fibres. A composite probe, which significantly reduces the background, is proposed and characterised in terms of its focusing performance and dispersion. The probe is then used to demonstrate multimodal CARS and TPEF imaging of fixed mouse tissue.

5.1. Optical setup

A simplified drawing of the setup for non-linear imaging through a multimode fibre using a femtosecond laser is shown in Figure 5.3. The setup was based on the system presented in Chapter 4 with implementing some features introduced in Chapter 3. Only the differences between the systems are discussed here.

The femtosecond laser (Coherent Chameleon Discovery) was the excitation source. The parameters of the laser were described in Section 2.1. Here, both output beams were used. The fixed beam at 1040 nm was used as CARS Stokes beam and could also be used as the excitation beam for SHG imaging. The tunable beam was used as CARS pump beam and the excitation beam for TPEF imaging.

The power and polarisation of the fixed beam were controlled using a pair of zero-order half-wave plates (HWP1, HWP2; Thorlabs WPHSM05-1053) and a Glan-laser calcite polariser (GT1; Thorlabs GL10-B). For the tunable beam, achromatic half-wave plates (HWP3, HWP4; Thorlabs AHWP05M-980) and a Glan-Taylor calcite polariser (GT2; Thorlabs GT10-B) were used.

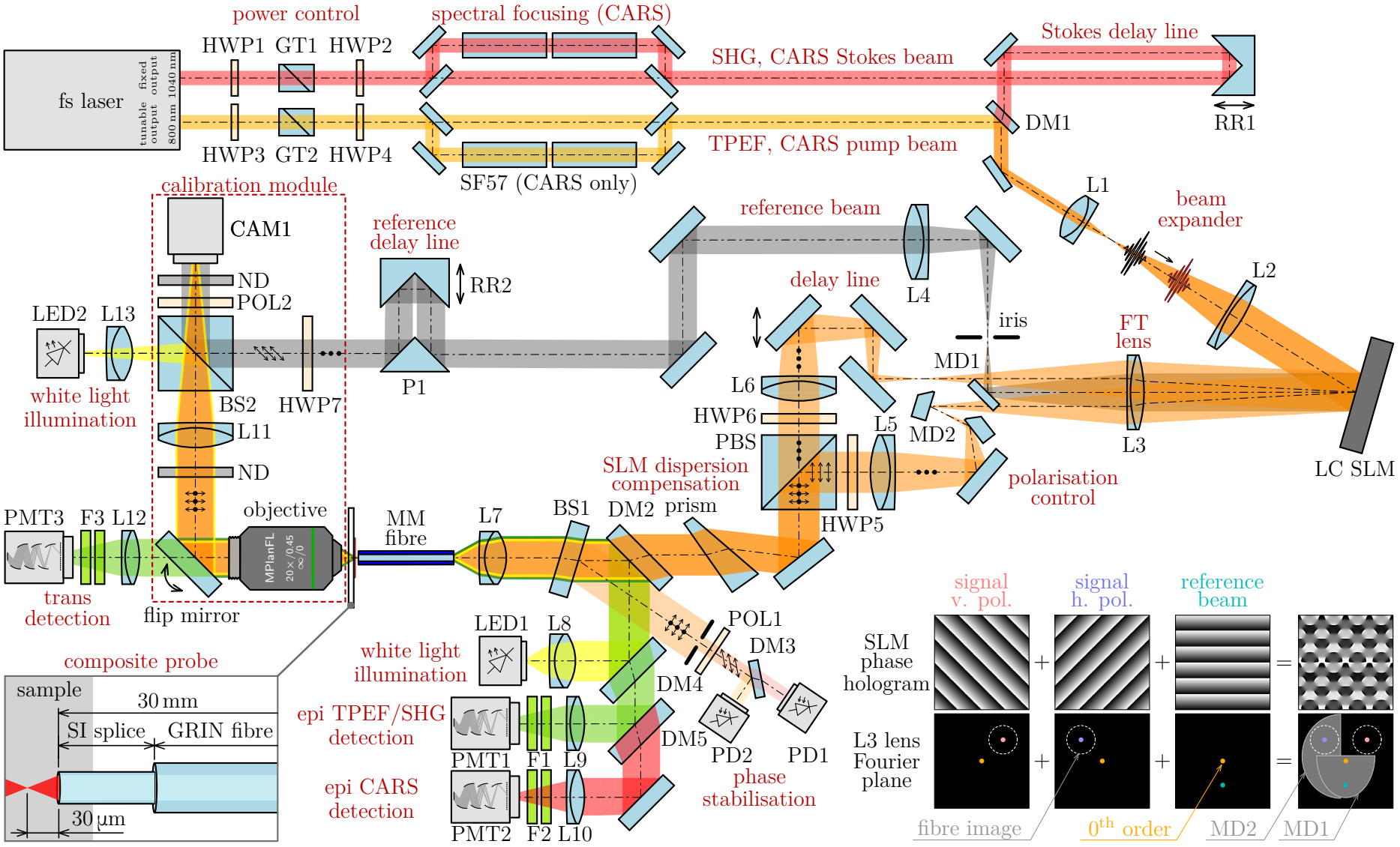

Figure 5.3: Simplified drawing of the setup for non-linear imaging through a multimode fibre using a femtosecond laser. BS – non-polarising beamsplitter, CAM – camera, DM – dichroic mirror, F – filter, GT – Glan-Taylor polariser, HWP – half-wave plate, LC SLM – liquid crystal spatial light modulator, L – lens, MD – D-shape mirror, ND – natural density filter, PD – photodiode, P – knife-edge right-angle prism mirror, PMT – photomultiplier tube, POL – polariser, PSB – polarising beamsplitter cube, RR – hollow roof prism mirror, SF57 – glass blocks. The insets show beams in the focal plane of lens L3 and the respective holograms and the composite probe.

For CARS imaging, glass blocks made of SF57 glass were added to both beams to implement spectral focusing. Two 110 mm long blocks (with an antireflection coating) were inserted in both beams, adding 49000 fs^2 of GDD at 800 nm (used as a pump beam) and 33000 fs^2 at 1040 nm (used as a Stokes beam) [134]. The rest of the optics added about 8000 fs^2 at 800 nm and 12000 fs^2 at 1040 nm (these values were measured using a home-built SEA TADPOLE system [182–185]). A 30 mm long fibre added about 1500 fs^2. By setting the pre-compensator built-in the tunable output of the laser to $-12000\,fs^2$, both beams were equally stretched by 46500 fs^2 of GDD. According to Equation (5.2), the pulse lengths in the sample plane thus were about 1300 fs and 930 fs for the pump and Stokes beams, respectively.

Both beams were combined on a dichroic mirror (DM1; Thorlabs DMLP1000) with an adjustable time delay of the pump beam (using a hollow roof prism mirror RR1; Thorlabs HRS1015-P01, placed on a motorised stage; Thorlabs PT1/M-Z8). The combined beam was expanded to fill the active area of the liquid crystal spatial light modulator. Identically to the system in Chapter 4, the SLM generated two signal beams (one for each input polarisation) and the reference beam.

A wedge prism (Edmund Optics 47-624) was used to compensate for the dispersion of the SLM, as discussed in Section 3.1, which necessitated adding an extra mirror into the beam for one of the two polarisations.

An extra $4f$ system was placed between BS1 and L7, which is, for simplicity, not shown in Figure 5.3. The only purpose of these two lenses was to relay the beam with unity magnification to extend the optical path. The relay was necessary to mount the multimode fibre vertically, which is more suitable for tissue imaging, as the tissue is typically submerged in a liquid. To not affect the stability of the system, most optical components were still mounted directly on the horizontal breadboard and placed on the optical table. Only the multimode fibre, lens L7, the objective, two relay lenses and four mirrors not shown in the drawing were placed on a separate vertical breadboard. The vertical breadboard was attached to the horizontal one using two large brackets.

Compared to the previous systems, the objective that focused light into the fibre was replaced with an achromatic lens (Thorlabs AC080-010-B). This lens increased the efficiency of the system. While the transmission of the objective originally used (Olympus MPlanFL N 20×) was about 87 % at 800 nm and about 48 % at 1040 nm, it had a very low ($< 10\,\%$) transmission between 910 nm and 990 nm. Thus, it would not be suitable for exciting eGFP, which has a maximum two-photon absorption at around 920 nm [186]. In comparison, the transmission of the lens was $> 95\,\%$ over the range of 760 nm–1040 nm. Since this lens was at the proximal end of the fibre, the increased optical aberrations had no noticeable effect on the aberrations of the focused point at the distal end of the fibre.

The distal end of the fibre was imaged onto the camera using an objective and an achromatic lens. Calibrating the probes with the distal end polished in a sharp tip (Figure 5.7c) for tissue imaging required calibrating in water (or another medium with a similar refractive index to the sample). Thus, a cover glass was placed between the fibre and the objective (Olympus Plan N 20×/0.40NA, corrected for the cover glass) and a drop of water was placed on top. The same procedure was used for flat probes and tissue imaging to minimise aberrations [121]. For imaging beads on a glass slide, the objective was calibrated in the air (using Olympus MPlanFL N 20×/0.45NA objective with no cover glass).

The sample was mounted on a three-axis stage build of two Thorlabs XR25P/M stages equipped with Thorlabs Z825B motorised actuators for lateral movement of the sample

and OptoSigma TAMM100-50C stage for focusing. All three axes were thus motorised. The OptoSigma stage was selected for its low backlash, essential for reliable focusing on flat samples and precise insertion of the fibre in the tissue.

For epi-detection, the signals generated in the sample were collected through the fibre and reflected off a long-pass dichroic mirror (DM2; Thorlabs M254C45), passed through another long-pass dichroic mirror (DM4; Thorlabs DMLP505) and then split by the third long-pass dichroic mirror (Thorlabs DMLP605) into CARS and TPEF/SHG channels. The signals were then filtered using a short-pass filter (Thorlabs FESH0700) and a band-pass filter (Thorlabs FBH650-40 for CARS, Semrock BrightLine 525/39 for TPEF, Thorlabs FBH520-10 for SHG) and focused on two photomultiplier tubes (PMT1, PMT2; Hamamatsu H10723-20). This configuration allowed simultaneous collection of CARS and TPEF or CARS and SHG signals. For transmission imaging, after removing the flip mirror in the calibration module, the signal was filtered using the same types of short-pass and band-pass filters (depending on the imaging modality) and focused on another photomultiplier tube (PMT3; Hamamatsu H10723-20).

The time overlap of the pump and Stokes was set using sum-frequency generation on a BBO crystal, as shown previously in Figure 4.4. A custom module with a focusing lens, the BBO crystal and a short pass filter was built for this purpose. The module included a colour camera (Basler ace acA640-750uc) to monitor the intensity of all three wavelengths generated in the crystal (second-harmonic generation of the pump beam, second-harmonic generation of the Stokes beam and sum-frequency generation of both beams), spatially separated on the camera. The position with the maximal intensity of the sum-frequency generation was found by adjusting the length of the delay line placed in the Stokes beam. Initially, this was performed before the SLM, where the beams had high power. Afterwards, the BBO crystal was mounted in place of the multimode fibre and the length of the delay line was re-adjusted.

To allow control over the polarisation of the focused points (discussed bellow in Section 5.4), an achromatic half-wave plate (HWP7; Thorlabs AHWP05M-980) was used to rotate the polarisation of the reference beam by 45°. A polariser (POL2; Thorlabs LPVIS100-MP2) was then placed in front of the camera in the calibration module to allow only horizontal linear polarisation or only vertical linear polarisation (depending on the angle of the polariser) to the camera.

Two cameras were mounted on two sides of the fibre probe to navigate over the samples (Figure 5.4). Both cameras were manually focused on the tip of the fibre. For navigating over the surface of the sample, a modified Logitech C270 webcam was used. A more detailed image of the sample was taken using a USB pen microscope. The sample could be illuminated by a blue LED through the fibre (LED1; Thorlabs M470F4), white LED in the calibration module (LED2, CREE XM-L2) or a custom-built ring of white LEDs attached to the fibre mount. The combination of both cameras then allowed for targeting structures on the surface of the sample and judging the distance from the surface.

(a) Logitech webcam (beads)

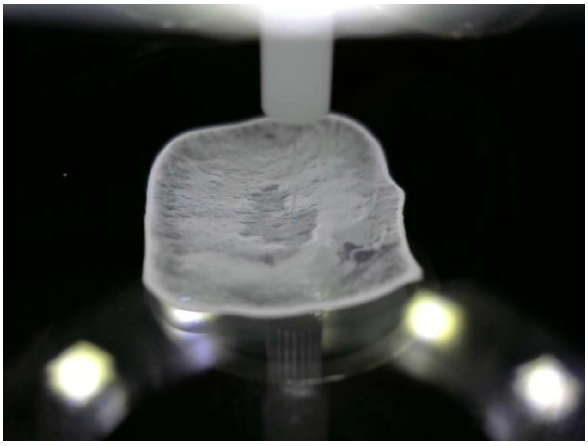

(b) USB pen microscope (beads)

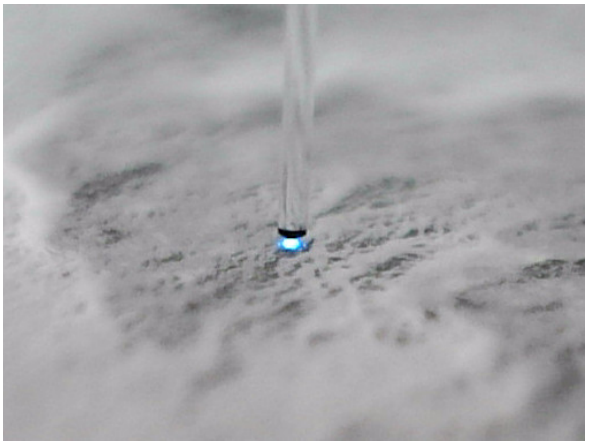

(c) Logitech webcam (brain)

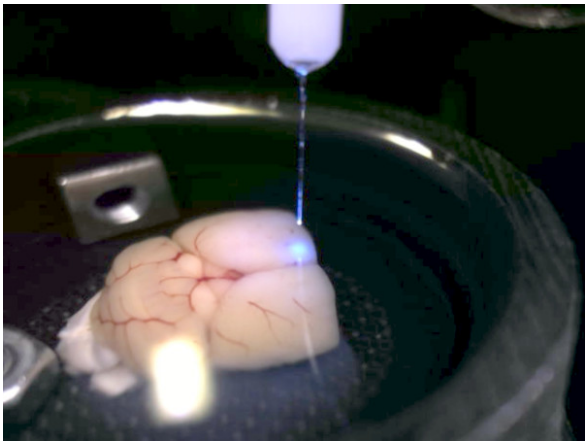

(d) USB pen microscope (brain)

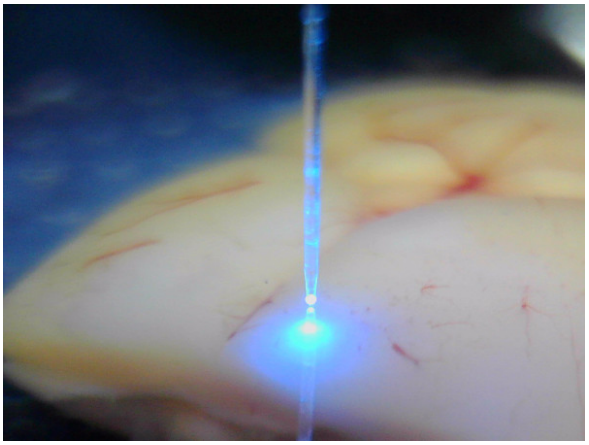

Figure 5.4: Images of two different samples (beads on a glass slide and a mouse brain) taken with two cameras integrated into the fibre imaging system. The Logitech webcam allowed rough navigation over the surface. Subsequently, the exact position and distance of the fibre from the surface could be judged on the images from the USB pen microscope, which had a higher magnification. The blue light comes from LED1 in Figure 5.3. The bright rectangles in (a) are a reflection of the ring of LEDs mounted above the sample. In (c) and (d), the fibre had a conical termination (same as in Figure 5.7b).

5.2. Fibre probe preparation

The probes consisting of a grade-index fibre only were prepared as described in Section 2.2. To prepare a composite spliced probe (Figure 5.13), the step-index fibre (CeramOptec Optran Ultra WFGE) and the graded-index fibre (Prysmian DrakaElite, CREOL F3 or YOFC GI2017-C) were first stripped off the acrylate coating. The GRIN fibre was cleaved to a flat facet at one end (which became the distal end of the probe) using Fujikura CT-101 cleaver. The step-index fibre was tapered to have the same core diameter as the graded-index fibre using 3SAE Large Diameter Splicing System LDS 2.5. Afterwards, the splicing system was used to cleave the taper on one end, splice it to the distal end of the GRIN fibre and cleave the other end, forming a short step-index splice with a precise length. As the last step, the proximal end of the graded-index fibre was cleaved to a flat facet using Fujikura CT-101 cleaver. The probe was then glued in two ceramic ferrules, as described in Section 2.2.

Many commercial multimode fibres used in this work have a high cladding-to-core diameter ratio. Since the size of the field of view is determined by the core diameter, the overall size of the probe was, in such cases, unnecessarily large, causing more significant damage to the tissue being imaged and making it harder to penetrate the tissue. Most of the cladding at the distal end of the fibre could be polished off to mitigate this issue, forming a conical distal end (see Figure 5.7b) [41, 65].

A custom polishing system was built to make custom polished terminations of the fibre probes (Figure 5.5). The ceramic ferrule with the fibre glued inside was clamped in a small chuck (PROXXON 28941). A NEMA 17 stepper motor could rotate the fibre along its axis. The repeatability of the rotation was ensured by using an inductive endstop. The fibre mount was magnetically attached to the rotor, allowing a quick inspection of the polished surface under a microscope.

The polishing was performed using three different polishing papers (Figure 5.6). The fibre was quickly polished to the desired shape in the first step using a 6 µm grit diamond polishing sheet (Thorlabs LF6D). Afterwards, the roughness of the surface was decreased using a 1 µm grit diamond polishing sheet (Thorlabs LF1D) and finally a 0.02 µm grit silicon dioxide polishing sheet (Thorlabs LFCF). The papers were attached to a replaceable aluminium disc using double-sided tape. The aluminium disc was rotated at a maximum of 1000 rpm using another NEMA 17 stepper motor. Both motors were controlled using custom-built electronics. The surface of the polishing disc was kept wet and clean during the process by rubbing against a lint-free wipe soaked in a solution of dishwashing liquid in water (which could be added during the polishing using a syringe). The polishing process was monitored using a camera (USB pen microscope).

Figure 5.7 shows different terminations of multimode fibre imaging probes. Figure 5.7a shows an unmodified distal end of the CREOL F3 fibre. Since this fibre has a large cladding-to-core ratio, it was feasible to polish off part of the cladding (5.7b) to form a conical probe to minimise the damage to the tissue being imaged. The core was not touched. Thus, the optical properties of the probe were not affected. Since no light propagated through the polished surface, achieving a surface with optical quality was unnecessary. The next step was also to polish the core (5.7c). Here, the core was polished at approximately 45°, forming a sharp tip. Since the output facet of such a probe was not flat, the probe had to be calibrated inside a medium with a similar refractive index as the tissue (in water, for example). In addition, since the light propagated through one of the polished surfaces, this surface had to be polished to a very low surface roughness.

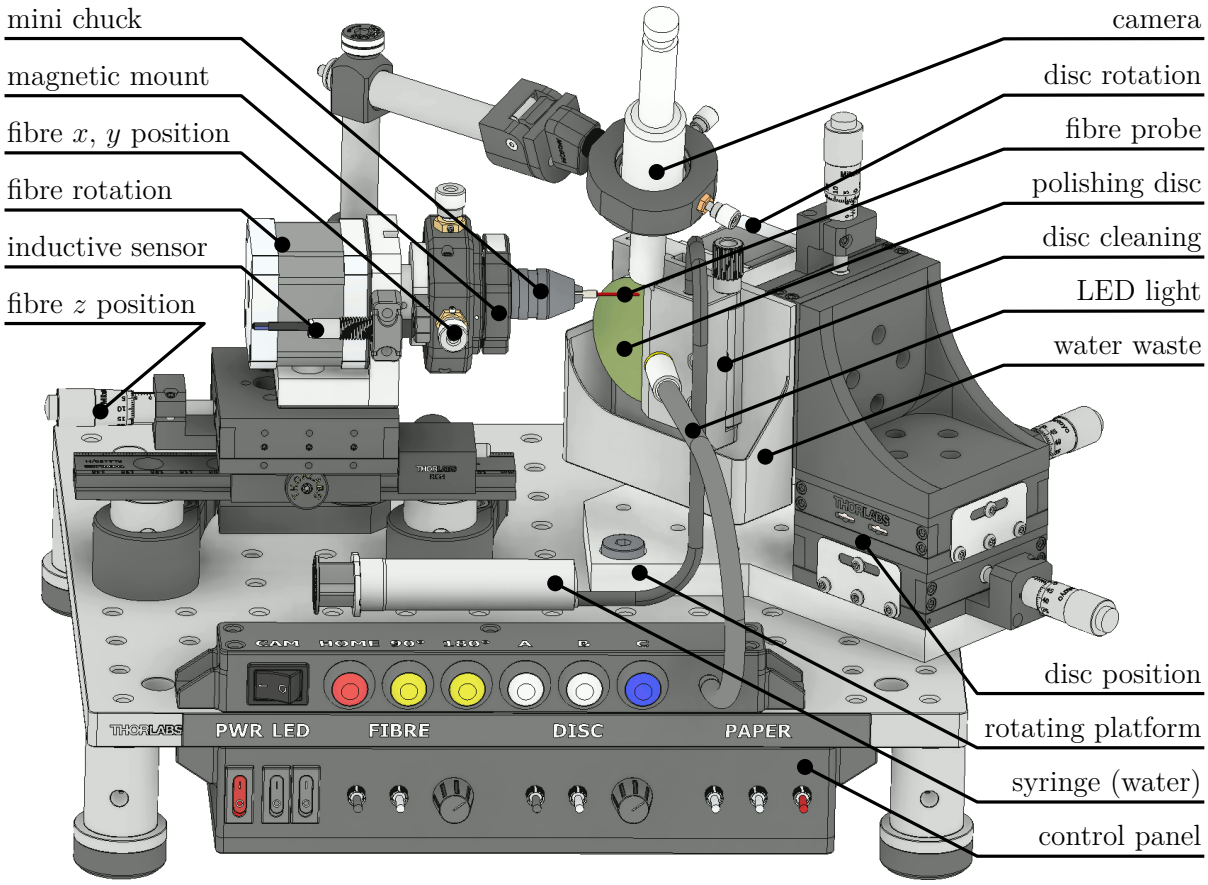

Figure 5.5: Polishing system used for modification of distal ends of fibre probes (see Figure 5.7 for examples). The multimode fibre, which was glued into a ceramic ferrule was attached in a chuck and polished using a rotating disc with polishing paper. The polishing was monitored using a USB pen microscope from the top.

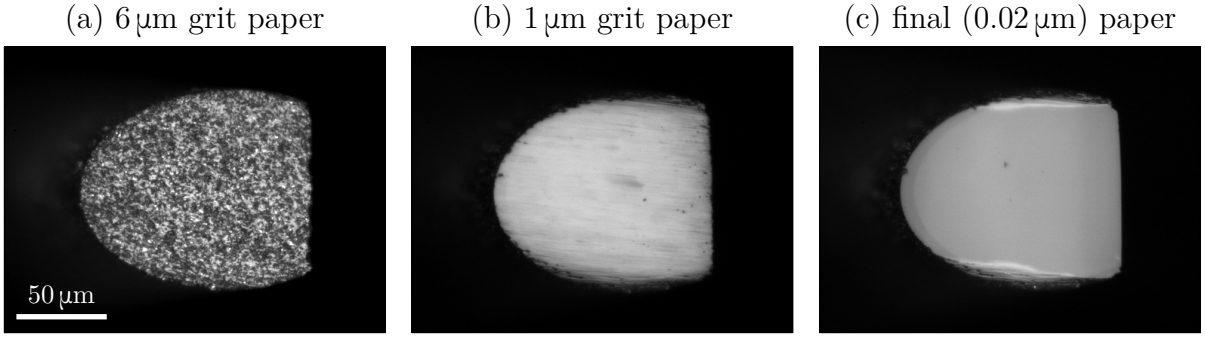

Figure 5.6: Surface of a multimode fibre after polishing using different polishing papers. The surface is the 45° side of a side-view probe (Figure 5.7d) before coating with a reflective layer.

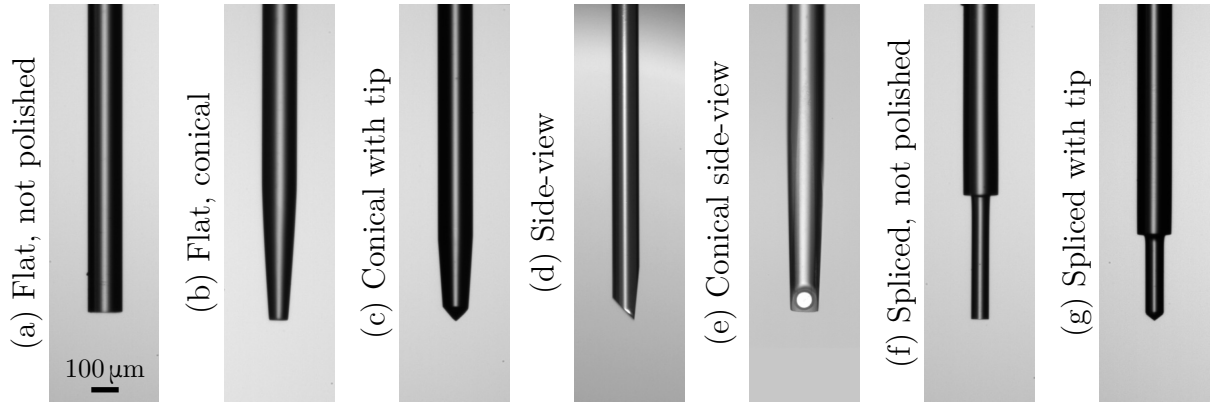

Figure 5.7: Distal ends of different types of fibre probes. (a) Unmodified distal end of a 62.5/125 µm (core/cladding) diameter fibre. (b) The same fibre with the cladding polished into a cone in order to minimise tissue damage and make the insertion into the sample easier. (c) In addition to the cladding, the core was polished into a sharp tip. This shape prevents tissue from sticking to the fibre. (d) Side-view probe [77]. (e) Side-view probe with parts of the cladding polished off (front side of the probe; the bright circle is the light guided in the core and reflected off the 45° facet, i.e., this circle is the field of view of the probe). (f) Unmodified spliced probe. The splice suppresses the non-linear background being generated in the fibre when used for CARS imaging. (g) Spliced probe with the splice being polished into a sharp tip.

This probe type was used for SHG imaging published in [187], where it helped with tissue sticking to the fibre and easier penetration. Another option for terminating fibre imaging probes is the side-view probe (Figure 5.7d) [77]. The side-view probe allows off-optical-axis imaging, similar to the probes in [23, 188–191], where a prism was attached or 3D printed to the end of the probe. Instead of securing a prism, the end of the fibre was polished at 45° and at about 8° on the opposite side. The 45° side was afterwards coated with a metal layer, forming a mirror. The light guided inside the fibre was thus reflected and exited the fibre through the 8° facet. This probe allowed imaging in a plane parallel to the axis of the fibre, which further reduced the damage to the tissue being imaged [43]. For fibres with a high cladding-to-core diameter ratio, parts of the cladding close to the distal end of the probe could be polished off to reduce the impact of the probe (Figure 5.7e).

5.3. Calibration procedure

The calibration of the endoscope was identical to the procedure described in Section 2.5 and Section 4.2.

Since femtosecond laser pulses were used, the length of the reference delay line had to be adjusted precisely to achieve interference of the signal and reference beams on the camera. The adjustment was made by generating a random speckle pattern at the input of the fibre and observing the amplitude of the oscillations on the camera while adjusting the length of the delay line (Figure 5.8). This procedure allowed setting the delay within a few micrometres from the optimal position giving maximal interference contrast.

By employing the optimal timing scheme described in Figure 2.5, whole calibration procedure of the CREOL F3 fibre took about a minute per wavelength and input polarisation, and thus the whole calibration necessary for CARS imaging (i.e., two wavelengths

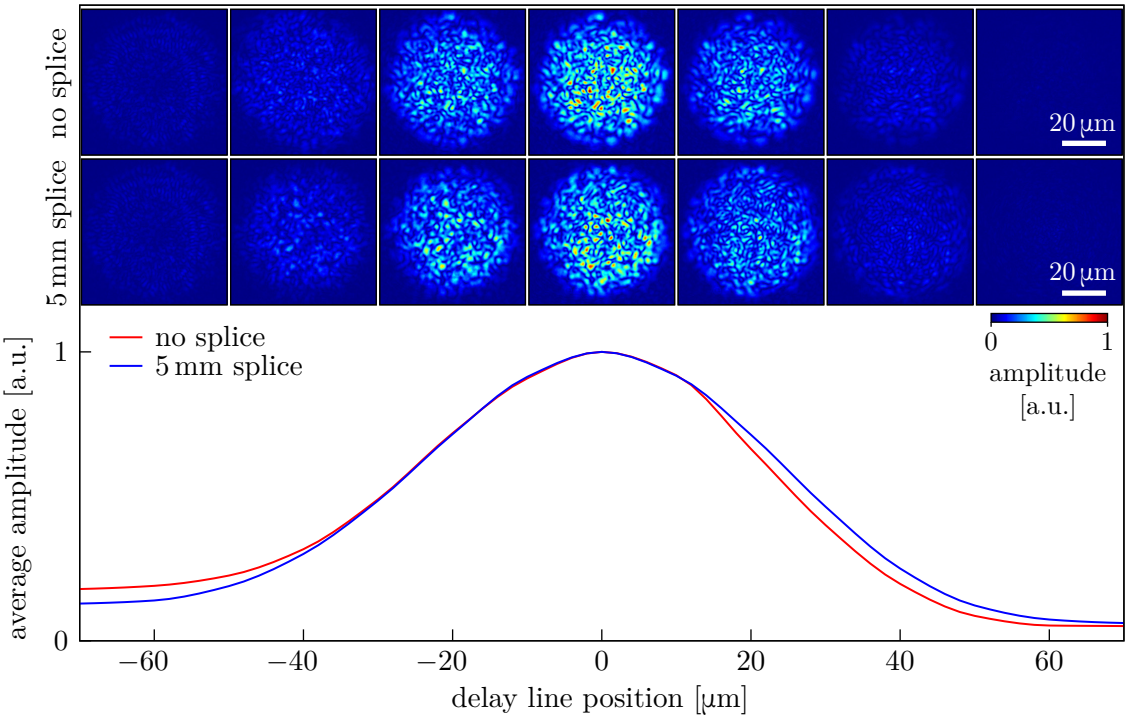

Figure 5.8: The amplitude at the distal end of the fibre measured at different positions of the delay line in the reference beam. The input of the fibre was filled with a random speckle pattern. The amplitude was consequently averaged across the field of view for each position (only a subset of images is displayed here).

and two input polarisations) took less than five minutes. For controlling the polarisation of the focused point (for SHG imaging), the calibration had to be run twice with changing the angle of a polariser (as discussed below in Section 5.4). Therefore, in that case, the whole calibration took less than ten minutes.

5.4. Polarisation control

The non-linear interaction of light with molecules during coherent anti-Stokes Raman scattering imaging or second-harmonic generation imaging results in excitation polarisation dependence of the generated signal. The polarisation sensitivity of CARS can be used, for example, to characterise the orientation of the lipid and water molecules inside the myelin sheath [152, 192, 193]. Similarly, during SHG imaging, the polarisation response allows, for example, for measurement of local collagen fibril orientation [194–197]. Accordingly, implementing the control over the polarisation of the focused point is beneficial for these non-linear imaging techniques and broadens the possible applications for diagnosing pathological states of tissue.

In Section 2.8, the input polarisation control (the control over the polarisation of the beam entering the fibre) was discussed. It was shown that it was necessary for efficient focusing when graded-index fibres were used. This section discusses output polarisation control (the control over the polarisation of the beam exiting the fibre). While the input polarisation control might be a necessary condition for the output polarisation control (especially for step-index fibres), it is not a sufficient condition and further modifications of the system presented in Section 2.1 were necessary.

Several techniques for polarisation control have been implemented in random media [198–200]. These, however, typically rely on strong mode coupling, which is not necessarily present in multimode fibres. In addition, the method presented in [200] requires a source with a bandwidth substantially larger than the bandwidth of the medium. Nevertheless, a polarisation control of the output of the multimode fibre was demonstrated in [201], where the mode coupling was artificially introduced by using a 2 m long fibre coiled to 5 loops and pressed by clamps. However, this study showed no spatial control of the output, making the method unsuitable for imaging.

Control of the polarisation of the focused point at the end of the fibre was demonstrated in [26], where two points with orthogonal polarisation states were generated at the output of the fibre. Generation of an arbitrary polarisation state of the focus was not demonstrated, nor was any imaging application. Here, the same technique was implemented into the endoscope for non-linear imaging.

Two spatially overlapping points with orthogonal polarisation states and with known relative phase difference had to be generated to produce an arbitrary in-plane polarisation state of the focused point at the distal end of the fibre. These two points formed a basis. The basis could be linear (e.g. horizontal and vertical polarisation) or circular (left-handed and right-handed polarisation). By adjusting the relative amplitude and phase of the two points, any in-plane polarisation state could be generated.

In [26], the two orthogonally polarised points were created by, in essence, simultaneously measuring two transmission matrices, one for each output polarisation state. The beam in the calibration module was split using a polarising beam displacer placed in front of the camera. Two images of the fibre were thus created on the camera, one per polarisation. This approach has, however, several limitations. Calcite beam displacers have a wavelength-dependent displacement, therefore, could not be used with a broadband light source like the femtosecond laser used here. A polarising beamsplitter cube could be used instead in conjunction with two cameras [90]. Nonetheless, this method yielded two orthogonally polarised points, but their relative phase was unknown. In addition, the relative phase was not guaranteed to be independent of the position of the point in the sample plane. Due to having two different images of the fibre, the relative position of the two points was also not known with adequate accuracy to overlap them at the distal end of the fibre.

Instead of splitting the beam in the calibration module, a polariser was placed before the camera, allowing only one polarisation state to be calibrated at a time. The calibration procedure thus had to be performed twice in total, with the polariser (POL2 in Figure 2.1) set to 0° and 90°. Thus, two sets of transmission matrices (one for each orientation of the polariser) were obtained to generate vertically and horizontally polarised points. The polarisation of the reference beam was rotated by 45° using a half-wave plate to achieve interference of the signal beam and the reference beam regardless of the orientation of the polariser.

The relative phase of these two points was initially unknown and had to be measured. This situation was similar to the relative phase between the two input polarisation beams as described in Section 2.5. Measuring the relative phase delay was performed by setting the polariser to 45°, displaying both (spatially overlapping) horizontally and vertically polarised points and monitoring the intensity while changing the relative phase difference between the two transmission matrices. When the two points were in phase, the polarisation of the resulting point was linear with 45° angle. The measured intensity behind the polariser was thus maximal. When in the opposite phase, the polarisation was linear

with 135° angle, and the intensity was minimal. Any other phase difference produced an elliptically (or circularly) polarised point. This step also allowed checking the spatial overlap of both points, as both should be focused onto the same camera pixel.

Mounting the polariser directly in front of the camera resulted in working polarisation control at the camera plane. Due to reflection phase changes on the mirrors in the calibration module, the polarisation of the point at the distal end of the fibre was not generally the same as the polarisation of the point on the camera. Figure 5.3 shows only one mirror for simplicity. In reality, three silver mirrors (Thorlabs PF10-03-P01) were placed between the objective and the camera. The additional mirrors were necessary to mount the fibre and, thus, the objective vertically. The issue with reflection phase changes was mitigated by measuring the reflection phase shifts and taking them into account when measuring the relative phase on the camera. The polariser (set to 45°) was once moved directly after the objective in the calibration module, and the relative phase measurement was repeated. The difference between the value measured with the polariser in both positions was the reflection phase change. This value was constant (for a given wavelength). Hence, it was sufficient to measure the phase shift once and use it to correct all the following values measured with the polariser in front of the camera. This procedure resulted in a polarisation control of the focused point at the fibre output.

The relative phase of the two output points for two polarisation states was a constant value for the given calibration, thus, did not have to be stabilised during the imaging. This is in contrast to the relative phase of the two input polarisation beams described in Section 2.5 and is a result of the two output beams having the same optical path.

After the relative phase of the two points was known and their spatial overlap was verified, a point with an arbitrary polarisation could be generated by adjusting the relative amplitude and phase of the two transmission matrices.

The performance of the polarisation control was evaluated in terms of the extinction ratios. The polariser in the calibration module was removed after the calibration, and another polariser of the same type (Thorlabs LPVIS100-MP2) was mounted directly after the objective in the calibration module. The polariser was rotated in 9 steps over a range of 180°, and HDR images of focused points on a line across the field of view were captured for each orientation (Figure 5.9). The intensity of the focused point for each orientation was extracted from the images. A sinusoidal function was then fitted to the data. The maximum and minimum values from the fit were used to calculate the extinction ratio (Figure 5.9b). In addition, after removing the polariser, it was verified that the power ratio and spot size were independent of the polarisation. The calculated extinction ratios in Figure 5.9b were noisy due to the random speckle background around the focused points. Nevertheless, the values were in all cases larger than 100 across the field of view, sufficient for polarization-resolved second-harmonic generation imaging in [187].

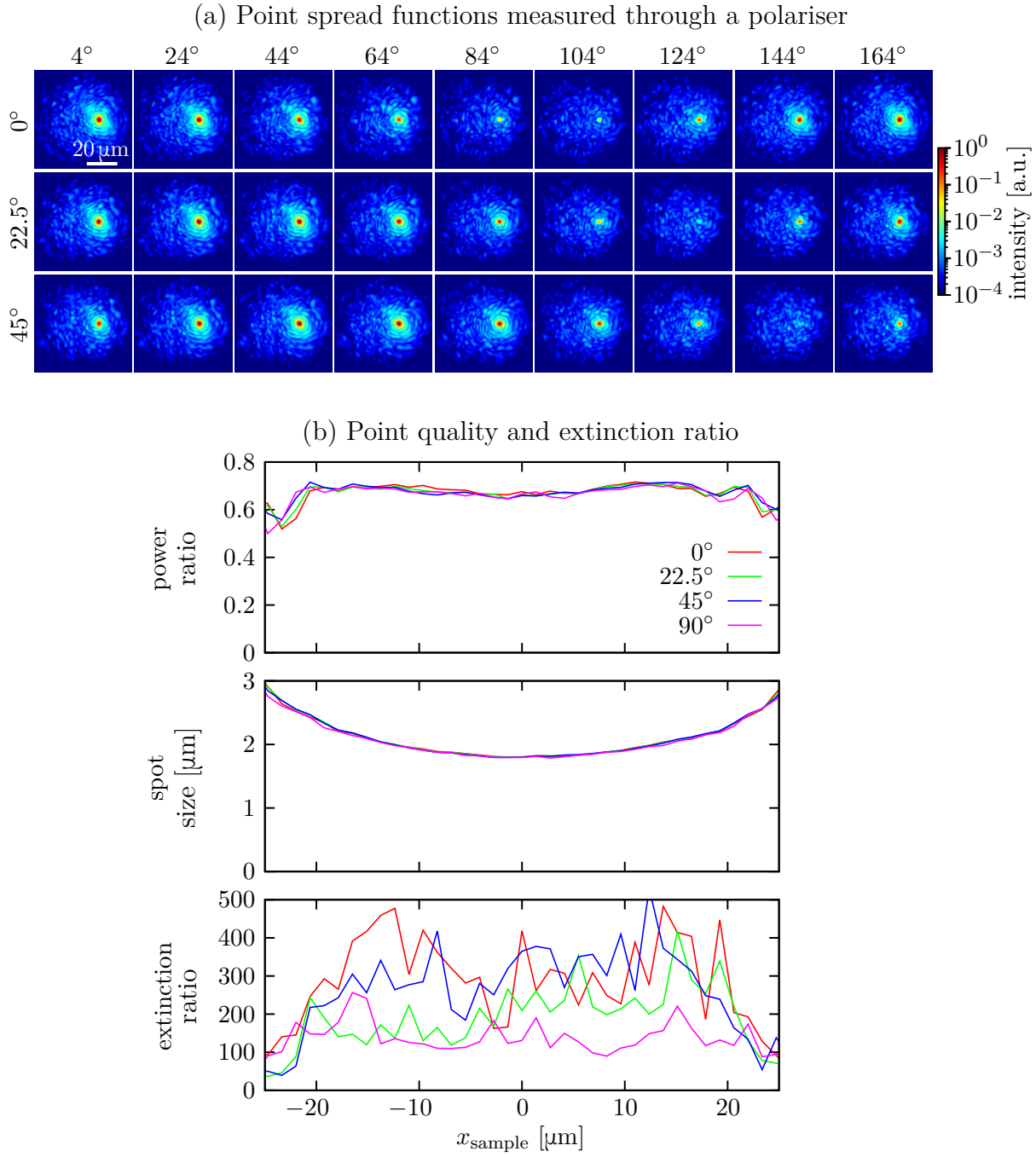

Figure 5.9: Evaluation of the performance of output point polarisation control. (a) Point spread functions (in logarithmic scale) of three focused points with different linear polarisation angles measured through a polariser with nine different orientations of its axis. (b) Power ratio, spot size and extinction ratio (measured using images in (a)) for four points along a line across the field of view with four different linear polarisations angles. The data was measured at 1040 nm using CREOL F3 fibre.

5.5. Background suppression

When fibres are used for delivery of the excitation beams for coherent anti-Stokes Raman scattering imaging, an unwanted background signal can be generated inside the fibre itself due to four-wave mixing (FWM) and other non-linear processes [168, 202–204]. This signal is of the same wavelength as the CARS signal (which is also a FWM process) generated in the sample. Consequently, removing it using spectral filters is impossible when the same fibre delivers the excitation beams and collects the CARS signal. Several solutions have been proposed to mitigate this issue, such as using hollow-core photonic crystal fibres [202, 204]. However, as standard multimode fibres were used in this work, none of these approaches was applicable. In [205, 206], the authors suppress the signal generated inside the delivery fibre by setting the polarisation of the pump and Stokes beams to be orthogonal inside this fibre. This approach, however, requires additional optics (a dual-wavelength wave-plate) being placed after the fibre. Thus, the approach was not applicable when the fibre was inserted directly into the tissue as the last optical element, and no bulky optical elements could be attached to its distal end. A different solution thus had to be used, based on breaking the beam propagating in the multimode fibre into low-intensity speckles.

Due to the self-imaging property of graded-index fibres, the focused point created in the sample plane close to the distal end of the fibre was re-imaged multiple times inside the fibre itself (Figure 5.10a). The fidelity of the foci gradually decreased due to imperfections of the fibre. Nevertheless, multiple high-intensity points were created in the glass fibre close to its distal end. The self-imaging distance ($\approx 400\,\mu m$, depending on the type of the fibre) was similar at both the pump and the Stokes wavelengths, making the points for the pump and the Stokes beams overlap inside the fibre in space. In addition, the self-imaging distance was short enough so that the points for the pump and Stokes beams overlapped time, at least for a few points closest to the distal end of the fibre. In these points, a potentially strong signal was generated by four-wave mixing.

The impact of the background generated in the fibre on CARS imaging is demonstrated in Figure 5.11. Here, $2\,\mu m$ beads on a glass slide were imaged using different fibre probes. The generated CARS signal was measured simultaneously both in transmission and in epi. After the beads were imaged, the sample was removed, and another image was captured to evaluate the intensity of the unwanted background. Ideally, no signal should be generated when no sample is in focus. The measured images, however, showed a strong signal. For the Prysmian fibre, the signal generated in the fibre was, in fact, of a higher intensity than the signal generated in the beads. The background intensity for the CREOL and YOFC fibre was comparable to the non-resonant signal generated in the glass slide.

The visible non-uniformity of the epi-collected signal generated in the beads and in the glass slide (Figure 5.11e) for the CREOL F3 and YOFC fibres with the splice was caused by a minor tilt of the sample. For the forward-generated CARS signal to get coupled into the fibre and be detected on the epi-PMT, it had to be reflected off the glass-air interface of the glass slide. Since the glass slide was about 1 mm thick, even a slight tilt of the glass slide (with respect to the axis of the fibre) caused the reflected light to miss the fibre core.

The two significantly brighter beads in the image with epi-detection and the YOFC fibre with no splice were beads placed on top of other beads (i.e., not all the beads were in the same layer). The scattering in the lower layer of beads significantly increased the epi-CARS signal generated in the upper layer of beads.

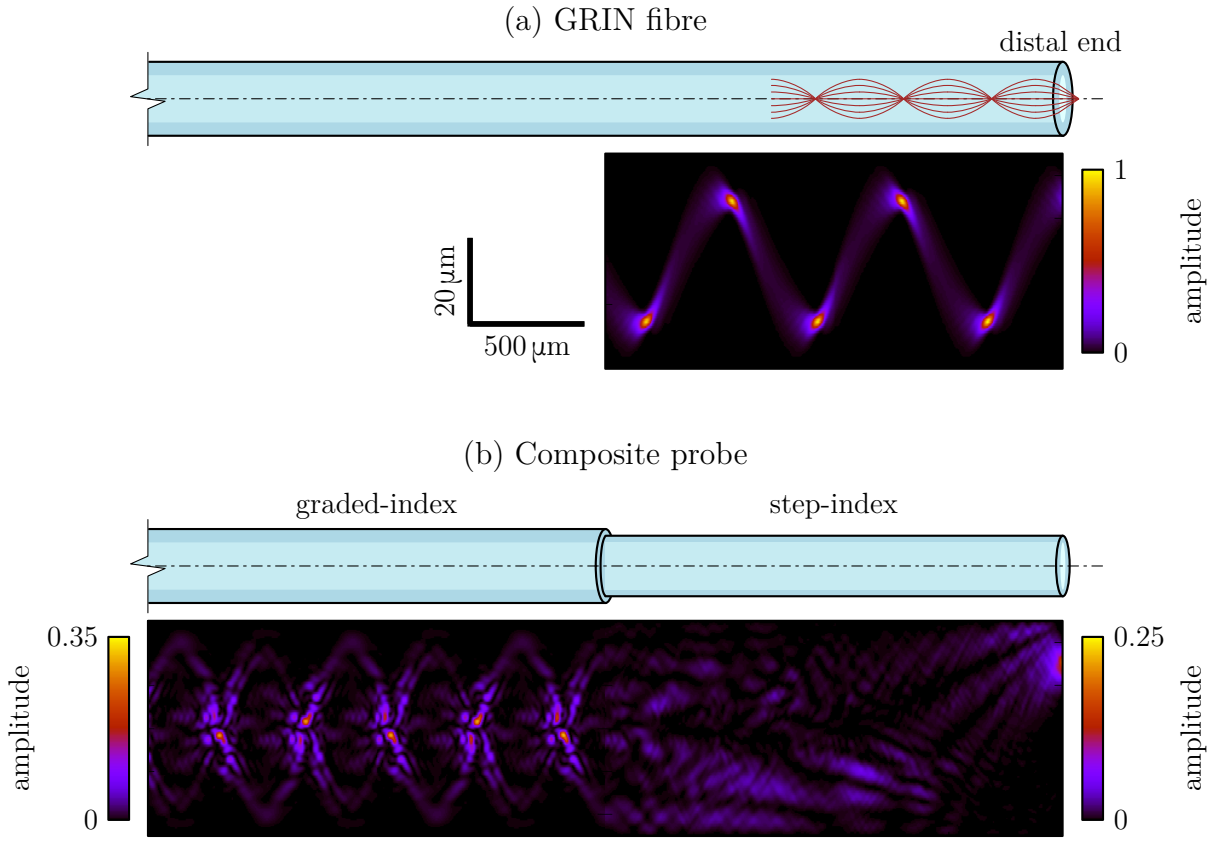

Figure 5.10: Self-imaging in graded-index multimode fibres and suppression of high-intensity points inside the composite probe by splicing a short piece of a step-index fibre to the distal end of the probe. The graphs show the amplitude of the optical field inside the fibre. The data was taken from the supplement to [70].

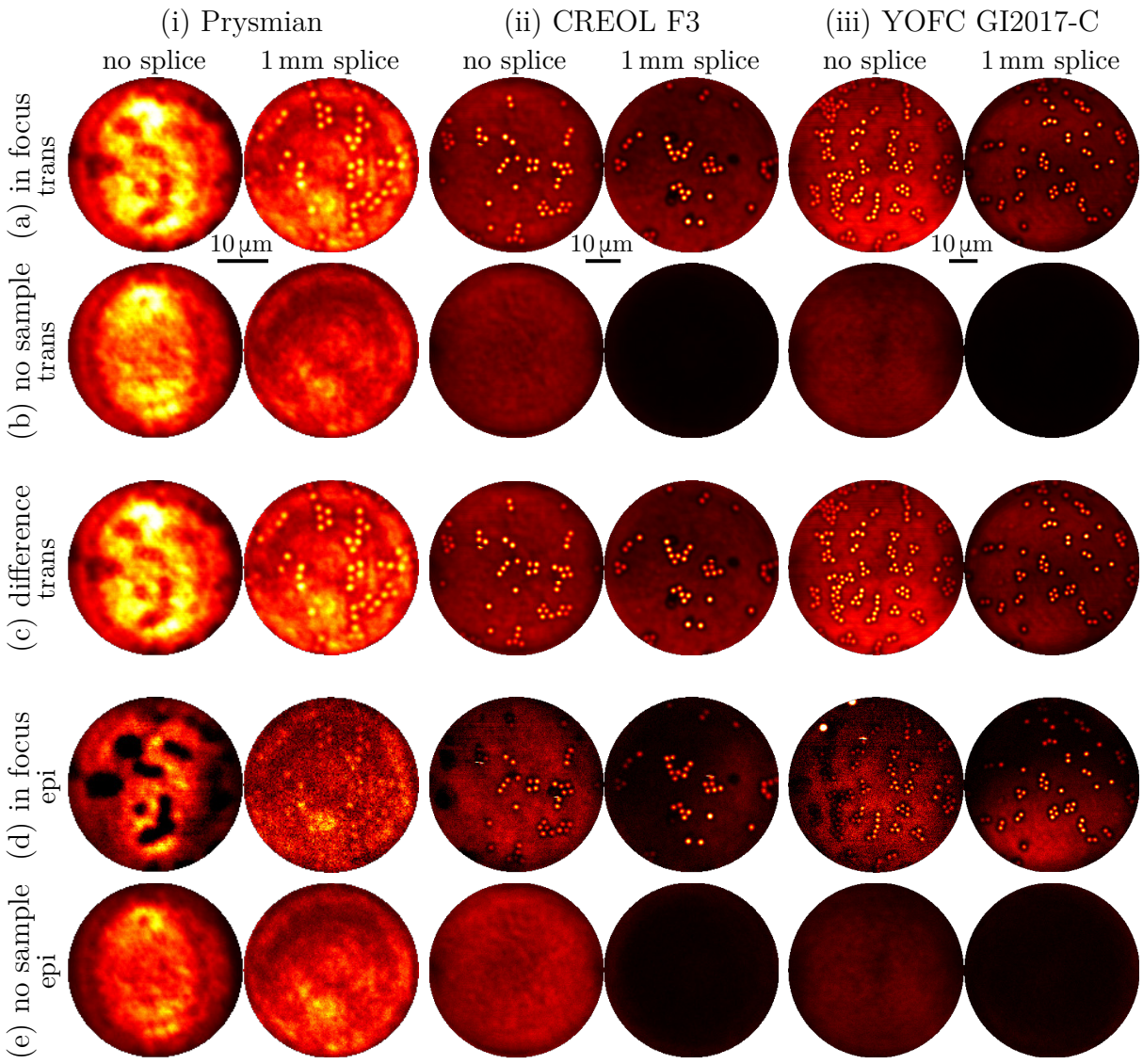

Figure 5.11: Demonstration of the background signal generated in the fibre and the suppression of the background by the addition of the splice to the distal end. For each probe, two images were taken: an image of 2 µm polystyrene beads on a glass slide and an image with no sample in focus. The signal was collected both in transmission and through the fibre (epi-detection).

These two effects illustrate that evaluating the intensity of the signal in epi for quantitative analysis of the background suppression might be problematic. In addition, the background signal generated in the fibre was partially reflected off the distal end facet due to the refractive index contrast between the glass and the air. This reflection further increased the intensity of the background signal detected in epi. During tissue imaging, this reflection would be substantially reduced as the refractive index of the media (about 1.33) would be closer to the refractive index of the fibre. This assumption was verified by immersing the distal end of the fibre in water. The water reduced the intensity of the background detected in epi by about an order of magnitude. Consequently, transmission images were used to evaluate the background suppression, as these were more indicative of the suppression levels when imaging inside a tissue.

The laser power during the imaging was close to the damage threshold of the beads. A strong signal was generated momentarily when a bead was photo-damaged, visible mainly in epi. Afterwards, the bead no longer generated the CARS signal. This effect is visible, for example, in the images captured with the CREOL F3 fibre. A bright horizontal line (coincident with the direction of the scan) was detected in epi. Afterwards, the bead was no longer detectable. The damage could be eliminated by decreasing the laser power, using a coarser scan (larger pixel pitch) or a faster scan (reducing the integration time or the trigger delay). These would, however, reduce the resolution or signal-to-noise ratio of the images. Another option would be beam-blanking during the hologram formation, as discussed in Chapter 4.

To test that the background signal was not generated in the laser and not in another optical component of the endoscopic system, a 700 nm long-pass filter was placed just before the lens (labelled L7 in Figure 5.3) and the signal was measured on the transmission PMT. Since the filter did not fit between the lens L7 and the fibre, it was replaced with an objective to rule out this lens. In all cases, the same intensity of the background was measured. This measurement proved that the signal was generated inside the fibre.

By blocking one beam at a time, it was verified that the background was generated only when both pump and Stokes beams were present. The signal also disappeared when the beams did not overlap in time (then, however, no signal CARS could be generated in the sample). When the foci for the two wavelengths did not spatially overlap in the sample plane in the lateral direction (which was done by generating the points in different pixels for each wavelength) or in the axial direction (done by propagating the transmission matrix for only one of the two wavelengths to a different plane), no signal was generated either. The intensity of the signal was quadratic in the pump power and linear in the Stokes power. These observations conclude that the background signal was generated due to four-wave mixing in the high-intensity points created inside the fibre due to the self-imaging.

The spectral dependence of the signal generated in the fibre was measured by performing CARS imaging with no sample inserted in the system. The system was calibrated for the fixed wavelength laser beam (used as CARS Stokes beam) at 1040 nm and for multiple wavelengths of the tunable beam (used as CARS pump beam), corresponding to Raman shifts from 2807 cm^{-1} to 3107 cm^{-1}. This range covers Raman shifts typically used for bio-imaging (lipids, proteins, DNA [207]) and PS and PMMA (used here for testing). Afterwards, CARS images with no sample were taken (the signal was collected in transmission), and the values were averaged over the field of view. The measured spectra in Figure 5.12 showed a significant difference between different fibres. The difference suggests that the intensity of the background signal was perhaps influenced by the details in

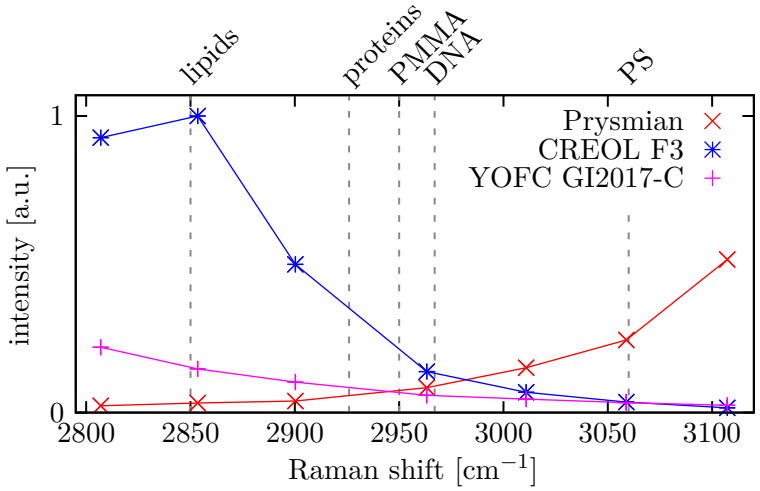

Figure 5.12: Spectral dependence of the signal generated in the fibre for three different graded-index fibres. The input power to the setup was constant for all measurements. The lines are a guide to the eye. The dashed lines show Raman shifts typically used for bio-imaging (lipids, proteins, DNA) and Raman shifts for imaging PS and PMMA (used for imaging beads for testing).

the doping (which were, unfortunately, not available for the commercial fibres). Nevertheless, the signal was generated in all GRIN fibres, as already demonstrated in Figure 5.11. Consequently, a method for suppressing the background was needed regardless of the type of graded-index fibre. For the rest of the experiments in this section, CREOL F3 fibre was used.

The background was generated due to the high-intensity points created due to the self-imaging property of the graded-index fibres. Using a fibre which did not have a self-imaging property would not allow the creation of high-intensity points. Instead, the beam would be spread into random speckles, with intensity supposedly low enough not to generate a noticeable signal. Step-index fibres do not support self-imaging. However, the bandwidth of step-index fibres is very low, making them inappropriate for usage with femtosecond pulses for reasonably long fibre probes, as shown in Chapter 3. Hence, a graded-index fibre had to be used. Instead, the distal end of the fibre had to be modified not to allow the creation of high-intensity points inside the fibre. Any modification that would break the focused points into random speckles would decrease the intensity of the background. For example, the distal facet of the fibre could be made diffusive. In the approach presented here, a short piece of a step-index fibre was spliced to the distal end of the graded-index fibre, forming a composite probe (Figure 5.13).

The graded-index part of the probe still had the self-imaging property, as shown in the fields in Figure 5.10. However, only a random speckle pattern was re-imaged, with a low probability of creating a high-intensity point. In addition, since the propagation of light through the step-index splice was very wavelength dependent, the fields for the pump and Stokes beams were uncorrelated in the graded-index fibre, further decreasing the intensity of the background.

Figure 5.11 shows, for three different graded-index fibres, that adding the step-index splice to the end of the graded-index fibre reduced the background generated in the probe. For the CREOL and YOFC fibre, the background dropped significantly below the intensity generated in the sample. Thus, the composite probe allowed CARS imaging of the

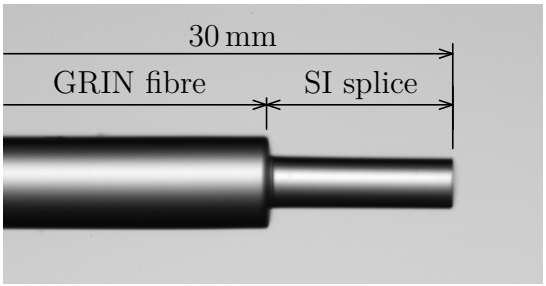

Figure 5.13: Distal end of the composite probe for four-wave mixing background suppression. The step-index fibre was tapered to have the same core diameter as the graded-index fibre. Then it was spliced to the graded-index fibre and the splice was cleaved to the desired length (here, 250 µm).

polystyrene beads with a sufficient signal-to-background ratio. However, the background suppression was insufficient for the Prysmian fibre to enable imaging. The high background generated in the Prysmian fibre shows that while adding the splice reduces the background, choosing a suitable graded-index fibre is also essential.

If the step-index splice were very short, the background suppression would be minimal, as it would have almost no effect on the beam. On the other hand, if the splice were too long, the bandwidth of the probe would be too low for femtosecond pulses. An optimal length of the splice thus had to be found. Consequently, the performance of the spliced probes was evaluated. In this section, the suppression of the background is discussed. In the following sections, the focusing performance and the dispersion of the probes are assessed. The composite probes were then used to demonstrate CARS imaging of polymer beads with chemical contrast using a femtosecond laser and spectral focusing and tissue imaging.

The only available step-index fibre with a sufficient numerical aperture (the same as the graded-index fibre or higher) was the CeramOptec Optran Ultra WFGE. This fibre, however, had a core diameter of 100 µm, significantly larger than any of the graded-index fibres used here. If spliced directly on a graded-index fibre with a small core size, the achievable power ratios would be very low, as the graded-index fibre would have significantly fewer modes than the step-index fibre. Thus, it would not be possible to control the propagation in the step-index fibre fully. The CeramOptec step-index fibre was thus tapered to have the same core diameter as the graded-index fibre before splicing. Such step-index fibre had only twice as many modes as the graded-index one (not counting the higher order modes, which were not excited due to the lower numerical aperture of the graded-index fibre). The tapering, however, resulted in a noticeable step on the probe due to the substantially different outer diameters of both fibres, as shown in Figure 5.13. This step did not affect the optical properties of the probe, nevertheless could be an issue if the probe was inserted deeper into tissue than the length of the splice. The problem could, if necessary, be mitigated by using a more dimensionally compatible pair of fibres. Alternatively, the distal end of the graded-index fibre could be polished into a conical shape before splicing, smoothing the step out.

Figure 5.14 shows the impact of the splice length (for the CREOL F3 fibre) on imaging polystyrene beads. For each splice length, two images were captured, one with the beads in focus and one with no sample (Figure 5.14a). For each bead position in a 40 µm diameter field of view (beads outside this area were excluded due to lower excitation intensity), a ratio of bead intensity and the intensity with no sample was calculated. This value was

(a) Images of PS beads

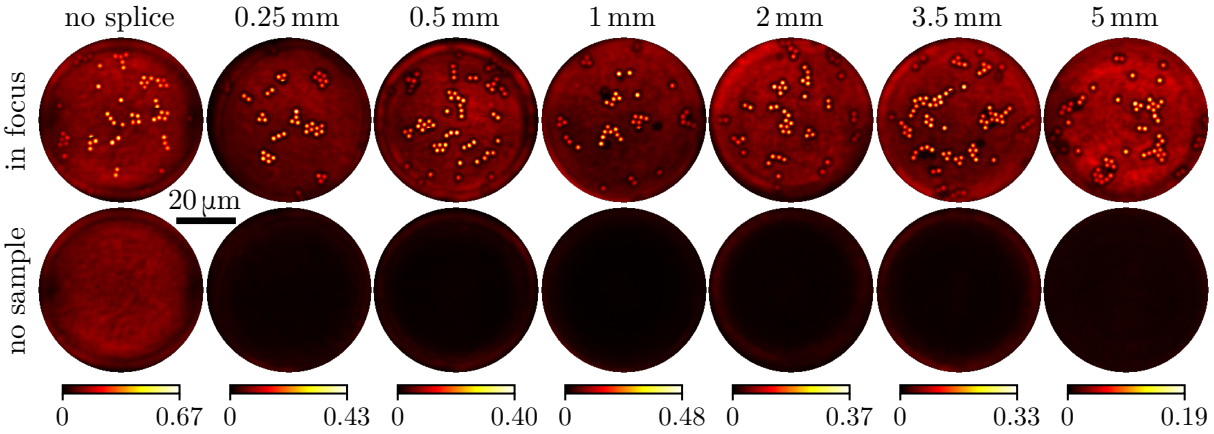

(b) Bead-to-background ratio

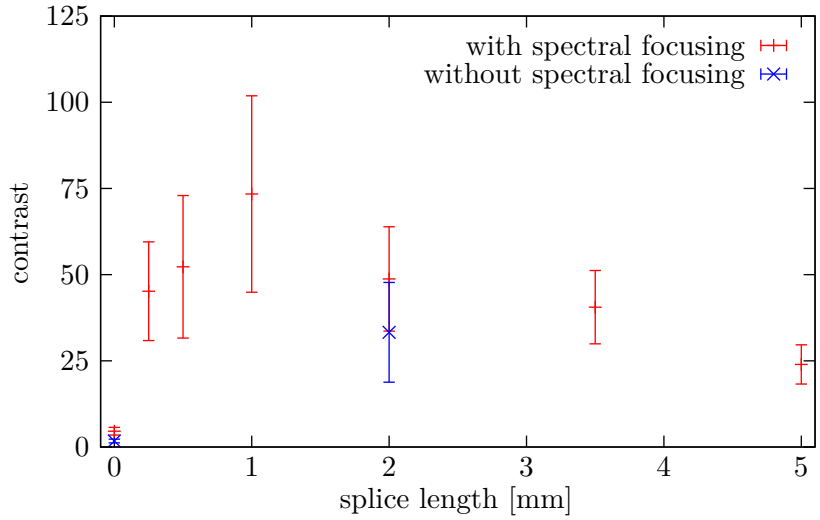

Figure 5.14: Suppression of the signal generated in the fibre by using the composite probe. (a) CARS images of 2 µm polystyrene beads on a glass slide for different splice lengths and images with no sample in focus. The excitation wavelengths were 789 nm and 1040 nm, corresponding to a Raman shift of 3059 cm^{-1}. The signal was collected in transmission and spectral focusing was implemented in the setup. (b) Bead-to-background ratio calculated from images in (a). The error bars show the standard deviation across the field of view.

then averaged over all beads (Figure 5.14b). In essence, the signal-to-background ratio was determined as a function of the length of the splice. This ratio increased with increasing splice length up a 1 mm long splice. Afterwards, the ratio started to drop again. This drop suggests that while the intensity of the background decreased with the increasing length of the splice, the intensity of the CARS signal excited in the sample dropped. For polystyrene, the optimal length of the splice was about 1 mm. The glass blocks were removed from both beams to verify that the splice reduced the background when spectral focusing was not used, and the experiment was repeated (for one splice length only). The blue data points in Figure 5.14b confirm that the background reduction was similar regardless of the spectral focusing.

The spectral dependence of the background suppression in the CREOL F3 fibre was tested by imaging at different Raman shifts with no sample in the system. The images (with the signal being collected in transmission) captured during this experiment are in Figure 5.15. This figure shows both the spectral dependence of the signal (that is, the blue data points in Figure 5.12 were calculated by averaging the values in each image in the first row of Figure 5.15) and the suppression of the background. In addition, the images show that the intensity of the background was often not the same across the field of view.

To estimate the level of background suppression for different splice lengths at different Raman shifts, the values in each image in Figure 5.15 were averaged and normalised to the value with no splice. Figure 5.16a shows that increasing the length of the splice decreased the intensity of the background signal. The actual level of suppression depended on the Raman shift, but for splices 2 mm or longer, the suppression was at least an order of magnitude. By averaging the data for all Raman shifts, the relative background suppression as a function of the length of the splice was obtained in Figure 5.16. The graph shows that the intensity of the background decreased with the length of the splice. However, these data points do not consider that the intensity of the signal generated in the sample also changed due to the power ratio and spot size. Using the measured power ratios and spot sizes for different splice lengths in Figure 5.18, the data were corrected for this change, assuming a quadratic dependence of the generated signal on the intensity of the pump beam and linear dependence on the intensity of the Stokes beam. The corrected data have a minimum for a 2 mm long splice. For this splice length, the signal-to-background ratio should be maximal. By CARS imaging of polystyrene beads in Figure 5.14, the optimal length was determined to be 1 mm. The spectral dependence of the background likely caused the difference. Nevertheless, a 1 mm to 2 mm long splice provided a level of background suppression sufficient for imaging.

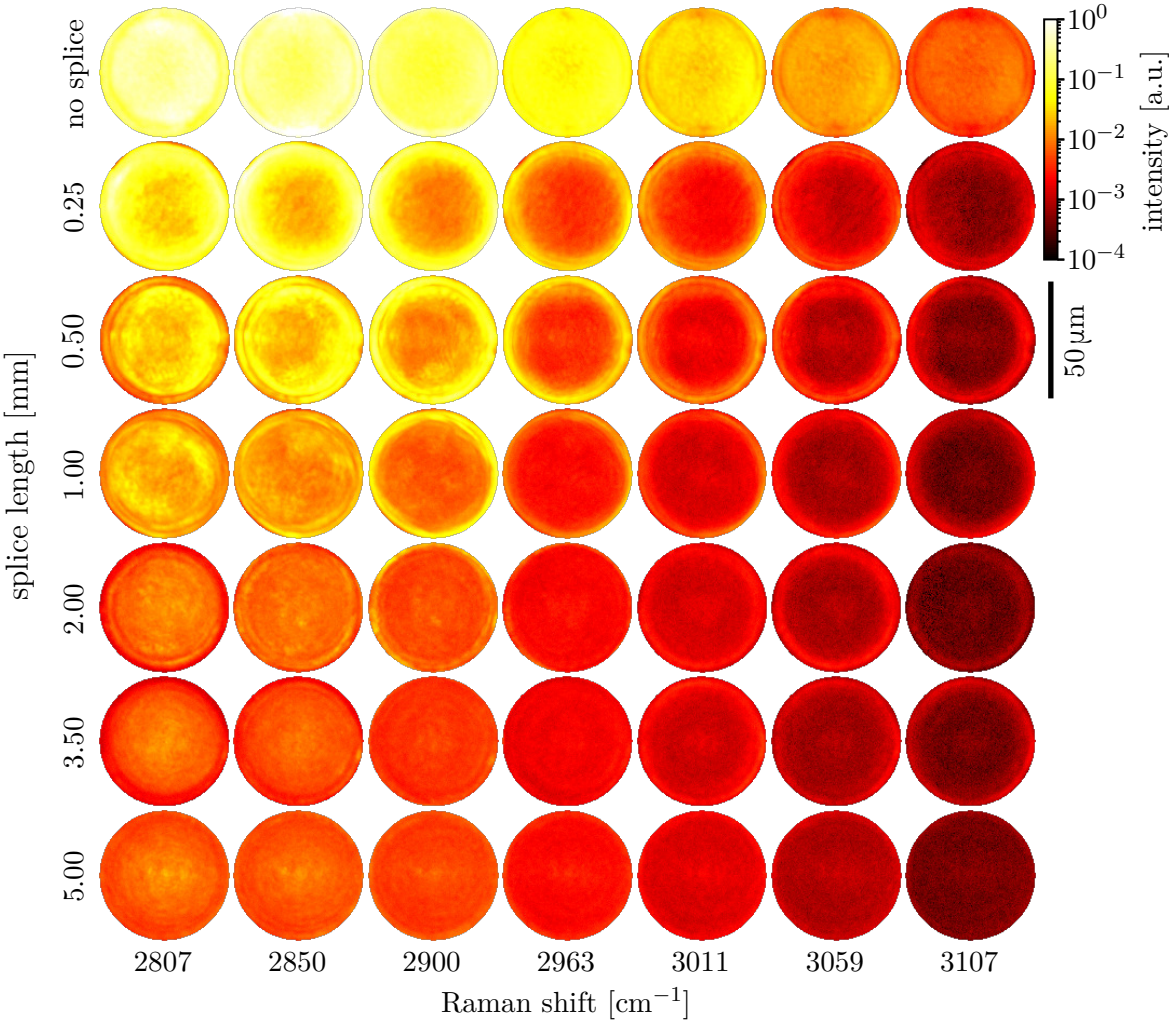

Figure 5.15: CARS images in logarithmic scale taken in transmission with no sample for different Raman shifts and splice lengths. The measured signal is the undesired non-linear background generated in the fibre due to self-imaging. The GRIN fibre was CREOL F3.

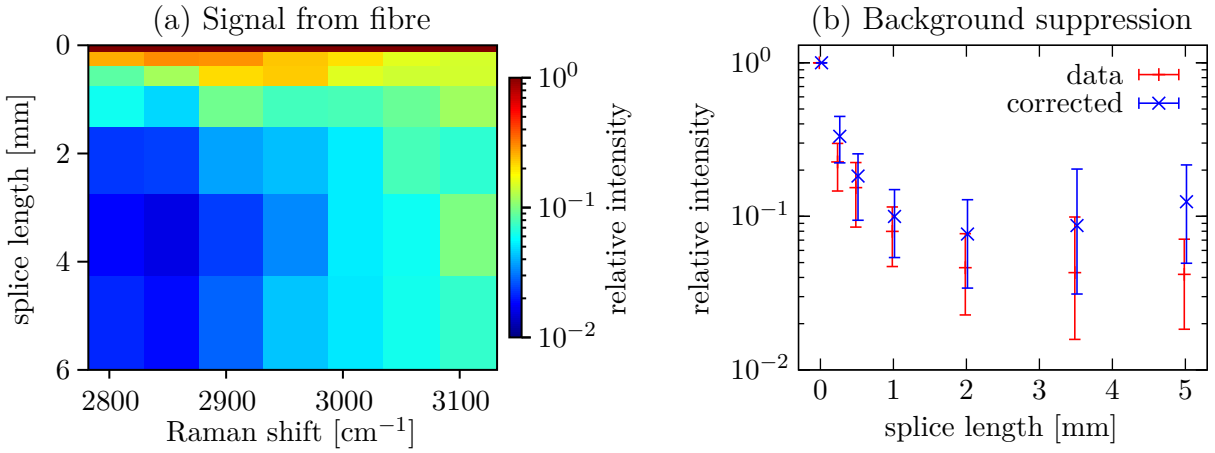

Figure 5.16: (a) Signal generated in the fibre as a function of a Raman shift and the length of the splice. The values were averaged over the whole field of view. (b) Signal generated in the fibre as a function of the length of the splice averaged over all Raman shifts. The figure shows both the measured data and data corrected for the drop in the excitation power (caused by the drop in the power ratio and increase in the spot size).

5.6. Focusing performance of composite probes

The focusing performance of the spliced probes was evaluated by measuring the three-dimensional point spread functions, as described in Section 2.6. Figure 5.17 shows an example of the lateral and axial point spread functions for a graded-index fibre (CREOL F3) with no splice, a graded-index fibre with a 2 mm and 5 mm splice and a step-index fibre (CeramOptec, tapered to 70 µm outer diameter to have the same core diameter as the graded-index fibre). For the step-index fibre, the point spread function was significantly longer (despite the fibre having a higher numerical aperture) and the intensity of the background was much higher (i.e., the power ratio was lower). These effects were both caused by the low bandwidth of the fibre and were expected of a step-index fibre. The point spread functions for the spliced probes were, in general, more similar to the graded-index fibre, as the length of the step-index splice was too short to noticeably impact the focusing performance of the probe.

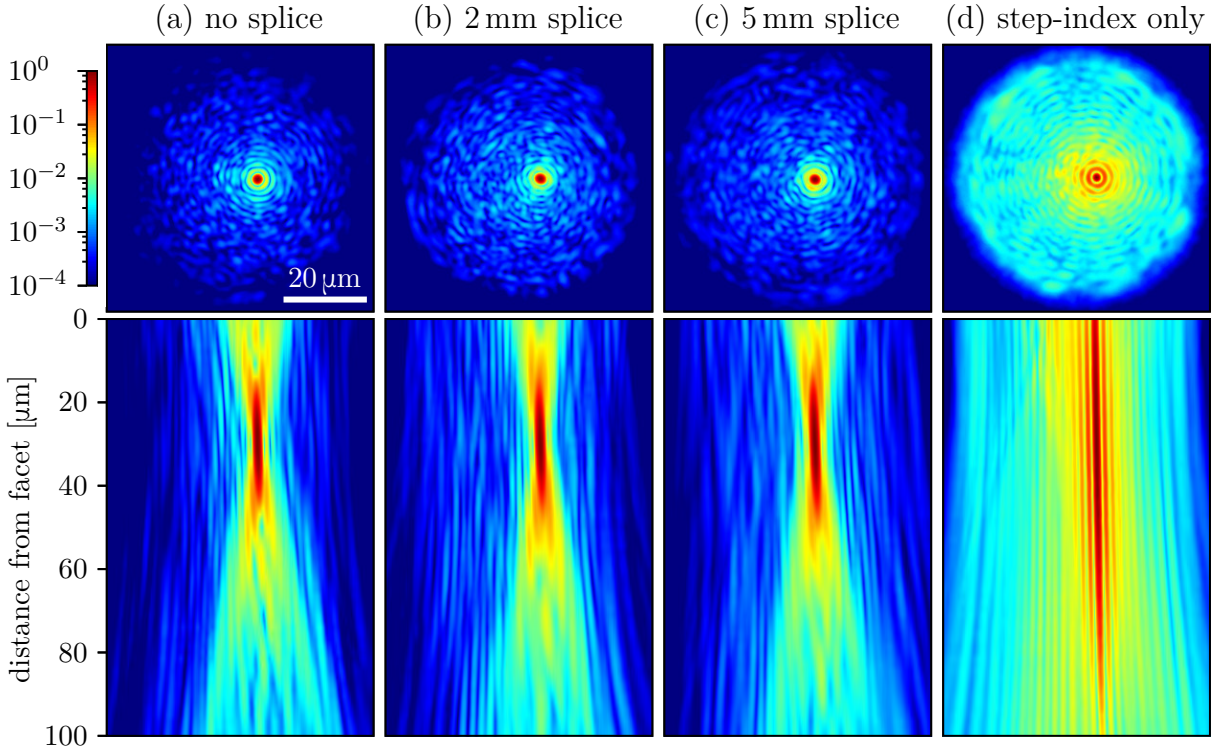

Figure 5.17: Lateral and axial point spread functions (measured using a femtosecond laser tuned to 789 nm) for graded-index fibre with no splice, graded-index fibre with two different splices and a step-index fibre with the same core diameter.

Figure 5.18a shows the power ratio and the lateral spot size across the field of view measured using the femtosecond laser at 789 nm. The data shows that the maximal achievable power ratio decreased, and the minimal spot size increased with the increasing length of the splice. On the other hand, especially for the 5 mm splice, the power ratio distribution across the field of view was more homogeneous. In this regard, the probes with long splices behaved more like step-index fibres. This is also shown in Figure 5.18b, which shows the power ratio and lateral and axial spot size as a function of the splice length. The error bars show the range of the values across the field of view. The error bar length thus indicates the difference between the maximal and minimal value in the field of view. Typically, the minimal spot size and highest power ratio were achieved for

(a) Power ratio and spot size distribution across the field of view

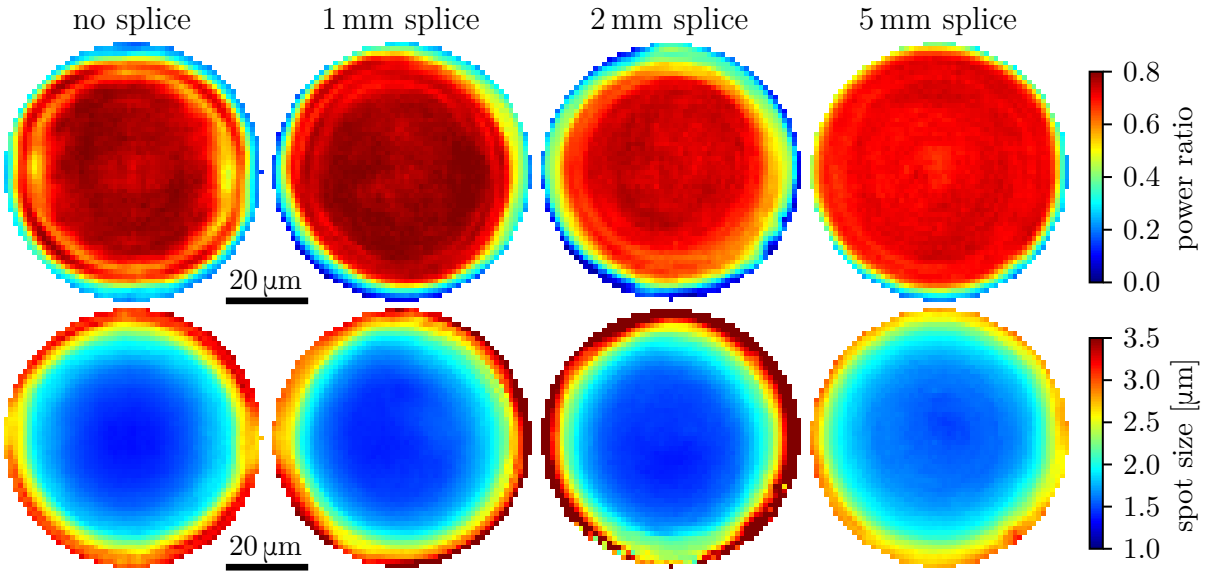

(b) Power ratio and spot size for different splices

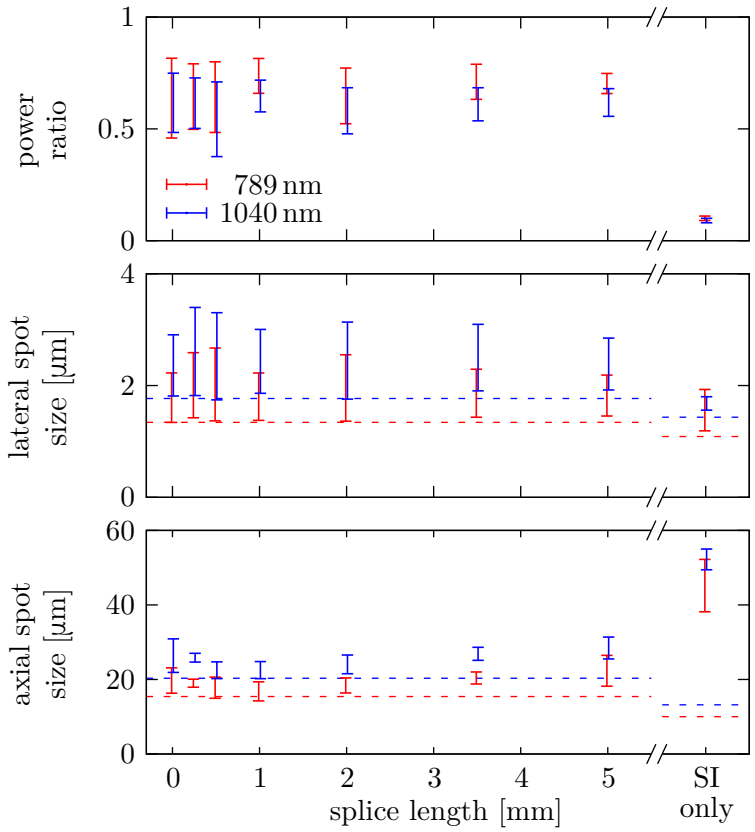

Figure 5.18: Focusing performance of the spliced probes. (a) Distribution of the power ratio and the lateral spot size across the field of view for different probes, measured at 789 nm. (b) Power ratio, lateral and axial spot size as a function of the length of the splice for two wavelengths. SI only was a step-index fibre tapered to the same core diameter. The error bars show the range of the values across the field of view. The dashed lines show the diffraction-limited spot size given by the numerical aperture of the probe.

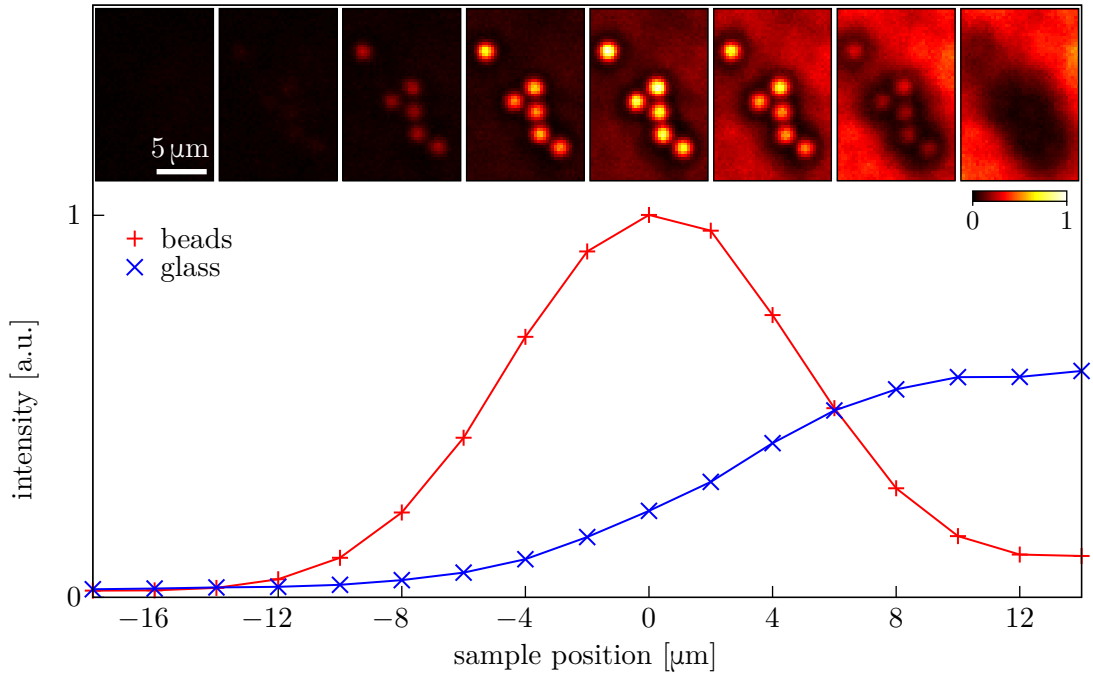

Figure 5.19: CARS z-stack of 2 µm polystyrene beads on a glass slide. The signal was collected in transmission. Positive sample positions mean that the sample was closer to the fibre facet. A fibre with a 5 µm long splice was used. The lines are a guide to the eye.

points close to the axis and the maximal spot size and lowest power ratio at the edge of the field of view. Thus, the ends of the error bars show values close to the axis and at the edge of the field of view.

For the graded-index fibre and fibres with a splice length up to 2 mm, both the lateral and axial spot sizes approached the diffraction-limited values for the numerical aperture of the fibre. For longer splices, the size of the points increased, and the maximal power ratio decreased. The power ratio was significantly lower for the step-index fibre, and the axial spot size was considerably higher than the diffraction-limited value. The exact values of the power ratio and lateral spot size for the step-index fibre vary slightly depending on the time overlap of the signal and reference beam during the calibration.

The length of the point spread function was verified by a z-stack of polystyrene beads on a glass slide (Figure 5.19) by physically moving the sample. The measured depth of focus was 11 µm (FWHM), a value comparable to the value measured using the picosecond laser in Figure 4.12. Figure 5.20 shows another approach to capturing the z-stack. Instead of physically moving the sample (Figure 5.20a), the focused point could be moved by propagating the transmission matrix into a different plane (Figure 5.20b), as describe in Section 2.5. Both methods produced similar results when imaging the beads. However, the results were not identical because the size of the focused points increased with increasing distance from the facet, as shown in Figure 2.24.

The bandwidth of step-index fibres is significantly lower than graded-index fibres, and they suffer from the chromato-axial memory effect, as discussed in Section 3.2. The step-index splice thus decreased the total bandwidth of the spliced probes compared to the bandwidth of the pure graded-index fibre. Figure 5.21 shows the evaluation of the wavelength tuning range of the spliced probes. After the calibration was performed using the femtosecond laser, the wavelength was tuned from the calibration wavelength

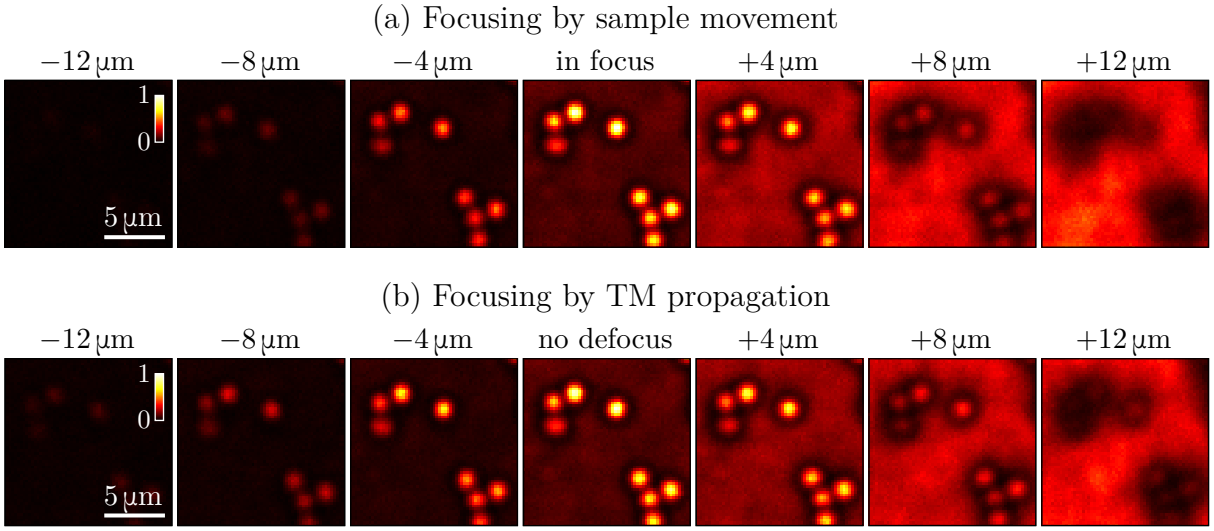

Figure 5.20: CARS z-stacks of 2 µm polystyrene beads on a glass slide measured (a) by physically moving the sample with respect to the fibre and (b) by a shift of the focal plane with respect to the fibre (by propagating the measured transmission matrix to a different plane) with the sample being stationary.

of 789 nm. Afterwards, the power ratio and the spot size of the points across the field of view were measured (Figure 5.21a). This data was used to calculate the wavelength tuning range as a function of the splice length. Figure 5.21b shows that the wavelength tuning range decreased with the increasing length of the splice. However, for the splice lengths used here, the change was small and thus had only a minor impact on imaging.

The chromato-axial memory effect in step-index fibres results in the focused point moving with wavelength along the axis of the fibre. The three-dimensional point spread functions were measured after the wavelength was tuned from the value used for the calibration to quantify the shift for the spliced fibres. The focal shift was determined by locating the maximum in each point spread function for each wavelength. This measurement could have been performed using the femtosecond laser for the graded-index and spliced fibres. However, using the femtosecond laser for the step-index fibre resulted in very long points and low power ratios (Figure 5.17d). Thus, the M Squared SolsTiS tunable CW laser (used in Chapter 3) was used in this experiment.

Figure 5.22a shows the axial point spread functions at the calibration wavelength of about 800 nm and after the wavelength was tuned from this value. Clearly, for the step-index fibre (which was tapered to 70 µm outer diameter to have the same core diameter as the graded-index fibre), the wavelength change did not result solely in a focus shift. Instead, multiple maxima were formed at some wavelengths. To simulate the situation when the 0.37 NA step-index fibre was used as a splice at the distal end of the 0.30 NA graded-index fibre, the angle of incidence to the step-index fibre was limited to 0.30 NA by multiplying the hologram on the SLM by a circular aperture. In this case, the point shifted without developing the second maximum.

Figure 5.22b shows the calculated axial positions of the points. For the CeramOptec step-index fibre tapered to 70 µm outer diameter, the axial shift was $-0.33\,\mu\text{m}\cdot\text{nm}^{-1}\cdot\text{mm}^{-1}$. This was a lower value than the one measured for Thorlabs FG050LGA in Figure 3.7 and the theoretically predicted value in [130]. This difference was likely caused by some differences in the refractive index profile of the fibres (which the manufacturers do not

(a) Power ratio and spot size

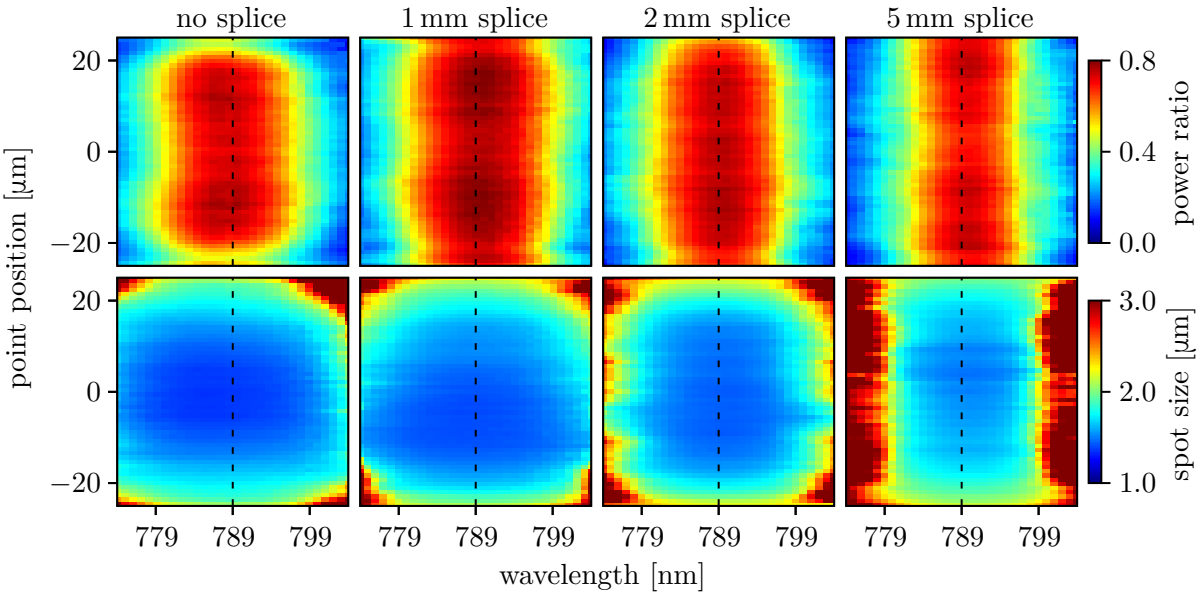

(b) Wavelength tuning range

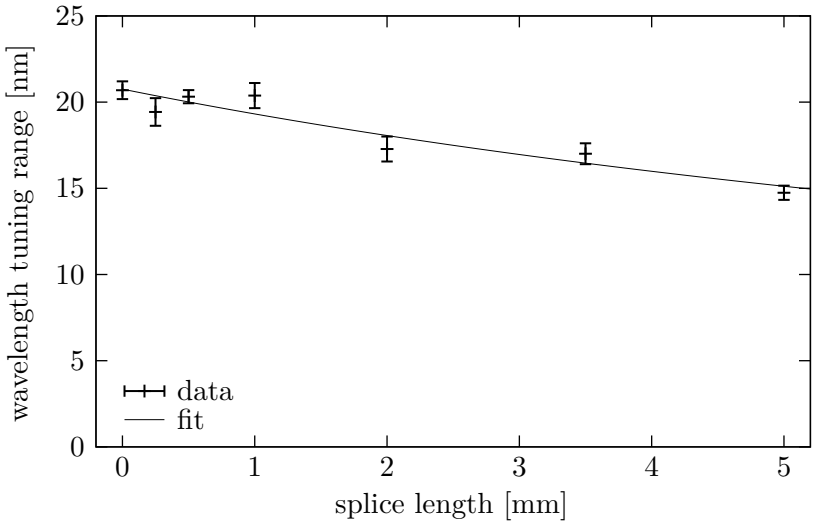

Figure 5.21: Wavelength tuning range (bandwidth) measurement. (a) Power ratio and spot size across the field of view after the wavelength was tuned from the calibration wavelength of 789 nm (indicated by the dashed line). (b) Wavelength tuning range as a function of the length of the splice. The error bars show the standard deviation of the values across the field of view. The line is a reciprocal fit.

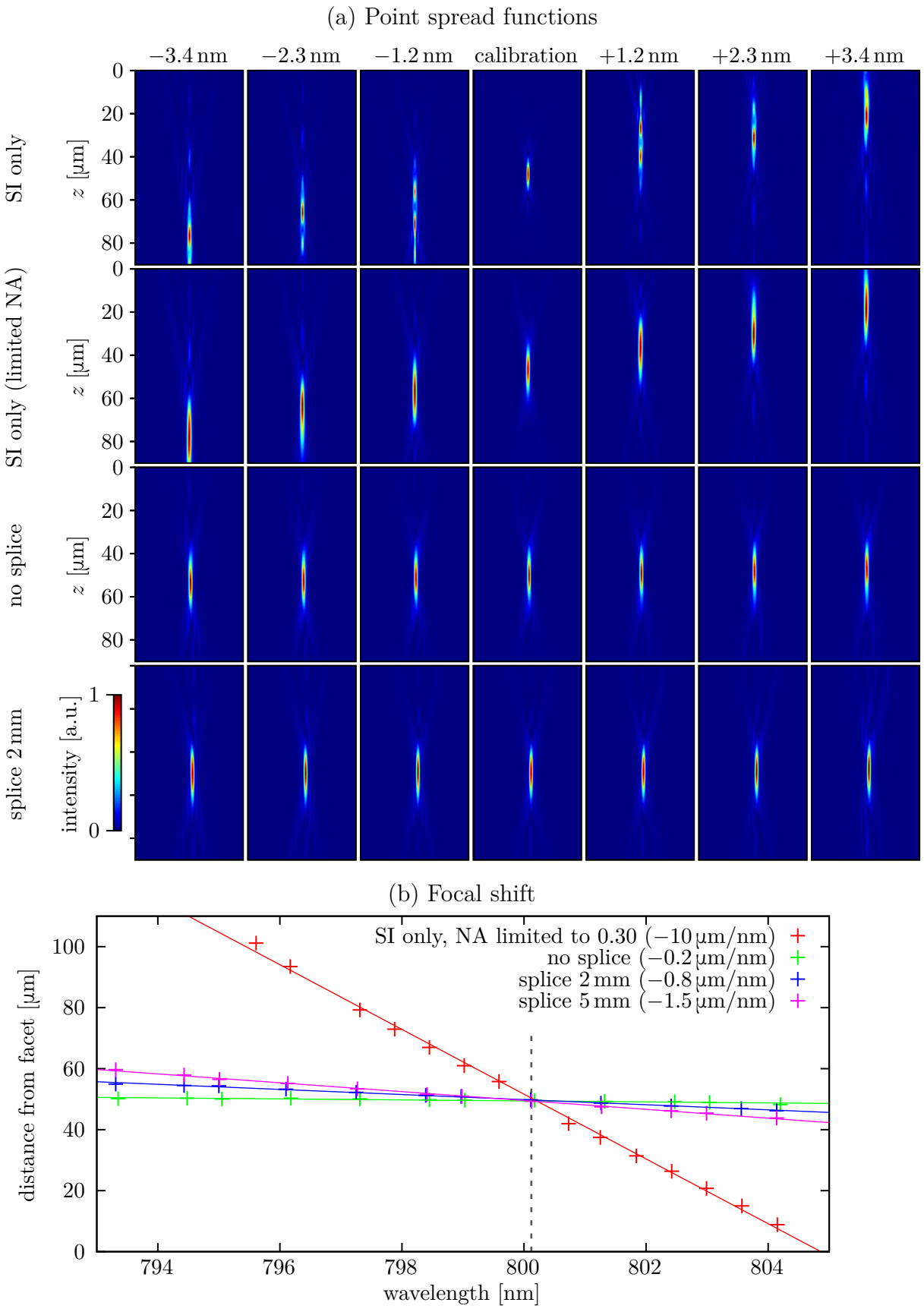

Figure 5.22: Axial shift of the focus after wavelength tuning for different probes, measured using a tunable CW laser. (a) Axial point spread functions. (b) Position of the focus. The dashed line denotes the calibration wavelength. The lines are linear fits (the slopes of the fits are in the legend).

provide). For the CREOL F3 graded-index fibre, the shift was $-0.007\,\mu m{\cdot}nm^{-1}{\cdot}mm^{-1}$, almost two orders of magnitude lower than shift for the step-index fibre. The shift for the spliced fibres was approximately equal to the total shift caused by the graded and step-index parts. For example, for the probe with 2 mm long splice (that is 2 mm long step-index fibre and 28 mm long graded-index fibre), the shift was approximately four times higher than the shift of the pure graded-index fibre, though still more than an order of magnitude lower than the shift for the pure step-index fibre. Consequently, the shift for the spliced fibre was still small, thus, had a minimal impact on imaging.

5.7. Dispersion measurement

In Section 3.4, the dispersion of a graded-index fibre was measured using the tunable CW laser. Since this laser was later unavailable, a different approach was used to measure the dispersion of the composite probes, utilising the femtosecond laser. To measure the dispersion, the setup in Figure 5.3 was modified. LED2 was replaced with a single-mode fibre (Thorlabs P1-780A-FC-1) connected to a home-built spectrometer, as shown in Figure 5.23. A natural density filter was placed before the single mode fibre to limit the power coupled into the single mode fibre and prevent non-linear effects in the fibre.

The spectrometer consisted of a collimation lens (L14; Thorlabs AC254-100-B-ML), diffraction grating (DG; Thorlabs GR25-1208), a lens (L16; Thorlabs AC254-125-B-ML) and a camera (CAM2; Basler ace 2 a2A1920-160umBAS). The spectra were measured by averaging multiple rows on the camera and the wavelength axis was calibrated using a tunable narrowband continuous-wave titanium-sapphire (TiS) laser (M Squared SolsTiS SA PSX F). In addition, a fraction of the beam was picked on a non-polarizing beamsplitter (BS3; Thorlabs BSW11) and focused on a photodiode (PD3; Vishay Semiconductors BPW34) using a lens (L15; Thorlabs AC254-060-B-ML) to measure the power coupled into the single-mode fibre.

After calibrating the system (as described in Section 5.3), lens L11 was removed from the calibration module. Afterwards, the beam reflected off the non-polarizing beamsplitter (BS2) was coupled into the single-mode fibre using an achromatic lens (L13; Thorlabs AC080-020-B-ML). This way, a single point created at the distal end of the multimode fibre was imaged onto the single-mode fibre. The exact position of the point coupled into the fibre was determined by raster-scanning the point across the field of view of the multimode fibre and measuring the power coupled into the single-mode fibre using the photodiode in the spectrometer (PD3). The reference beam was coupled into the same fibre as well. By adjusting the length of the delay line in the reference beam, interference of both beams in the spectrometer was achieved. By stepping the phase of the signal beam, the spectral phase and amplitude were measured as shown in Figure 5.24.

The measurement of the spectral phase was performed without the fibre and with different fibre probes (Figure 5.25a). Due to reflections in the system, the measured spectra included a high-frequency component. Consequently, the measured data were low-pass filtered. Identically to the measurement in Section 3.4, the spectral phase measured with no fibre was subtracted to obtain the spectral phase difference introduced by the fibre (Figure 5.25b). Afterwards, a third-degree polynomial was fitted to the measured spectral phase to determine the group delay dispersion and third-order dispersion (Figure 5.25c,d).

Identically to the measurement in Section 5.3, a pure graded-index fibre (with no splice) introduced almost no third-order dispersion. The fibre added only $50\,fs^2{\cdot}mm^{-1}$ of group velocity dispersion, in agreement with the measurement performed in Section 5.3 (which

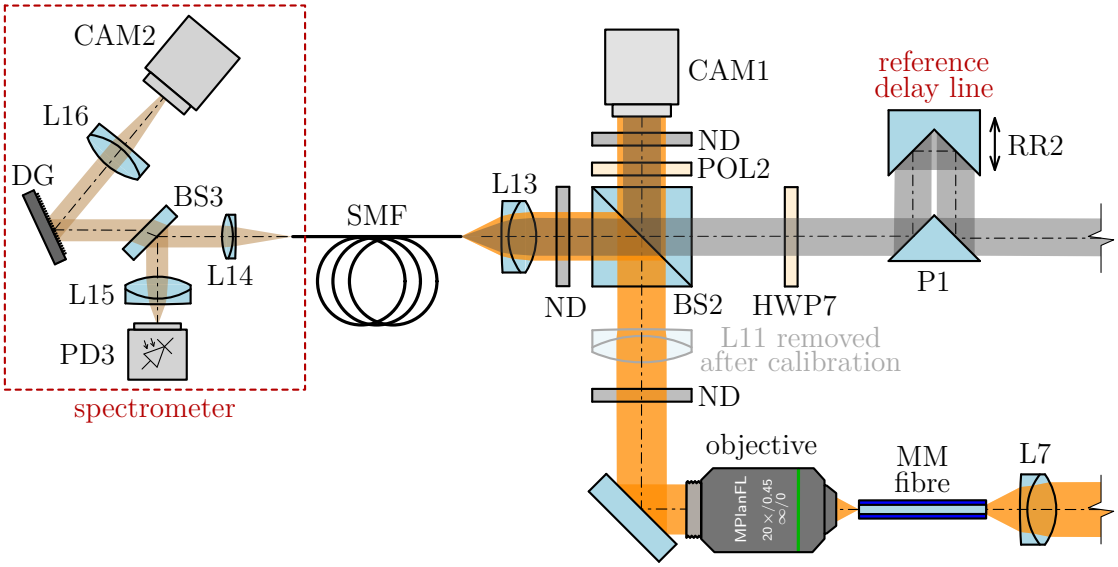

Figure 5.23: Setup modifications for dispersion measurement. In addition, the reference beam was picked off before the spatial light modulator. The rest of the setup was identical to Figure 5.3. BS – non-polarising beamsplitter, CAM – camera, DF – diffraction grating, L – lens, ND – natural density filter, P – knife-edge right-angle prism mirror, PD – photodiode, POL – polariser, RR – hollow roof prism mirror. SMF – single-mode fibre.

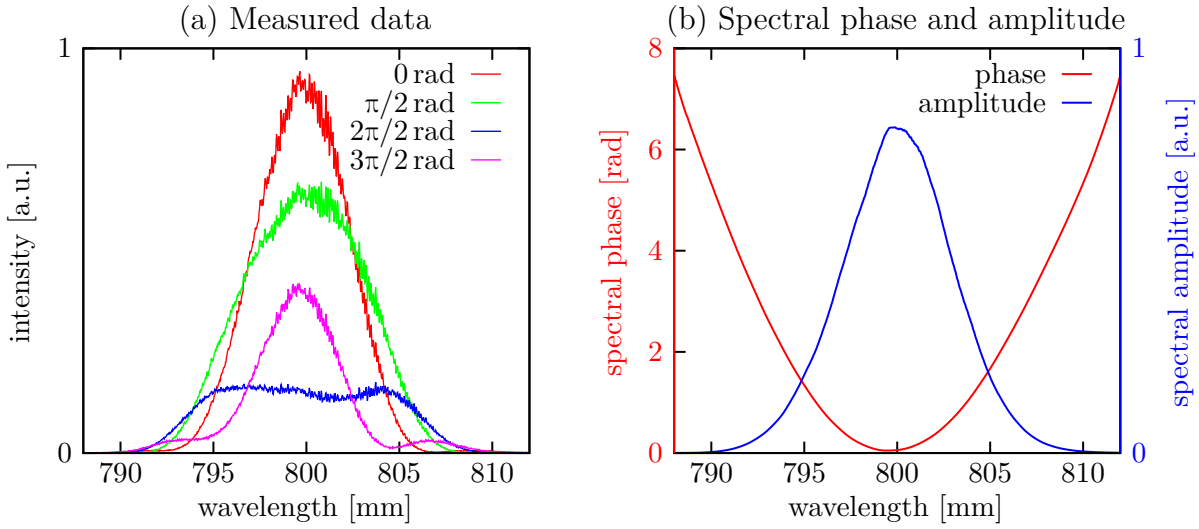

Figure 5.24: Spectral phase and spectral amplitude measurement. (a) An example of measured data for four phase shifts of the signal beam. (b) Spectral phase and amplitude calculated from the measured data.

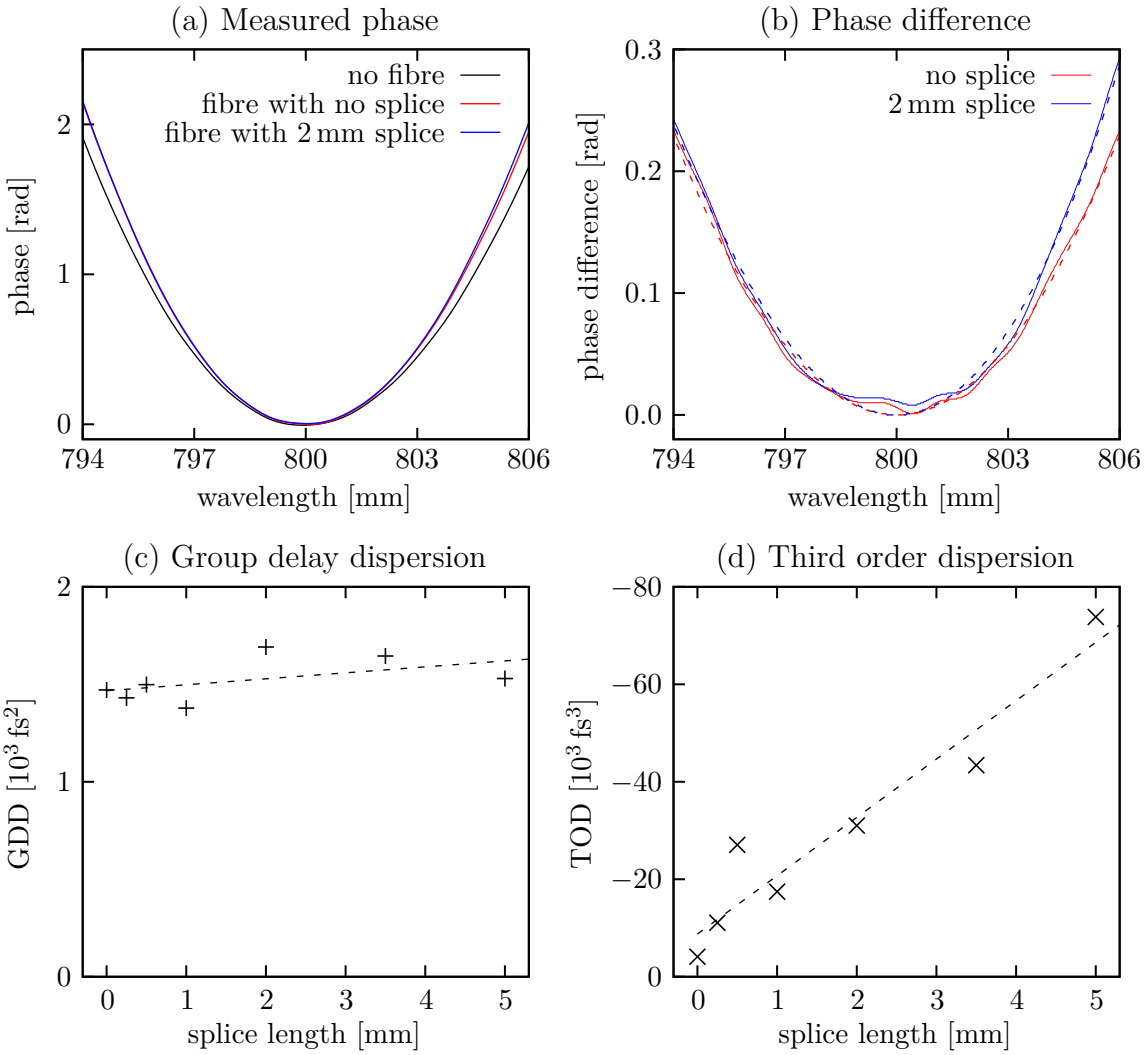

Figure 5.25: Dispersion measurement. (a) Spectral phase measured with no fibre mounted in the setup and with two fibre probes. (b) Difference of the spectral phase with and without fibre mounted in the setup for two different probes. The dashed lines are third-order polynomial fits. (c) Group delay dispersion and (d) third-order dispersion calculated from the fits for probes with different splice lengths. The dashed line is a linear fit.

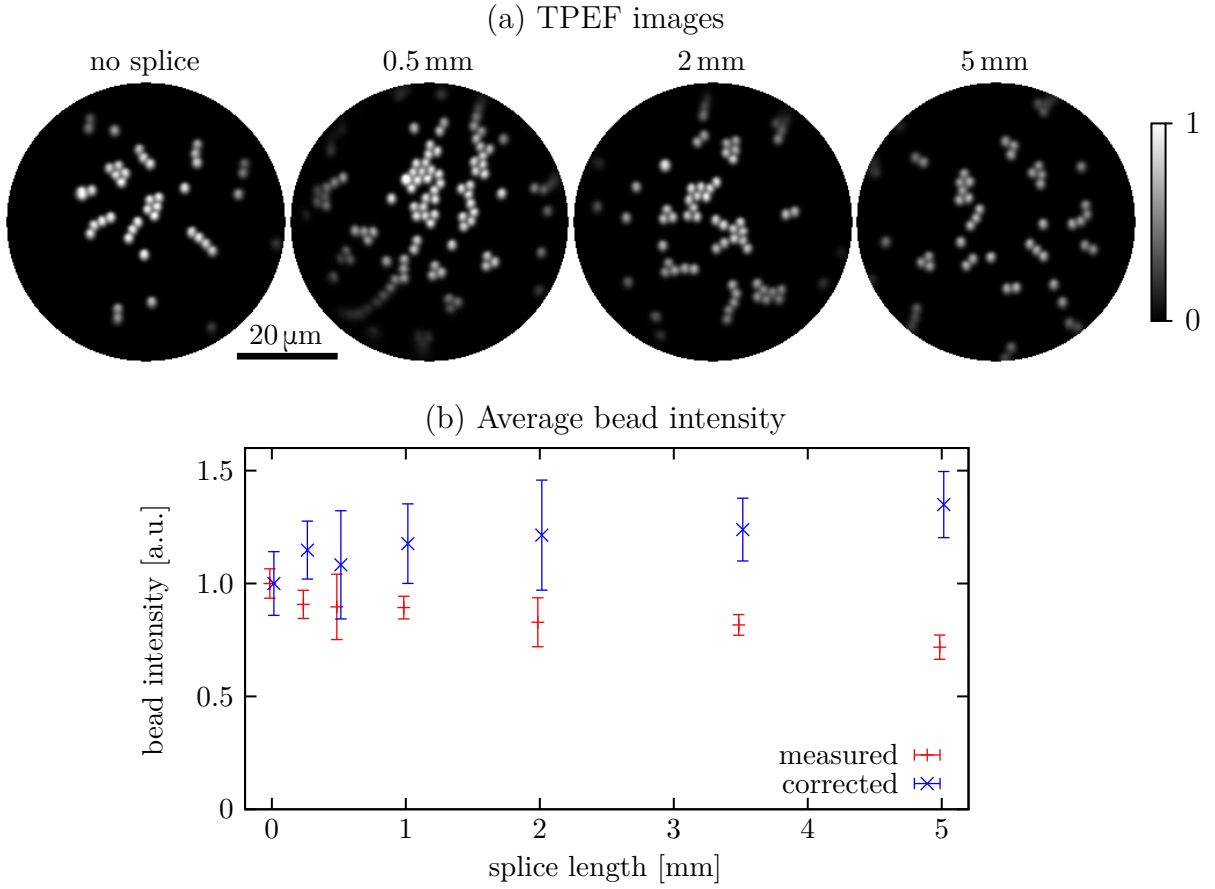

Figure 5.26: TPEF imaging of 2 µm fluorescent beads. (a) TPEF images taken using probes with different splice lengths. For all images, the input power to the setup was constant. (b) Average intensity of the beads as a function of the length of the splice. The error bars show one standard deviation of the intensity across the field of view. The graph also shows data corrected for the drop in the excitation power caused by the decrease in the power ratio and increase of the spot size for longer splice lengths (see Figure 5.18).

was performed using a different graded-index fibre and a slightly different wavelength). Adding the splice to the probe did not significantly change the value of group delay dispersion. However, negative third-order dispersion was added by the splice.

By fitting the spectral phase measured with no fibre in the system, it was found that the system without the fibre (and not including the SF57 glass blocks) introduced about 11500 fs^2 of group delay dispersion and about 73000 fs^3 of third-order dispersion. These values were inaccurate, as they included the objective in the calibration module and a half-wave plate in the reference beam. Nevertheless, the values measured without the fibre show that the amount of third-order dispersion introduced by the fibre was comparable to the value added by other optical elements in the system.

To approximately verify the measurement of the dispersion, 2 µm fluorescent beads (Nile Red, Polysciences Fluospheres F8825) on a glass slide were imaged using two-photon excitation fluorescence using different fibre probes (Figure 5.26). The average fluorescence intensity of the beads across the field of view was evaluated. As shown in Figure 5.26b, the fluorescence intensity decreased with the increasing length of the splice. The measured values, however, did not take into account the change in the point quality (the size and the power ratio) caused by the splice, discussed in Section 5.6. The measured data was

corrected for that phenomenon, assuming quadratic dependence of the fluorescence on the excitation intensity. After applying the correction, the fluorescence intensity slightly increased with the length of the splice. This increase agreed with the results obtained by measuring the spectral phase. That is, the negative third-order dispersion of the spliced probe was partially compensating for the positive third-order dispersion of the system. Nevertheless, the measurement performed with the beads confirmed that adding a short step-index splice to the graded-index fibre had only a small effect on the pulse length in the sample plane.

5.8. Spectral resolution

Spectral focusing (Figure 5.1) allows CARS imaging with chemical contrast using a broadband light source like a femtosecond laser. By applying the same amount of GDD to both beams, the spectral resolution is increased beyond the spectral width of the light source. Different Raman shifts (within the spectral width of the laser) can then be excited by changing the time delay between the pump and Stokes beams.

The spectral focusing is demonstrated in Figure 5.27 by CARS imaging a mix of 2 µm PS and 2.5 µm PMMA beads on a glass slide. Both beads were excited simultaneously when the SF-57 glass blocks were not installed in the system. Changing the time delay had only a small impact on the contrast between both beads (Figure 5.27a). The change in relative intensity of the different types of beads when changing the time delay was likely caused by not compensating the GDD added by the setup to the Stokes beam since the laser has a built-in pre-chirp pulse compressor only in the tunable beam (used as the pump beam). Thus, some level of spectral focusing was still present. When the glass blocks were installed in the beams, the PS beads generated signal at a different delay (the time delay was converted to the Raman shift using Equation (5.3)) to PMMA beads (Figure 5.27b). By capturing two images with two different time delays, the two types of beads could be differentiated (Figure 5.28). Hence, a chemical contrast was achieved by means of spectral focusing. The result is similar to what was achieved in Figure 4.12 by using a picosecond laser system and tuning the wavelength of the pump beam.

Due to the chromato-axial memory effect, step-index fibres focus different wavelengths to different distances from the facet. If such fibre was used for CARS imaging with a broadband laser and the effect was different for the pump and the Stokes beams, different Raman shifts could be excited in different parts of the point spread function. To verify that this did not occur with the spliced probes, three time-delay sweeps were measured with different positions of the beads with respect to the focused point (beads in focus and ±5 µm from the focus), as shown in Figure 5.30. The three measured spectra had the same position of the maxima. Thus, the same Raman shift was excited within the whole length of the point spread function.

To evaluate the spectral resolution, CARS imaging inside dimethyl sulfoxide (DMSO) at the 2919 cm^{-1} Raman transition (the spectral width of this peak is 16 cm^{-1} FWHM) was performed. The fibre imaging system was calibrated 30 µm from the facet at 798 nm (pump) and 1040 nm (Stokes). Afterwards, the distal end of the fibre was submerged into the DMSO, and a series of images with different time delays were taken. By averaging the values in each image across the field of view and converting the time delays to Raman shifts, the spectrum was obtained (Figure 5.29).

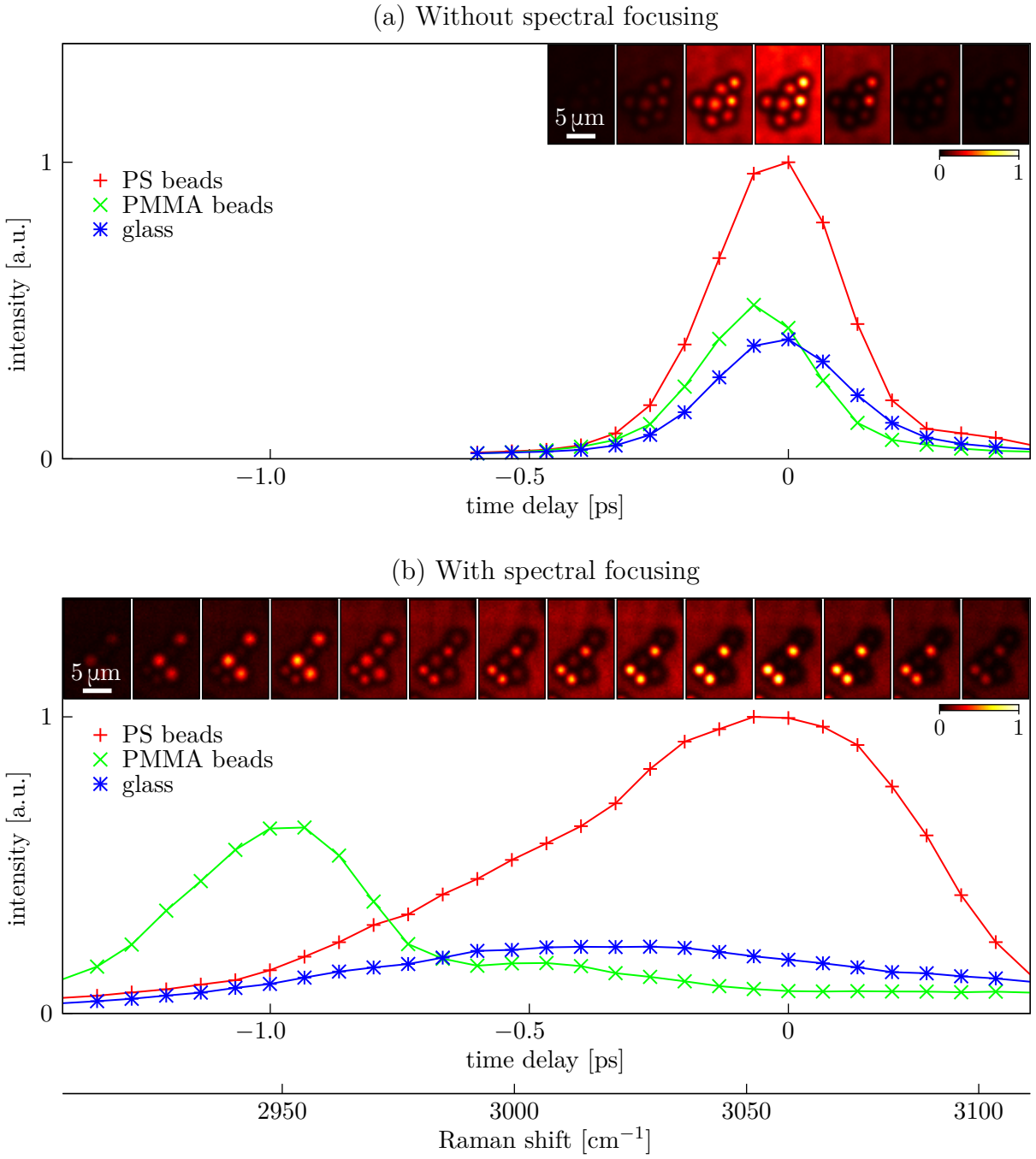

Figure 5.27: Intensity of the CARS signal generated by the sample as a function of the time delay between the Stokes and the pump pulses without and with spectral focusing. For spectral focusing, the delay was converted to Raman shift. The sample was a mix of 2 µm PS and 2.5 µm PMMA beads on a glass slide. A spliced probe consisting of CREOL F3 graded-index fibre and a 2 mm long step-index splice was used. The generated CARS signal was collected in transmission. The lines are a guide to the eye.

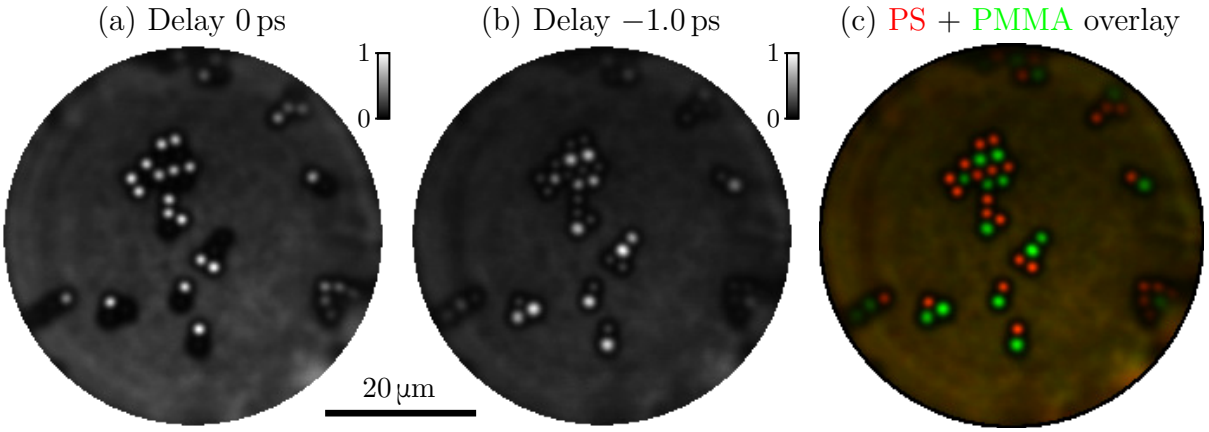

Figure 5.28: Demonstration of spectral focusing on imaging a mix of 2 µm polystyrene and 2.5 µm PMMA beads on a glass slide. (a), (b) CARS images with two different delays of the Stokes beams that maximize the intensity of either type of the bead (see Figure 5.27b). (c) Overlay of both images demonstrating the chemical contrast. A spliced probe consisting of CREOL F3 graded-index fibre and a 2 mm long step-index splice was used. The generated CARS signal was collected in transmission.

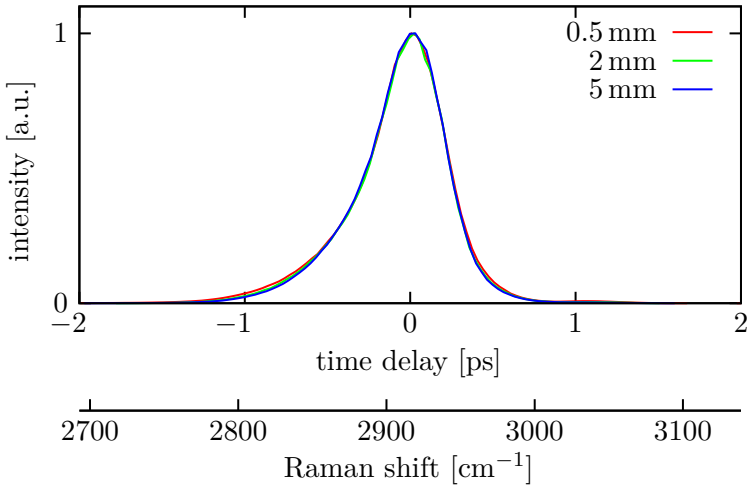

Figure 5.29: Spectral resolution measurement. The graph shows the intensity of a CARS signal generated in DMSO as a function of the time delay between the Stokes and pump beams (which was converted to Raman shift).

(a) Images with defocus

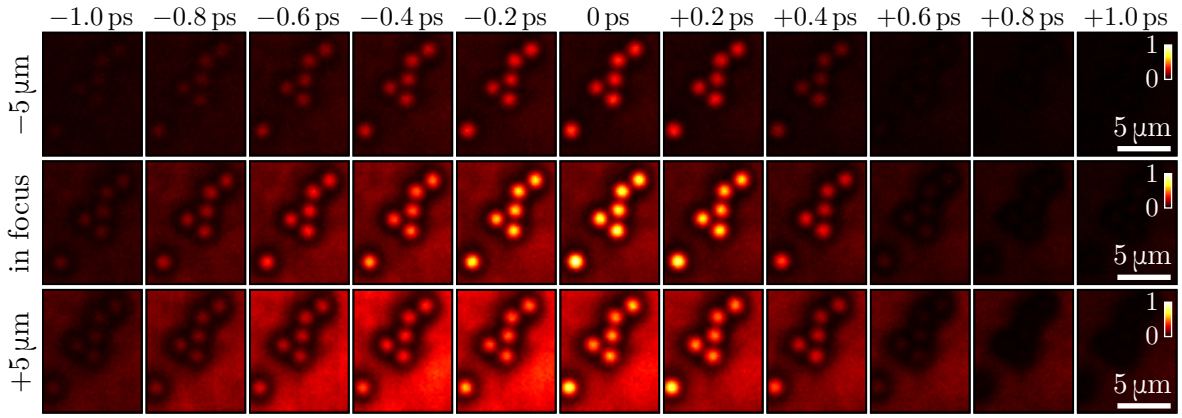

(b) Measured spectra

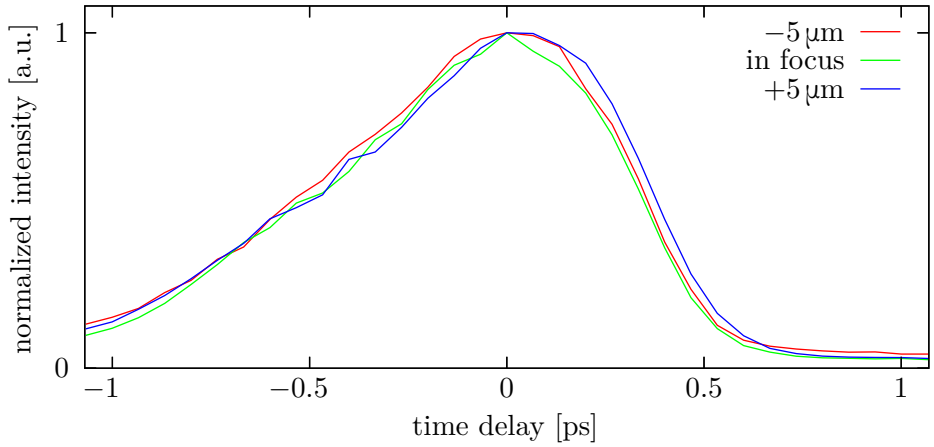

Figure 5.30: Spectral focusing at different parts of the axial point spread function using a fibre with a 2 mm long splice. (a) CARS images of 2 µm polystyrene beads on a glass slide taken with the beads placed at three different distances (in focus and ±5 µm out of focus) taken with different time delays between the Stokes and pump beams. (b) The average intensity of the beads as a function of the time delay for the three distances. The identical position of the maxima confirms that the same Raman shift was excited through the whole length of the point spread function.

The measured spectral width was 55 cm^{-1} (corresponding to a time delay of 0.50 ps), independent of the splice length. The theoretical spectral resolution for 46500 fs^2 of GDD used in the setup according to Equation (5.1) was 28 cm^{-1}. The resolution achieved in this system was thus lower than expected. Although the measurement could not be performed with a probe with no splice due to the high background, the fact that the spectral width did not vary with the length of the splice shows that the spliced probes did not affect the spectral resolution.

Numerous changes to the setup were tested to narrow down the source of this discrepancy, including removing the prism for dispersion compensation, disabling the input polarisation control, altering the spatial overlap of the points, or changing the laser power. None of these modifications, however, increased the spectral resolution. Performing imaging of the same sample in a home-built laser scanning microscope gained the expected spectral width. Thus, the reason for the decreased spectral resolution of the endoscopic

system was not found. Nevertheless, the achieved resolution would be sufficient for bio-imaging, e.g., to differentiate proteins and lipids.

5.9. Working distance

The multimode fibre endoscope could, in principle, be calibrated at any distance from the facet (working distance), with the extreme being infinity (far-field imaging) [47]. Since the spot size increased with the working distance due to the reduced effective numerical aperture (Figure 2.24), the peak intensity and the resolution decreased. Nevertheless, imaging was still possible, as demonstrated in Figure 5.31 on two-photon excitation fluorescence imaging of 2 µm fluorescent beads (Sigma Aldrich L4530-1ML) on a glass slide. When imaging 300 µm from the facet, the field of view was much larger than the core size. However, the individual beads could not be resolved due to the large spot size. When imaging 50 µm from the facet, the field of view was close to the size of the core. The resolution was higher, and the individual beads could be resolved.

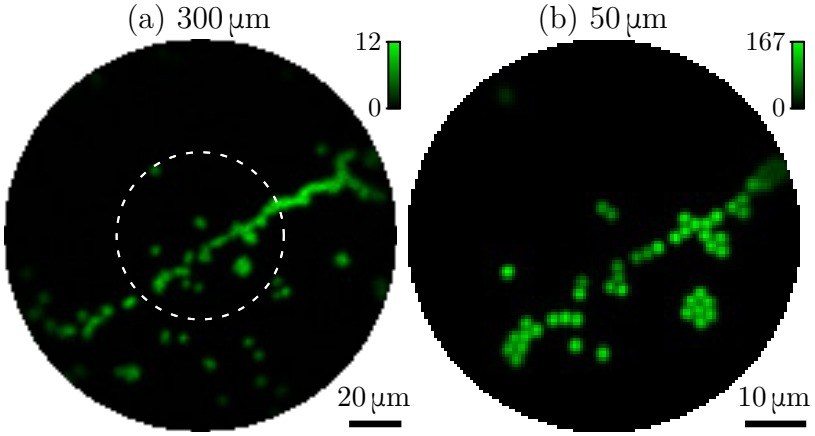

Figure 5.31: TPEF images of 2 µm fluorescent beads on glass slide taken with two different working distances of the endoscope (the sample was moved between the images so the beads are in focus in both images). The dashed circle in (a) shows the area imaged in (b).

Imaging long distances from the facet is possible in the air or another transparent media. The scattering inside the tissue (between the fibre facet and the focal plane) plays a significant role in tissue imaging. It limits the maximal working distance, similar to the maximal imaging depth in a standard scanning microscope. For imaging through a multimode fibre, the collection efficiency also drops significantly with working distance due to the minimal collection area (limited by the core size).

The limitation of the working distance is demonstrated in Figure 5.32 on TPEF and CARS imaging on a surface of a fixed cerebellum slice (details of this sample are in Section 5.10), with the fibre being very close to the surface. A series of images were captured at different distances from the facet by numerically propagating the transmission matrices to other planes. The figure shows the average measured intensity of the structures at each distance. The exact shape of the measured curves depends on the sample being imaged. That is, on the scattering properties of the tissue and on the structures being imaged (very bright structures could be imaged further away from the facet). In general, imaging with a sufficient signal-to-noise ratio was possible over a few tens of micrometres from the facet.

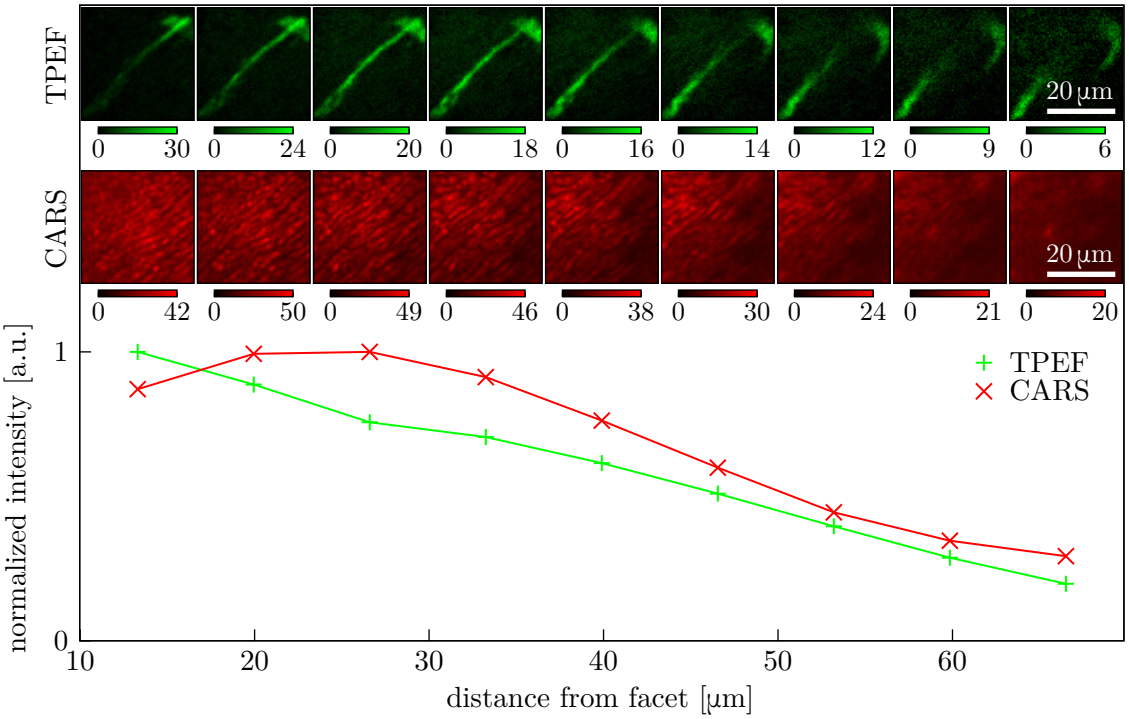

Figure 5.32: Intensity of CARS and TPEF signals inside of mouse brain (cerebellum) as a function of the working distance (distance of the focal plane from the facet). An overlay of the CARS and TPEF images for distance of 20 µm is shown in Figure 5.40. The lines are a guide to the eye.

5.10. Tissue imaging

The imaging capability of the fibre imaging system developed in this thesis was tested on two-photon excitation fluorescence and coherent anti-Stokes Raman scattering imaging of fixed mouse tissue. Brains and sciatic nerves were obtained from wild-type and transgenic Tg(Thy1-EGFP)MJrs/J adult mice. Mice were transcardially perfused with 4 % paraformaldehyde (PFA) and further fixed for 24 to 48 hours. The samples were then stored in phosphate-buffered saline (PBS) until imaging.

Before imaging, the samples were embedded in 2 % agarose in PBS to ensure the stability of the sample in the system during imaging (Figure 5.33). The agarose blocks were then attached to the sample stage and immersed in PBS.

A whole brain from the transgenic mouse was used to demonstrate two-photon excitation fluorescence imaging. For the first demonstration in Figure 5.34, the system was configured for CARS imaging. That is, the glass blocks for spectral focusing were installed in the system, stretching the laser pulses and decreasing the efficiency of two-photon excitation. In addition, both laser outputs were used, that is, wavelengths of 802 nm and 1040 nm. The non-degenerate excitation [208, 209] using the combination of two laser pulses yields an effective wavelength of about 905 nm, efficiently exciting the green fluorescent protein (GFP). The time overlap of the two beams was set to maximise the fluorescence signal. The composite probe was used, consisting of the YOFC FI2017-C graded-index fibre and 1 mm long step-index splice. Note that the images in Figure 5.34 were taken with the probe being inserted deeper than was the length of the splice, and part of the graded-index fibre, as well as the step at their interface, were thus inside

(a) Sciatic nerve (b) Mouse brain

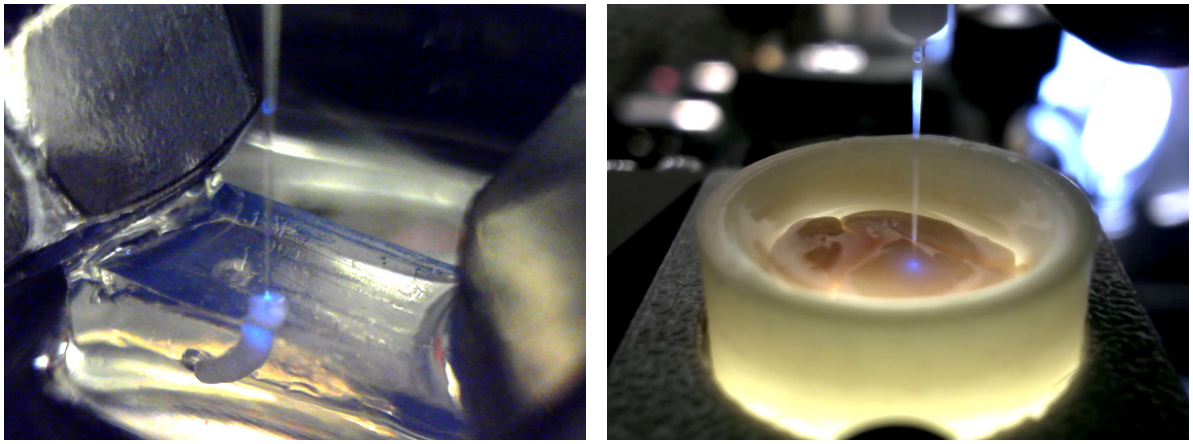

Figure 5.33: Examples of sample mounting. Both the sciatic nerve and mouse brain were mounted using agarose. The blue light came from LED1 in Figure 5.3 and was used for navigation over the sample. The images were captured using the webcam mounted in the setup and focused onto the distal end of the fibre.

the tissue, causing no issues with the insertion. This system configuration was chosen to demonstrate that it also allowed TPEF imaging. The total laser power in the plane was 69 mW and 114 mW for the tunable and fixed beams, respectively. Only part (determined by the power ratio) of the laser power was in the focused point, exciting the fluorescence. The rest was randomly spread across the field of view as a speckle pattern. The power ratios were about 61 % and 39 % for the tunable and fixed beam, respectively. The excitation powers thus were 42 mW and 45 mW for the tunable and fixed beam, respectively. The fibre was calibrated 30 µm from the facet. The diameter of the field of view during imaging was set to 66 µm, as the signal quickly dropped outside this area. The integration time was set to 2 ms, and the pixel pitch was 0.46 µm. This configuration resulted in each image taking about 100 s. The generated fluorescence was collected through the same multimode fibre (epi-detection). The images in Figure 5.34 show that the endoscope could perform TPEF imaging inside tissue with sufficient signal-to-noise ratio and image somas and surrounding processes and subcellular structures.

Figure 5.35 shows the sectioning capability of the endoscope. After the fibre was inserted into the brain, three images were taken at three focal planes by numerically propagating the transmission matrices to different planes. These images were performed using the composite consisting of the YOFC FI2017-C graded-index fibre and 1.5 mm long step-index splice. In addition, the probe was coated with a thin layer of parylene. Parylene is a hydrophobic polymer, which limits tissue sticking to the fibre facilitating smoother penetration of the probe into the tissue and its easier cleaning after the experiment. For the excitation, only the tunable beam of the laser was used this time, with the wavelength set to 920 nm. The glass blocks were removed from the system, and the pre-compensator built into the laser was set to 11000 fs^2 (which was the maximal value at this wavelength) to compensate for the dispersion in the system and the fibre and make the two-photon excitation efficient. The excitation power (in the focused point) was about 60 mW. The images in Figure 5.35 show that sectioning was achieved, as different structures could be imaged at different distances from the facet.

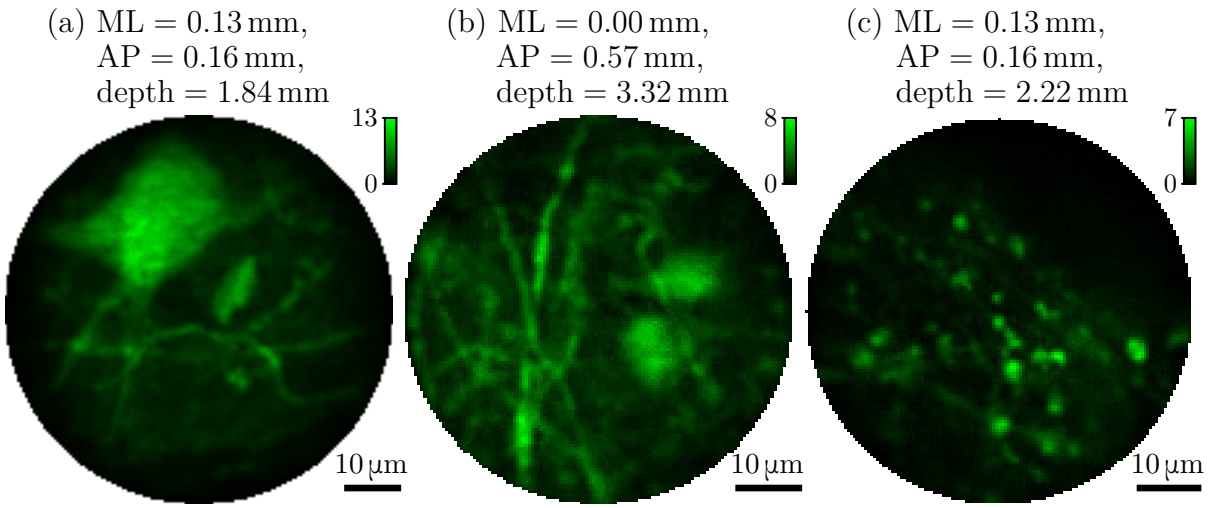

Figure 5.34: TPEF imaging inside different parts of a fixed transgenic mouse brain showing (a), (b) soma and surrounding processes, and (c) dendritic subcellular structures, possibly dendritic spines or axonal boutons. The captions show the approximate anterior-posterior (AP) and medial-lateral (ML) stereotaxic coordinates in reference to the bregma point and the depth at which the images were captured.

Label-free coherent anti-stokes Raman scattering imaging was demonstrated by imaging a sciatic nerve extracted from a wild-type mouse (Figure 5.36). The composite fibre probe was used, which consisted of the CREOL F3 graded-index fibre and a 2 mm long step-index splice. The probe was calibrated 30 µm from the facet at 802 nm (pump) and 1040 nm (Stokes), corresponding to Raman shift of 2853 cm^{-1} (optimal for exciting lipids). The power in the focused points was 52 mW (pump) and 28 mW (Stokes). The CARS signal was collected using the same multimode fibre (epi-detection). The diameter of the field of view was 66 µm; the pixel pitch was 0.23 µm and the integration time was set to 2 ms. The time overlap of the beams was set to maximise the contrast in the images. Figure 5.36 shows that the myelin sheaths surrounding the axons were visible as rings in the transversal cut and lines in the lateral cut of the sciatic nerve. The images showed no excessive background, confirming that the composite probe suppressed the signal generation in the fibre. An attempt was made to image the same sample using a pure CREOL F3 graded-index fibre (with no splice). However, the intensity of the background was so high that it was impossible to find any structures in the images.

The non-linear interaction of light with molecules during coherent anti-Stokes imaging results in excitation polarisation dependence of the generated signal [192, 193]. In the case of myelin, the intensity of the signal depends on the membrane orientation since the long lipid chains are always aligned perpendicular to the membrane [210]. As discussed in Section 5.4, the endoscope could generate any in-plane polarisation state of the focused point. This allowed demonstration of the polarisation sensitivity in Figure 5.37 on imaging myelin in a transverse section of the sciatic nerve.

In this demonstration, the three images were captured in a sequence. A complete image using horizontal polarisation was captured first, followed by the second image using vertical polarisation. If the sample moved during the imaging, the movement would result in a shift between the images, possibly making any analysis problematic. The endoscope, in principle, allowed complete random-access of the points (both their position and polarisation). Thus, the order of the polarisation and position of the point could

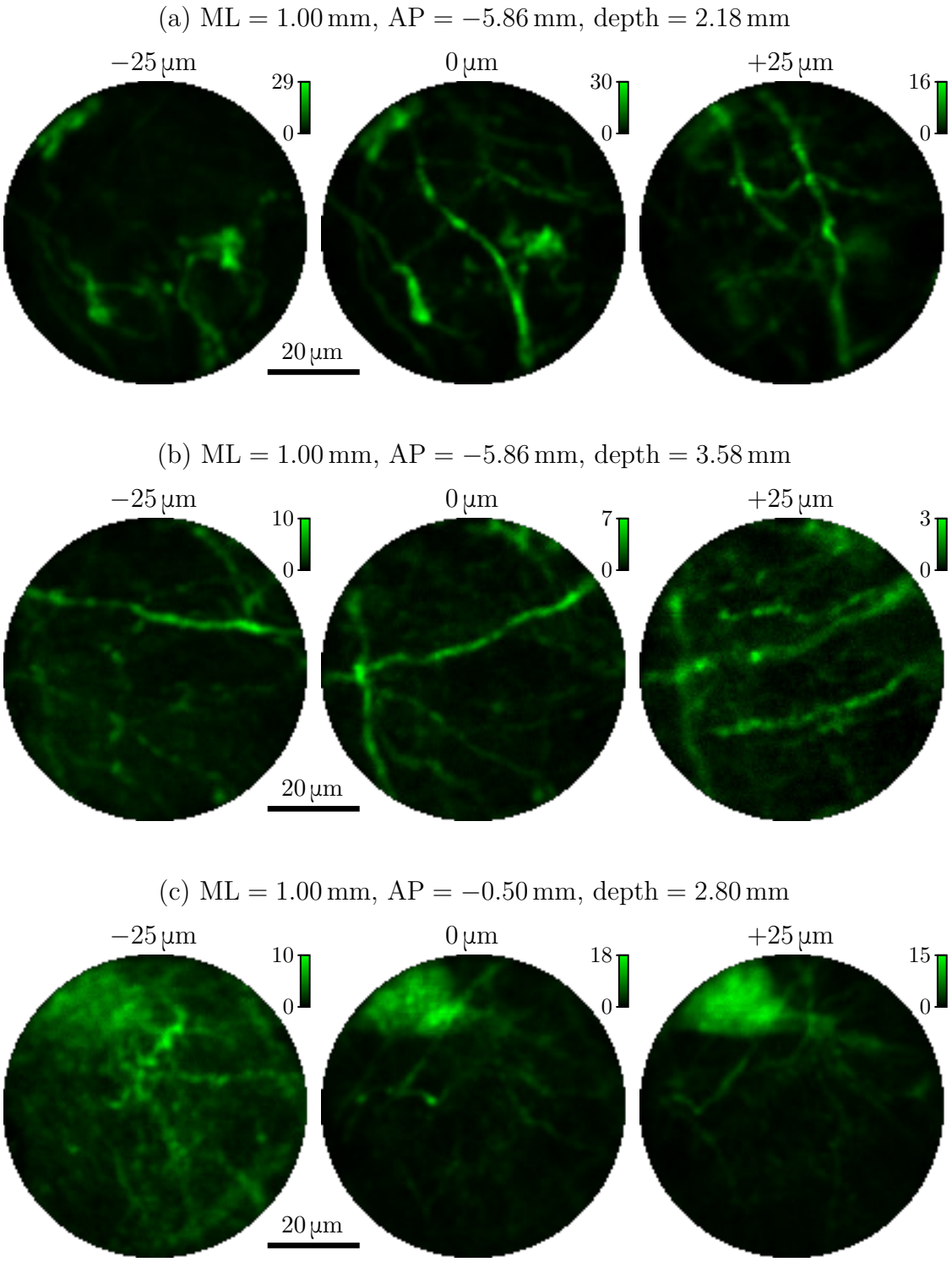

Figure 5.35: Demonstration of the sectioning capability of the endoscope during TPEF imaging inside a fixed mouse brain in (a), (b) cerebellum, and (c) subcortical structures. During each set of the three images, the fibre was stationary inside the tissue, and the refocus was achieved by applying a different sequence of holograms on the SLM. The captions show the approximate anterior-posterior (AP) and medial-lateral (ML) stereotaxic coordinates in reference to the bregma point and the depth at which the images were captured.

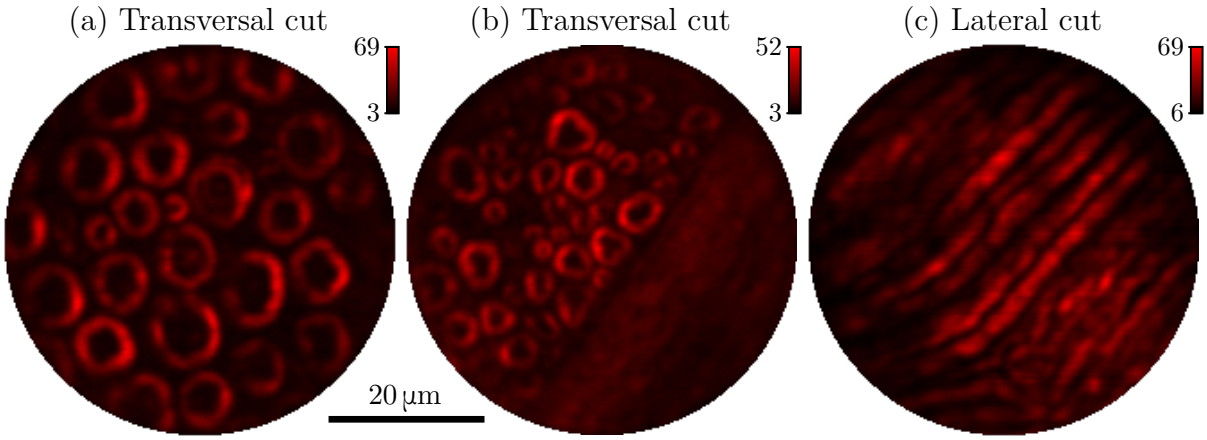

Figure 5.36: CARS images of a sciatic nerve taken from a wild-type mouse. All three images were taken on the surface of the sample.

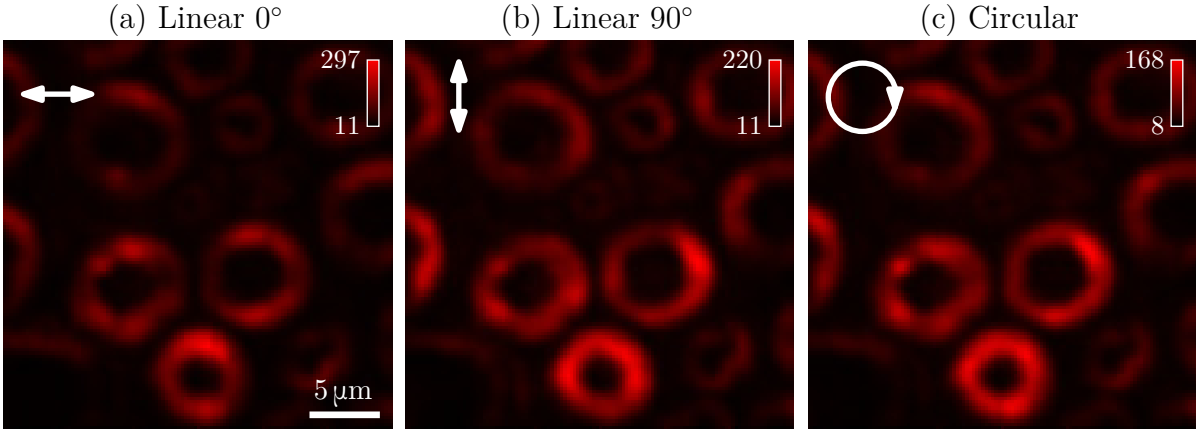

Figure 5.37: Excitation polarisation dependence of the CARS signal of myelin in a transverse section of the sciatic nerve taken from a wild-type mouse. The arrows show the polarisation direction of the excitation beams.

be interchanged. That is, the point would be scanned across the field of view only once, and for every position, multiple values using different polarisations would be measured. Multiple images would take the same time regardless of the order used. However, changing the polarisation during the scan would ensure the alignment of the resulting images. Alternatively, to measure the membrane orientation, only the pixels required for the analysis could be scanned (selected based on an initial full-frame scan done using a circular polarisation), as demonstrated on second-harmonic generation imaging in [187] using the endoscope and imaging software developed in this thesis.

The images above were taken using 2 ms integration time. To show shortening the integration time still allowed imaging, in Figure 5.38, the integration time was reduced to 0.5 ms, which still allowed imaging with a good signal-to-noise ratio. Compared to the demonstration in Chapter 4 (Figure 4.10), the decrease in the integration time had a significantly lower impact on the signal-to-noise ratio (despite the imaging being faster due to a shorter delay between individual pixels). This had three reasons. The most important was triggering the acquisition by the SLM, which synchronised the integration time with the refresh rate (flickering) of the SLM. In addition, the signal from the PMT was filtered using a 10 kHz third-order low-pass filter, which reduced the noise. Lastly,

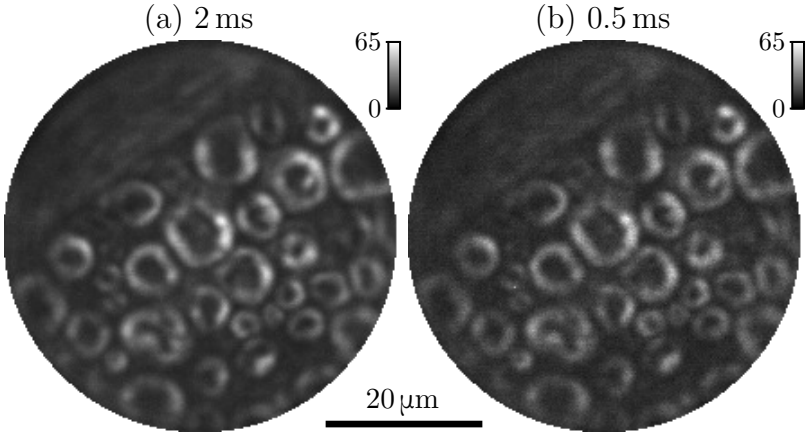

Figure 5.38: CARS images of a sciatic nerve captured using two different integration times.

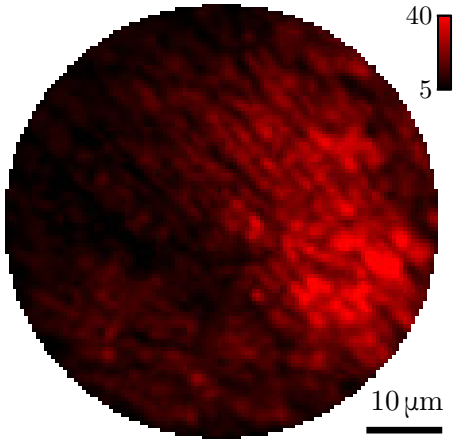

Figure 5.39: CARS image of myelin sheaths in the corpus callosum of mouse brain taken with the probe inserted 1.5 mm inside the tissue.

due to the changes in multiplexing of the individual analogue inputs of the DAQ card (see Figure 2.5c), the card captured 2.4 times more samples (when a single PMT was used) during the integration time compared to the configuration used in Chapter 4 and the crosstalk between the individual channels was reduced.

The images of the sciatic nerve were taken on the surface of the samples, as the fixed sciatic nerve was too hard to insert the fibre. To demonstrate imaging deep in tissue, myelinated nerve fibres in the corpus callosum were imaged in Figure 5.39. Here, the fibre was inserted about 1.5 mm deep into the tissue, significantly deeper than could be imaged in a standard scanning microscope.

In Figure 5.34, it was shown that the configuration of the endoscope typically used for CARS could be used for TPEF imaging as well, despite the stretched pulses, resulting in lower excitation efficiency. Consequently, it was possible to perform simultaneous two-photon excitation fluorescence and coherent anti-stokes Raman scattering imaging when two detectors with different filters were used. The multimodal CARS and TPEF imaging is demonstrated in Figure 5.40. In these images, a surface of a cut from the transgenic mouse brain cerebellum was imaged. The green TPEF channel shows the axons and the red CARS channel shows the myelin sheath. The TPEF image was sparse due to sparse labelling, while label-free CARS showed dense myelin structures in the focal plane.

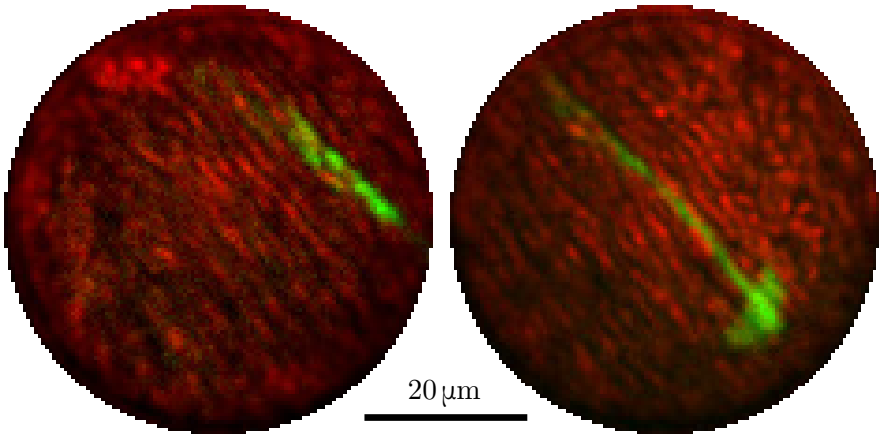

Figure 5.40: Multimodal CARS (red channel) and TPEF (green channel) imaging on the surface of a fixed cerebellum slice extracted out of a transgenic mouse brain. Both channels were recorded during a single scan on two different PMTs.

5.11. Summary

In this chapter, two-photon excitation fluorescence (TPEF) and coherent anti-Stokes Raman scattering (CARS) imaging through a single multimode fibre endoscope using a femtosecond laser was presented.

The system used in Chapter 4 was used and modified to utilise a femtosecond laser with two synchronised outputs (one of them with a tunable wavelength) as an excitation source. In addition, the prism-based SLM dispersion correction was implemented, and the timing of the data acquisition was triggered by the spatial light modulator (as discussed in Chapter 3), increasing the pixel rate up to about 170 Hz and decreasing the impact of the SLM refresh frequency (flickering) on the measured imaging data. The endoscope also employed polarisation control of the focused point. By changing the hologram on the SLM, any in-plane polarisation state of the point could be generated. Such polarisation control can be useful, especially for second-harmonic generation imaging.

After testing CARS imaging of polymer beads using the femtosecond laser, it was realised that a strong background was generated in the fibre probe. This signal, generated via four-wave mixing (FWM), arose from the self-imaging property of graded-index fibres. In essence, the focused points were created not only in the sample plane but also inside the fibre generating a strong background signal, spectrally overlapping with the CARS signal.

In Chapter 4, CARS imaging of PS and PMMA beads was performed using a picosecond laser system. The Prysmian fibre was used, and no noticeable unwanted background signal was observed. When the same fibre was used with the femtosecond laser to probe the same Raman shift, a very strong signal was generated in the fibre. In fact, at this Raman shift and using this fibre, the intensity of the background generated in the fibre was so strong that its suppression by more than an order of magnitude was insufficient to image the polystyrene beads. The reason for this immense difference, unfortunately, remained unexplained. When the strong background in the Prysmian fibre was discovered, performing additional characterisations using the same or a different picosecond laser system was no longer practicable. Since only one of the femtosecond laser outputs was tunable, measuring using different wavelengths (and the same Raman shifts)

was impossible. Thus, it was impossible to determine if the background was caused by using femtosecond pulses (despite the pulses being stretched to about one picosecond for spectral focusing), an unfortunate choice of wavelengths or whether there were other causes.

Since the primary cause of the background was not known, the sources of the background had to be suppressed. The field inside the fibre had to be broken into a low-intensity random speckle pattern and uncorrelated for the two wavelengths used for CARS. Completely replacing the graded-index fibre with a step-index fibre (which does not have the self-imaging property and would thus not create the foci) was not feasible due to the low bandwidth. Consequently, a short piece ($\leq 5\,\mathrm{mm}$) of a step-index fibre was used and fusion-spliced at the distal end of the graded-index fibre. Thus, the resulting composite probe behaved more like a graded-index fibre and had a relatively high bandwidth while not generating the high-intensity points inside the fibre.

The composite probes consisting of YOFC GI2017-C or a custom-drawn CREOL F3 graded-index fibre and a splice made out of CeramOptec Optran Ultra WFGE step-index fibre (tapered to have the same core diameter as the graded-index fibre) allowed imaging of polymer beads on a glass slide. Adding even a 0.25 mm long splice reduced the background. The total reduction was one to two orders of magnitude, depending on the splice length and the Raman shift used. The intensity of the background dropped significantly with the increasing length of the splice. At the same time, however, the intensity of the signal generated in the sample decreased as well. By CARS imaging of polystyrene beads (at $3059\,\mathrm{cm}^{-1}$) and characterising of the background suppression over a wider range of Raman shift ($2807\,\mathrm{cm}^{-1}$ to $3107\,\mathrm{cm}^{-1}$, which covers the typical Raman shifts used for bio-imaging) the optimal length of the splice was found to be about 1 mm to 2 mm.

The focusing performance of the composite probes was tested. It was found that adding a few millimetres long splice to the graded-index fibre had only a small impact on the achievable power ratios and spot size. The bandwidth, and thus the wavelength tuning range after the calibration, decreased with the increasing length of the splice. However, this decrease for the short splices was also slight and was caused mainly by the focused point shifting axially with wavelength, as expected from a step-index fibre. The dispersion measurement showed that adding the splice had minimal effect on the group delay dispersion introduced by the fibre. The splice, however, added negative third-order dispersion. The values were, however, comparable to the dispersion introduced by other optical elements in the endoscope. The negligible impact of the splice on the foci and the dispersion was also verified by TPEF imaging of fluorescent beads.

Tissue imaging using the composite probes was performed to test the background suppression on a more realistic sample. Probes consisting of two different graded-index fibres and different lengths of the step-index fibre were used to image myelinated nerve fibres in a sciatic nerve extracted from a mouse and in the cerebellum of a mouse brain. The images had sufficient contrast without any noticeable background. When trying to image with a graded-index fibre without the splice, the intensity of the background signal generated in the fibre was so high that no structures were visible. These images showed that adding the short splice to the distal end of the graded-index fibre effectively suppressed the background and made label-free CARS imaging of biologically relevant structures possible. The epi-detection was possible despite the CARS signal being generated predominantly in the forward direction (thus epi-detection relying on scattering in the underlying tissue) and the small collection area of the fibre probe.

In addition to CARS, TPEF imaging of neurons in a fixed transgenic mouse brain was shown. The sectioning capability was demonstrated by numerically propagating the transmission matrices of the fibre into different planes and thus shifting the focal plane (refocusing) by only changing the holograms projected on the spatial light modulator. The two non-linear imaging techniques were combined to perform multimodal imaging in the fixed cerebellum.

The presented work thus showed that multimodal imaging through a multimode fibre of structures deep is possible with a sufficient signal-to-background ratio by performing simultaneous CARS imaging of myelin in the white matter, and TPEF imaging of mossy fibres expressing GFP in the cerebellum of a fixed brain from a mouse.

The suppression of the background generated in the fibre, the characterisation of the composite probes and the multimodal CARS and TPEF imaging presented in this chapter were published in [70]. Furthermore, the fibre imaging system built for this work was used for the implementation of polarisation-resolved second-harmonic generation imaging through a multimode fibre (not part of this thesis), published in [187]. The fibre polishing system presented here was used for the preparation of the side-view probes in [77], which were used for in-vivo linear fluorescence imaging in mouse brain published in [43].

Conclusions

The presented thesis deals with non-linear imaging through a multimode fibre endoscope. The thesis was focused mainly on the technical aspects of implementing non-linear imaging using multimode fibres. The goal was to implement two-photon excitation fluorescence (TPEF) and coherent anti-Stokes scattering (CARS) imaging through a single multimode fibre endoscope.

The first chapter was a brief introduction to the multimode fibre calibration procedure which is needed to turn a single multimode fibre into a point scanning microscope with a small footprint. The endoscope was then built, characterised and optimised in the second chapter.

The third chapter investigated the bandwidth of a multimode fibre imaging system and its impact on focusing a femtosecond laser beam through the multimode fibre. It was found that compensating the dispersion of the off-axis holograms displayed on the spatial light modulator was necessary to use the entire bandwidth of the fibres. As expected, a bandwidth of reasonably long (at least 30 mm) step-index fibre was found too low for using it with a femtosecond laser, making graded-index fibres the type of choice. Nevertheless, a significant difference between the different graded-index fibres tested further emphasised the need for proper selection of the fibre for non-linear imaging applications. This study, partially published in [68], was a substantial step towards efficiently focusing laser pulses through a multimode fibre. Moreover, it enabled implementing non-linear imaging techniques through a single multimode fibre, mainly CARS imaging.

CARS microscopy through a single multimode fibre was demonstrated in the fourth chapter. CARS imaging of polystyrene and polymethyl methacrylate beads on a glass slide was performed using a picosecond laser and the fibre imaging system developed in the previous chapter. This demonstration, published in [69], has the potential to be the least invasive and fastest label-free endoscopic bio-imaging method with chemical contrast reported so far. It demonstrates that it is feasible to perform CARS imaging through a multimode fibre of structures as small as 2 μm with integration times as low as 1 ms. Despite the low collection efficiency of the probe, epi-detection was successfully demonstrated, which paves the way for other non-linear imaging techniques such as stimulated Raman spectroscopy (SRS) or third-harmonic generation (THG), where the epi-detection relies mainly on scattering.

The fifth chapter presented multimodal CARS and TPEF imaging through a multimode fibre. When implementing CARS imaging and using a femtosecond excitation source, a strong background signal generated in the graded-index fibre probe was discovered, which diminished the contrast of the images. This signal was a direct consequence of the self-imaging property of the graded-index fibre, which resulted in high-intensity points inside the probe. A composite probe consisting of a long graded-index fibre and a few millimetres long step-index fibre spliced at the distal end of the probe was proposed

to mitigate the issue. This probe, published in [70] and patented, reduced the background by more than an order of magnitude while maintaining sufficient bandwidth for focusing femtosecond pulses, an essential step for CARS imaging of tissue.

The research in this thesis increased the capabilities of multimode fibre endoscopes by CARS imaging. It led to the implementation of SHG imaging (which is not part of this thesis but was demonstrated in [187] using the imaging system developed in this thesis). These techniques, together with TPEF (also shown here) form a basis for optical biopsies. Implementing them through the miniature multimode fibre thus could lead towards diagnosing tumours deep in tissue with minimal damage.

While the presented work showed that it is feasible to perform non-linear imaging techniques, including label-free imaging, through a multimode fibre, there is still a long way towards a practical implementation for, for example, clinical applications. In addition, some issues with the current implementation remained unsolved. Thus, the first step of follow-up research should be to address the two issues with CARS imaging with a femtosecond laser that have not been fully explained here, namely, the exact source of the background signal generated in the fibre and the reduced spectral resolution of CARS compared to a microscope. While the background was suppressed sufficiently to allow imaging, narrowing down its exact source would require performing additional measurements using the picosecond laser system and using a femtosecond laser system at different wavelengths (neither of which was possible at the time of discovering the background) as well as another type of graded-index fibres. As for the reduced spectral resolution, this would require a more in-depth characterisation of the pulses in the sample plane.

Another technological progress could be made in developing the multimode fibre probes. Tissue imaging would greatly benefit from using the side-view probes, now commonly used within ISI Complex Photonics group for linear imaging in-vivo. In addition, the probes should ideally have a larger numerical aperture. While the highest numerical aperture of currently commercially available graded-index fibres is about 0.30, advances in manufacturing fibres and graded-index lenses could potentially allow higher values. A dimensionally more suitable pair of step-index and graded-index fibre should be found if it is necessary to continue using the composite probe for background suppression.

A substantial step towards applications would be to implement the non-linear techniques using a digital micromirror device (DMD) as a spatial light modulator, used commonly for linear imaging through multimode fibres. DMDs offer about two orders of magnitude higher frame rates than liquid-crystal spatial light modulators. Their low efficiency (caused by a binary amplitude modulation) and high dispersion makes them challenging to use with pulsed light sources for non-linear imaging techniques, where high excitation powers and proper control over the dispersion are necessary. This could, however, change soon when phase-modulating micromirror devices (PLMs) become commercially available. Currently, these devices from Texas Instruments are only available as samples. Combining a PLM with a higher-power laser system would allow non-linear imaging with frame rates more suitable for in-vivo applications.

These steps would then open the possibilities for biological applications. Thus, the next step would be testing tissue imaging, including diagnosing tumorous tissue or other pathological states. Showing that such determination could be done in-vivo would set the scene for possible clinical applications of the endoscope.

References

[1] THEER, Patrick and Winfried DENK. On the Fundamental Imaging-Depth Limit in Two-Photon Microscopy. *Journal of the Optical Society of America A*. 2006, vol. 23, no. 12, pp. 3139–3149. ISSN 1520-8532. Available from: doi:10.1364/JOSAA.23.003139.

[2] GU, Min, Xiaosong GAN, Aernout KISTEMAN and Ming Gun XU. Comparison of Penetration Depth between Two-Photon Excitation and Single-Photon Excitation in Imaging through Turbid Tissue Media. *Applied Physics Letters*. 2000, vol. 77, no. 10, pp. 1551–1553. ISSN 1077-3118. Available from: doi:10.1063/1.1308059.

[3] DENG, Xiaoyuan and Min GU. Penetration Depth of Single-, Two-, and Three-Photon Fluorescence Microscopic Imaging through Human Cortex Structures: Monte Carlo Simulation. *Applied Optics*. 2003, vol. 42, no. 16, pp. 3321–3329. ISSN 1539-4522. Available from: doi:10.1364/AO.42.003321.

[4] XIAO, Yujie, Peng DENG, Yaoguang ZHAO, Shasha YANG and Bo LI. Three-Photon Excited Fluorescence Imaging in Neuroscience: From Principles to Applications. *Frontiers in Neuroscience*. 2023, vol. 17, pp. 1085682. ISSN 1662-453X. Available from: doi:10.3389/fnins.2023.1085682.

[5] YILDIRIM, Murat, Hiroki SUGIHARA, Peter T. C. SO and Mriganka SUR. Functional Imaging of Visual Cortical Layers and Subplate in Awake Mice with Optimized Three-Photon Microscopy. *Nature Communications*. 2019, vol. 10, no. 1, pp. 177. ISSN 2041-1723. Available from: doi:10.1038/s41467-018-08179-6.

[6] JI, Na, Daniel E. MILKIE and Eric BETZIG. Adaptive Optics via Pupil Segmentation for High-Resolution Imaging in Biological Tissues. *Nature Methods*. 2010, vol. 7, no. 2, pp. 141–147. ISSN 1548-7105. Available from: doi:10.1038/nmeth.1411.

[7] MITTMANN, Wolfgang, Damian J. WALLACE, Uwe CZUBAYKO, Jan T. HERB, Andreas T SCHAEFER, Loren L. LOOGER, Winfried DENK and Jason N. D. KERR. Two-Photon Calcium Imaging of Evoked Activity from L5 Somatosensory Neurons in Vivo. *Nature Neuroscience*. 2011, vol. 14, no. 8, pp. 1089–1093. ISSN 1546-1726. Available from: doi:10.1038/nn.2879.

[8] TZANG, Omer, Eyal NIV, Sakshi SINGH, Simon LABOUESSE, Greg MYATT and Rafael PIESTUN. Wavefront Shaping in Complex Media with a 350 kHz Modulator via a 1D-to-2D Transform. *Nature Photonics*. 2019, vol. 13, no. 11, pp. 788–793. ISSN 1749-4893. Available from: doi:10.1038/s41566-019-0503-6.

[9] GIGAN, Sylvain, Ori KATZ, Hilton B. de AGUIAR, Esben Ravn ANDRESEN, Alexandre AUBRY, Jacopo BERTOLOTTI, Emmanuel BOSSY, Dorian BOUCHET, Joshua BRAKE, Sophie BRASSELET, Yaron BROMBERG, Hui CAO, Thomas CHAIGNE, Zhongtao CHENG, Wonshik CHOI, Tomáš ČIŽMÁR, Meng CUI, Vincent R. CURTIS, Hugo DEFIENNE, Matthias HOFER, Ryoichi HORISAKI, Roarke HORSTMEYER, Na JI, Aaron K. LAVIOLETTE, Jerome MERTZ, Christophe MOSER, Allard P. MOSK, Nicolas C. PÉGARD, Rafael PIESTUN, Sebastien POPOFF, David B. PHILLIPS, Demetri PSALTIS, Babak RAHMANI, Hervé RIGNEAULT, Stefan ROTTER, Lei TIAN, Ivo M. VELLEKOOP, Laura WALLER, Lihong WANG, Timothy WEBER, Sheng XIAO, Chris XU, Alexey YAMILOV, Changhuei YANG and Hasan YILMAZ. Roadmap on Wavefront Shaping and Deep Imaging in Complex Media. *Journal of Physics: Photonics*. 2022, vol. 4, no. 4, pp. 042501. ISSN 2515-7647. Available from: doi:10.1088/2515-7647/ac76f9.

[10] CAO, Hui, Allard Pieter MOSK and Stefan ROTTER. Shaping the Propagation of Light in Complex Media. *Nature Physics*. 2022, vol. 18, no. 9, pp. 994–1007. ISSN 1745-2473. Available from: doi:10.1038/s41567-022-01677-x.

[11] FLUSBERG, Benjamin A., Eric D. COCKER, Wibool PIYAWATTANAMETHA, Juergen C. JUNG, Eunice L. M. CHEUNG and Mark J. SCHNITZER. Fiber-Optic Fluorescence Imaging. *Nature Methods*. 2005, vol. 2, no. 12, pp. 941–950. ISSN 1548-7105. Available from: doi:10.1038/nmeth820.

[12] HOPKINS, H. H. and N. S. KAPANY. A Flexible Fibrescope, Using Static Scanning. *Nature*. 1954, vol. 173, no. 4392, pp. 39–41. ISSN 1476-4687. Available from: doi:10.1038/173039b0.

[13] ORTH, Antony, Martin PLÖSCHNER, Emma. R. WILSON, Ivan S. MAKSYMOV and Brant C. GIBSON. Optical Fiber Bundles: Ultra-slim Light Field Imaging Probes. *Science Advances*. 2019, vol. 5, no. 4, pp. eaav1555. ISSN 2375-2548. Available from: doi:10.1126/sciadv.aav1555.

[14] GÖBEL, Werner, Jason N. D. KERR, Axel NIMMERJAHN and Fritjof HELMCHEN. Miniaturized Two-Photon Microscope Based on a Flexible Coherent Fiber Bundle and a Gradient-Index Lens Objective. *Optics Letters*. 2004, vol. 29, no. 21, pp. 2521–2523. ISSN 1539-4794. Available from: doi:10.1364/OL.29.002521.

[15] JUNG, Juergen C. and Mark J. SCHNITZER. Multiphoton Endoscopy. *Optics Letters*. 2003, vol. 28, no. 11, pp. 902–904. ISSN 1539-4794. Available from: doi:10.1364/OL.28.000902.

[16] FLUSBERG, Benjamin A., Juergen C. JUNG, Eric D. COCKER, Erik P. ANDERSON and Mark J. SCHNITZER. In Vivo Brain Imaging Using a Portable 39 Gram Two-Photon Fluorescence Microendoscope. *Optics Letters*. 2005, vol. 30, no. 17, pp. 2272–2274. ISSN 1539-4794. Available from: doi:10.1364/OL.30.002272.

[17] GHOSH, Kunal K., Laurie D. BURNS, Eric D. COCKER, Axel NIMMERJAHN, Yaniv ZIV, Abbas El. GAMAL and Mark J. SCHNITZER. Miniaturized Integration of a Fluorescence Microscope. *Nature Methods*. 2011, vol. 8, no. 10, pp. 871–878. ISSN 1548-7105. Available from: doi:10.1038/nmeth.1694.

[18] BOCARSLY, Miriam E., Wan-chen JIANG, Chen WANG, Joshua T. DUDMAN, Na JI and Yeka APONTE. Minimally Invasive Microendoscopy System for in Vivo Functional Imaging of Deep Nuclei in the Mouse Brain. *Biomedical Optics Express*. 2015, vol. 6, no. 11, pp. 4546–4556. ISSN 2156-7085. Available from: doi:10.1364/BOE.6.004546.

[19] AHARONI, Daniel and Tycho M. HOOGLAND. Circuit Investigations With Open-Source Miniaturized Microscopes: Past, Present and Future. *Frontiers in Cellular Neuroscience*. 2019, vol. 13, pp. 141. ISSN 1662-5102. Available from: doi:10.3389/fncel.2019.00141.

[20] CAMPOS, Pauline, Jamie J. WALKER and Patrice MOLLARD. Diving into the Brain: Deep-Brain Imaging Techniques in Conscious Animals. *Journal of Endocrinology*. 2020, vol. 246, no. 2, pp. R33–R50. ISSN 1479-6805. Available from: doi:10.1530/JOE-20-0028.

[21] ANTONINI, Andrea, Andrea SATTIN, Monica MORONI, Serena BOVETTI, Claudio MORETTI, Francesca SUCCOL, Angelo FORLI, Dania VECCHIA, Vijayakumar P. RAJAMANICKAM, Andrea BERTONCINI, Stefano PANZERI, Carlo LIBERALE and Tommaso FELLIN. Extended Field-of-View Ultrathin Microendoscopes for High-Resolution Two-Photon Imaging with Minimal Invasiveness. *eLife*. 2020, vol. 9, pp. e58882. ISSN 2050-084X. Available from: doi:10.7554/eLife.58882.

[22] STAMATAKIS, Alice M, Shanna L. RESENDEZ, Kai-Siang CHEN, Morgana FAVERO, Jing LIANG-GUALLPA, Jonathan J. NASSI, Shay Q. NEUFELD, Koen VISSCHER and Kunal K. GHOSH. Miniature Microscopes for Manipulating and Recording in Vivo Brain Activity. *Microscopy*. 2021, vol. 70, no. 5, pp. 399–414. ISSN 2050-5701. Available from: doi:10.1093/jmicro/dfab028.

[23] WANG, Taejun, Qingyun LI, Peng XIAO, Jinhyo AHN, Young Eun KIM, Youngrong PARK, Minjun KIM, Miyeoun SONG, Euiheon CHUNG, Wan Kyun CHUNG, G-One AHN, Sungjee KIM, Pilhan KIM, Seung-Jae MYUNG and Ki Hean KIM. Gradient Index Lens Based Combined Two-Photon Microscopy and Optical Coherence Tomography. *Optics Express*. 2014, vol. 22, no. 11, pp. 12962–12970. ISSN 1094-4087. Available from: doi:10.1364/OE.22.012962.

[24] BARRETTO, Robert P. J., Tony H. KO, Juergen C. JUNG, Tammy J. WANG, George CAPPS, Allison C. WATERS, Yaniv ZIV, Alessio ATTARDO, Lawrence RECHT and Mark J. SCHNITZER. Time-Lapse Imaging of Disease Progression in Deep Brain Areas Using Fluorescence Microendoscopy. *Nature Medicine*. 2011, vol. 17, no. 2, pp. 223–228. ISSN 1078-8956. Available from: doi:10.1038/nm.2292.

[25] BARBERA, Giovanni, Rachel JUN, Yan ZHANG, Bo LIANG, Yun LI and Da-Ting LIN. A Miniature Fluorescence Microscope for Multi-Plane Imaging. *Scientific Reports*. 2022, vol. 12, no. 1, pp. 16686. ISSN 2045-2322. Available from: doi:10.1038/s41598-022-21022-9.

[26] ČIŽMÁR, Tomáš and Kishan DHOLAKIA. Shaping the Light Transmission through a Multimode Optical Fibre: Complex Transformation Analysis and Applications in Biophotonics. *Optics Express*. 2011, vol. 19, no. 20, pp. 18871–18884. ISSN 1094-4087. Available from: doi:10.1364/OE.19.018871.

[27] DI LEONARDO, Roberto and Silvio BIANCHI. Hologram Transmission through Multi-Mode Optical Fibers. *Optics Express*. 2011, vol. 19, no. 1, pp. 247–254. ISSN 1094-4087. Available from: doi:10.1364/OE.19.000247.

[28] MAHALATI, Reza Nasiri, Ruo Yu GU and Joseph M. KAHN. Resolution Limits for Imaging through Multi-Mode Fiber. *Optics Express*. 2013, vol. 21, no. 2, pp. 1656–1668. ISSN 1094-4087. Available from: doi:10.1364/OE.21.001656.

[29] PAPADOPOULOS, Ioannis N., Salma FARAHI, Christophe MOSER and Demetri PSALTIS. Increasing the Imaging Capabilities of Multimode Fibers by Exploiting the Properties of Highly Scattering Media. *Optics Letters*. 2013, vol. 38, no. 15, pp. 2776–2778. ISSN 1539-4794. Available from: doi:10.1364/OL.38.002776.

[30] MAURER, Christian, Alexander JESACHER, Stefan BERNET and Monika RITSCH-MARTE. What Spatial Light Modulators Can Do for Optical Microscopy. *Laser & Photonics Reviews*. 2011, vol. 5, no. 1, pp. 81–101. ISSN 1863-8880. Available from: doi:10.1002/lpor.200900047.

[31] TURTAEV, Sergey, Ivo T. LEITE, Kevin J. MITCHELL, Miles J. PADGETT, David B. PHILLIPS and Tomáš ČIŽMÁR. Comparison of Nematic Liquid-Crystal and DMD Based Spatial Light Modulation in Complex Photonics. *Optics Express*. 2017, vol. 25, no. 24, pp. 29874. ISSN 1094-4087. Available from: doi:10.1364/OE.25.029874.

[32] RUDOLF, Benjamin, Yang DU, Sergey TURTAEV, Ivo T. LEITE and Tomáš ČIŽMÁR. Thermal Stability of Wavefront Shaping Using a DMD as a Spatial Light Modulator. *Optics Express*. 2021, vol. 29, no. 25, pp. 41808. ISSN 1094-4087. Available from: doi:10.1364/OE.442284.

[33] CARAVACA-AGUIRRE, Antonio M., Eyal NIV, Donald B. CONKEY and Rafael PIESTUN. Real-Time Resilient Focusing through a Bending Multimode Fiber. *Optics Express*. 2013, vol. 21, no. 10, pp. 12881–12887. ISSN 1094-4087. Available from: doi:10.1364/OE.21.012881.

[34] LOTERIE, Damien, Demetri PSALTIS and Christophe MOSER. Bend Translation in Multimode Fiber Imaging. *Optics Express*. 2017, vol. 25, no. 6, pp. 6263–6273. ISSN 1094-4087. Available from: doi:10.1364/OE.25.006263.

[35] LIU, Yan, Guangde LI, Qi QIN, Zhongwei TAN, Muguang WANG and Fengping YAN. Bending Recognition Based on the Analysis of Fiber Specklegrams Using Deep Learning. *Optics & Laser Technology*. 2020, vol. 131, pp. 106424. ISSN 00303992. Available from: doi:10.1016/j.optlastec.2020.106424.

[36] FARAHI, Salma, David ZIEGLER, Ioannis N. PAPADOPOULOS, Demetri PSALTIS and Christophe MOSER. Dynamic Bending Compensation While Focusing through a Multimode Fiber. *Optics Express*. 2013, vol. 21, no. 19, pp. 22504–22514. ISSN 1094-4087. Available from: doi:10.1364/OE.21.022504.

[37] GU, Ruo Yu, Reza Nasiri MAHALATI and Joseph M. KAHN. Design of Flexible Multi-Mode Fiber Endoscope. *Optics Express*. 2015, vol. 23, no. 21, pp. 26905–26918. ISSN 1094-4087. Available from: doi:10.1364/OE.23.026905.

[38] BOONZAJER FLAES, Dirk E., Jan STOPKA, Sergey TURTAEV, Johannes F. de BOER, Tomáš TYC and Tomáš ČIŽMÁR. Robustness of Light-Transport Processes to Bending Deformations in Graded-Index Multimode Waveguides. *Physical Review Letters*. 2018, vol. 120, no. 23, pp. 233901. ISSN 0031-9007. Available from: doi:10.1103/PhysRevLett.120.233901.

[39] PAPADOPOULOS, Ioannis N., Salma FARAHI, Christophe MOSER and Demetri PSALTIS. High-Resolution, Lensless Endoscope Based on Digital Scanning through a Multimode Optical Fiber. *Biomedical Optics Express*. 2013, vol. 4, no. 2, pp. 260–270. ISSN 2156-7085. Available from: doi:10.1364/BOE.4.000260.

[40] OHAYON, Shay, Antonio CARAVACA-AGUIRRE, Rafael PIESTUN and James J. DICARLO. Minimally Invasive Multimode Optical Fiber Microendoscope for Deep Brain Fluorescence Imaging. *Biomedical Optics Express*. 2018, vol. 9, no. 4, pp. 1492–1509. ISSN 2156-7085. Available from: doi:10.1364/BOE.9.001492.

[41] TURTAEV, Sergey, Ivo T. LEITE, Tristan ALTWEGG-BOUSSAC, Janelle M. P. PAKAN, Nathalie L. ROCHEFORT and Tomáš ČIŽMÁR. High-Fidelity Multimode Fibre-Based Endoscopy for Deep Brain in Vivo Imaging. *Light: Science & Applications*. 2018, vol. 7, no. 92. ISSN 2047-7538. Available from: doi:10.1038/s41377-018-0094-x.

[42] VASQUEZ-LOPEZ, Sebastian A., Raphaël TURCOTTE, Vadim KOREN, Martin PLÖSCHNER, Zahid PADAMSEY, Martin J. BOOTH, Tomáš ČIŽMÁR and Nigel J. EMPTAGE. Subcellular Spatial Resolution Achieved for Deep-Brain Imaging in Vivo Using a Minimally Invasive Multimode Fiber. *Light: Science & Applications*. 2018, vol. 7, no. 110. ISSN 2047-7538. Available from: doi:10.1038/s41377-018-0111-0.

[44] WEN, Zhong, Liqiang WANG, Xuanhao ZHANG, Yaoguang MA, Xu LIU, Clemens KAMINSKI and Qing YANG. Fast Volumetric Fluorescence Imaging with Multimode Fibers. *Optics Letters*. 2020, vol. 45, no. 17, pp. 4931–4934. ISSN 1539-4794. Available from: doi:10.1364/OL.398177.

[45] CHOI, Youngwoon, Changhyeong YOON, Moonseok KIM, Taeseok Daniel YANG, Christopher FANG-YEN, Ramachandra R. DASARI, Kyoung Jin LEE and Wonshik CHOI. Scanner-Free and Wide-Field Endoscopic Imaging by Using a Single Multimode Optical Fiber. *Physical Review Letters*. 2012, vol. 109, no. 20, pp. 203901. ISSN 0031-9007. Available from: doi:10.1103/PhysRevLett.109.203901.

[46] ČIŽMÁR, Tomáš and Kishan DHOLAKIA. Exploiting Multimode Waveguides for Pure Fibre-Based Imaging. *Nature Communications*. 2012, vol. 3, no. 1027. ISSN 2041-1723. Available from: doi:10.1038/ncomms2024.

[47] LEITE, Ivo T., Sergey TURTAEV, Dirk E. BOONZAJER FLAES and Tomáš ČIŽMÁR. Observing Distant Objects with a Multimode Fiber-Based Holographic Endoscope. *APL Photonics*. 2021, vol. 6, no. 3, pp. 036112. ISSN 2378-0967. Available from: doi:10.1063/5.0038367.

[48] PLÖSCHNER, Martin, Věra KOLLÁROVÁ, Zbyněk DOSTÁL, Jonathan NYLK, Thomas BARTON-OWEN, David E. K. FERRIER, Radim CHMELÍK, Kishan DHOLAKIA and Tomáš ČIŽMÁR. Multimode Fibre: Light-sheet Microscopy at the Tip of a Needle. *Scientific Reports*. 2016, vol. 5, no. 1, pp. 18050. ISSN 2045-2322. Available from: doi:10.1038/srep18050.

[49] LOTERIE, Damien, Salma FARAHI, Ioannis PAPADOPOULOS, Alexandre GOY, Demetri PSALTIS and Christophe MOSER. Digital Confocal Microscopy through a Multimode Fiber. *Optics Express*. 2015, vol. 23, no. 18, pp. 23845–23858. ISSN 1094-4087. Available from: doi:10.1364/OE.23.023845.

[50] LOTERIE, Damien, Sebastianus A. GOORDEN, Demetri PSALTIS and Christophe MOSER. Confocal Microscopy through a Multimode Fiber Using Optical Correlation. *Optics Letters*. 2015, vol. 40, no. 24, pp. 5754–5757. ISSN 1539-4794. Available from: doi:10.1364/OL.40.005754.

[51] MORALES-DELGADO, Edgar E., Demetri PSALTIS and Christophe MOSER. Two-Photon Imaging through a Multimode Fiber. *Optics Express*. 2015, vol. 23, no. 25, pp. 32158–32170. ISSN 1094-4087. Available from: doi:10.1364/OE.23.032158.

[52] SIVANKUTTY, Siddharth, Esben Ravn ANDRESEN, Rosa COSSART, Géraud BOUWMANS, Serge MONNERET and Hervé RIGNEAULT. Ultra-Thin Rigid Endoscope: Two-Photon Imaging through a Graded-Index Multi-Mode Fiber. *Optics Express*. 2016, vol. 24, no. 2, pp. 825–841. ISSN 1094-4087. Available from: doi:10.1364/OE.24.000825.

[53] KAKKAVA, Eirini, Marilisa ROMITO, Donald B. CONKEY, Damien LOTERIE, Konstantina M. STANKOVIC, Christophe MOSER and Demetri PSALTIS. Selective Femtosecond Laser Ablation via Two-Photon Fluorescence Imaging through a Multimode Fiber. *Biomedical Optics Express*. 2019, vol. 10, no. 2, pp. 423–433. ISSN 2156-7085. Available from: doi:10.1364/BOE.10.000423.

[54] TURCOTTE, Raphaël, Carla C. SCHMIDT, Martin J. BOOTH and Nigel J. EMPTAGE. Volumetric Two-Photon Fluorescence Imaging of Live Neurons Using a Multimode Optical Fiber. *Optics Letters*. 2020, vol. 45, no. 24, pp. 6599–6602. ISSN 1539-4794. Available from: doi:10.1364/OL.409464.

[55] MEZIL, Sylvain, Antonio M. CARAVACA-AGUIRRE, Philippe MOREAU, Irène WANG, Paul C. BEARD and Emmanuel BOSSY. Single-Shot Hybrid Photoacoustic-Fluorescent Microendoscopy through a Multi-Mode Fiber with Wavefront Shaping. *Biomedical Optics Express*. 2020, vol. 11, no. 10, pp. 5717–5727. ISSN 2156-7085. Available from: doi:10.1364/BOE.400686.

[56] STELLINGA, Daan, David B. PHILLIPS, Simon Peter MEKHAIL, Adam SELYEM, Sergey TURTAEV, Tomáš ČIŽMÁR and Miles J. PADGETT. Time-of-Flight 3D Imaging through Multimode Optical Fibers. *Science*. 2021, vol. 374, no. 6573, pp. 1395–1399. ISSN 0036-8075. Available from: doi:10.1126/science.abl3771.

[57] AMITONOVA, Lyubov V. and Johannes F. de BOER. Compressive Imaging through a Multimode Fiber. *Optics Letters*. 2018, vol. 43, no. 21, pp. 5427–5430. ISSN 1539-4794. Available from: doi:10.1364/OL.43.005427.

[58] AMITONOVA, Lyubov V. and Johannes F. de BOER. Endo-Microscopy beyond the Abbe and Nyquist Limits. *Light: Science & Applications*. 2020, vol. 9, no. 1, pp. 81. ISSN 2047-7538. Available from: doi:10.1038/s41377-020-0308-x.

[59] LAN, Mingying, Di GUAN, Li GAO, Junhui LI, Song YU and Guohua WU. Robust Compressive Multimode Fiber Imaging against Bending with Enhanced Depth of Field. *Optics Express*. 2019, vol. 27, no. 9, pp. 12957–12962. ISSN 1094-4087. Available from: doi:10.1364/OE.27.012957.

[60] DONG, Zhenyu, Zhong WEN, Chenlei PANG, Liqiang WANG, Lan WU, Xu LIU and Qing YANG. A Modulated Sparse Random Matrix for High-Resolution and High-Speed 3D Compressive Imaging through a Multimode Fiber. *Science Bulletin*. 2022, pp. S2095927322001219. ISSN 20959273. Available from: doi:10.1016/j.scib.2022.03.017.

[61] GUSACHENKO, Ivan, Mingzhou CHEN and Kishan DHOLAKIA. Raman Imaging through a Single Multimode Fibre. *Optics Express*. 2017, vol. 25, no. 12, pp. 13782–13798. ISSN 1094-4087. Available from: doi:10.1364/OE.25.013782.

[62] DENG, Sunan, Damien LOTERIE, Georgia KONSTANTINOU, Demetri PSALTIS and Christophe MOSER. Raman Imaging through Multimode Sapphire Fiber. *Optics Express*. 2019, vol. 27, no. 2, pp. 1090–1098. ISSN 1094-4087. Available from: doi:10.1364/OE.27.001090.

[63] KONSTANTINOU, Georgia, Antoine BONIFACE, Damien LOTERIE, Eirini KAKKAVA, Demetri PSALTIS and Christophe MOSER. Improved Two-Photon Polymerization through an Optical Fiber Using Coherent Beam Shaping. *Optics and Lasers in Engineering*. 2023, vol. 160, pp. 107232. ISSN 0143-8166. Available from: doi:10.1016/j.optlaseng.2022.107232.

[64] BIANCHI, Silvio and Roberto DI LEONARDO. A Multi-Mode Fiber Probe for Holographic Micromanipulation and Microscopy. *Lab Chip*. 2012, vol. 12, no. 3, pp. 635–639. ISSN 1473-0189. Available from: doi:10.1039/C1LC20719A.

[65] LEITE, Ivo T., Sergey TURTAEV, Xin JIANG, Martin ŠILER, Alfred CUSCHIERI, Philip St. J. RUSSELL and Tomáš ČIŽMÁR. Three-Dimensional Holographic Optical Manipulation through a High-Numerical-Aperture Soft-Glass Multimode Fibre. *Nature Photonics*. 2018, vol. 12, no. 1, pp. 33–39. ISSN 1749-4885. Available from: doi:10.1038/s41566-017-0053-8.

[66] BEGLEY, R. F., A. B. HARVEY and R. L. BYER. Coherent anti-Stokes Raman Spectroscopy. *Applied Physics Letters*. 1974, vol. 25, no. 7, pp. 387–390. ISSN 1077-3118. Available from: doi:10.1063/1.1655519.

[67] MEYER, Tobias, Mario CHEMNITZ, Martin BAUMGARTL, Thomas GOTTSCHALL, Torbjörn PASCHER, Christian MATTHÄUS, Bernd F. M. ROMEIKE, Bernhard R. BREHM, Jens LIMPERT, Andreas TÜNNERMANN, Michael SCHMITT, Benjamin DIETZEK and Jürgen POPP. Expanding Multimodal Microscopy by High Spectral Resolution Coherent Anti-Stokes Raman Scattering Imaging for Clinical Disease Diagnostics. *Analytical Chemistry*. 2013, vol. 85, no. 14, pp. 6703–6715. ISSN 0003-2700. Available from: doi:10.1021/ac400570w.

[71] VELLEKOOP, Ivo M. and Allard P. MOSK. Universal Optimal Transmission of Light Through Disordered Materials. *Physical Review Letters*. 2008, vol. 101, no. 12, pp. 120601. ISSN 0031-9007. Available from: doi:10.1103/PhysRevLett.101.120601.

[72] VELLEKOOP, Ivo M. and Allard P. MOSK. Focusing Coherent Light through Opaque Strongly Scattering Media. *Optics Letters*. 2007, vol. 32, no. 16, pp. 2309–2311. ISSN 1539-4794. Available from: doi:10.1364/OL.32.002309.

[73] MOSK, Allard P., Ad LAGENDIJK, Geoffroy LEROSEY and Mathias FINK. Controlling Waves in Space and Time for Imaging and Focusing in Complex Media. *Nature Photonics*. 2012, vol. 6, no. 5, pp. 283–292. ISSN 1749-4893. Available from: doi:10.1038/nphoton.2012.88.

[74] CONKEY, Donald B., Antonio M. CARAVACA-AGUIRRE and Rafael PIESTUN. High-Speed Scattering Medium Characterization with Application to Focusing Light through Turbid Media. *Optics Express*. 2012, vol. 20, no. 2, pp. 1733. ISSN 1094-4087. Available from: doi:10.1364/OE.20.001733.

[75] ČIŽMÁR, Tomáš, Michael MAZILU and Kishan DHOLAKIA. In Situ Wavefront Correction and Its Application to Micromanipulation. *Nature Photonics*. 2010, vol. 4, no. 6, pp. 388–394. ISSN 1749-4893. Available from: doi:10.1038/nphoton.2010.85.

[76] AMITONOVA, Lyubov V., Adrien DESCLOUX, Joerg PETSCHULAT, Michael H. FROSZ, Goran AHMED, Fehim BABIC, Xin JIANG, Allard P. MOSK, Philip St.J. RUSSELL and Pepijn W. H. PINKSE. High-Resolution Wavefront Shaping with a Photonic Crystal Fiber for Multimode Fiber Imaging. *Optics Letters*. 2016, vol. 41, no. 3, pp. 497–500. ISSN 1539-4794. Available from: doi:10.1364/OL.41.000497.

[78] REN, Yu-Xuan, Rong-De LU and Lei GONG. Tailoring Light with a Digital Micromirror Device: Tailoring Light with a Digital Micromirror Device. *Annalen der Physik*. 2015, vol. 527, no. 7-8, pp. 447–470. ISSN 0003-3804. Available from: doi:10.1002/andp.201500111.

[79] SONG, Yuanping, Robert M. PANAS and Jonathan B. HOPKINS. A Review of Micromirror Arrays. *Precision Engineering*. 2018, vol. 51, pp. 729–761. ISSN 0141-6359. Available from: doi:10.1016/j.precisioneng.2017.08.012.

[80] GOORDEN, Sebastianus A., Jacopo BERTOLOTTI and Allard P. MOSK. Superpixel-Based Spatial Amplitude and Phase Modulation Using a Digital Micromirror Device. *Optics Express*. 2014, vol. 22, no. 15, pp. 17999–18009. ISSN 1094-4087. Available from: doi:10.1364/OE.22.017999.

[81] PLÖSCHNER, Martin, Branislav STRAKA, Kishan DHOLAKIA and Tomáš ČIŽMÁR. GPU Accelerated Toolbox for Real-Time Beam-Shaping in Multimode Fibres. *Optics Express*. 2014, vol. 22, no. 3, pp. 2933–2947. ISSN 1094-4087. Available from: doi:10.1364/OE.22.002933.

[82] LEE, Wai-Hon. Binary Computer-Generated Holograms. *Applied Optics*. 1979, vol. 18, no. 21, pp. 3661–3669. ISSN 1539-4522. Available from: doi:10.1364/AO.18.003661.

[83] DAVIS, Jeffrey A., Don M. COTTRELL, Juan CAMPOS, María J. YZUEL and Ignacio MORENO. Encoding Amplitude Information onto Phase-Only Filters. *Applied Optics*. 1999, vol. 38, no. 23, pp. 5004–5013. ISSN 1539-4522. Available from: doi:10.1364/AO.38.005004.

[84] DI LEONARDO, Roberto, Francesca IANNI and Giancarlo RUOCCO. Computer Generation of Optimal Holograms for Optical Trap Arrays. *Optics Express*. 2007, vol. 15, no. 4, pp. 1913–1922. ISSN 1094-4087. Available from: doi:10.1364/OE.15.001913.

[85] GERCHBERG, R. W. and W. O. SAXTON. A Practical Algorithm for the Determination of Phase from Image and Diffraction Plane Pictures. *Optik*. 1972, vol. 35, no. 2, pp. 237–246. ISSN 0030-4026.

[86] MENDOZA-YERO, Omel, Gladys MÍNGUEZ-VEGA and Jesús LANCIS. Encoding Complex Fields by Using a Phase-Only Optical Element. *Optics Letters*. 2014, vol. 39, no. 7, pp. 1740–1743. ISSN 1539-4794. Available from: doi:10.1364/OL.39.001740.

[87] MITCHELL, Kevin J., Sergey TURTAEV, Miles J. PADGETT, Tomáš ČIŽMÁR and David B. PHILLIPS. High-Speed Spatial Control of the Intensity, Phase and Polarisation of Vector Beams Using a Digital Micro-Mirror Device. *Optics Express*. 2016, vol. 24, no. 25, pp. 29269–29282. ISSN 1094-4087. Available from: doi:10.1364/OE.24.029269.

[88] ARRIZÓN, Victor. Complex Modulation with a Twisted-Nematic Liquid-Crystal Spatial Light Modulator: Double-Pixel Approach. *Optics Letters*. 2003, vol. 28, no. 15, pp. 1359–1361. ISSN 1539-4794. Available from: doi:10.1364/OL.28.001359.

[89] POPOFF, S. M., G. LEROSEY, R. CARMINATI, M. FINK, A. C. BOCCARA and S. GIGAN. Measuring the Transmission Matrix in Optics: An Approach to the Study and Control of Light Propagation in Disordered Media. *Physical Review Letters*. 2010, vol. 104, no. 10, pp. 100601. ISSN 0031-9007. Available from: doi:10.1103/PhysRevLett.104.100601.

[90] PLÖSCHNER, Martin, Tomáš TYC and Tomáš ČIŽMÁR. Seeing through Chaos in Multimode Fibres. *Nature Photonics*. 2015, vol. 9, no. 8, pp. 529–535. ISSN 1749-4885. Available from: doi:10.1038/nphoton.2015.112.

[91] HUANG, Guoqiang, Daixuan WU, Jiawei LUO, Yin HUANG and Yuecheng SHEN. Retrieving the Optical Transmission Matrix of a Multimode Fiber Using the Extended Kalman Filter. *Optics Express*. 2020, vol. 28, no. 7, pp. 9487–9500. ISSN 1094-4087. Available from: doi:10.1364/OE.389133.

[92] ROTHE, Stefan, Hannes RADNER, Nektarios KOUKOURAKIS and Jürgen CZARSKE. Transmission Matrix Measurement of Multimode Optical Fibers by Mode-Selective Excitation Using One Spatial Light Modulator. *Applied Sciences*. 2019, vol. 9, no. 1, pp. 195. ISSN 2076-3417. Available from: doi:10.3390/app9010195.

[93] TURTAEV, Sergey, Ivo T. LEITE and Tomáš ČIŽMÁR. Multimode Fibres for Micro-Endoscopy. *Optofluidics, Microfluidics and Nanofluidics*. 2015, vol. 2, pp. 31–35. ISSN 2300-7435. Available from: doi:10.1515/optof-2015-0004.

[94] CARAVACA-AGUIRRE, Antonio M. and Rafael PIESTUN. Single Multimode Fiber Endoscope. *Optics Express*. 2017, vol. 25, no. 3, pp. 1656–1665. ISSN 1094-4087. Available from: doi:10.1364/OE.25.001656.

[95] WU, Zhenhua, Jiawei LUO, Yuanhua FENG, Xiaojie GUO, Yuecheng SHEN and Zhaohui LI. Controlling 1550-Nm Light through a Multimode Fiber Using a Hadamard Encoding Algorithm. *Optics Express*. 2019, vol. 27, no. 4, pp. 5570–5580. ISSN 1094-4087. Available from: doi:10.1364/OE.27.005570.

[96] RESISI, Shachar, Yehonatan VIERNIK, Sebastien M. POPOFF and Yaron BROMBERG. Wavefront Shaping in Multimode Fibers by Transmission Matrix Engineering. *APL Photonics*. 2020, vol. 5, no. 3, pp. 036103. ISSN 2378-0967. Available from: doi:10.1063/1.5136334.

[97] PAPADOPOULOS, Ioannis N., Salma FARAHI, Christophe MOSER and Demetri PSALTIS. Focusing and Scanning Light through a Multimode Optical Fiber Using Digital Phase Conjugation. *Optics Express*. 2012, vol. 20, no. 10, pp. 10583–10590. ISSN 1094-4087. Available from: doi:10.1364/OE.20.010583.

[98] N'GOM, Moussa, Theodore B. NORRIS, Eric MICHIELSSEN and Raj Rao NADAKUDITI. Mode Control in a Multimode Fiber through Acquiring Its Transmission Matrix from a Reference-Less Optical System. *Optics Letters*. 2018, vol. 43, no. 3, pp. 419–422. ISSN 1539-4794. Available from: doi:10.1364/OL.43.000419.

[99] DRÉMEAU, Angélique, Antoine LIUTKUS, David MARTINA, Ori KATZ, Christophe SCHÜLKE, Florent KRZAKALA, Sylvain GIGAN and Laurent DAUDET. Reference-Less Measurement of the Transmission Matrix of a Highly Scattering Material Using a DMD and Phase Retrieval Techniques. *Optics Express*. 2015, vol. 23, no. 9, pp. 11898–11911. ISSN 1094-4087. Available from: doi:10.1364/OE.23.011898.

[100] ZHAO, Tianrui, Liang DENG, Wen WANG, Daniel S. ELSON and Lei SU. Bayes' Theorem-Based Binary Algorithm for Fast Reference-Less Calibration of a Multimode Fiber. *Optics Express*. 2018, vol. 26, no. 16, pp. 20368–20378. ISSN 1094-4087. Available from: doi:10.1364/OE.26.020368.

[101] STASIO, Nicolino, Donald B. CONKEY, Christophe MOSER and Demetri PSALTIS. Light Control in a Multicore Fiber Using the Memory Effect. *Optics Express*. 2015, vol. 23, no. 23, pp. 30532–30544. ISSN 1094-4087. Available from: doi:10.1364/OE.23.030532.

[102] AMITONOVA, Lyubov V., Allard P. MOSK and Pepijn W. H. PINKSE. Rotational Memory Effect of a Multimode Fiber. *Optics Express*. 2015, vol. 23, no. 16, pp. 20569–20575. ISSN 1094-4087. Available from: doi:10.1364/OE.23.020569.

[103] LI, Shuhui, Simon A. R. HORSLEY, Tomáš TYC, Tomáš ČIŽMÁR and David B. PHILLIPS. Memory Effect Assisted Imaging through Multimode Optical Fibres. *Nature Communications*. 2021, vol. 12, no. 3751. ISSN 2041-1723. Available from: doi:10.1038/s41467-021-23729-1.

[104] CARAVACA-AGUIRRE, Antonio M., Adrien CARRON, Sylvain MEZIL, Irène WANG and Emmanuel BOSSY. Optical Memory Effect in Square Multimode Fibers. *Optics Letters*. 2021, vol. 46, no. 19, pp. 4924–4927. ISSN 1539-4794. Available from: doi:10.1364/OL.436134.

[105] LI, Shuhui, Charles SAUNDERS, Daniel J. LUM, John MURRAY-BRUCE, Vivek K. GOYAL, Tomáš ČIŽMÁR and David B. PHILLIPS. Compressively Sampling the Optical Transmission Matrix of a Multimode Fibre. *Light: Science & Applications*. 2021, vol. 10, no. 1, pp. 88. ISSN 2047-7538. Available from: doi:10.1038/s41377-021-00514-9.

[106] GORDON, George S. D., Milana GATARIC, Alberto Gil C. P. RAMOS, Ralf MOUTHAAN, Calum WILLIAMS, Jonghee YOON, Timothy D. WILKINSON and Sarah E. BOHNDIEK. Characterizing Optical Fiber Transmission Matrices Using Metasurface Reflector Stacks for Lensless Imaging without Distal Access. *Physical Review X*. 2019, vol. 9, no. 4, pp. 041050. ISSN 2160-3308. Available from: doi:10.1103/PhysRevX.9.041050.

[107] CARAMAZZA, Piergiorgio, Oisín MORAN, Roderick MURRAY-SMITH and Daniele FACCIO. Transmission of Natural Scene Images through a Multimode Fibre. *Nature Communications*. 2019, vol. 10, no. 2029. ISSN 2041-1723. Available from: doi:10.1038/s41467-019-10057-8.

[108] BORHANI, Navid, Eirini KAKKAVA, Christophe MOSER and Demetri PSALTIS. Learning to See through Multimode Fibers. *Optica*. 2018, vol. 5, no. 8, pp. 960–966. ISSN 2334-2536. Available from: doi:10.1364/OPTICA.5.000960.

[109] KAKKAVA, Eirini, Babak RAHMANI, Navid BORHANI, Uğur TEĞIN, Damien LOTERIE, Georgia KONSTANTINOU, Christophe MOSER and Demetri PSALTIS. Imaging through Multimode Fibers Using Deep Learning: The Effects of Intensity versus Holographic Recording of the Speckle Pattern. *Optical Fiber Technology*. 2019, vol. 52, pp. 101985. ISSN 1068-5200. Available from: doi:10.1016/j.yofte.2019.101985.

[110] BŪTAITĖ, Unė G., Hlib KUPIANSKYI, Tomáš ČIŽMÁR and David B. PHILLIPS. How to Build the "Optical Inverse" of a Multimode Fibre. *Intelligent Computing*. 2022, vol. 2022, pp. 2022/9816026. ISSN 2771-5892. Available from: doi:10.34133/2022/9816026.

[111] LINNENBERGER, Anna M. Advanced SLMs for Microscopy. In: *Adaptive Optics and Wavefront Control for Biological Systems IV*: *Adaptive Optics and Wavefront Control for Biological Systems IV*. San Francisco, United States: SPIE, 2018, pp. 1050204. Available from: doi:10.1117/12.2290455.

[112] MEADOWLARK OPTICS, Inc. *LCOS Spatial Light Modulator Phase Calibration Using a Diffractive Method*. 2018.

[113] JÁKL, Petr, Martin ŠILER, Jan JEŽEK, Ángel CIFUENTES, Johanna TRÄGÅRDH, Pavel ZEMÁNEK and Tomáš ČIŽMÁR. Endoscopic Imaging Using a Multimode Optical Fibre Calibrated with Multiple Internal References. *Photonics*. 2022, vol. 9, no. 1, pp. 37. ISSN 2304-6732. Available from: doi:10.3390/photonics9010037.

[114] FRENCH, Rebecca, Sylvain GIGAN and Otto L. MUSKENS. Snapshot Fiber Spectral Imaging Using Speckle Correlations and Compressive Sensing. *Optics Express*. 2018, vol. 26, no. 24, pp. 32302–32316. ISSN 1094-4087. Available from: doi:10.1364/OE.26.032302.

[115] FLORENTIN, Raphael, Vincent KERMENE, Agnes DESFARGES-BERTHELEMOT and Alain BARTHELEMY. Fast Transmission Matrix Measurement of a Multimode Optical Fiber With Common Path Reference. *IEEE Photonics Journal*. 2018, vol. 10, no. 5, pp. 1–6. ISSN 1943-0647. Available from: doi:10.1109/JPHOT.2018.2866681.

[116] DELEN, N. and B. HOOKER. Free-Space Beam Propagation between Arbitrarily Oriented Planes Based on Full Diffraction Theory: A Fast Fourier Transform Approach. *Journal of the Optical Society of America A*. 1998, vol. 15, no. 4, pp. 857–867. ISSN 1520-8532. Available from: doi:10.1364/JOSAA.15.000857.

[117] LI, Junchang, Zujie PENG and Yunchang FU. Diffraction Transfer Function and Its Calculation of Classic Diffraction Formula. *Optics Communications*. 2007, vol. 280, no. 2, pp. 243–248. ISSN 0030-4018. Available from: doi:10.1016/j.optcom.2007.08.053.

[118] GOMES, André D., Sergey TURTAEV, Yang DU and Tomáš ČIŽMÁR. Near Perfect Focusing through Multimode Fibres. *Optics Express*. 2022, vol. 30, no. 7, pp. 10645–10663. ISSN 1094-4087. Available from: doi:10.1364/OE.452145.

[119] TUČKOVÁ, Tereza, Martin ŠILER, Dirk E. BOONZAJER FLAES, Petr JÁKL, Sergey TURTAEV, Stanislav KRÁTKÝ, Rainer HEINTZMANN, Hana UHLÍŘOVÁ and Tomáš ČIŽMÁR. Computational Image Enhancement of Multimode Fibre-Based Holographic Endo-Microscopy: Harnessing the Muddy Modes. *Optics Express*. 2021, vol. 29, no. 23, pp. 38206–38220. ISSN 1094-4087. Available from: doi:10.1364/OE.434848.

[120] BOOTH, Martin J. Microscope Resolution Estimation and Normalised Coordinates. 2020. Available from: doi:10.5281/zenodo.4302488.

[121] TURCOTTE, Raphaël, Carla C. SCHMIDT, Nigel J. EMPTAGE and Martin J. BOOTH. Focusing Light in Biological Tissue through a Multimode Optical Fiber: Refractive Index Matching. *Optics Letters*. 2019, vol. 44, no. 10, pp. 2386–2389. ISSN 1539-4794. Available from: doi:10.1364/OL.44.002386.

[122] MORALES-DELGADO, Edgar E., Salma FARAHI, Ioannis N. PAPADOPOULOS, Demetri PSALTIS and Christophe MOSER. Delivery of Focused Short Pulses through a Multimode Fiber. *Optics Express*. 2015, vol. 23, no. 7, pp. 9109–9120. ISSN 1094-4087. Available from: doi:10.1364/OE.23.009109.

[123] VELSINK, Matthias C., Lyubov V. AMITONOVA and Pepijn W. H. PINKSE. Spatiotemporal Focusing through a Multimode Fiber via Time-Domain Wavefront Shaping. *Optics Express*. 2021, vol. 29, no. 1, pp. 272–290. ISSN 1094-4087. Available from: doi:10.1364/OE.412714.

[124] LIU, Bohao and Andrew M. WEINER. Space–Time Focusing in a Highly Multimode Fiber via Optical Pulse Shaping. *Optics Letters*. 2018, vol. 43, no. 19, pp. 4675–4678. ISSN 1539-4794. Available from: doi:10.1364/OL.43.004675.

[125] STEIGER, Ruth, Stefan BERNET and Monika RITSCH-MARTE. SLM-based off-Axis Fourier Filtering in Microscopy with White Light Illumination. *Optics Express*. 2012, vol. 20, no. 14, pp. 15377–15384. ISSN 1094-4087. Available from: doi:10.1364/OE.20.015377.

[126] GENG, Qiang, Chenglin GU, Jiyi CHENG and Shih-chi CHEN. Digital Micromirror Device-Based Two-Photon Microscopy for Three-Dimensional and Random-Access Imaging. *Optica*. 2017, vol. 4, no. 6, pp. 674–677. ISSN 2334-2536. Available from: doi:10.1364/OPTICA.4.000674.

[127] LEACH, Jonathan, Graham M. GIBSON, Miles J. PADGETT, Elric ESPOSITO, Gail MCCONNELL, Amanda J. WRIGHT and John M. GIRKIN. Generation of Achromatic Bessel Beams Using a Compensated Spatial Light Modulator. *Optics Express*. 2006, vol. 14, no. 12, pp. 5581–5587. ISSN 1094-4087. Available from: doi:10.1364/OE.14.005581.

[128] HOFFMANN, Maximilian, Ioannis N. PAPADOPOULOS and Benjamin JUDKEWITZ. Kilohertz Binary Phase Modulator for Pulsed Laser Sources Using a Digital Micromirror Device. *Optics Letters*. 2018, vol. 43, no. 1, pp. 22–25. ISSN 1539-4794. Available from: doi:10.1364/OL.43.000022.

[129] PARSONS, Earl Ryan, Randall PATTERSON, James YOUNG and Paul F. KOLESAR. The Impact of Effective Modal Bandwidth on 100G SWDM Transmission Over 250 m OM5 and Left-Tilt OM4 Multimode Fibers. *Journal of Lightwave Technology*. 2018, vol. 36, no. 24, pp. 5841–5848. ISSN 0733-8724. Available from: doi:10.1109/JLT.2018.2878666.

[130] DEVAUD, Louisiane, Marc GUILLON, Ivan GUSACHENKO and Sylvain GIGAN. Chromato-Axial Memory Effect in Step Index Multimode Fibers. *APL Photonics*. 2021, vol. 6, no. 12. ISSN 2378-0967. Available from: doi:10.1063/5.0067892.

[131] MOSLEHI, Behzad, Joseph W. GOODMAN and Eric G. RAWSON. Bandwidth Estimation for Multimode Optical Fibers Using the Frequency Correlation Function of Speckle Patterns. *Applied Optics*. 1983, vol. 22, no. 7, pp. 995–999. ISSN 1539-4522. Available from: doi:10.1364/AO.22.000995.

[132] ZHU, Ping, Rana JAFARI, Travis JONES and Rick TREBINO. Complete Measurement of Spatiotemporally Complex Multi-Spatial-Mode Ultrashort Pulses from Multimode Optical Fibers Using Delay-Scanned Wavelength-Multiplexed Holography. *Optics Express*. 2017, vol. 25, no. 20, pp. 24015–24023. ISSN 1094-4087. Available from: doi:10.1364/OE.25.024015.

[133] GUANG, Zhe, Michelle RHODES and Rick TREBINO. Measuring Spatiotemporal Ultrafast Field Structures of Pulses from Multimode Optical Fibers. *Applied Optics*. 2017, vol. 56, no. 12, pp. 3319–3324. ISSN 1539-4522. Available from: doi:10.1364/AO.56.003319.

[134] POLYANSKIY, Mikhail N. *Refractive Index Database* [online]. [Visited on 2021-8-21]. Available from: `https://refractiveindex.info`.

[135] JESACHER, Alexander, Stefan BERNET and Monika RITSCH-MARTE. Colour Hologram Projection with an SLM by Exploiting Its Full Phase Modulation Range. *Optics Express*. 2014, vol. 22, no. 17, pp. 20530–20541. ISSN 1094-4087. Available from: doi:10.1364/OE.22.020530.

[136] EVERALL, Neil J. Confocal Raman Microscopy: Performance, Pitfalls, and Best Practice: Invited Lecture at the Symposium "50 Years of SAS: Looking to the Future with Vibrational Spectroscopy" at Pittcon 2008, New Orleans, Louisiana. *Applied Spectroscopy*. 2009, vol. 63, no. 9, pp. 245A–262A. ISSN 1943-3530. Available from: doi:10.1366/000370209789379196.

[137] XIE, X. Sunney, Ji-Xin CHENG and Eric POTMA. Coherent Anti-Stokes Raman Scattering Microscopy. In: *Handbook of Biological Confocal Microscopy*. New York, NY: Springer, 2006, pp. 595–606. ISBN 978-0-387-25921-5.

[138] CHENG, Ji-Xin and X. Sunney XIE. Coherent Anti-Stokes Raman Scattering Microscopy: Instrumentation, Theory, and Applications. *The Journal of Physical Chemistry B*. 2004, vol. 108, no. 3, pp. 827–840. ISSN 1520-5207. Available from: doi:10.1021/jp035693v.

[139] POTMA, Eric O. and X. Sunney XIE. CARS Microscopy for Biology and Medicine. *Optics and Photonics News*. 2004, vol. 15, no. 11, pp. 40–45. ISSN 1541-3721. Available from: doi:10.1364/OPN.15.11.000040.

[140] RIGNEAULT, Hervé and Pascal BERTO. Tutorial: Coherent Raman Light Matter Interaction Processes. *APL Photonics*. 2018, vol. 3, no. 9, pp. 091101. ISSN 2378-0967. Available from: doi:10.1063/1.5030335.

[141] ZHANG, Chi and Ji-Xin CHENG. Perspective: Coherent Raman Scattering Microscopy, the Future Is Bright. *APL Photonics*. 2018, vol. 3, no. 9, pp. 090901. ISSN 2378-0967. Available from: doi:10.1063/1.5040101.

[142] SAAR, B. G., C. W. FREUDIGER, J. REICHMAN, C. M. STANLEY, G. R. HOLTOM and X. S. XIE. Video-Rate Molecular Imaging in Vivo with Stimulated Raman Scattering. *Science*. 2010, vol. 330, no. 6009, pp. 1368–1370. ISSN 0036-8075. Available from: doi:10.1126/science.1197236.

[143] DI NAPOLI, Claudia, Iestyn POPE, Francesco MASIA, Wolfgang LANGBEIN, Pete WATSON and Paola BORRI. Quantitative Spatiotemporal Chemical Profiling of Individual Lipid Droplets by Hyperspectral CARS Microscopy in Living Human Adipose-Derived Stem Cells. *Analytical Chemistry*. 2016, vol. 88, no. 7, pp. 3677–3685. ISSN 0003-2700. Available from: doi:10.1021/acs.analchem.5b04468.

[144] PATEL, Imran I., Christian STEUWE, Stefanie REICHELT and Sumeet MAHAJAN. Coherent Anti-Stokes Raman Scattering for Label-Free Biomedical Imaging. *Journal of Optics*. 2013, vol. 15, no. 9, pp. 094006. ISSN 2040-8978. Available from: doi:10.1088/2040-8978/15/9/094006.

[145] LATKA, Ines, Sebastian DOCHOW, Christoph KRAFFT, Benjamin DIETZEK and Jürgen POPP. Fiber Optic Probes for Linear and Nonlinear Raman Applications – Current Trends and Future Development: Fiber Optic Raman Probes. *Laser & Photonics Reviews*. 2013, vol. 7, no. 5, pp. 698–731. ISSN 1863-8880. Available from: doi:10.1002/lpor.201200049.

[146] EVANS, Conor L. and X. Sunney XIE. Coherent Anti-Stokes Raman Scattering Microscopy: Chemical Imaging for Biology and Medicine. *Annual Review of Analytical Chemistry*. 2008, vol. 1, no. 1, pp. 883–909. ISSN 1936-1335. Available from: doi:10.1146/annurev.anchem.1.031207.112754.

[147] UCKERMANN, Ortrud, Roberta GALLI, Sandra TAMOSAITYTE, Elke LEIPNITZ, Kathrin D. GEIGER, Gabriele SCHACKERT, Edmund KOCH, Gerald STEINER and Matthias KIRSCH. Label-Free Delineation of Brain Tumors by Coherent Anti-Stokes Raman Scattering Microscopy in an Orthotopic Mouse Model and Human Glioblastoma. *PLoS ONE*. 2014, vol. 9, no. 9, pp. e107115. ISSN 1932-6203. Available from: doi:10.1371/journal.pone.0107115.

[148] BOCKLITZ, Thomas W., Firas Subhi SALAH, Nadine VOGLER, Sandro HEUKE, Olga CHERNAVSKAIA, Carsten SCHMIDT, Maximilian J. WALDNER, Florian R. GRETEN, Rolf BRÄUER, Michael SCHMITT, Andreas STALLMACH, Iver PETERSEN and Jürgen POPP. Pseudo-HE Images Derived from CARS/TPEF/SHG Multimodal Imaging in Combination with Raman-spectroscopy as a Pathological Screening Tool. *BMC Cancer*. 2016, vol. 16, pp. 534. ISSN 1471-2407. Available from: doi:10.1186/s12885-016-2520-x.

[149] WANG, Thomas D. and Jacques VAN DAM. Optical Biopsy: A New Frontier in Endoscopic Detection and Diagnosis. *Clinical Gastroenterology and Hepatology*. 2004, vol. 2, no. 9, pp. 744–753. ISSN 1542-3565. Available from: doi:10.1016/S1542-3565(04)00345-3.

[150] KRAFFT, Christoph, Iwan W. SCHIE, Tobias MEYER, Michael SCHMITT and Jürgen POPP. Developments in Spontaneous and Coherent Raman Scattering Microscopic Imaging for Biomedical Applications. *Chemical Society Reviews*. 2016, vol. 45, no. 7, pp. 1819–1849. ISSN 1460-4744. Available from: doi:10 . 1039 / C5CS00564G.

[151] KRAFFT, Christoph, Michael SCHMITT, Iwan W. SCHIE, Dana CIALLA-MAY, Christian MATTHÄUS, Thomas BOCKLITZ and Jürgen POPP. Label-Free Molecular Imaging of Biological Cells and Tissues by Linear and Nonlinear Raman Spectroscopic Approaches. *Angewandte Chemie International Edition*. 2017, vol. 56, no. 16, pp. 4392–4430. ISSN 1433-7851. Available from: doi:10 . 1002 / anie . 201607604.

[152] WANG, Haifeng, Yan FU, Phyllis ZICKMUND, Riyi SHI and Ji-Xin CHENG. Coherent Anti-Stokes Raman Scattering Imaging of Axonal Myelin in Live Spinal Tissues. *Biophysical Journal*. 2005, vol. 89, no. 1, pp. 581–591. ISSN 0006-3495. Available from: doi:10.1529/biophysj.105.061911.

[153] FU, Yan, T. Brandon HUFF, Han-Wei WANG, Ji-Xin CHENG and Haifeng WANG. Ex Vivo and in Vivo Imaging of Myelin Fibers in Mouse Brain by Coherent Anti-Stokes Raman Scattering Microscopy. *Optics Express*. 2008, vol. 16, no. 24, pp. 19396–19409. ISSN 1094-4087. Available from: doi:10.1364/OE.16.019396.

[154] HENRY, Francis P., Daniel CÔTÉ, Mark A. RANDOLPH, Esther A. Z. RUST, Robert W. REDMOND, Irene E. KOCHEVAR, Charles P. LIN and Jonathan M. WINOGRAD. Real-Time In Vivo Assessment of the Nerve Microenvironment with Coherent Anti–Stokes Raman Scattering Microscopy: *Plastic and Reconstructive Surgery*. 2009, vol. 123, pp. 123S–130S. ISSN 0032-1052. Available from: doi:10 . 1097/PRS.0b013e318191c5b8.

[155] WELTE, Michael A. As the Fat Flies: The Dynamic Lipid Droplets of Drosophila Embryos. *Biochimica et Biophysica Acta*. 2015, vol. 1851, no. 9, pp. 1156–1185. ISSN 1388-1981. Available from: doi:10.1016/j.bbalip.2015.04.002.

[156] EVANS, Conor L., Eric O. POTMA, Mehron PUORIS'HAAG, Daniel COTE, Charles P. LIN and X. Sunney XIE. Chemical Imaging of Tissue in Vivo with Video-Rate Coherent Anti-Stokes Raman Scattering Microscopy. *Proceedings of the National Academy of Sciences*. 2005, vol. 102, no. 46, pp. 16807–16812. ISSN 0027-8424. Available from: doi:10.1073/pnas.0508282102.

[157] MITTAL, Richa, Mihaela BALU, Petra WILDER-SMITH and Eric O. POTMA. Achromatic Miniature Lens System for Coherent Raman Scattering Microscopy. *Biomedical Optics Express*. 2013, vol. 4, no. 10, pp. 2196–2206. ISSN 2156-7085. Available from: doi:10.1364/BOE.4.002196.

[158] JOHNS, Maureen, Cole A. GILLER, Dwight C. GERMAN and Hanli LIU. Determination of Reduced Scattering Coefficient of Biological Tissue from a Needle-like Probe. *Optics Express*. 2005, vol. 13, no. 13, pp. 4828–4842. ISSN 1094-4087. Available from: doi:10.1364/OPEX.13.004828.

[159] DÉBARRE, Delphine, Nicolas OLIVIER and Emmanuel BEAUREPAIRE. Signal Epidetection in Third-Harmonic Generation Microscopy of Turbid Media. *Optics Express*. 2007, vol. 15, no. 14, pp. 8913–8924. ISSN 1094-4087. Available from: doi:10.1364/OE.15.008913.

[160] ZIRAK, Peyman, Gregor MATZ, Bernhard MESSERSCHMIDT, Tobias MEYER, Michael SCHMITT, Jürgen POPP, Ortrud UCKERMANN, Roberta GALLI, Matthias KIRSCH, Martin Josef WINTERHALDER and Andreas ZUMBUSCH. Invited Article: A Rigid Coherent Anti-Stokes Raman Scattering Endoscope with High Resolution and a Large Field of View. *APL Photonics*. 2018, vol. 3, no. 9, pp. 092409. ISSN 2378-0967. Available from: doi:10.1063/1.5027182.

[161] PSHENAY-SEVERIN, Ekaterina, Hyeonsoo BAE, Karl REICHWALD, Gregor MATZ, Jörg BIERLICH, Jens KOBELKE, Adrian LORENZ, Anka SCHWUCHOW, Tobias MEYER-ZEDLER, Michael SCHMITT, Bernhard MESSERSCHMIDT and Jürgen POPP. Multimodal Nonlinear Endomicroscopic Imaging Probe Using a Double-Core Double-Clad Fiber and Focus-Combining Micro-Optical Concept. *Light: Science & Applications*. 2021, vol. 10, no. 207. ISSN 2047-7538. Available from: doi:10.1038/s41377-021-00648-w.

[162] THALHAMMER, Gregor, Richard W. BOWMAN, Gordon D. LOVE, Miles J. PADGETT and Monika RITSCH-MARTE. Speeding up Liquid Crystal SLMs Using Overdrive with Phase Change Reduction. *Optics Express*. 2013, vol. 21, no. 2, pp. 1779–1797. ISSN 1094-4087. Available from: doi:10.1364/OE.21.001779.

[163] BARTLETT, Terry A., Bill C. MCDONALD and James HALL. Adapting Texas Instruments DLP Technology to Demonstrate a Phase Spatial Light Modulator. In: *Emerging Digital Micromirror Device Based Systems and Applications XI*: *Emerging Digital Micromirror Device Based Systems and Applications XI*. San Francisco, United States: SPIE, 2019, pp. 27. Available from: doi:10.1117/12.2514483.

[164] KETCHUM, Remington S. and Pierre-Alexandre BLANCHE. Diffraction Efficiency Characteristics for MEMS-Based Phase-Only Spatial Light Modulator with Nonlinear Phase Distribution. *Photonics*. 2021, vol. 8, no. 3, pp. 62. ISSN 2304-6732. Available from: doi:10.3390/photonics8030062.

[165] OUYANG, Bing, Sue GONG, Tom LAWRENCE and James HALL. Evaluating Texas Instruments Phase Light Modulator (PLM). In: *Ocean Sensing and Monitoring XIV*: *Ocean Sensing and Monitoring XIV*. Orlando, United States: SPIE, 2022, pp. 18. ISBN 978-1-5106-5112-8. Available from: doi:10.1117/12.2623938.

[166] DENG, Xianyue, Chin-I TANG, Chuan LUO and Yuzuru TAKASHIMA. Diffraction Efficiency of MEMS Phase Light Modulator, TI-PLM, for Quasi-Continuous and Multi-Point Beam Steering. *Micromachines*. 2022, vol. 13, no. 6, pp. 966. ISSN 2072-666X. Available from: doi:10.3390/mi13060966.

[167] GUAN, Jiafan, Zhipeng DONG, Xianyue DENG and Yuzuru TAKASHIMA. Optical Enhancement of Diffraction Efficiency of Texas Instruments Phase Light Modulator for Beam Steering in Near Infrared. *Micromachines*. 2022, vol. 13, no. 9, pp. 1393. ISSN 2072-666X. Available from: doi:10.3390/mi13091393.

[168] LUKIC, Aleksandar, Sebastian DOCHOW, Hyeonsoo BAE, Gregor MATZ, Ines LATKA, Bernhard MESSERSCHMIDT, Michael SCHMITT and Jürgen POPP. Endoscopic Fiber Probe for Nonlinear Spectroscopic Imaging. *Optica*. 2017, vol. 4, no. 5, pp. 496–501. ISSN 2334-2536. Available from: doi:10.1364/OPTICA.4.000496.

[169] SAAR, Brian G., Richard S. JOHNSTON, Christian W. FREUDIGER, X. Sunney XIE and Eric J. SEIBEL. Coherent Raman Scanning Fiber Endoscopy. *Optics Letters*. 2011, vol. 36, no. 13, pp. 2396–2398. ISSN 1539-4794. Available from: doi:10.1364/OL.36.002396.

[170] HELLERER, Thomas, Annika M.K. ENEJDER and Andreas ZUMBUSCH. Spectral Focusing: High Spectral Resolution Spectroscopy with Broad-Bandwidth Laser Pulses. *Applied Physics Letters*. 2004, vol. 85, no. 1, pp. 25–27. ISSN 1077-3118. Available from: doi:10.1063/1.1768312.

[171] ROCHA-MENDOZA, Israel, Wolfgang LANGBEIN and Paola BORRI. Coherent Anti-Stokes Raman Microspectroscopy Using Spectral Focusing with Glass Dispersion. *Applied Physics Letters*. 2008, vol. 93, no. 20, pp. 201103. ISSN 1077-3118. Available from: doi:10.1063/1.3028346.

[172] LANGBEIN, Wolfgang, Israel ROCHA-MENDOZA and Paola BORRI. Coherent Anti-Stokes Raman Micro-Spectroscopy Using Spectral Focusing: Theory and Experiment. *Journal of Raman Spectroscopy*. 2009, vol. 40, no. 7, pp. 800–808. ISSN 1097-4555. Available from: doi:10.1002/jrs.2264.

[173] FU, Dan, Gary HOLTOM, Christian FREUDIGER, Xu ZHANG and Xiaoliang Sunney XIE. Hyperspectral Imaging with Stimulated Raman Scattering by Chirped Femtosecond Lasers. *The Journal of Physical Chemistry B*. 2013, vol. 117, no. 16, pp. 4634–4640. ISSN 1520-5207. Available from: doi:10.1021/jp308938t.

[174] HERDZIK, Krzysztof P., Konstantinos N. BOURDAKOS, Peter B. JOHNSON, Adam P. LISTER, Aleksandra P. PITERA, Chun-yu GUO, Peter HORAK, David J. RICHARDSON, Jonathan H. V. PRICE and Sumeet MAHAJAN. Multimodal Spectral Focusing CARS and SFG Microscopy with a Tailored Coherent Continuum from a Microstructured Fiber. *Applied Physics B*. 2020, vol. 126, no. 5, pp. 84. ISSN 1432-0649. Available from: doi:10.1007/s00340-020-7406-6.

[175] KEARNEY, Sean P. Bandwidth Optimization of Femtosecond Pure-Rotational Coherent Anti-Stokes Raman Scattering by Pump/Stokes Spectral Focusing. *Applied Optics*. 2014, vol. 53, no. 28, pp. 6579–6585. ISSN 1539-4522. Available from: doi:10.1364/AO.53.006579.

[176] PORQUEZ, J. G. and A. D. SLEPKOV. Application of Spectral-Focusing-CARS Microscopy to Pharmaceutical Sample Analysis. *AIP Advances*. 2018, vol. 8, no. 9, pp. 095213. ISSN 2158-3226. Available from: doi:10.1063/1.5027273.

[177] MOHSENI, Mojtaba, Christoph POLZER and Thomas HELLERER. Resolution of Spectral Focusing in Coherent Raman Imaging. *Optics Express*. 2018, vol. 26, no. 8, pp. 10230–10241. ISSN 1094-4087. Available from: doi:10.1364/OE.26.010230.

[178] NEMOTO, Tomomi, Ryosuke KAWAKAMI, Terumasa HIBI, Koichiro IIJIMA and Kohei OTOMO. Two-Photon Excitation Fluorescence Microscopy and Its Application in Functional Connectomics. *Microscopy*. 2015, vol. 64, no. 1, pp. 9–15. ISSN 2050-5701. Available from: doi:10.1093/jmicro/dfu110.

[179] CAMPAGNOLA, P.J. and C.-Y. DONG. Second Harmonic Generation Microscopy: Principles and Applications to Disease Diagnosis. *Laser & Photonics Reviews*. 2011, vol. 5, no. 1, pp. 13–26. ISSN 1863-8880. Available from: doi:10.1002/lpor.200910024.

[180] PATTERSON, George H. and David W. PISTON. Photobleaching in Two-Photon Excitation Microscopy. *Biophysical Journal*. 2000, vol. 78, no. 4, pp. 2159–2162. ISSN 0006-3495. Available from: doi:10.1016/S0006-3495(00)76762-2.

[181] TURCOTTE, Raphaël, Carla C. SCHMIDT, Martin J. BOOTH and Nigel J. EMPTAGE. *Two-Photon Fluorescence Imaging of Live Neurons Using a Multimode Optical Fiber*. Neuroscience, 2020. Available from: doi:10.1101/2020.04.27.063388.

[182] FITTINGHOFF, David N., Ian A. WALMSLEY, Jason L. BOWIE, John N. SWEETSER, Richard T. JENNINGS, Marco A. KRUMBÜGEL, Kenneth W. DELONG and Rick TREBINO. Measurement of the Intensity and Phase of Ultraweak, Ultrashort Laser Pulses. *Optics Letters*. 1996, vol. 21, no. 12, pp. 884–886. ISSN 1539-4794. Available from: doi:10.1364/OL.21.000884.

[183] BOWLAN, Pamela, Pablo GABOLDE, Aparna SHREENATH, Kristan MCGRESHAM, Rick TREBINO and Selcuk AKTURK. Crossed-Beam Spectral Interferometry: A Simple, High-Spectral-Resolution Method for Completely Characterizing Complex Ultrashort Pulses in Real Time. *Optics Express*. 2006, vol. 14, no. 24, pp. 11892–11900. ISSN 1094-4087. Available from: doi:10.1364/OE.14.011892.

[184] BOWLAN, Pamela, Pablo GABOLDE, Matthew A. COUGHLAN, Rick TREBINO and Robert J. LEVIS. Measuring the Spatiotemporal Electric Field of Ultrashort Pulses with High Spatial and Spectral Resolution. *Journal of the Optical Society of America B*. 2008, vol. 25, no. 6, pp. A81–A92. ISSN 0740-3224. Available from: doi:10.1364/JOSAB.25.000A81.

[185] BOWLAN, Pamela, Ulrike FUCHS, Rick TREBINO and Uwe D. ZEITNER. Measuring the Spatiotemporal Electric Field of Tightly Focused Ultrashort Pulses with Sub-Micron Spatial Resolution. *Optics Express*. 2008, vol. 16, no. 18, pp. 13663–13675. ISSN 1094-4087. Available from: doi:10.1364/OE.16.013663.

[186] HE, Hongsen, Huajun TANG, Meng ZHOU, Hei MING LAI, Tian QIAO, Yuxuan REN, Cora S. W. LAI, Ho KO, Xiaoming WEI, Zhongmin YANG, Kevin K. TSIA and Kenneth K. Y. WONG. Deep-Tissue Two-Photon Microscopy with a Frequency-Doubled All-Fiber Mode-Locked Laser at 937 Nm. *Advanced Photonics Nexus*. 2022, vol. 1, no. 02, pp. 026001. ISSN 2791-1519. Available from: doi:10.1117/1.APN.1.2.026001.

[188] MAO, Youxin, Shoude CHANG, Sherif SHERIF and Costel FLUERARU. Graded-Index Fiber Lens Proposed for Ultrasmall Probes Used in Biomedical Imaging. *Applied Optics*. 2007, vol. 46, no. 23, pp. 5887–5894. ISSN 1539-4522. Available from: doi:10.1364/AO.46.005887.

[189] LI, Jiawen, Simon THIELE, Bryden C. QUIRK, Rodney W. KIRK, Johan W. VERJANS, Emma AKERS, Christina A. BURSILL, Stephen J. NICHOLLS, Alois M. HERKOMMER, Harald GIESSEN and Robert A. MCLAUGHLIN. Ultrathin Monolithic 3D Printed Optical Coherence Tomography Endoscopy for Preclinical and Clinical Use. *Light: Science & Applications*. 2020, vol. 9, no. 124. ISSN 2047-7538. Available from: doi:10.1038/s41377-020-00365-w.

[190] WANG, Tianshi, Antonius F. W. van der STEEN and Gijs van SOEST. Numerical Analysis of Astigmatism Correction in Gradient Refractive Index Lens Based Optical Coherence Tomography Catheters. *Applied Optics*. 2012, vol. 51, no. 21, pp. 5244–5252. ISSN 1539-4522. Available from: doi:10.1364/AO.51.005244.

[191] KIM, Jun Ki, Woei Ming LEE, Pilhan KIM, Myunghwan CHOI, Keehoon JUNG, Seonghoon KIM and Seok Hyun YUN. Fabrication and Operation of GRIN Probes for in Vivo Fluorescence Cellular Imaging of Internal Organs in Small Animals. *Nature Protocols*. 2012, vol. 7, no. 8, pp. 1456–1469. ISSN 1750-2799. Available from: doi:10.1038/nprot.2012.078.

[192] BÉLANGER, E., S. BÉGIN, S. LAFFRAY, Y. DE KONINCK, R. VALLÉE and D. CÔTÉ. Quantitative Myelin Imaging with Coherent Anti-Stokes Raman Scattering Microscopy: Alleviating the Excitation Polarization Dependence with Circularly Polarized Laser Beams. *Optics Express*. 2009, vol. 17, no. 21, pp. 18419–18432. ISSN 1094-4087. Available from: doi:10.1364/OE.17.018419.

[193] De VITO, Giuseppe, Angelo BIFONE and Vincenzo PIAZZA. Rotating-Polarization CARS Microscopy: Combining Chemical and Molecular Orientation Sensitivity. *Optics Express*. 2012, vol. 20, no. 28, pp. 29369–29377. ISSN 1094-4087. Available from: doi:10.1364/OE.20.029369.

[194] ODIN, Christophe, Thomas GUILBERT, Alia ALKILANI, Olena P. BORYSKINA, Vincent FLEURY and Yann LE GRAND. Collagen and Myosin Characterization by Orientation Field Second Harmonic Microscopy. *Optics Express*. 2008, vol. 16, no. 20, pp. 16151–16165. ISSN 1094-4087. Available from: doi:10.1364/OE.16.016151.

[195] ROUÈDE, Denis, Emmanuel SCHAUB, Jean-Jacques BELLANGER, Frédéric EZAN, Jean-Claude SCIMECA, Georges BAFFET and François TIAHO. Determination of Extracellular Matrix Collagen Fibril Architectures and Pathological Remodeling by Polarization Dependent Second Harmonic Microscopy. *Scientific Reports*. 2017, vol. 7, no. 1, pp. 12197. ISSN 2045-2322. Available from: doi:10.1038/s41598-017-12398-0.

[196] GOLARAEI, Ahmad, Leila B. MOSTAÇO-GUIDOLIN, Vaishnavi RAJA, Roya NAVAB, Tao WANG, Shingo SAKASHITA, Kazuhiro YASUFUKU, Ming-Sound TSAO, Brian C. WILSON and Virginijus BARZDA. Polarimetric Second-Harmonic Generation Microscopy of the Hierarchical Structure of Collagen in Stage I-III Non-Small Cell Lung Carcinoma. *Biomedical Optics Express*. 2020, vol. 11, no. 4, pp. 1851–1863. ISSN 2156-7085. Available from: doi:10.1364/BOE.387744.

[197] TOKARZ, Danielle, Richard CISEK, Ariana JOSEPH, Sylvia L. ASA, Brian C. WILSON and Virginijus BARZDA. Characterization of Pathological Thyroid Tissue Using Polarization-Sensitive Second Harmonic Generation Microscopy. *Laboratory Investigation*. 2020, vol. 100, no. 10, pp. 1280–1287. ISSN 0023-6837. Available from: doi:10.1038/s41374-020-0475-7.

[198] GUAN, Yefeng, Ori KATZ, Eran SMALL, Jianying ZHOU and Yaron SILBERBERG. Polarization Control of Multiply Scattered Light through Random Media by Wavefront Shaping. *Optics Letters*. 2012, vol. 37, no. 22, pp. 4663–4665. ISSN 1539-4794. Available from: doi:10.1364/OL.37.004663.

[199] TRIPATHI, Santosh, Richard PAXMAN, Thomas BIFANO and Kimani C. TOUSSAINT. Vector Transmission Matrix for the Polarization Behavior of Light Propagation in Highly Scattering Media. *Optics Express*. 2012, vol. 20, no. 14, pp. 16067–16076. ISSN 1094-4087. Available from: doi:10.1364/OE.20.016067.

[200] De AGUIAR, Hilton B., Sylvain GIGAN and Sophie BRASSELET. Polarization Recovery through Scattering Media. *Science Advances*. 2017, vol. 3, no. 9, pp. e1600743. ISSN 2375-2548. Available from: doi:10.1126/sciadv.1600743.

[201] XIONG, Wen, Chia Wei HSU, Yaron BROMBERG, Jose Enrique ANTONIO-LOPEZ, Rodrigo AMEZCUA CORREA and Hui CAO. Complete Polarization Control in Multimode Fibers with Polarization and Mode Coupling. *Light: Science & Applications*. 2018, vol. 7, no. 54. ISSN 2047-7538. Available from: doi:10.1038/s41377-018-0047-4.

[202] BRUSTLEIN, Sophie, Pascal BERTO, Richard HOSTEIN, Patrick FERRAND, Cyrille BILLAUDEAU, Didier MARGUET, Alistair MUIR, Jonathan KNIGHT and Hervé RIGNEAULT. Double-Clad Hollow Core Photonic Crystal Fiber for Coherent Raman Endoscope. *Optics Express*. 2011, vol. 19, no. 13, pp. 12562–12568. ISSN 1094-4087. Available from: doi:10.1364/OE.19.012562.

[203] BALU, Mihaela, Gangjun LIU, Zhongping CHEN, Bruce J. TROMBERG and Eric O. POTMA. Fiber Delivered Probe for Efficient CARS Imaging of Tissues. *Optics Express*. 2010, vol. 18, no. 3, pp. 2380–2388. ISSN 1094-4087. Available from: doi:10.1364/OE.18.002380.

[204] LOMBARDINI, Alberto, Vasyl MYTSKANIUK, Siddharth SIVANKUTTY, Esben Ravn ANDRESEN, Xueqin CHEN, Jérôme WENGER, Marc FABERT, Nicolas JOLY, Frédéric LOURADOUR, Alexandre KUDLINSKI and Hervé RIGNEAULT. High-Resolution Multimodal Flexible Coherent Raman Endoscope. *Light: Science & Applications*. 2018, vol. 7, no. 10. ISSN 2047-7538. Available from: doi:10.1038/s41377-018-0003-3.

[205] WANG, Zhiyong, Liang GAO, Pengfei LUO, Yaliang YANG, Ahmad A. HAMMOUDI, Kelvin K. WONG and Stephen T. C. WONG. Coherent Anti-Stokes Raman Scattering Microscopy Imaging with Suppression of Four-Wave Mixing in Optical Fibers. *Optics Express*. 2011, vol. 19, no. 9, pp. 7960–7970. ISSN 1094-4087. Available from: doi:10.1364/OE.19.007960.

[206] WANG, Zhiyong, Yongjun LIU, Liang GAO, Yuanxin CHEN, Pengfei LUO, Kelvin K. WONG and Stephen T. C. WONG. Use of Multimode Optical Fibers for Fiber-Based Coherent Anti-Stokes Raman Scattering Microendoscopy Imaging. *Optics Letters*. 2011, vol. 36, no. 15, pp. 2967–2969. ISSN 1539-4794. Available from: doi:10.1364/OL.36.002967.

[207] LU, Fa-Ke, Srinjan BASU, Vivien IGRAS, Mai P. HOANG, Minbiao JI, Dan FU, Gary R. HOLTOM, Victor A. NEEL, Christian W. FREUDIGER, David E. FISHER and X. Sunney XIE. Label-Free DNA Imaging in Vivo with Stimulated Raman Scattering Microscopy. *Proceedings of the National Academy of Sciences*. 2015, vol. 112, no. 37, pp. 11624–11629. ISSN 0027-8424. Available from: doi:10.1073/pnas.1515121112.

[208] MAHOU, Pierre, Maxwell ZIMMERLEY, Karine LOULIER, Katherine S. MATHO, Guillaume LABROILLE, Xavier MORIN, Willy SUPATTO, Jean LIVET, Delphine DÉBARRE and Emmanuel BEAUREPAIRE. Multicolor Two-Photon Tissue Imaging by Wavelength Mixing. *Nature Methods*. 2012, vol. 9, no. 8, pp. 815–818. ISSN 1548-7105. Available from: doi:10.1038/nmeth.2098.

[209] SADEGH, Sanaz, Mu-Han YANG, Christopher G. L. FERRI, Martin THUNEMANN, Payam A. SAISAN, Zhe WEI, Erik A. RODRIGUEZ, Stephen R. ADAMS, Kivilcim KILIÇ, David A. BOAS, Sava SAKADŽIĆ, Anna DEVOR and Yeshaiahu FAINMAN. Efficient Non-Degenerate Two-Photon Excitation for Fluorescence Microscopy. *Optics Express*. 2019, vol. 27, no. 20, pp. 28022–28035. ISSN 1094-4087. Available from: doi:10.1364/OE.27.028022.

[210] POTMA, Eric O. and X. Sunney XIE. Detection of Single Lipid Bilayers with Coherent Anti-Stokes Raman Scattering (CARS) Microscopy. *Journal of Raman Spectroscopy*. 2003, vol. 34, no. 9, pp. 642–650. ISSN 1097-4555. Available from: doi:10.1002/jrs.1045.

Research outputs

Publications

Publications related to the thesis

- STIBŮREK, Miroslav, Petra ONDRÁČKOVÁ, Tereza TUČKOVÁ, Sergey TURTAEV, Martin ŠILER, **Tomáš PIKÁLEK**, Petr JÁKL, André GOMES, Jana KREJČÍ, Petra KOLBÁBKOVÁ, Hana UHLÍŘOVÁ and Tomáš ČIŽMÁR. 110 µm Thin Endo-Microscope for Deep-Brain in Vivo Observations of Neuronal Connectivity, Activity and Blood Flow Dynamics. *Nature Communications*. 2023, vol. 14, pp. 1897. ISSN 2041-1723. Available from: doi:10.1038/s41467-023-36889-z

- **PIKÁLEK, Tomáš**, Miroslav STIBŮREK, Stephen SIMPSON, Tomáš ČIŽMÁR and Johanna TRÄGÅRDH. Suppression of the Non-Linear Background in a Multimode Fibre CARS Endoscope. *Biomedical Optics Express*. 2022, vol. 13, no. 2, pp. 862–864. ISSN 2156-7085. Available from: doi:10.1364/BOE.450375

- CIFUENTES, Angel, **Tomáš PIKÁLEK**, Petra ONDRÁČKOVÁ, Rodrigo AMEZCUA-CORREA, José Enrique ANTONIO-LOPEZ, Tomáš ČIŽMÁR and Johanna TRÄGÅRDH. Polarization-Resolved Second-Harmonic Generation Imaging through a Multimode Fiber. *Optica*. 2021, vol. 8, no. 8, pp. 1065–1074. ISSN 2334-2536. Available from: doi:10.1364/OPTICA.430295

- SILVEIRA, Beatriz M., **Tomáš PIKÁLEK**, Miroslav STIBŮREK, Petra ONDRÁČKOVÁ, Petr JÁKL, Ivo T. LEITE and Tomáš ČIŽMÁR. Side-View Holographic Endomicroscopy via a Custom-Terminated Multimode Fibre. *Optics Express*. 2021, vol. 29, no. 15, pp. 23083–23095. ISSN 1094-4087. Available from: doi:10.1364/OE.426235

- TRÄGÅRDH, Johanna, **Tomáš PIKÁLEK**, Mojmír ŠERÝ, Tobias MEYER, Jürgen POPP and Tomáš ČIŽMÁR. Label-Free CARS Microscopy through a Multimode Fibre Endoscope. *Optics Express*. 2019, vol. 27, no. 21, pp. 30055–30066. ISSN 1094-4087. Available from: doi:10.1364/OE.27.030055

- **PIKÁLEK, Tomáš**, Johanna TRÄGÅRDH, Stephen SIMPSON and Tomáš ČIŽMÁR. Wavelength Dependent Characterization of a Multimode Fibre Endoscope. *Optics Express*. 2019, vol. 27, no. 20, pp. 28239–28253. ISSN 1094-4087. Available from: doi:10.1364/OE.27.028239

Other publications

- TINOCO, Hector A., Jakub HOLZER, **Tomáš PIKÁLEK**, Zdeněk BUCHTA, Josef LAZAR, Alice CHLUPOVÁ, Tomáš KRUML and Pavel HUTAŘ. Determination of Elastic Parameters of Si3N4 Thin Films by Means of a Numerical Approach and Bulge Tests. *Thin Solid Films*. 2019, vol. 672, pp. 66–74. ISSN 0040-6090. Available from: doi:10.1016/j.tsf.2018.12.039

- BUCHTA, Zdeněk, Martin ŠARBORT, Martin ČÍŽEK, Václav HUCL, Šimon ŘEŘUCHA, **Tomáš PIKÁLEK**, Štěpánka DVOŘÁČKOVÁ, František DVOŘÁČEK, Jan KŮR, Pavel KONEČNÝ, Martin WEIGL, Josef LAZAR and Ondřej ČÍP. System for Automatic Gauge Block Length Measurement Optimized for Secondary Length Metrology. *Precision Engineering*. 2017, vol. 49, pp. 322–331. ISSN 0141-6359. Available from: doi:10.1016/j.precisioneng.2017.03.002

Conferences

Conference proceedings

- STIBŮREK, Miroslav, Petr JÁKL, **Tomáš PIKÁLEK**, Petra ONDRÁČKOVÁ and Tomáš ČIŽMÁR. Custom: Terminated Multimode Fibre Probe for Holographic Micro-Endoscopy. In: *22nd Polish-Slovak-Czech Optical Conference on Wave and Quantum Aspects of Contemporary Optics*: *22nd Polish-Slovak-Czech Optical Conference on Wave and Quantum Aspects of Contemporary Optics*. Wojanow, Poland: SPIE, 2022, pp. 38. ISBN 978-1-5106-6111-0. Available from: doi:10.1117/12.2664219

- TRÄGÅRDH, Johanna, **Tomáš PIKÁLEK**, Miroslav STIBŮREK, Stephen SIMPSON, Angel CIFUENTES and Tomáš ČIŽMÁR. CARS Microscopy Through a Multimode Fiber Probe with Reduced Four-Wave Mixing Background. In: *Biophotonics Congress: Biomedical Optics 2022 (Translational, Microscopy, OCT, OTS, BRAIN)*: *Clinical and Translational Biophotonics*. Fort Lauderdale, Florida: Optica Publishing Group, 2022, pp. JM3A.43. ISBN 978-1-957171-03-6. Available from: doi:10.1364/TRANSLATIONAL.2022.JM3A.43

- TRÄGÅRDH, Johanna, **Tomáš PIKÁLEK**, Miroslav STIBŮREK, Rodrigo AMEZCUA-CORREA, José Enrique ANTONIO-LOPEZ and Tomáš ČIŽMÁR. Suppressing the Non-linear Fiber Background in Multimode Fiber Endoscopy. In: *Frontiers in Optics + Laser Science 2021*: *Frontiers in Optics*. Washington, DC: Optica Publishing Group, 2021, pp. JTu1A.118. Available from: doi:10.1364/FIO.2021.JTu1A.118

- CIFUENTES, Angel, Johanna TRÄGÅRDH, **Tomáš PIKÁLEK**, Petra ONDRÁČKOVÁ, Rodrigo AMEZCUA-CORREA, José Enrique ANTONIO-LOPEZ and Tomáš ČIŽMÁR. Excitation Polarization Resolved Second Harmonic Generation Microscopy Through a Multimode Optical Fiber. In: *Biophotonics Congress 2021*: *Novel Techniques in Microscopy*. Washington, DC: Optica Publishing Group, 2021, pp. NTh1C.3. ISBN 978-1-943580-85-9. Available from: doi:10.1364/NTM.2021.NTh1C.3

- CIFUENTES, Angel, Johanna TRÄGÅRDH, **Tomáš PIKÁLEK**, Mojmír ŠERÝ, Denis AKIMOV, Tobias MEYER, Jürgen POPP, Rodrigo AMEZCUA-CORREA and Tomáš ČIŽMÁR. Non-Linear Label-Free Imaging through a Multimode Graded Index Optical Fibre. *EPJ Web of Conferences*. 2020, vol. 238, pp. 04006. ISSN 2100-014X. Available from: doi:10.1051/epjconf/202023804006

- TRÄGÅRDH, Johanna, **Tomáš PIKÁLEK**, Mojmír ŠERÝ, Denis AKIMOV, Tobias MEYER, Jürgen POPP and Tomáš CIŽMÁR. Coherent Anti-Stokes Raman Scattering Microscopy through a Multimode Fiber Endoscope. In: *Biomedical Spectroscopy, Microscopy, and Imaging*: *Biomedical Spectroscopy, Microscopy, and Imaging*. Online Only, France: SPIE, 2020, pp. 6. ISBN 978-1-5106-3490-9. Available from: doi:10.1117/12.2555080

- TRÄGÅRDH, Johanna, **Tomáš PIKÁLEK**, Stephen SIMPSON, Petr JÁKL, Martin ŠILER, Tomáš TYC and Tomáš ČIŽMÁR. Towards Focusing Broad Band Light through a Multimode Fiber Endoscope. In: *Adaptive Optics and Wavefront Control for Biological Systems V*. San Francisco, United States: SPIE, 2019, pp. 18. ISBN 978-1-5106-2414-6. Available from: doi:10.1117/12.2510449

- ŠARBORT, Martin, Šimon ŘEŘUCHA, **Tomáš PIKÁLEK**, Tomáš FOŘT, Josef LAZAR, Miroslava HOLÁ and Jindřich OULEHLA. Using Spatial Light Modulator for Correction of Wavefront Reflected from Optically Rough Surface. In: *Speckle 2018: VII International Conference on Speckle Metrology*. Janów Podlaski, Poland: SPIE, 2018, pp. 38. ISBN 978-1-5106-2297-5. Available from: doi:10.1117/12.2318705

- **PIKÁLEK, Tomáš**, Martin ŠARBORT, Ondřej ČÍP, Minh Tuan PHAM, Adam LEŠUNDÁK, Lenka PRAVDOVÁ and Zdeněk BUCHTA. Phase and Group Refractive Indices of Air Calculation by Fitting of Phase Difference Measured Using a Combination of Laser and Low-Coherence Interferometry. In: *SPIE Optical Metrology*. Munich, Germany: 2017, pp. 103293I. Available from: doi:10.1117/12.2269952

- HOLZER, Jakub, **Tomáš PIKÁLEK**, Zdeněk BUCHTA, Josef LAZAR, Hector Andres TINOCO, Alice CHLUPOVÁ and Tomáš KRUML. Development of the Bulge Test Equipment for Measuring Mechanical Properties of Thin Films. In: *Metal 2017: 26th International Conference on Metallurgy and Materials*. Brno: 2017, pp. 1053–1058. ISBN 978-80-87294-79-6

- BUCHTA, Zdeněk, Martin ŠARBORT, Martin ČÍŽEK, Václav HUCL, Šimon ŘEŘUCHA, **Tomáš PIKÁLEK**, Štěpánka DVOŘÁČKOVÁ, František DVOŘÁČEK, Jan KŮR, Pavel KONEČNÝ, Josef LAZAR and Ondřej ČÍP. Automatic System for Gauge Block Calibration Optimized to Meet Legal Length Metrology Requirements. In: *20th Slovak-Czech-Polish Optical Conference on Wave and Quantum Aspects of Contemporary Optics*. Jasná, Slovakia: 2016, pp. 101420O. Available from: doi:10.1117/12.2263367

Other conference contributions

- 21st Czech-Polish-Slovak Optical Conference on Wave and Quantum Aspects of Contemporary Optics, Lednice 2018. Poster: *Wavelength dependent characterization of a multimode fibre endoscope*

- Laser 57, Třešť 2017. Talk: *Interferometric measurement of a deformation of a thin membrane during the bulge test*
- Laser 56, Třešť 2016. Talk: *Air refractive index measurement using low-coherence interferometry*

Applied outputs

Patents

- ČIŽMÁR, Tomáš, **Tomáš PIKÁLEK**, Johanna TRÄGÅRDH and Miroslav STIBŮREK. Composite optical fibre for holographic endoscopy. 2022. Patent no. 309415

Utility models

- LAZAR, Josef, Zdeněk BUCHTA and **Tomáš PIKÁLEK**. An optical radiation source assembly with an optional coherence length. 2018. Utility model no. 31749
- **PIKÁLEK, Tomáš**, Václav HUCL, Stanislav KRÁTKÝ, Vladimír KOLAŘÍK and Ondřej ČÍP. Non-contact light scattering sensor for surface diagnostics. 2019. Utility model no. 33047